Design, synthesis and biological evaluation of novel lipid-based nanoparticle delivery system for metabolic re-engineering

A thesis submitted for the degree of Doctor of Philosophy from Imperial College London

Leigh Pauline Brody

Imperial College London

Metabolic and Molecular Imaging Group

The copyright of this thesis rests with the author and is made available under a Creative Commons Attribution Non-Commercial No Derivatives licence. Researchers are free to copy, distribute or transmit the thesis on the condition that they attribute it, that they do not use it for commercial purposes and that they do not alter, transform or build upon it. For any reuse or redistribution, researchers must make clear to others the licence terms of this work. Additionally, this work is licensed under a Creative Commons Attribution 3.0 Unported License.

Abstract

Dietary supplementation with fibre has been shown to ameliorate features of the metabolic syndrome and inhibit malignant growth in certain types of cancer. These effects have been linked to short-chain fatty acids (SCFA), mostly acetate. However, the ubiquitous role of SCFAs in metabolism, combined with a short tissue half-life and the non-targeted nature of oral and peripheral administrations make achieving phenotypically relevant levels of SCFA by standard delivery techniques challenging and limit their therapeutic potential. Liposomal encapsulation of a therapeutic agent overcomes these issues by protecting against degradation, increasing circulation time and passively targeting both the liver and tumour tissue.

In this research project, I have designed a bifunctional liposome formulation to transport SCFA, monitored their distribution and uptake utilising visualisation by MRI, PET/CT and fluorescence microscopy. These bifunctional liposomes were useful for effectively encapsulating small molecules within their aqueous core, which in this case was acetate, and capable of acetate delivery into cells while also being amenable to cellular imaging. I have shown that preferential delivery of liposome encapsulated acetate (LITA) nanoparticles to key sites of metabolic control provide beneficial therapeutic effects in animal models of both obesity and cancer. Chronic administration of LITA nanoparticles in an obeseogenic model led to a significant reduction in adiposity, intrahepatocellular lipid, inflammatory tone and genetic indication of a decrease fatty acid synthesis in the liver. Application of LITA in a murine xenograft model caused an inhibition of tumour growth in three colorectal cancer cell lines: HT-29, HCT116 p53+/+ and HCT116 p53-/-. The mechanisms for these two outcomes are not fully defined; however cellular energy homeostasis of both scenarios was restored. These results indicate that LITA nanoparticles can be used to improve multiple metabolic pathways, *in vivo*.

Declaration of Contributors

The majority of the work in thesis was performed by the author. All collaboration and assistance is described below.

Chapter 2

Liposome formulations were in collaboration with Dr. Andrew Miller and carried out with the help of Dr. Meliz Sahuri. ^{1}H-NMR spectroscopy scans of liposome samples were performed by Dr. Harry Parkes.

Chapter 3

Serum analysis carried out to obtain concentrations of metabolic and inflammatory markers were performed by the Core Biochemical Assay Laboratory located in Cambridge, UK. The Microarray study and analysis was carried out with the help of the Genomic Medicine platform, in particular Dr. Tom Oates and Dr. Enrico Petretto.

Chapter 4

Luciferase-stable CRC cell lines HCTp53+/+ and HCTp53-/- were supplied in collaboration by Dr. Samer Alzoubi and Dr. Nabil Hajji.

Acknowledgements

This thesis is the end of my journey in obtaining my PhD, upon which many people have contributed and given their support. Having started this field of research as a masters student, I certainly did not imaging defending a PhD thesis several years later, and now could not imagine doing anything else.

I would like to express my immense gratitude to my supervisors Professor Jimmy Bell Professor Gary Frost and Professor Nabil Hajji, for taking me on board and giving me the opportunity to work on such a multidisciplinary project. They have been supportive and given me the freedom to pursue various projects without objection and allowing me to learn from my successes and failures. I am also thankful to my other advisors, Dr. Louise Thomas, Dr. Andy Miller, who provided encouraging and constructive feedback. I could not have asked for a more supportive and patient group to see me through this journey. Special thank you to Dr. Jim Parkinson for his painstaking efforts reviewing this thesis and for all the laughs shared over the years.

To my comrades, past and present, in the Metabolic and Molecular Imaging group and the Biological Imaging Unit, thank you for making these past years a memorable learning experience and made my time here enjoyable. Long live the Cyclotron Building!

To all my friends at home, thank you for the long-distance support and visits over the years. Your friendships have kept me grounded as the person I left as and have helped me evolve into the person I am today. To all my friends abroad, you've been my surrogate family and I could not have done this without you. I am truly and earnestly grateful for all your support, encouragement and love. Especially my NH family, for who I can truly call this place home.

Most importantly, I would like to thank my family for being generally wonderful whilst being so far away. In particular, my parents, who have instilled within me a love for pursuing my interests and would not be who I am today without you. My siblings, Dave and Rick, who has been incredibly supportive along this journey. Dave, for being the best host when I returned home and being so supportive to my various pursuits; and Rick, for putting up with my tough love over the years and never forgetting that I'm always right. I would also like to thank my grandmother, Grace Forrest, who has a very special place in my heart. To all of you, I thank you.

Table of Contents

Abstract **2**

Declaration of Contributors **3**

Acknowledgements **4**

Table of Contents **6**

List of Figures **11**

List of Tables **17**

List of Equations **19**

Abbreviations **20**

Chapter 1 ..... **24**

General Introduction **24**

1.1 Introduction 25

1.2 The obesity pandemic 25

1.3 Adiposity 26

1.3.1 Differential Roles of Fat Depots *27*

1.3.2 Monitoring of adipose tissue *29*

1.4 Liver Metabolism 29

1.4.1 Altered liver function in the obese state *32*

1.4.2 Monitoring of Liver Fat *33*

1.4.3 Lipotoxicity and Inflammation *34*

1.4.4 Mitochondria *36*

1.5 Dietary Fibre and Obesity 40

1.5.1 Short- Chain Fatty Acids *41*

1.5.2 Acetate Formation and Metabolism 46

1.5.3 Epigenetic modifications 48

1.6 Obesity and cancer 49

1.6.1 Metabolic deregulation 50

1.6.2 Warburg Effect 51

1.6.3 Randle hypothesis 53

1.6.4 SCFA effects on select pathways 55

1.6.6 Limitations of SCFA in obesity and cancer paradigms 56

1.7 Liposomal nanoparticles 57

1.7.1 Principles of liposomes 57

1.7.2 Liposome structure 58

1.7.3 Liposome delivery 59

1.7.2 Tumour specific liposomal delivery 60

1.8 Imaging Modalities for *in vivo* Studies 62

1.8.1 Magnetic Resonance Imaging 63

1.8.2 Computed Tomography 65

1.8.3 Positron Emission Tomography 66

1.8.4 Fluorescence microscopy 66

1.9 Aims and Objectives 67

Chapter 2 68

Formulation and Characterisation of Liposomal Encapsulation of Acetate (*LITA*) 68

2.1 Introduction 69

2.1.1 Aims of Studies 70

2.2 Methods 71

2.2.1 Materials 71

2.2.2 Study 1: Liposome Preparation and Formulation 73

2.2.3 Study 2: Short-Chain Fatty Acid Encapsulation 73

2.2.4 Study 3: Liposome Characterisation 74

2.2.5 Study 4: Liposomal Bio Distribution and in vivo Optimisation 76

2.3 Results 81

2.3.1 Study 1: Liposome Preparation and Formulation 81

2.3.2 Study 2: ^{1}H NMR Spectroscopy of Encapsulated Acetate in Liposomes 91

2.3.3 Study 3: Liposome Characterisation ^{1}H NMR Spectroscopy to Determine Encapsulated Acetate Concentration 94

2.3.4 Study 4: Liposomal Biodistribution and in vivo Optimisation 113

2.3.4 Study 5: Liposomal Encapsulation of Butyrate and Propionate 131

2.4 Chapter Discussion 134

2.4.3 Conclusion 139

Chapter 3 140

***In Vivo* Biological Evaluation of liposome encapsulated acetate nanoparticles (LITA) 140**

3.1 Introduction 141

3.1.1 Aims of Studies 142

3.2 Methods 143

3.2.1 Materials 143

3.2.2 Study 1: Chronic LITA Nanoparticle Administration on an Obesogenic Background 145

3.2.3 Study 2: Chronic LITA Nanoparticle Administration in Metabolic Cages 153

3.2.4 Statistical Analysis 154

3.3 Results 155

3.3.1 Study 1: Chronic LITA Nanoparticle Administration on an Obesogenic Background .. 155

3.3.2 Study 2: Chronic LITA Nanoparticle Administration in Metabolic Cages 195

3.4 Chapter Discussion 200

3.4.4 Conclusion 212

Chapter 4 214

***In Vivo* Biological Evaluation of LITA-xenograft in Tumour Models 214**

4.1 Introduction 215

4.1.1 Aims of Studies 216

4.2 Methods 217

4.2.1 Materials 217

4.2.1.2 In vivo cancer cell lines 217

4.2.2 Study 1: Liposome Preparation, Formulation and Characterisation for Xenograft Model Application 218

4.2.2 Study 2: LITA effects in a Colorectal Cancer Xenograft Model 219

4.3 Results 223

4.3.1 Study 1: Liposome Preparation, Formulation and Characterisation for Xenograft Model Application 223

4.3.2 Study 2: LITA-xenograft effects in a Colorectal Cancer Xenograft Models 228

4.4 Discussion 249

4.5 Conclusion 259

Chapter 5 260

Final Discussion 260

5.1 Final conclusions 261

5.2 Discussion of Methods Used 262

Chapter 3 262

Chapter 4 262

5.3 Limitations to studies 263

5.4 future studies 264

References 266

Appendices 295

List of Figures

Figure 1.1 The central role of the liver in Glucose and Lipid Homeostasis.....31

Figure 1.2 Localisation and monitoring of fat.....34

Figure 1.3 Modulation of Adipose Tissue with Obesity.....36

Figure 1.4 Bioenergetic Functions of Mitochondria 38

Figure 1.5 Hepatic Lipid Metabolism in Health and Disease 40

Figure 1.6 Molecular Figure Structures of Short- Chain Fatty Acids 42

Figure 1.7 Short- Chain Fatty Acid Uptake and Absorption.....44

Figure 1.8 Schematic representation of the effects of short-chain fatty acid 45

Figure 1.9 Metabolic pathways for acetate via acetyl-CoA.....47

Figure 1.10 Schematic diagram of histone acetylation and deacetylation.....49

Figure 1.11 Metabolic Deregulation and Cancer 50

Figure 1.12 Schematic representation of the Warburg Effect.....52

Figure 1.13 Schematic diagram of the Randle cycle 54

Figure 1.14 Basic liposome structure 58

Figure 1.15 Schematic of tumour by nanoparticles via Enhanced Permeation and Retention (EPR) effect.....61

Figure 1.16 Summary of imaging modalities 63

Figure 2.1 Chemical structures of the lipids incorporated into the liposomal bilayer.....72

Figure 2. 2 Illustration of the Float-A-lyzer G2 column 74

Figure 2.3 Liposomal nanoparticle profiles before and after dialysis.....85

Figure 2.4 Size of liposomes after formulation and dialysis- target lipid: 1,2-distearoyl-sn-glycero-3-phosphocholine (DSPC).....86

Figure 2.5 Size of liposomes after formulation and dialysis- target lipid: 3β-Hydroxy-5-cholestene, 5-Cholesten-3β-ol (cholesterol).....87

Figure 2.6 Size of liposomes after formulation and dialysis- target lipid: 1,2-distearoyl-sn-glycero-3-phosphoethanolamine-N-[methoxy(polyethylene glycol)-2000] (DSPE-PEG^{2000}).....88
Figure 2.7 Size of liposomes after formulation and dialysis- N1-cholesteryloxycarbonyl-3,7-diazanonane-1,9-diamine lipid (CDAN).....89
Figure 2. 8 ^{1}H NMR spectra of acetate with added albumin.....92
Figure 2.9 ^{1}H NMR spectra of acetate encapsulated liposomes with added albumin.....93
Figure 2.10 ^{1}H NMR spectra of LITA formulated with 1M acetate.....95
Figure 2.11 ^{1}H NMR spectra of LITA nanoparticles and sodium lactate.....96
Figure 2.12 Acetate encapsulated within the liposomes and measured by 1H MRS - target lipid: 1,2-distearoyl-sn-glycero-3-phosphocholine (DSPC).....99
Figure 2.13 Acetate encapsulated within the liposomes and measured by 1H MRS - target lipid: 3β-Hydroxy-5-cholestene, 5-Cholesten-3β-ol (cholesterol).....100
Figure 2.14 Acetate encapsulated within the liposomes and measured by ^{1}H MRS – target lipid: 1,2-distearoyl-sn-glycero-3-phosphoethanolamine-N- methoxy(polyethylene glycol)-2000] (DSPE-PEG^{2000}).....101
Figure 2.15 Acetate encapsulated within the liposomes and measured by 1H MRS - N1-cholesteryloxycarbonyl-3,7-diazanonane-1,9-diamine lipid (CDAN).....102
Figure 2.16 LITA nanoparticle characterisation- size and payload formulated with 1mM acetate.....105
Figure 2.17 LITA nanoparticle characterisation- size and payload formulated with 10mM acetate.....106
Figure 2. 18 LITA nanoparticle characterisation- size and payload formulated with 100mM acetate.....107
Figure 2.19 LITA nanoparticle characterisation- size and payload formulated with 10M acetate.....108
Figure 2.20 LITA nanoparticle design principles.....111
Figure 2.21 Liposomal nanoparticle sizing method after completed formulation.....112

Figure 2.22 LITA nanoparticle tumour localisation LITA-Rhd identification in the liver by histological fluorescence imaging 114
Figure 2.23 LITA nanoparticle tumour localisation LITA-Rhd identification in the spleen by histological fluorescence imaging 115
Figure 2. 24 LITA nanoparticle tumour localisation LITA-Rhd identification in the kidney by histological fluorescence imaging 116
Figure 2.25 A nanoparticle tumour localisation LITA-Rhd identification in the heart by histological fluorescence imaging 117
Figure 2.26 T1 measurement following administration of LITA nanoparticle conjugated with gadolinium (LITA-Gd) 122
Figure 2.27 PET/CT fused image after injection with [^{18}F]FDG conjugated liposomes 125
Figure 2.28 Standard Uptake Value (SUV) and Area under the curve (AUC) from muscle for 30min post-injection of [18F]FDG or [18F]FDG conjugated liposomes 126
Figure 2.29 Standard Uptake Value (SUV) and Area under the curve (AUC) from heart for 30min post-injection of [^{18}F]FDG or [^{18}F]FDG conjugated liposomes 127
Figure 2.30 Standard Uptake Value (SUV) and Area under the curve (AUC) from brain for 30min post-injection of [18F]FDG or [18F]FDG conjugated liposomes 128
Figure 2. 31 Standard Uptake Value (SUV) and Area under the curve (AUC) from liver for 30min post-injection of [18F]FDG or [18F]FDG conjugated liposomes 129
Figure 2.32 Standard Uptake Value (SUV) and Area under the curve (AUC) from kidneys for 30min post-injection of [18F]FDG or [18F]FDG conjugated liposomes 130
Figure 2.33 Butyrate encapsulated liposomal formulation and characterisation 132
Figure 2.34 Propionate encapsulated liposomal formulation and characterisation 133

Figure 3.1 Timeline of the model carried out for liposomal therapeutic study 145
Figure 3. 2 Effects of average and cumulative food intake of chronic i.p. injections of control to LITA nanoparticles in ad libitum fed mice on high fat diet 156

Figure 3.3 Effects on body weight of chronic i.p. injections of control to LITA nanoparticles in mice on high fat diet 157
Figure 3.4 Whole body adiposity before and after control or LITA administration measured *in vivo* by MRS 159
Figure 3.5 Whole body adiposity change after control and LITA administration measured *in vivo* by ^{1}H MRS.....160
Figure 3.6 Fat distribution in mice after 10 week study on high fat diet with either control or LITA nanoparticle administration 162
Figure 3.7 Adipocyte cell number in mice after 10 week study with either control or LITA nanoparticle administration.....165
Figure 3.8 Adipocyte cell dimensions in mice after 10 week study with either control or LITA nanoparticle administration.....166
Figure 3.9 Lipid content in the liver before (A) and after (B) control and LITA administration as determined by ^{1}H MRS 169
Figure 3. 10 Change in lipid content in the liver as an effect to chronic i.p. control or LITA administration as determined by ^{1}H MRS.....170
Figure 3.11 Organ weight following chronic i.p. injections of either control or LITA nanoparticles during 10 week study 172
Figure 3.12 Organ weight to total body weight ratio in mice following chronic i.p. injections of either control or LITA nanoparticles during 10 week study.....174
Figure 3.13 Serum analysis of metabolic marker of obesity in control and LITA groups.....177
Figure 3.14 Serum analysis of inflammatory marker of obesity in control and LITA groups178
Figure 3.15 Quantitative relative intensity of western blot examining histone deacetylase (HDACs) in total proteins isolated from liver tissue after 10 week obesogenic study in mice receiving either control or LITA administration.....181
Figure 3.16 Western blot bands of histone deacetylase (HDACs) in total proteins isolated from liver tissue after 10 week obesogenic study in mice receiving either control or LITA administration 182

Figure 3.17 Quantitative relative intensity of western blot examining uncoupling protein-1 in brown adipose tissue after 10 week obesogenic study in mice receiving either control or LITA administration.....183
Figure 3.18 Western blot bands of uncoupling protein-1 in brown adipose tissue after 10 week obesogenic study in mice receiving either control or LITA administration 184
Figure 3.19 MA plots of signal intensity for outlier detection and quality control of samples post 10 week chronic study of either LITA or control nanoparticle administration for final analysis.....186
Figure 3.20 Microarray intensity distributions of samples post 10 week chronic study of either LITA or control nanoparticle administration 187
Figure 3.21 A volcano plot of differentially expressed genes in liver tissue from 10 week study of chronic i.p. administration of either LITA or control nanoparticles 188
Figure 3.22 qRT-PCR analysis of gene expression fold changes in mRNA isolated from the liver as a result of chronic LITA treatment in obesogenic model.....190
Figure 3.23 Quantitative relative intensity of western blot examining histone residues in histones isolated from liver tissue after 10 week obesogenic study in mice receiving either control or LITA administration.....193
Figure 3.24 Western blot bands of histone residue proteins in histones isolated from the liver after 10 week obesogenic study in mice receiving either control or LITA administration 194
Figure 3.25 Metabolic cage monitoring of mice after 7 day LITA or control nanoparticle administration- Food and drink intake 196
Figure 3.26 Metabolic cage monitoring of mice after 7 day LITA or control nanoparticle administration- VO_2 and VCO_2 197
Figure 3.27 Metabolic cage monitoring of mice after 7 day LITA or control nanoparticle administration- RER and heat 198
Figure 3.28 Metabolic cage monitoring of mice after 7 day LITA or control nanoparticle administration- XAMB, XTOT and ZTOT.....199

Figure 3.29 Proposed mechanisms on fatty acid synthesis following hepatic delivery.....210
Figure 3.30 Proposed mechanism of global LITA activity following hepatic delivery.....211

Figure 4.1 Liposomal nanoparticle sizing method after completed formulation.....225
Figure 4.2 LITA-Rhd-xenograft nanoparticle tumour localisation LITA-Rhd-xenograft identification in the xenograft tumour by histological fluorescence imaging.....227
Figure 4.3 Effects of LITA-xenograft nanoparticles in murine HT-29 colorectal tumour growth 229
Figure 4.4 Effects of LITA nanoparticles in murine HT-29 colorectal tumours 231
Figure 4.5 Effects of LITA-xenograft nanoparticles in murine HT-29 colorectal tumours at the end of the study.....233
Figure 4.6 Effects of LITA-xenograft nanoparticles in HCT116 p5+/+ colorectal tumour growth.....236
Figure 4.7 Bioluminescence imaging for control or LITA-xenograft treated HCT 116 p53+/+ colorectal cancer cell lines tumour model.....239
Figure 4.8 Bioluminescence imaging for control or LITA-xenograft treated HCT 116 p53+/+ colorectal cancer cell lines tumour model.....240
Figure 4.9 Effects of LITA-xenograft nanoparticles in HCT116 p53-/- colorectal tumour growth.....243
Figure 4.10 Bioluminescence imaging for control or LITA-xenograft treated HCT 116 p53-/- colorectal cancer cell lines tumour model.....246
Figure 4.11 Bioluminescence imaging for control or LITA-xenograft treated HCT 116 p53-/- colorectal cancer cell lines tumour model.....247
Figure 4.12 Effect of LITA-xenograft on Cancer Cell Metabolism 258
Figure 4.13 Mitochondrial responses to dichloracetate administration.....256

Figure 5.1 Mitochondrial calorimetry.....265

List of Tables

Table 2.1 Percentage molar and lipid components of potential liposome formulations.....82

Table 2.2 Quantitative summary from formulation with varying molarities and incorporated lipids 90

Table 2.3 Quantitative summary of acetate encapsulated within the liposomes and measured by ^{1}H MRS 103

Table 2.4 Percentage molar components of liposome formulations.....110

Table 2.5 Histological evaluation of LITA-Rhd at differing acetate concentrations and injection methods.....118

Table 2.6 Histology time course of LITA-Rhd in selected organs.....120

Table 2.7 T1 measurements post administration of LITA nanoparticle conjugated with gadolinium (LITA-Gd) 123

Table 3.1 Ingredients of diets used in feeding studies.....144

Table 3.2 Total white adipose tissue extracted by dissection in mice after 10 week study on high fat diet with either control or LITA nanoparticle administration 163

Table 3.3 Adipocyte cell isolation in mice after 10 week study with either control or LITA nanoparticle administration.....167

Table 3.4 Organ weight following chronic i.p. injections of either control or LITA nanoparticles during 10 week study 173

Table 3. 5 Organ weight to total body weight ratio following chronic i.p. injections of either control or LITA nanoparticles during 10 week study.....175

Table 3.6 Serum analysis from 10 week obesogenic study in mice receiving either chronic LITA or control nanoparticles administration 179

Table 3.7 Summary of qRT-PCR analysis of gene expression fold changes in mRNA isolated from the liver as a result of chronic LITA treatment in obesogenic model.....191

Table 4.1 Effects of LITA-xenograft nanoparticles in murine HT-29 colorectal tumour growth 230

Table 4.2 Summary of qRT-PCR analysis of gene expression fold changes in mRNA isolated from the tumour as a result of chronic LITA-xenograft treatment in HT-29 colorectal cancer xenograft model 234

Table 4.3 Effects of LITA-xenograft nanoparticles in murine HCT116 p5+/+ colorectal tumour growth 237

Table 4.4 Bioluminescence imaging for HCT 116 p53+/+ colorectal cancer cell lines tumour model 241

Table 4.5 Effects of LITA-xenograft nanoparticles in murine HCT116 p5-/- colorectal tumour growth 244

Table 4.6 Bioluminescence imaging for HCT 116 p53-/- colorectal cancer cell lines tumour model 248

List of Equations

Equation 2.1 T_1 values were averaged as mean ± SEM. Unpaired t-test was carried out for statistical analysis. 78

Equation 2.2 Standard Uptake Value (SUV) to obtain uptake of [^{18}F]FDG from PET/CT acquired image 80

Equation 4.1 Volume equation used to measure tumour from calliper 221

Abbreviations

ACC	acetyl-CoA carboxylase
ACO	acyl-CoA oxidase
ACOX1	peroxisomal acly-coenzyme A oxidase 1
AMP	adenosine monophosphate
AMPK	AMP-activated protein kinase
AT	adipose tissue
ATP	adenosine triphosphate
AUC	area under the curve
BAT	brown adipose tissue
BMI	body mass index
CDAN	N^1-cholesteryloxycarbonyl-3,7-diazanonane-1,9-diamine
CLAMS	Comprehensive Lab Animal Monitoring System
CT	computed tomography
CPT-1	carnitine palmitoyltransferase 1
CRC	colorectal cancer
D_2O	deuterium oxide
DAPI	4',6-diamidino-2-phenylindole
DC cholesterol hydrochloride	3ß-[N-(N',N'-dimethylaminoethane)-carbamoyl]cholesterol
DDAB	Dimethyldioctadecylammonium
DIO	diet-induced-obesity
DLPC	1,2-dilauroyl-*sn*-glycero-3-phosphocholine
DMEM	Dulbecco's Modified Eagle Medium
DNL	*de novo* lipogenesis
DOPE	1,2-dioleoyl-*sn*-glycero-3-phosphoethanolamine

DSPE-PEG	1,2-distearoyl-*sn*-glycero-3-phosphoethanolamine-N-[methoxy(polyethylene glycol)
EPR	enhanced permeability and retention
ER	endoplasmic reticulum
FAS	fatty acid synthase
FCS	fetal calf serum
FDG	fluorodeoxyglucose
FID	free induction decay
FFA	free fatty acid
FOV	field of view
Gd	gadolinium
GPR	G-protein-coupled receptor
HAT	histone acetyltransferase
HCC	hepatocellular carcinoma
HDAC	histone deacetylase
HDACi	HDAC inhibitor
HEPES	4-(2-hydroxyethyl)-1-piperazineethanesulfonic acid
HFD	high fat diet
IL	interleukin
i.p.	intraperitoneal
IR	insulin resistance
i.v.	intraveneous
IVC	individually vented cages
KC/GRO	chemokine gro-alpha/ growth-related protein
IHCL	intrahepatocellular lipid
LCFA	Long chain fatty acids
LITA	liposomal encapsulated acetate

LIMMA	Linear Models for MicroArray
MRI	magnetic resonance imaging
MRS	magnetic resonance spectroscopy
MS	metabolic syndrome
NADH	nicotinamide adenine dinucleotide
NAFLD	non-alcoholic fatty liver disease
NASH	non-alcoholic steatohepatitis
NM	nanometer
NMR	nuclear magnetic resonance
OXPHOS	oxidative phosphorylation
PCA	perchloric acid
PDI	polydispersity index
PEI	Polyethylenimine
PEG	polyethylene glycol
PET	positron emission tomography
PPARα	peroxisome proliferator-activated receptor α
ppm	parts per million
qPCR	quantitative real-time PCR
RER	respiratory exchange ratio
RES	reticuloendothelial system
RF	radiofrequency
Rhd	rhodamine
ROI	region of interest
ROS	reactive oxygen species
RS	resistant starch
SAT	subcutaneous adipose tissue

SCFA	short chain fatty acid
SD	standard deviation
SE	spin echo
SEM	standard error of mean
SI	signal intensity
SREBP-1	sterol regulatory element binding protein
SUV	standard uptake value
T	Tesla
T1	relaxation time in longitudinal direction
TCA	tricarboxylic acid
TE	echo time
TG	triglyceride
TNF-α	tumour necrosis factor-α
TOF	time-of-flight
TR	repetition time
UCP	uncoupling protein
VAT	visceral adipose tissue
VCO_2	carbon dioxide expiration
VLDL	very low-density lipoprotein
VO_2	oxygen consumption
WAT	white adipose tissue
WT	wild type
XAMB	horizontal beam breaks
XTOT	total x-axis ambulation
ZTOT	vertical beam breaks

Chapter 1

General Introduction

1.1 Introduction

Cellular metabolic dysregulation is a central premise in the development of many chronic diseases including obesity and cancer [1,2]. Central to this effect appears to be the mitochondrion, either through decline in function or simply a reduction in number and mitochondrial mass [3,4]. These effects compromise not only the metabolic fluxes associated with these cellular organelles, but also appears to affect the ability of cells to manage changes in redox and reactive oxidation species (ROS) production [5, 6]. Due to the increased rates of obesity and corresponding problems associated with metabolic disequilibrium, there is an urgent demand for interventional therapeutic strategies. The desired response to an obese state is typically focused on diet and exercise, however these have been shown to be unsustainable in the long-term [7]. Although bariatric surgery has arisen as a potential long-term solution to the obesity problem, it is not applicable to the general population, it is costly and not without clinical complications [8]. Recently, there has been renewed interest in the potential of metabolic engineering, through the use of small molecules, to achieve metabolic retransformation of abnormal cells and tissues [9-11]. However, making sufficient and sustained metabolic impact though such methods can be difficult, since a suitable small molecule(s) needs to be identified and an appropriate mode of delivery. This clearly requires a new approach if we are to tackle the challenge of metabolic dysregulation *in vivo*.

1.2 The obesity pandemic

Obesity is a major growing health concern affecting people in both developed and underdeveloped nations. Estimates from the World Health Organization in 2010 stated that 1.5 billion adults today (around 35% of the world's population) are thought to be overweight or obese. Obesity occurs because of a positive energy balance, whereby over nutrition exceeds the energy expenditure [12].

A key feature of obesity, the metabolic syndrome (MS), represents a common clinical condition in countries with high incidence of obesity and western dietary patterns [13]. MS is a cluster of medical disorders that, when simultaneously occurring, increase the risk for developing type II diabetes, insulin sensitivity, elevated triglyceride levels, cardiovascular disease, hypertension, lipotoxicity, inflammation and some types of cancer [12,14].

Energy homeostasis is the multi-system balance in energy intake by feeding and energy expenditure by physical activity, basal metabolic rate and adaptive thermogenesis [15]. Energy intake is primarily partitioned towards homeostatic energy expenditure with excess nutrients being stored in the form of triglycerides (TGs) in white adipose tissue (WAT). In some circumstances this deposition of TGs extends to ectopic tissue including liver, pancreas and skeletal muscle [16].

1.3 Adiposity

Modern Western lifestyle is associated with chronic exposure to excess intake of carbohydrates and lipids and reduced physical activity [17]. Following digestion, lipids are stored as neutral triglycerides in cells known as adipocytes which increase in size in response. In a balanced environment, TG storage during energy intake is offset by fat mobilisation during fasting or situations with elevated energy demands [18-21]. However, in an obese state the storage of TGs is the predominant behaviour of adipocytes. One of the primary compensatory responses, to obesity-induced excess TG storage, is the enlargement of adipocytes (hypertrophy). When hypertrophic adipocytes exceed their fatty acid (FA) storage capacity, lipids are then stored in other tissues leading functional impairment [22].

Adipocytes are an important component of adipose tissue which also contains connective tissue, nerve fibres, vascular cells, lymph nodes, immune cells fibroblasts and preadipocytes [23]. Adipose tissue not only responds to sensory signals from traditional hormone systems but also expresses and secretes factors with important endocrine functions [24]. Adipose tissue is divided into specific regional depots with differences in structural organisation, cellular size and biological function [25]. The specific location and distribution of adipose tissue within the body is an important factor when defining the health risks of obesity.

1.3.1 Differential Roles of Fat Depots

In humans, body-fat can be found throughout the body and although its constitutive cells (adipocytes) are the same across the body, body-fat appears to be arranged in distinctive depots, with location-specific functions, yet working in coordination with each other [26-28]. A list of body-fat depots identified in humans includes subcutaneous, internal, gluteofemoral, 'visceral', intermuscular and pericardial [29]. It should be noted that there are numerous subdivisions of body-fat, with some scientists basing their classification purely on anatomical location; with others insisting that body-fat depots should be classified solely on metabolic basis [30, 31]. What is important to note is that there is large variability in body-fat distribution across the human population and that this confers different effects on metabolic health.

1.3.1.1 Subcutaneous adipose tissue

Subcutaneous adipose tissue (SAT) is found underneath the skin in the femerogluteal regions, back and anterior abdominal wall and interspersed in skeletal muscle [32]. SAT is a key depot for fat storage in periods of excess energy intake and energy supply in periods of fasting, starvation, or exercise. SAT also appears to act as a buffer during intake of dietary lipids, thereby protecting other tissues from lipotoxic effects [33].

1.3.1.2 Visceral adipose tissue

Visceral adipose tissue (VAT) is located in the abdominal cavity and surrounds the internal organs. VAT is highly associated with disturbances to lipid metabolism, insulin resistance, diabetes, inflammation, hypertension and cardiovascular disease [34, 35]. VAT mass correlates with the development of insulin resistance, while total or subcutaneous tissue does not [36-38].

1.3.1.3 Intra-hepatocellular fat

Intra-hepatocellular fat is located within the liver and is deposited when triglycerides, derived from circulating FAs upon insulin resistance (IR)-induced dysregulation of peripheral lipolysis, accumulate in the liver cells [39]. Accumulation of lipids leads to a reversible condition known as fatty liver and may be accompanied by progressive inflammation, fibrosis, cirrhosis and hepatocellular carcinoma [40].

1.3.1.4 Brown adipose tissue

The largest region of brown adipose tissue (BAT) is found in the upper back region of rodents (interscapular). In humans, small areas are found in the thorax region (supraclavicular) and abdomen [41]. The primary function of BAT is to generate body heat in a nonshivering form. There are indications that the nonshivering heat generation provided by this depot plays a role in the development of obesity [42]. Although adult humans possess only a small percentage of BAT compared to WAT has been shown to be negatively correlated to obesity. Active BAT is known to be able to increase energy expenditure, thus the possibility to pharmacologically increase BAT amount or activity would be a potential treatment for obesity [43, 44].

1.3.2 Monitoring of adipose tissue

There are a number of methods for estimating relative body adiposity, of which measuring the body mass index (BMI; weight divided by height squared) is the gold standard and most widely used. There is a strong correlation between BMI and overall bodyweight, however a substantial number of publications report limitations to this technique when taking athletes and different ethnic groups into consideration [45-47]. Another method of estimating overall obesity is through the method of waist circumference, which is commonly used as a proxy of abdominal obesity [48-50]. These indirect methods of body composition analysis cannot determine the distribution profile of visceral adipose tissue, thus the need to accurately phenotype an individual is carried out by non-invasive imaging techniques. These common techniques, such as magnetic resonance imaging (MRI) and magnetic resonance spectroscopy (MRS), enable the measurement of regional adipose content, in addition to liver, pancreatic and muscle fat can be obtained [51].

1.4 Liver Metabolism

The liver is the metabolic centre of the body and is located between the absorptive surfaces of the gastrointestinal tract where it performs a key role in many pathways involved with nutrient homeostasis such as carbohydrates, lipids and proteins [52-55]. It is also the main detoxifying organ and the only site where molecules such as bile, clotting factors and other serum proteins are synthesised [56]. The central role of the liver in controlling carbohydrate and lipid homeostasis makes it particularly vulnerable to the effects of the overall metabolic state of the body [57].

The liver governs energy homeostasis by its ability to metabolise glucose, fatty acids and controlling overall lipid circulation. During periods of fasting, an adequate supply of glucose

to the tissues is orchestrated by the liver through breakdown of glycogen stores within hepatocytes (glycogenolysis) and de novo synthesis (gluconeogenesis) [58]. In the fed state glucose is derived principally from the diet stimulating insulin release, which in turn promotes glucose uptake by different tissues, inhibits liver gluconeogenesis and lipolysis in adipose tissue. In some physiological conditions, free fatty acids (FFAs) released from adipose tissue are known to contribute to central and peripheral insulin resistance through their accumulation in skeletal muscle and liver. Additionally, there are fat-derived signals, including tumour necrosis factor-α (TNF-α), resistin and adiponectin, which modulate insulin sensitivity and fatty acid metabolism in muscle and liver [59]. This complex system to control lipid and glucose homeostasis is shown in Figure 1.1.

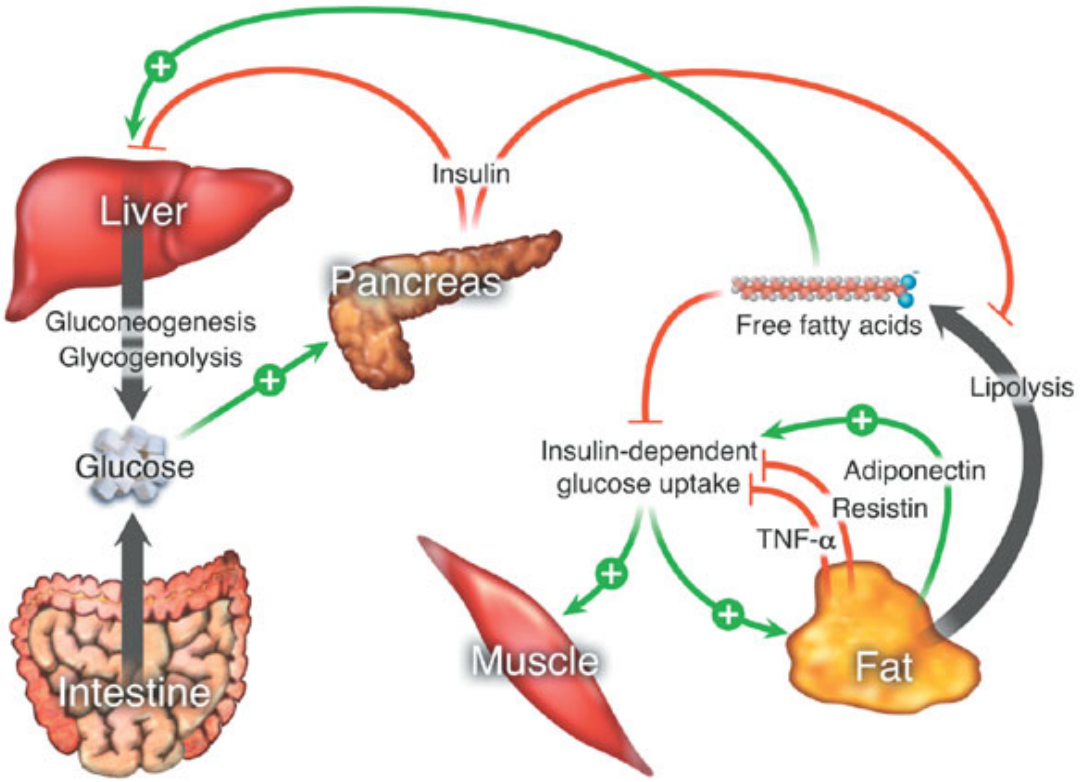


Figure 1.1 The central role of the liver in Glucose and Lipid Homeostasis

An overview of the central role of the liver in energy homeostasis. Glucose derived from diet (intestine) or endogenous sources (liver) stimulates insulin secretion, promoting glucose uptake by skeletal muscle and fat. Glucose uptake opposes hepatic glycogenolysis and gluconeogenesis, and inhibits fat lipolysis. Free fatty acids liberated from adipose tissue (via lipolysis) contribute to insulin resistance in skeletal muscle and liver. Additional fat-derived signals, including TNF-α, resistin and adiponectin, modulate insulin sensitivity and fatty acid metabolism in muscle and liver. Green arrows depict an increase in activity, whereas the red arrows depict a decrease in activity. Figure from Evans R et al., 2004.

1.4.1 Altered liver function in the obese state

Hepatic metabolism helps maintain nutrient homeostasis throughout the body. The individual steps in hepatic metabolism are orchestrated by a delicate interplay of hormones, nuclear receptors, intracellular signalling pathways and transcription factors (Figure 1.6). Dysregulation of nutrient metabolism is a key step during the process of chronic liver disease that induces an inflammatory state, cellular damage, and impaired hepatic insulin signalling leading to insulin resistance. Insulin resistance causes an increase in lipolysis and failure to supress glycolysis and gluconeogenesis in the liver. Furthermore, increased uptake of FAs and glucose causes progressive deposition of triglycerides leading to hepatic steatosis [60]. *De novo* lipogenesis (DNL) further contribute to hepatic steatosis [61], and hepatocytic lipid accumulation predisposes to overproduction of ROS, endoplasmic reticulum (ER) stress and lipotoxicity [62-64]. Fabbrini et al. have further suggested that increased liver fat is an independent indicator of multi-organ insulin resistance and postulate that the observed relationship between increased visceral fat and metabolic disease is essentially a confounding factor due to the correlation between visceral and liver fat [65]. More recently, Magkos et al. have shown that increased adiposity, without an increase in liver fat, does not cause abnormalities in adipose tissue, skeletal muscle and hepatic insulin sensitivity, or very low-density lipoprotein (VLDL) metabolism [66].

Intra-hepatocellular lipid content (IHCL) is an accumulation of lipid within the hepatocytes thus increasing the availability of fatty acids and inflammatory adipokines to the liver. In turn, the resulting accumulation of IHCL is associated with metabolic syndrome risk factors and progress to the more severe liver diseases such as non-alcoholic fatty liver disease (NAFLD). NAFLD is the most common liver disease in Western society [56, 67] and is characterised by lipid accumulation within hepatocytes and may progress to non-alcoholic steatohepatitis (NASH), the extreme form of NAFLD and is regarded as a major cause of cirrhosis of the liver [68]. These triggers of inflammation in the liver can however be

positively modulated by the anti-inflammatory markers. One in particular, adiponectin, has been shown to lower adiposity in liver [69, 70].

In order to investigate the effects of obesity, a robust model must be established *in vivo*. Recent studies have shown that diet-induced-obesity (DIO) murine models can provide a good platform for the study of NAFLD and NASH [71]. Rodents fed on high fat diet have increased inflammation, oxidative stress and lipogenesis and also display a increase in adiponectin concentrations, which then progress to insulin resistance, obesity, steatosis, steatohepatitis and fibrosis [71]. In a study by Xu et al., high fat feeding of animals caused elevated concentrations of glucose, insulin, FFAs, TGs, TNF-α and finally liver steatosis [72].

1.4.2 Monitoring of Liver Fat

Measurement of ectopic fat, especially liver fat, has become an important goal in light of the previous discussion. The lipid content of the liver can be evaluated by a number of invasive and non-invasive methods [73]. Until recently, needle biopsy, in combination with electron microscopy and oil staining, was the most commonly used technique and considered the golden standard for monitoring lipid accumulation in the liver. This technique has limited application in tissues such as the heart and pancreas and has practical and ethical issues even when applied to the liver, making it incompatible with longitudinal studies as it can cause bleeding and inflammation. Today, the advent non-invasive imaging techniques, including computerized tomography (CT), magnetic resonance spectroscopy (MRS) have revolutionized the study of ectopic fat. Both MRI and MRS allow for a fast and reproducible quantitative measurement of adipose tissue and ectopic fat, including the liver, pancreas, heart and skeletal muscle (Figure 1.2). Whereas MRI provides quantitative information about adipose tissue, ^{1}H MRS has become the gold-standard for assessing lipid content of liver [51,74, 75].

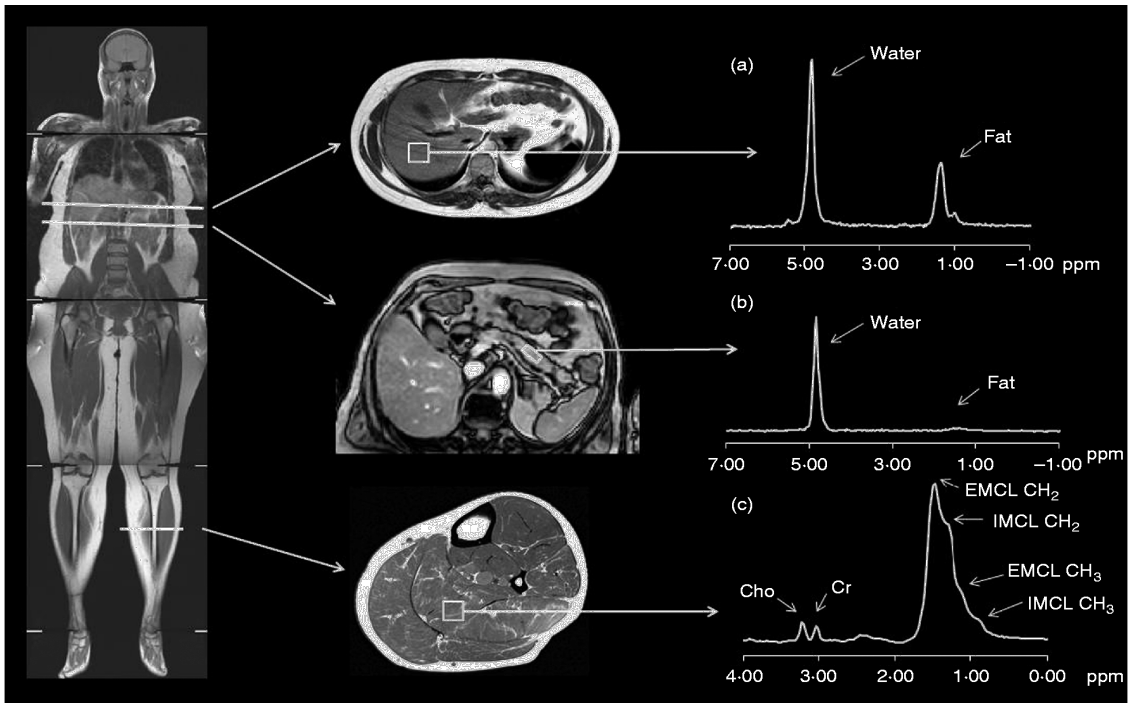


Figure 1.2 Localisation and monitoring of Ectopic Fat Accumulation

Measurement of fat content by ^{1}H-magnetic resonance spectroscopy. Transverse magnetic resonance images were taken through the abdomen to identify the liver and pancreas, and the lower leg to identify soleus and tibialis muscles. Voxels were placed in the organ of interest avoiding bone, blood vessels and obvious fatty streaks. ^{1}H-magnetic resonance spectra were obtained in approximately 2 min from (a) the liver, (b) pancreas and (c) soleus muscle. Figure from Thomas EL et al., 2012.

1.4.3 Lipotoxicity and Inflammation

Lipotoxicity is a metabolic condition that results from excess FFA accumulation in non-adipose tissue and has a harmful effect on the organelles within the cell, particularly the mitochondria, reducing their capacity to orchestrate lipid metabolism [76].

Chronic inflammation is widely observed in the obese state and commonly has many elevated markers of inflammation [24]. One recent study conducted by Zhang et al. in mice showed that consuming a high fat diet (HFD) induces an inflammatory response that precedes the development of obesity; however, by pharmacologically preventing this inflammatory response, there was a protection against weight gain [77].

In addition to being a storage site for triglycerides, adipocytes produce and secrete a number of these markers of inflammation and endocrine hormones, such as leptin, adiponectin, resistin, TNF-α and interleukin-6 (IL-6) [78]. Adipocytes regulate both hormonal (such as insulin) and sympathetic (such as adrenergic) stimulation [79]. Adipose tissue has also been shown to have macrophage infiltration as a result of obesity [80]. Figure 1.3 shows the pro- and anti-inflammatory adipokines released by adipose tissue in healthy and obese states [81].

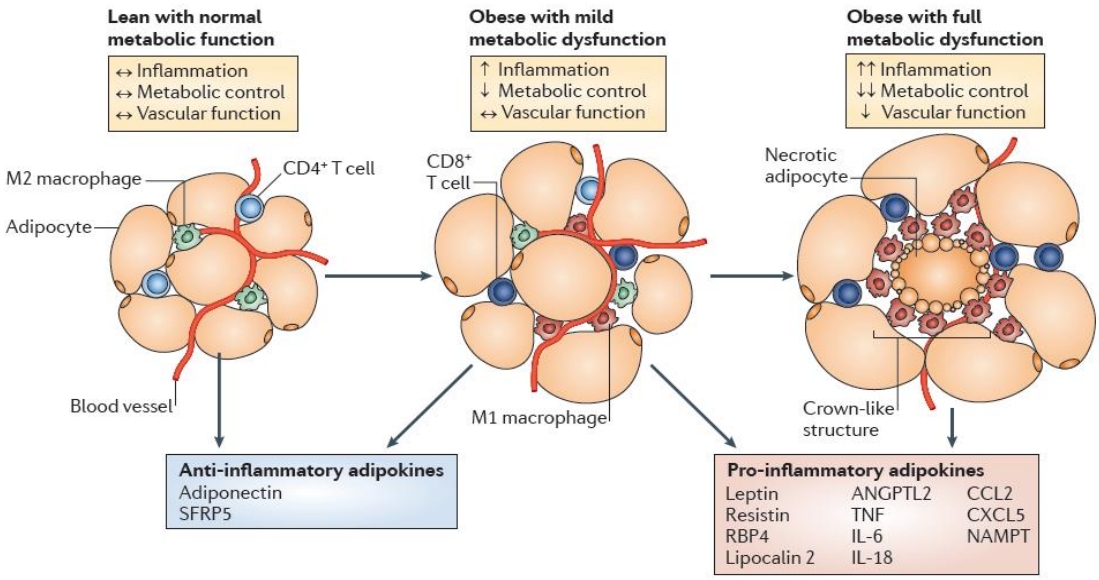


Figure 1.3 Modulation of Adipose Tissue with Obesity

Adipose tissue changes its morphology with increased obesity which can be categorised into three distinct phenotypic groups; lean with normal metabolic function, obese with mild metabolic dysfunction and obese with full metabolic dysfunction. As obesity develops 1) the adipocytes gets bigger due to increased storage of triglycerides, 2) the number of macrophages increases, 3) the vasculature decreases relative to tissue size and 4) anti-inflammatory adipokines are replaced with pro-inflammatory adipokines. In obese adipose tissue with full metabolic dysfunction crown like structures are seen which are macrophages circling around the necrotic adipocytes. Figure from Ouchi et al., 2011.

1.4.4 Mitochondria

Mitochondria are double-membrane bound organelles that play a critically and relevant role in energy homeostasis, metabolism, apoptosis, regulation and cell viability [82]. Mitochondria are prominently responsible for generating most of the chemical energy utilised by cells known as adenosine triphosphate (ATP), through respiration, and to regulate cellular metabolism [83]. The primary set of reactions involved in ATP production is collectively

known as the tricarboxylic acid cycle (TCA cycle) or the Krebs cycle. In addition to ATP production, mitochondria maintain key metabolic processes such as lipolysis, glycolysis, fatty acid β-oxidation, ketogenesis and fatty acid synthesis. Figure 1.5 shows an overview of the numerous mitochondrial pathways involved in energy homeostasis. In addition, the mitochondria generate intermediates for biosynthesis and reactive oxygen species (ROS) that serve as a secondary messenger to mediate signal transduction and metabolism. This balance is maintained through normal mitochondrial function matching oxidative phosphorylation (OXPHOS) and dissipation of the proton gradient [84].

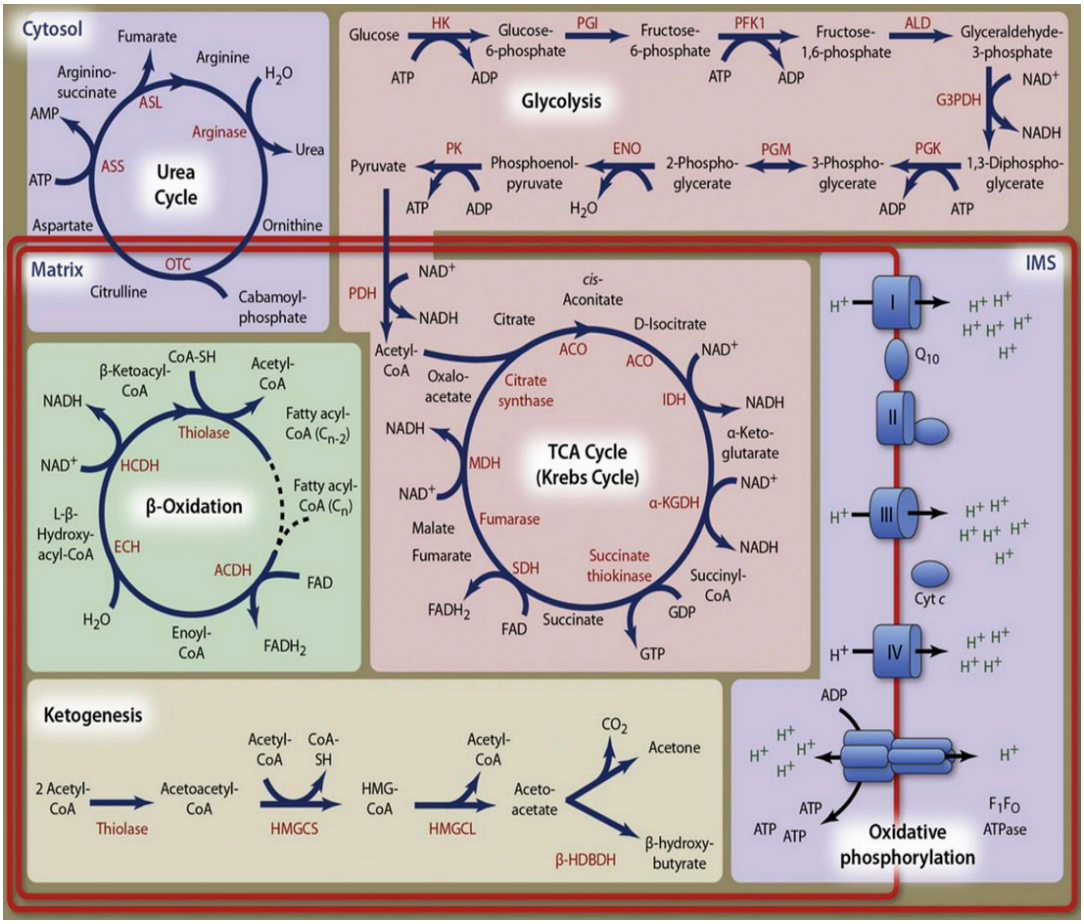


Figure 1.4 Bioenergetic Functions of Mitochondria

This simplified diagram displays the critical bioenergetic circuitries that mitochondria host. These pathways include the tricarboxylic acid (TCA) cycle, or Krebs cycle, glycolysis, oxidative phosphorylation, the urea cycle, β-oxidation, and ketogenesis. Mitochondrial compartmentalisation provides optimal microenvironment for these and other biosynthetic and catabolic pathways to coincide. Several intermediate reactions and all transporters have been omitted for clarity. Figure adapted from Gulluzzi, Lorenzo et al., 2012.

Several characteristics make mitochondria a very unique organelle. One such example is the variable concentration of mitochondria present in specific tissue types. In particular, BAT has a high concentration of mitochondria per lipid droplet, in order to maintain body heat, which makes the tissue itself appear brown [85]. The mitochondria are also densely populated in

liver cells, due to the greater demand for ATP [86]. Mitochondrial content of otherwise similar cells can vary substantially and can affect the central function of the cell through the prominent role of energy production. Observations that the number of mitochondria in adipose tissue from obese people is reduced, suggests that impaired mitochondrial activity could cause a predisposition to obesity. In addition, studies have shown that mitochondria biogenesis is also altered in obesity [87].

Given the diverse array of unique metabolic functions centralised in the liver, an energy imbalance could cause impairment of mitochondrial function. One consequence of hepatic lipid accumulation, or “fatty liver”, is increased mitochondrial fat oxidation without compensatory electron transport chain activity, leading to “stressed” mitochondria and the production of ROS [88]. These events are thought to play a pivotal role in the subsequent development of inflammation and lipotoxicity, creating an aberrant cellular environment which contributes to NASH, hepatic fibrosis and cirrhosis [63].

In summary, it is widely accepted that the liver is a central organ in lipogenesis, gluconeogenesis and cholesterol metabolism and that these functions can be considerably compromised in obesity. As observed recently, a variety of pathological conditions highlighted the importance of metabolic functions within the liver. An increase in the prevalence of obesity and the metabolic syndrome promotes pathophysiological changes that cause NAFLD and may lead to cirrhosis and NASH. Alteration in insulin response, beta-oxidation, lipid storage and transport, autophagy and an imbalance of inflammatory markers are held accountable for these changes. Figure 1.6 shows the key metabolic pathways that regulate hepatic metabolism, specifically, the cross talk between lipid metabolism and mitochondria and in both the healthy and unhealthy state.

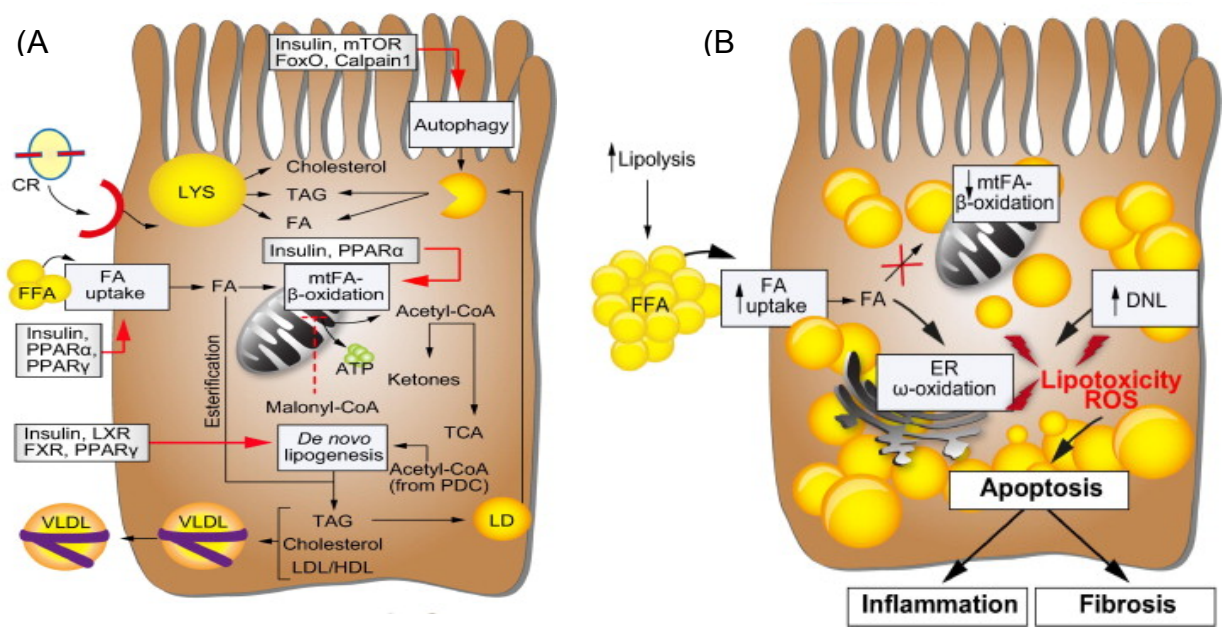


Figure 1.5 Hepatic Lipid Metabolism in Health and Disease

In a healthy hepatocyte **(A)** free fatty acids (FFA) are actively taken up by various fatty acid (FA) transporters under the control of insulin and nuclear receptor signalling and are oxidized in the mitochondrially, providing ATP for the TCA cycle. Under fatty liver conditions **(B)** increased peripheral lipolysis, upregulation of fatty acid transporters, an increase in *de novo* lipogenesis (DNL) and a reduction in mitochondrial β-oxidation promote fatty acid toxicity and the release of reactive oxidation species. This leads to the induction of hepatocyte apoptosis, the invasion of activation of inflammatory cells and fibrogenesis. Figure from Bechmann et al., 2012.

1.5 Dietary Fibre and Obesity

The World Health Organization has suggested that a diet consisting of a high level of indigestible carbohydrates could improve the health state of an individual by weight loss or improving overall health [89]. Dietary patterns that include fruit, vegetables and whole grains are recommended. Carbohydrates can be classified into two main groups; digestible

(soluble) or indigestible (insoluble, or resistant) depending where in the gastrointestinal track they are digested[90]. Dietary intervention studies have shown that a diet consisting of high levels of indigestible carbohydrates reduces blood glucose levels, body weight and body fat content [91]. Increased dietary fibre consumption have also been associated with a reduction in cancer occurrences, specifically colorectal cancer [92-94]. Early observations concerning the metabolic differences between cancer and normal cells were made by Otto Warburg, who showed that cancer cells are inherently dependent on glycolysis for production of chemical energy [95]. There is now mounting evidence that this increased glycolysis results from the influence of multiple molecular pathways, including adaptive responses to the hypoxic tumour microenvironment, oncogenic signalling, and mitochondrial dysfunction[96-98]. The glycolytic phenotype offers growth advantages to cancer cells by resisting apoptosis, and facilitating tumour spread and metastasis [99]. It has been suggested that microbial fibre fermentation maybe important in relation to fibre intake and colon cancer prevention[100]. Thus, the inverse relationship between dietary fibres and the development metabolic syndrome and some forms of cancer raises interest into the bioactive components of dietary fibres [101-104]. The mechanisms responsible for this observation are still unclear, however several modes of action have been proposed [105-107]. One such mechanism that has attracted particular attention in recent years is the potential role that some of the by-products of the fermentation of the resistant dietary fibre, principally the short-chain fatty acids, may have on metabolic dysfunction in the liver and adipose tissue [108-111] .

1.5.1 Short- Chain Fatty Acids

Short-chain fatty acids (SCFA) are a sub-group of fatty acids that are produced by the microbiota in the colon and the distal small intestine from resistant starch (RS), dietary fibre and other low-digestible polysaccharides during fermentation. Microbial fermentation of

these dietary products yields three main SCFA: acetate, propionate and butyrate as significant end products [112, 113]. Their molecular structure is shown in Figure 1.6.

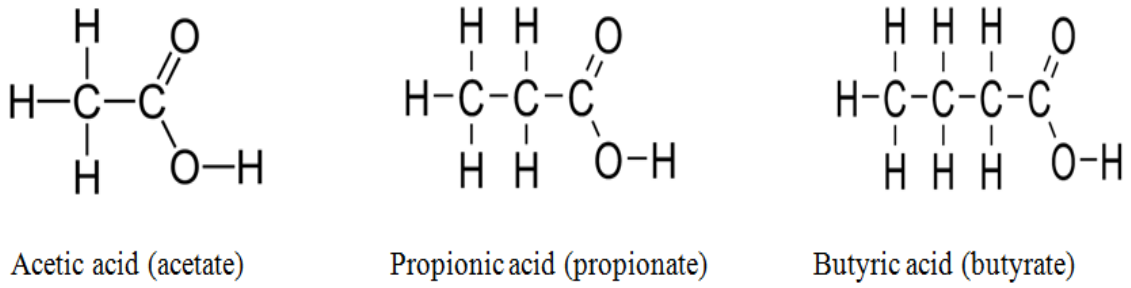


Figure 1.6 Molecular Figure Structures of Short- Chain Fatty Acids

The three main short-chain fatty acids fermented by the microbiota in the colon: acetate, propionate and butyrate. Figure from Al-Lahham et al., 2010.

The rate of fermentation of fibre varies according to type and food source; e.g. fibre derived from grains is fermented much more slowly and less completely than that from fruits and vegetables [114]. The ratio of SCFA produced by fermentation may vary, depending on the source and type of dietary fibre. In the large intestine the concentrations of acetate, propionate and butyrate is approximately 60, 20 and 20 mmol/kg [115]. SCFAs produced in the colon are absorbed by colon mucosal cells, play a significant role in maintaining the normal physiological function of the colonic mucosa, normal bowel function and prevent pathology through their actions in the lumen and on the colonic musculature and vasculature and through their metabolism by colonocytes [116]. After SCFAs are absorbed by the colonic mucosa, they pass through the colonic wall and are absorbed and transported via the portal

vein to the liver, and the fraction not absorbed is distributed into the general circulatory system to other organs and tissues for metabolism [117].

The concentration of SCFA in peripheral circulation is directly correlated with the intake of resistant starch [118]. SCFAs have been shown to have effects in different parts of the body. Butyrate has been shown to be the preferred energy source of the colonocytes, over propionate and acetate, in a ratio of 90:30:50 [119, 120]. Acetate and propionate are also utilised by colonocytes; remaining propionate and acetate is metabolised in the liver, with some acetate consumed by peripheral tissues, where they are substrates for gluconeogenesis and lipogenesis [121, 122].

The mechanism by which SCFA is absorbed in the lumen is unknown. The effects of SCFA in the intestinal lumen are potentially induced via the activation of specific receptors and/or via absorption in epithelial cells. In 2003, two research groups independently identified that SCFAs with 1-6 carbons atoms, such as acetate, propionate and butyrate are a natural ligand of the G-protein-coupled receptor 41 and 41 (GPR41 and GPR43) [123, 124]. Both receptors decrease adenylyl cyclase concentrations in cells and increase Ca+2 concentrations. The receptors exert their functions by coupling with Gi/o and/or Gq; GPR41 with Gi/o and GPR43 with both. It has also been shown that acetate is less potent to GPR41 than propionate and butyrate and GPR43 is activated similarly by the three SCFAs [123]. Figure 1.7 provides an overview for SCFA uptake and absorption.

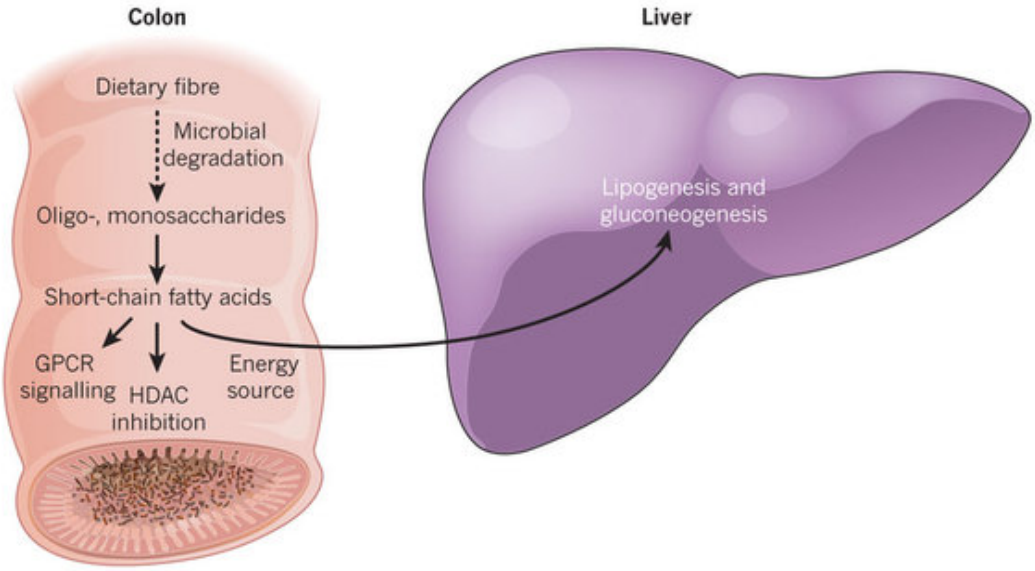


Figure 1.7 Short- Chain Fatty Acid Uptake and Absorption

Complex carbohydrates, such as dietary fibre that are resistant to amylase digestion, are metabolized by the colonic microbiota to oligosaccharides and monosaccharides and then fermented to short-chain fatty acid end-products, mainly acetate, propionate and butyrate. Short-chain fatty acids are absorbed in the colon, where butyrate provides energy for colonic epithelial cells, and acetate and propionate reach the liver and peripheral organs, where they are substrates for gluconeogenesis and lipogenesis. In addition to being energy sources, short-chain fatty acids control colonic gene expression by inhibiting the enzyme histone deacetylase (HDAC) and metabolic regulation by signalling through G-protein-coupled receptors (GPCRs), such as GPR41 or GPR43. Figure from Tremaroll & Backhed, 2012.

Over the last two decades, the principle role of SCFA has evolved from a culprit in the pathogenesis of carbohydrate-induced diarrhoeas to a pluripotent benefactor of multiple epithelial functions. These beneficial metabolic effects include post-prandial satiety, reductions in fat mass, inflammation, stabilisation of blood glucose levels and thus improvements in insulin sensitivity [125-128]. Once absorbed, SCFAs are metabolized at

three major sites in the body: 1) cells of the caecum-colonic epithelium that use butyrate as a major substrate for maintenance-energy; 2) liver cells that metabolize residual acetate and propionate used for gluconeogenesis; and 3) muscle cells that generate energy from the oxidation of residual acetate [129]. In addition, 50% to 70% of acetate is also taken up by the liver and VAT and in response increases insulin sensitivity. Figure 1.8 shows an overview of the numerous physiological processes affected by SCFA uptake.

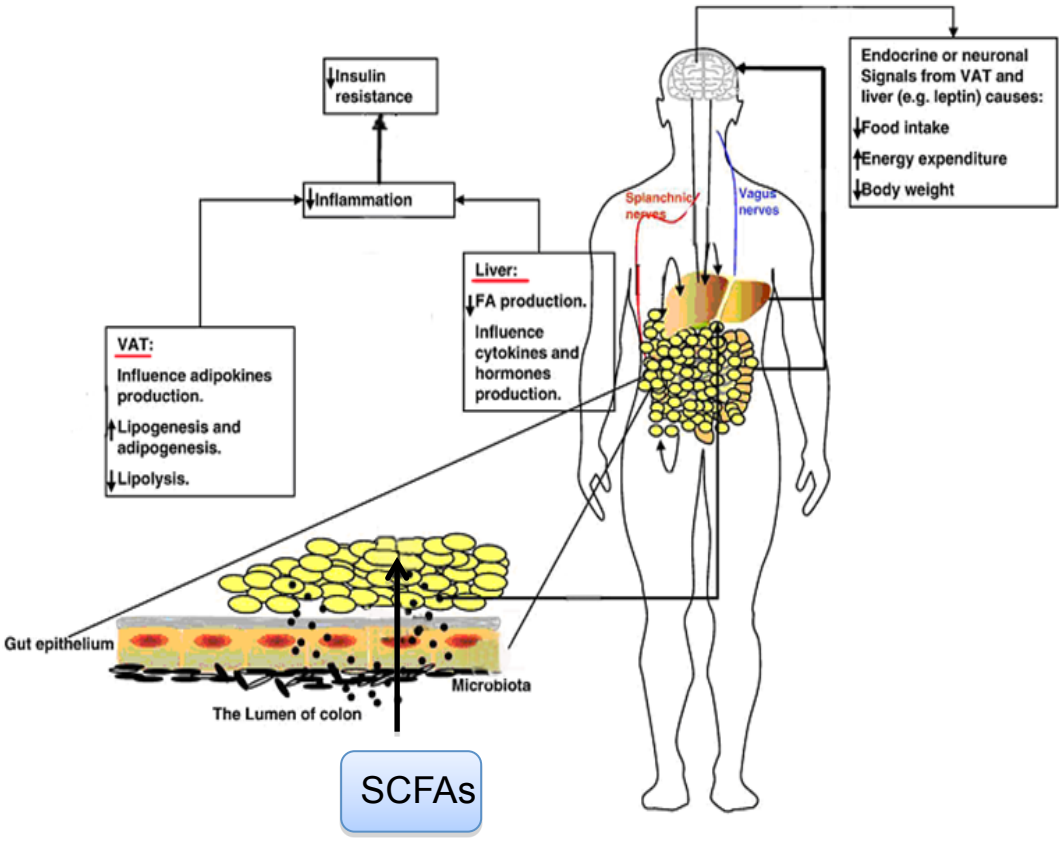


Figure 1.8 Schematic representation of the effects of short-chain fatty acid

SCFA are produced by the fermentation of undigested food by the colonic microbiota, passes the gut epithelium into the peripheral system and reduces the production and the release of FA from VAT and liver. Potentially this leads to an inhibition of inflammation and therefore to insulin sensitivity. As a result of SCFA influences of the production of hormones by VAT and liver, the endo-, para- and auto-crine and neuronal pathways (via vagus and splanchnic nerves) are initiated to reduce food intake and to influence other metabolic effects. Figure adopted from Al-Lahham et al., 2010.

1.5.2 Acetate Formation and Metabolism

Acetate is critical to all forms of life and is the most common building block for biosynthesis, playing a central role in cellular metabolism. When bound to coenzyme A, it is fundamental to the metabolism of carbohydrates and fats. Unlike longer-chain carboxylic acids (FAs), acetate or acetic acid do not occur naturally in triglycerides. Acetyl-CoA functions as intermediate in both the synthesis and breakdown of many organic molecules. Particularly in the mitochondria, acetyl-CoA is used to fuel the TCA cycle, which is a fundamental energy producing pathway in all aerobic organisms as well as producing the essential building block for biosynthesis of many molecules including FA and nucleotides [130]. Figure 1.9 shows the complex involvement acetate has is numerous pathways and functions.

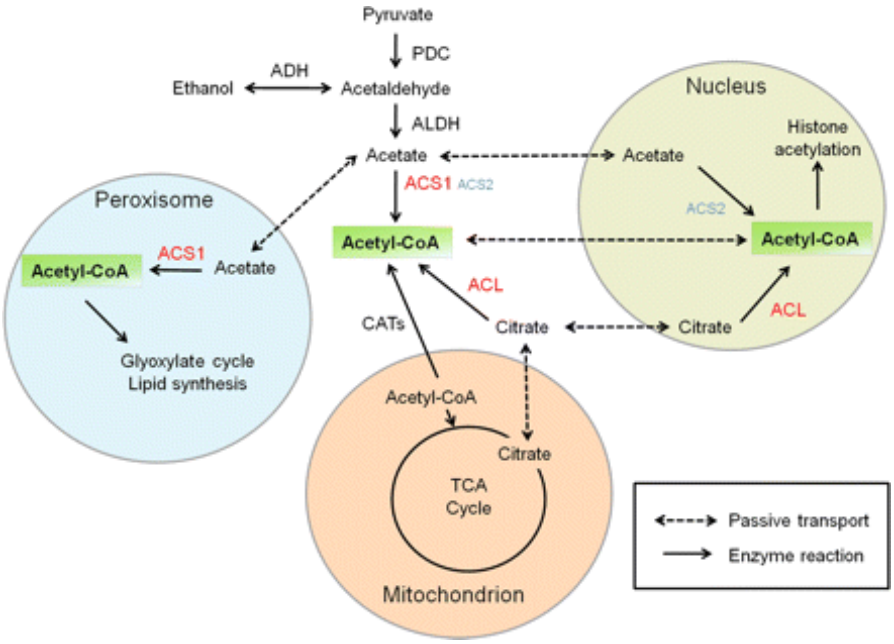


Figure 1.9 Metabolic pathways for acetate via acetyl-CoA

Different pathways by which acetate is utilised; the pyruvate- acetaldehyde- acetate pathway has vital roles in acetyl-CoA production. Mitochondrial acetyl-CoA supplied from the mitochondrion-associated pyruvate dehydrogenase complex or β-oxidation is used to replenish the mitochondrial tricarboxylic acid (TCA) cycle. Therefore, mitochondrial acetyl-CoA is essential in the production of energy sources for the survival and normal growth of cells. cytosolic acetyl-CoA is an essential building block for the biosynthesis of fatty acids and numerous secondary metabolites. Acetyl-CoA carboxylase mainly controls fatty acid synthesis via malonyl-CoA production from cytosolic acetyl-CoA. Acetyl-CoA synthetase (ACS1 and ACS2) are highlight for Acetly-CoA converstion points. Figure from Lee, Seunghoon et al., 2011.

1.5.3 Epigenetic modifications

Epigenetic modifications play a key role in the regulation of gene expression, the process by which information stored in a gene is used to synthesise a functional gene product [131]. Epigenetic modification can occurs at many levels (and forms) in the genome and associated components, from methylation of DNA to acetylation of histone proteins. The introduction of an acetyl group, most commonly in the form of acetyl-CoA, into a molecule is known acetylation. Acetylation occurs as a co- or post-translational modification of proteins, in particular histones. Histone acetylation is one mechanistic by which genetic transcription can be modulated, causing the chromatin on the DNA to expand. In turn, a deacetylation can take place, preventing gene transcription encouraging a balance. This equilibrium between acetylated and deacetylated states of histones is governed by two different sets of enzymes: histone acetytransferase (HATs) and histone deacetylase (HDAC) respectively [132]. Figure 1.10 shows a simplified diagram of epigenetic mechanisms.

Many small molecules have been identified as potential HDAC inhibitors (HDACi) [133, 134], one of these is the SCFA butyrate [135, 136]. Apparently the inhibitor activity of butyrate is not only important from a nutritional aspect[137] but may also have the potential to profoundly influence cell differentiation, proliferation and motility and inducing cell cycle arrest and apoptosis [138].

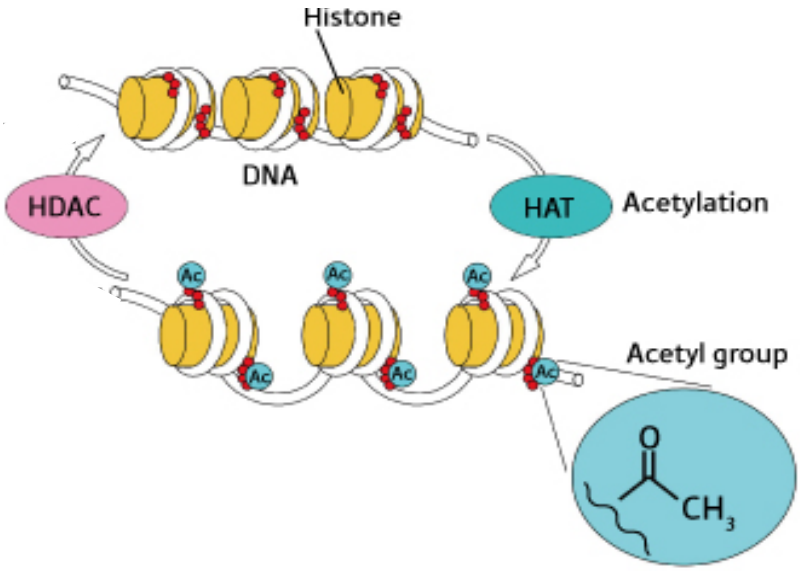


Figure 1.10 Schematic diagram of histone acetylation and deacetylation

DNA winds around histone proteins and are acetylated by histone acetyltransferase (HATs), shown in teal, which causes the strands to loosen allowing for gene expression due to the presence of acetyl-CoA. Deacetylation of the histone proteins is caused by histone deacetylase (HDAC), which is shown in pink. Figure adopted from Yoshida, M et al., 2008.

1.6 Obesity and cancer

Obesity is an established risk and progression factor for many cancers, including breast [139] and colon cancer [140-142]. Multiple hormones, growth factors, cytokines, insulin, leptin and other mediators associated with the metabolic perturbations of the obese state enable crosstalk between macrophages, adipocytes, endothelial cells, other microenvironmental components, and epithelial cells. As shown in Figure 1.11, these obesity-associated factors contribute to cancer-related processes (including growth signaling, inflammation, vascular alterations, and several pathways associated with tumour-initiating cell enrichment, invasion, and metastasis) [143, 144]. In particular, the relationship between obesity and colorectal cancer (CRC) has been a subject of interest as the

prevalence of obesity continues to increase [145, 146]. The presumptive link between obesity and CRC remains challenging, as other confounding factors may influence the development of CRC; however CRC is thought to be an obesity-related cancer and is therefore a reasonable line of cancer to use in this study.

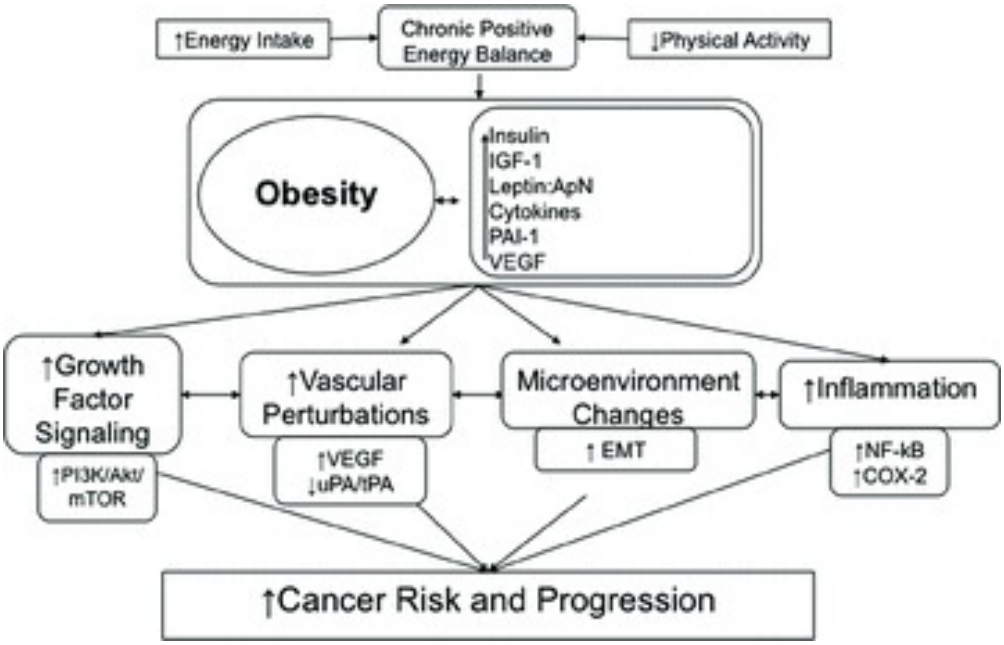


Figure 1.11 Metabolic Deregulation and Cancer

Mechanistic overview of key biological mechanisms which correlate between obesity criteria and increased cancer risk. Figure from Hursting, S et al., 2012.

1.6.1 Metabolic deregulation

The relationship between obesity-related metabolic stresses and cancer are now well accepted. In 2000, Weinberg proposed, a series of six complex elements necessary for tumour development. These include uncontrolled cell growth, angiogenesis, replicative immortality, sustained proliferative signalling, evading growth suppressors and activating invasion and metastasis [147]. Recently, altered cellular energy metabolism has re-emerged as a hallmark of cancer, leading to newfound efforts are directed at exploiting these

differences as biomarkers and therapeutic targets [148]. Understanding the relationship between metabolites in the tumour environment will advance the ability to characterise, treat and potentially prevent cancers and other diseases that have not been approached from the metabolic perspective.

1.6.2 Warburg Effect

The concept that tumours are metabolically different has grown to encompass other cellular pathways, such as fatty acid oxidation, glutamine metabolism and lipid biogenesis [149]. Fatty acid synthesis and lipid biogenesis are particularly active in proliferating cells due to synthesis of cell membranes [150]. This increased demand is, in part, met by an altered metabolic programme known as the “Warburg Effect” [95, 151]. This reliance of cancer cells on aerobic glycolysis was proposed in the 1920s by Otto Warburg, which led him to be awarded the Nobel Prize, despite the fact that for the next few decades it was mostly ignored by researchers working in the field of cancer. In recent years we have seen a renewed interest on the ‘Warburg Effect’, becoming a catalyst for investigations attempting to explain the biological relationship between cellular metabolites and cancer [152-154]. The alteration in tumour metabolism reflects a switch from oxidative phosphorylation to glycolysis, resulting in excess pyruvate and lactate production (Figure 1.12). This characteristic metabolic profile provides an opportunity to distinguish cancer cells from normal cells, a phenomenon that has been successfully exploited by the use of PET [155].

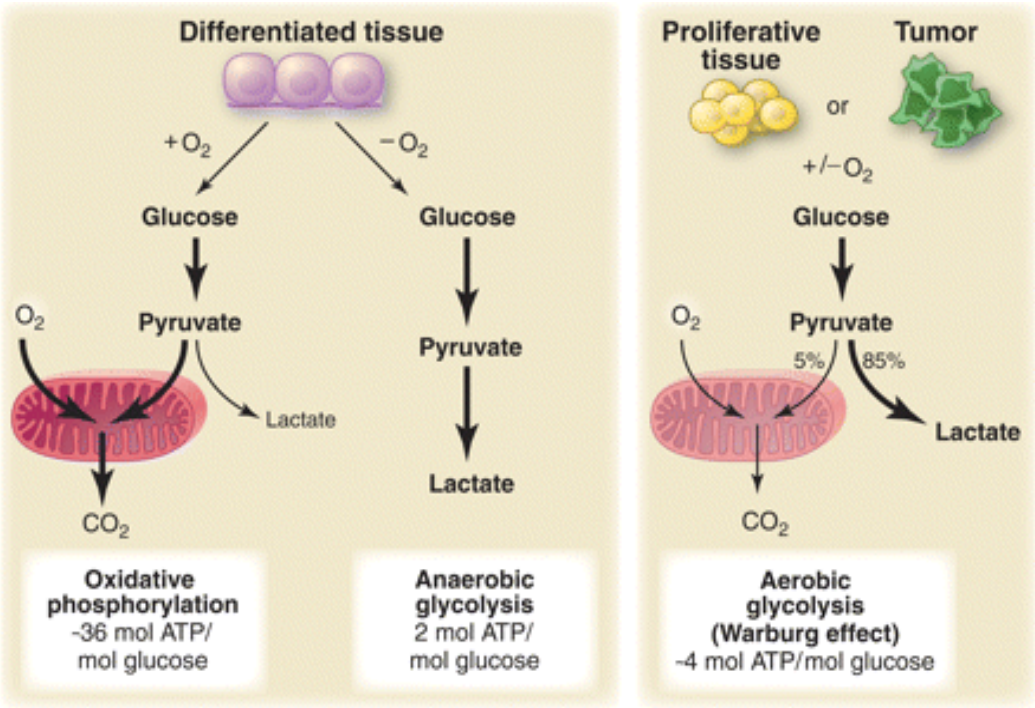


Figure 1.12 Schematic representation of the Warburg Effect

This figure outlines the differences between oxidative phosporylation, anaerobic glycolysis and aerobic glycolysis in normal and cancerous tissue. In the left panel the figure shows the normal, non-profilerating tissues generate pyruvate via glycolysis in the presence of oxygen. Essential for this process, oxygen is required for the final electron acceptor to completely oxidise glucose. When oxygen is limited, as in the right hand panel, cells redirect the pyruvate generated by glycolysis away from mitochondrial oxidative phosphorylation by generating lactate. This generation of lactate during anaerobic glycolysis allows glycolysis to continue (by cycling from NADH back to NAD+), but results in minimal ATP production when compared to oxidative phosporylation. Mitochondria maintain some level of oxidative phosphorylation in both cancer and normal cells, though aerobic glycolysis is less efficient than oxidative phosporylation for generating ATP (~36 mol ATP: 2 mol ATP). In normal proliferating cells, ~10% of the glucose is diverted into biosynthetic pathways upstream of pyruvate production. Figure from Heiden et al., 2009.

1.6.3 Randle hypothesis

The interaction between glucose and fatty acid metabolism has been examined from a number of angles. The Randle cycle was proposed more than 30 years ago as a mechanism whereby products of lipolysis (fatty acids and ketone bodies) would inhibit glycolysis in normal cells to maintain stable ATP production [156, 157]. According to this mechanism, abundant acetyl-CoA causes feedback inhibition of pyruvate dehydrogenase and increases the level of TCA intermediates, specifically citrate, to inhibit phosphofructokinase, both of which reduce the rate of glycolysis (Figure 1.13). Although it has been pointed out that the Randle cycle has only been persuasively demonstrated *in vitro*, under the condition that intracellular glucose is fixed, the fatty acids availability is variable [158].

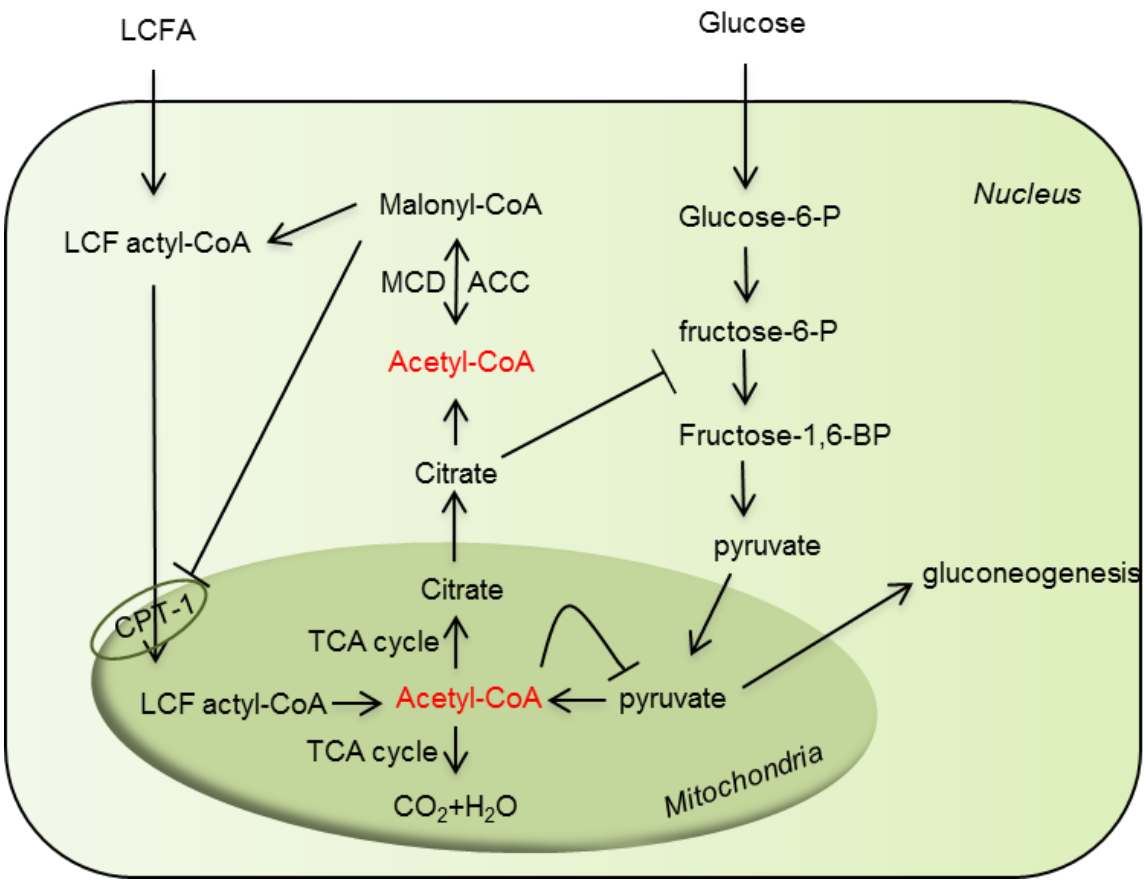


Figure 1.13 Schematic diagram of the Randle cycle

The Randle cycle demonstrates the interaction between glucose uptake, metabolism and consequent inhibition and effects of fatty acid oxidation on the inhibition of glucose utilisation. Glucose enters the cell and the reaction of glycolysis drives the carbon atoms to pyruvate where they are oxidised at acetyl-CoA (shown in red). The fate of acetyl-CoA is complete oxidation in the TCA cycle or return to the cytosol via citrate for conversion back to acetyl-CoA and subsequent long-chain fatty acid via malonyl-CoA. The synthesis of malonyl-CoA is catalyzed by acetyl-CoA carboxylase (ACC) and once produced will inhibit the import of long-chain fatty acyl-CoAs (LCFacyl-CoA) into the mitochondria via inhibition of carnitine palmitoyltransferase 1 (CPT-1). This effectively blocks the oxidation of fatty acids leading to increased triacylglyceride synthesis.

1.6.4 SCFA effects on select pathways

Supplementation with dietary fibre has been shown to amend features of the metabolic syndrome and attenuate malignant growth in certain cancers, in particular colon cancer [159, 160]. Oxidation of SCFA, particularity acetate, is the initial step in the TCA cycle, a fundamental energy producing pathway in all aerobic organisms**.** Oxidative phosphorylation generates the majority of energy required for cellular function in normal differentiated cells. In contrast, cancer cells rely primarily on aerobic glycolysis; a metabolic shift termed the Warburgh effect that comprises attenuation of energy production via mitochondrial beta-oxidation [152]. In malignant cells, the inhibition of glucose uptake and metabolism by products of SCFA breakdown is thought to preferentially inhibit aerobic glycolysis and supress the uncontrolled cellular proliferation [161, 162].

As previously introduced, the ubiquitously expressed HDACs family are part of a transcriptional co-repressor complex that influences various tumour suppressor genes, making HDAC inhibitors (HDACi) an important emerging class of chemotherapeutic agents [163]. The interest in HDACi is due to studies, specifically in butyrate, which show deregulated expression in pathological states such as cancer through the modulation of histones via acetylation [164, 165]. These complex modifications result in a characteristic pattern of acetylation which allows access of transcription factors and other regulatory proteins to certain DNA sequences but prevents access to others [166].

Studies investigating the diverse range of cancer inducing agents have led to the hypothesis that initial mitochondrial dysfunction results in biochemical and genetic deviations associated with malignancy. Exploiting pathways that link cellular energy metabolism and regulation of

gene expression is a promising therapeutic approach for the treatment of various disease states, including both obesity and cancer [161].

1.6.6 Limitations of SCFA in obesity and cancer paradigms

Supplementation with dietary fibre has been shown to improve features of the metabolic syndrome and attenuate malignant growth in certain cancers [137, 159]. Food sources of dietary fibres can act by changing the nature of the contents of the gastrointestinal tract by changing how other nutrients and chemicals are absorbed [167]. To achieve the desired phenotypic changes described here, the amount of dietary fibres required by consumption would be higher than physiologically possible. In addition, there are disadvantages of consuming a diet high in fibre, including significant intestinal gas production, bloating and potential constipation [168]. Fibre supplementation may be similarly beneficial, however the consumption of large qualities can also lead to gas, bloating and discomfort [169]. Thus, consuming enough indigestible carbohydrates to have a positive impact on health can be difficult, and may therefore not be sustainable for the general population.

Current evidence regarding the underlying mechanisms of SCFA, specifically acetate, is unclear. Exogenous acetate delivery has demonstrated inconsistent effects on weight gain, mitochondrial function and markers of lipogenic and lipolytic activity in both human and rodent models [126, 170]. This ambiguity may arise from the ubiquitous role acetate plays in cellular metabolism, combined with the non-targeted nature of oral and peripheral administration [125, 171]. In addition, the adversely low pH of acetate and its rapid clearance from the circulation limit its therapeutic potential when administered systemically [172]. The therapeutic limitations of SCFA also extend to cancer models, however are thwarted by a short half-life and first-pass hepatic clearance [173].

1.7 Liposomal nanoparticles

Drug delivery systems are being exploited to circumvent some of the non-ideal properties of free drug administration and provide better control over the pharmacokinetics of the encapsulated drug relative to free drugs. Nanoparticles have many advantages in cancer therapy with the small size which can enter tumour vasculature via the enhanced permeability and retention effect (EPR) whilst offering a long circulation half-life and prolonged exposure time of tumour tissue to anticancer agents [174]. Specifically, liposomes have drawn increasing interest due to their ability to delivery drugs in the optimum dosage range. The quantification of exact number of drugs being delivered via liposomal carriers has seldom been investigated.

Liposomes are vesicles which have become a commonplace within technology of all sectors and specialities. The industrial applications of liposomes include drug delivery vehicles in medicine, adjuvants in vaccination, signal enhancers/carriers in medical diagnostics and analytical biochemistry, solubilizers for various ingredients as well as support matrix for various ingredients and penetration enhancer in cosmetics [175, 176]. Liposomal encapsulation of therapeutic agents addresses a number of current drug delivery issues by improving bioavailability, extending treatment effects and reducing dosing [177].

1.7.1 Principles of liposomes

Liposomes are composed of lipid constituents, with hydrophobic head groups and hydrophilic tails groups (Figure 1.14). When hydrated, the lipids aggregate together to form self-assembled bilayer vesicles, similar to a membrane, which encloses an aqueous compartment. This aqueous cavity has traditionally been used as drug delivery vehicles by encapsulating water soluble molecules in order to improve drug pharmacokinetics [178-180]. Liposomes are typically characterised by their size, shape and lamellarity. The application of

liposomes can dictate the combination or choice of lipids incorporated and the preparation process in order to formulate a particle for a specific purpose.

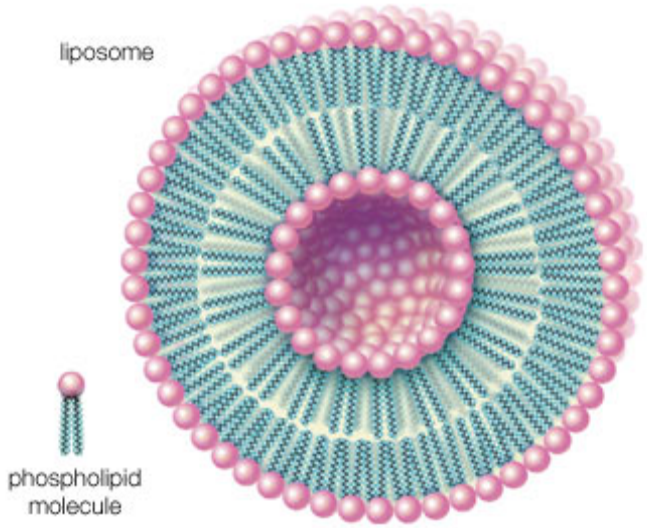


Figure 1.14 Basic liposome structure

A schematic of the structure of a liposome; a spherical vesicle that is comprised of lipid constituents with hydrophobic head groups and hydrophilic tails groups. The core of a liposome is aqueous which allows for encapsulation of molecules of interest. Figure from Encyclopaedia Britannica, Inc, 2007.

1.7.2 Liposome structure

The bio-distribution of liposomes is dependent on many factors including, formulation composition, liposome size, surface charge, concentration of constitute lipids, route of injection and the total volume injected *in vivo*. Formulation composition of a liposome can determine the rigidity or fluidity of the membrane by using particular phospholipids. Size is an important factor for *in vivo* application, affecting clearance and distribution, with liposomes larger than 100μm being unsuitable for therapeutic use due to uptake by

macrophages [180]. Zeta potential is a measure of liposomal stability, whereby the surface charge enables particles to repel each another and prevent agglomeration [181-183].

1.7.3 Liposome delivery

Liposomes can specifically or nonspecifically absorb onto the cell surface. Liposomes can also fuse with the cell membrane, and release their contents into the cell cytoplasm, or can be destabilized by certain cell membrane components when adsorbed on the surface Liposome can undergo the direct or transfer-protein-mediated exchange of lipid components with the cell membrane or be subjected to a specific or nonspecific endocytosis. In the case of endocytosis, a liposome can be delivered by the endosome into the lysosome [184].

For *in vivo* applications and prolonged circulations of liposomes, the liposome bilayer is frequently coated with the neutral polymer polyethylene glycol (PEG), which is routinely used in the modification of the physiochemical properties of a liposome in order to minimize the bioadhesion and immunological response [185, 186]. The incorporation of PEG into the lipid membrane increases the hydration of the liposome which makes them unrecognizable to macrophages and significantly prolongs their circulation half-life. Without a PEG layer, liposomes are also extremely prone to uptake by the reticuloendothelial system (RES), a class of cells of the immune system that take up particular substances in the defence against foreign bodies [187, 188]. It has been shown that liposomes bearing a surface decorated with the neutral hydrophilic PEG polymer benefit from prolonged circulation times with half-lives reported from 2 to 24 hours in rodents, and as high as 45 hours in humans [189]. The presence of PEG molecules on the liposome surface results in the exclusion of other macromolecules from the outer layer by occupying the space immediately adjacent to the vesicles through its flexible chain and forms a protective layer which reduces the liposome

recognition by opsonins in the blood [190, 191]. These liposomes are referred to as sterically stabilised or “stealth” liposomes, due to the inhibition of both electrostatic and hydrophobic interactions of plasma components with the liposome bilayer.

1.7.2 Tumour specific liposomal delivery

In 1974, Gregoriadis et al. first proposed liposomes for delivery of cancer therapeutics [192] . Since then liposomes based therapeutics have found their way into clinical application and are often a therapeutic tool of choice given their numerous advantages as pharmaceutical carriers. There are numerous studies using liposomes as drug delivery systems in cancer therapy which have had a success in patient response. One such example has been achieved by formulations such as Doxil® which consists of a liposome formulation encapsulating the anti-cancer drug doxorubicin and has been approved for metastatic breast cancer [193, 194].

This process involves the complex interplay of a range of specialised cells, growth factors, signalling molecules and regulatory elements. It has been shown that potential therapeutics of 30kDa and above are able to accumulate in tumour tissue due to the EPR effect [195]. This effect coined by Maeda in 1989, shown in Figure 1.15, describes a tumour endothelium vasculature, which due to its “leakiness” allows the penetration of macromolecular particles through to tumours[196].

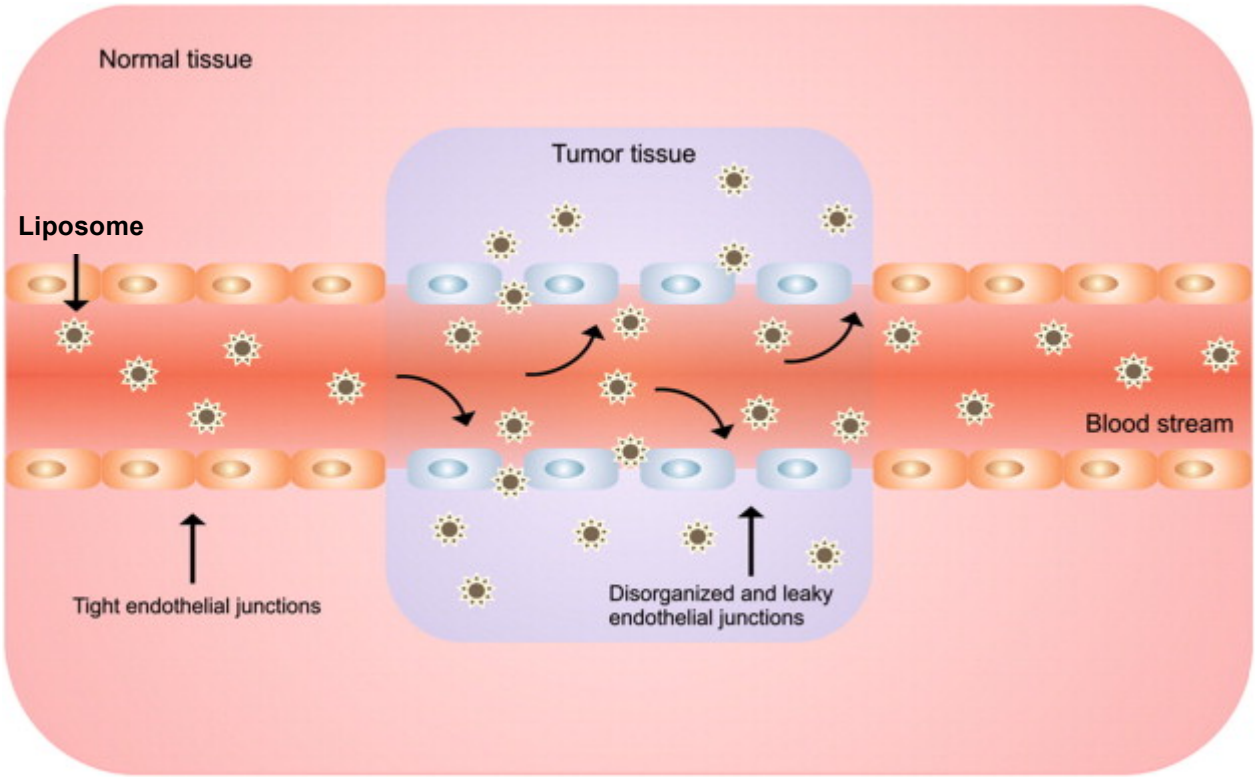


Figure 1.15 Schematic of tumour by nanoparticles via Enhanced Permeation and Retention (EPR) effect

Normal tissue does not have endothelial gaps wide enough to allow for macromolecules or nanoparticle agents to leak into the extracellular tissue lining blood vessels. Tumour tissue has a disrupted endothelial layer, allowing of larger particles to “seep” into the tumour extracellular domain. Figure from Prakash, S. et al., 2011.

As mentioned previously a relatively high level of PEG was incorporated into the lipid bilayer, which achieves prolonged and sustained drug delivery. These lipids retain the biocompatible ‘stealth’ effect, thus an increase in the PEG lipid can thereby increase the blood half-life and can achieve delivery to a tumour *in vivo* [197, 198].

1.8 Imaging Modalities for *in vivo* Studies

In addition to the encapsulation of drugs within a liposome, equipping the particle with contrast generating agents for imaging allows for powerful image-supervised drug delivery. The application of nanotechnology platforms to imaging has opened up opportunities for the use of multifunctional nanoparticles systems in the study of metabolic disorder detection and therapy. This process has been made possible through the use of specific particles that can be tracked, monitored and their distribution quantified. Molecular imaging techniques make use of modalities which cover a range of frequencies from the electromagnetic spectrum. More recently even the use of multiple modalities in combination has been used. Figure 1.16 shows a sample of the now numerous imaging modalities that can be utilised for molecular imaging, each with their own advantage and disadvantage [199]. The most commonly used techniques in molecular imaging are magnetic resonance imaging (MRI), optical imaging and nuclear imaging (positron emission tomography (PET)) [200].

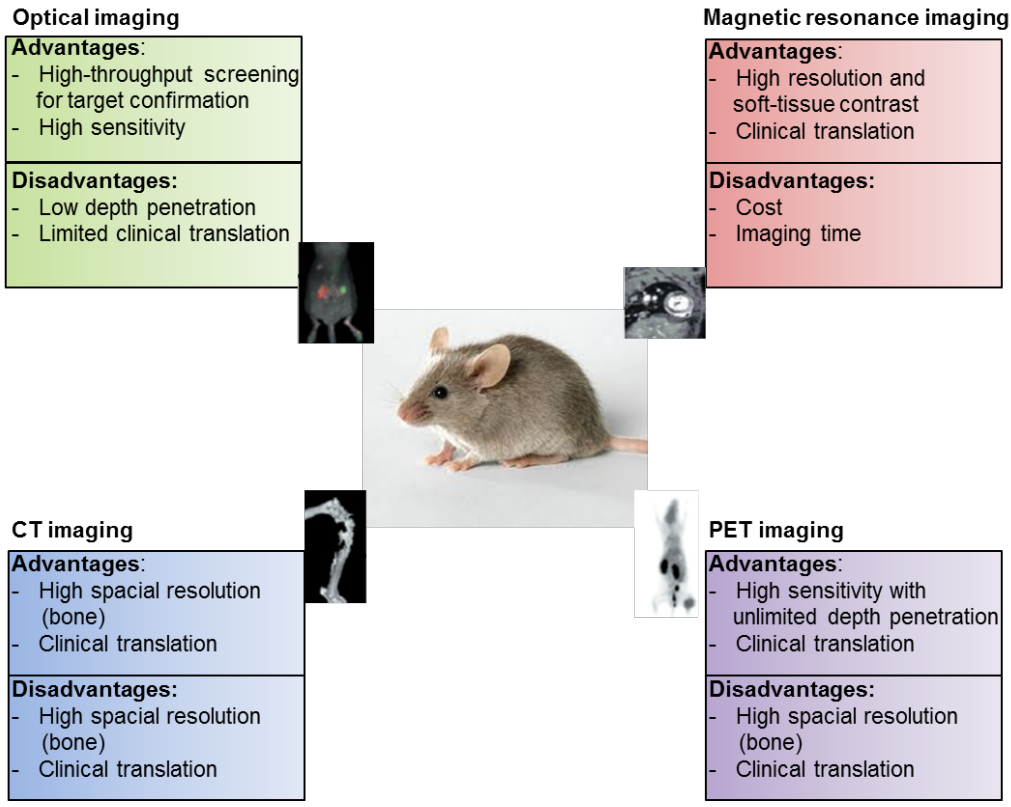


Figure 1.16 Summary of imaging modalities

Each modality has particular characteristics, advantages and disadvantages which are highlighted in the figure. CT, computed tomography; PET, positron emission tomography.

1.8.1 Magnetic Resonance Imaging

Magnetic Resonance Imaging (MRI) is a powerful non-ionising, non-invasive imaging tool, with high tissue contrast, making it ideal for longitudinal studies on the same subject, which why it is widely used in pre-clinical and clinical studies. MRI, unlike nuclear imaging techniques such as PET, is relatively insensitive but it has better spatial resolution and can be used repeatedly on the same subject without any adverse effects. The vast majority of MRI is based upon the manipulation of a particular nuclei, most commonly hydrogen, in a magnetic field. This constant magnetic field is usually produced by a super-conducting magnet, a tightly wound wire through which an electric current is passed. Producing this

current requires a huge amount of energy, thus the wire is maintained at -270°C with liquid nitrogen and helium [201].

Once a sample containing water is placed within this strong external magnetic field, almost all of the hydrogen nuclei begin in spin, or precess, in a gyrating fashion around the magnetic moment, termed B_0, and line up parallel or anti-parallel to the direction of the magnetic field. The frequency at which the hydrogen nuclei precess is termed the Lamour frequency and is directly proportional to the local magnetic field strength. The higher the field strength of the magnet, measured in Tesla (T), the more protons align with the field.

Encapsulated within the MRI scanner, three variable gradient magnets alter the magnetic fields along the x, y or z axes. The gradient magnets alter the main magnetic field on a very local level allowing “slicing” in any direction to take place within the sample. The MRI machine creates a unique magnetic field for each voxel (a volumetric unit within an MRI scanned section) and therefore a unique Lamour frequency.

In order to generate an MRI image, a radiofrequency (RF) coil placed around the region of interest is used to deliver an RF pulse. This pulse, applied at the appropriate Lamour frequency, perturbs precessing hydrogen nuclei, flipping them into the plane perpendicular to B_0, also referred to as the transverse plane). After the RF pulse, the precessing nuclei relax and recover to the longitudinal plane while decaying in the transverse plane. The longitudinal and transverse magnetizations occur simultaneously but are two completely different processes. The recovery/relaxation along the longitudinal plane is referred T_1 recovery,

whereas relaxation in the transverse plane is referred to T_2 recovery. The dissipation of energy in the form of T1 and T2 within each voxel is recorded by the RF coil and the scanner's computer manipulates this data via complex Fourier transformation, generating an MRI image. [202, 203].

1.8.1.1 Gadolinium Contrast Agent

MRI contrast agents are routinely used in clinical diagnosis as they provide reliable means to improve image contrast. One of the most commonly used contrast agent, Gadolinium (Gd), consists of a paramagnetic metal core, which is complexed into a strongly chelating ligand. Incorporating gadolinium complexes into liposome membranes yields paramagnetically labelled liposomes which significantly enhance proton relativity and are therefore MRI visible [204-206].

1.8.2 Computed Tomography

The computed tomography (CT) system is formed from an X-ray source and detector. The subject is placed between the source and the detector which acquires a series of projections. These projections are then used to generate a three dimensional image, with the contrast generated from the difference absorption of the X-rays through different tissues. CT can produce very high resolution images, however is limited by lack of soft tissue contrast [207]. For this reason, CT is not routinely used as an imaging tool alone but often used in combination with other imaging techniques such as position emission tomography [199].

1.8.3 Positron Emission Tomography

In Positron Emission Tomography (PET) imaging, radioisotopes decay emitting a positron and neutrino. The positron is annihilated when it comes in contact with an electron emitting 2 anti-parallel γ-rays. The energy of the γ-rays emitted is 511keV and detected almost simultaneously by an array of detectors surrounding the subject and this allows the localisation and quantification of the radioisotope in the subject [208]. The radioisotopes used in PET imaging include, but not limited to, ^{18}F and ^{11}C. One main application of PET is tumour imaging together with ^{18}Fluorodeoxyglucose (^{18}F-FDG), which is taken up by metabolically active cells and following phosphorylation by glucokinase is trapped inside allowing for activity to be measured [209, 210].

1.8.4 Fluorescence microscopy

In fluorescence imaging, the properties of certain molecules known as fluorochromes, are exploited for their ability to fluoresce. Fluorescence is the ability to absorb energy from an external excitation light of a particular wavelength and to re-emit the light at a longer wavelength and lower energy, which can be detected by ultrasensitive cameras. Fluorescence techniques, mainly fluorescence microscopy, have been routinely used *in vitro* and *ex vivo* applications in molecular and cellular biology. This has been extended into non-invasive *in vivo* imaging [211]. Fluorescence imaging using excitation in the visible range (400-600nm) has been widely used *in vitro* and *ex vivo*, it is limited *in vivo* by the penetration depth of excitation light (1-2mm) [212].

1.9 Aims and Objectives

The work contained in this thesis focuses on the design, evaluation and implementation of a liposomal formulation for the *in vivo* delivery of acetate in animal models of obesity and cancer. I hypothesis that cellular metabolic dysfunction can be re-engineered *in vivo* by the targeted delivery of acetate. In chapter 2, I explore the potential of preferential delivery of liposome encapsulated acetate (LITA) nanoparticles by utilising this liposome as a viable delivery vesicle for acetate. This consists of a panel of potential liposome formulations, tested and characterised to determine the ideal vehicle for acetate. Short- and long-term biodistribution assessment was carried out by means of histological techniques, MRI and ^{18}F-FDG-PET/CT. This delivery system aimed to address many of the issues associated with the delivery of small molecule to target organs in obesity and cancer murine models.

The metabolic potential of liposomal encapsulated acetate (LITA) nanoparticles was assessed in multiple *in vivo* models, examining a wide range of metabolic outcomes. In chapters 3 and 4 I employed the developed SCFA encapsulated vector in animal models of both obesity and malignancy. Chapter 3 examines the effects of LITA in an obesogenic background to determine how acetate delivery could change the landscape of the obese state *in vivo*. Metabolic, phenotypic, molecular and epigenetic analysis was carried out to determine the effects of the LITA nanoparticle. Chapter 3 also explores the short term effects of metabolic response to the LITA nanoparticle *in vivo* in a non-obese state. Chapter 4 examines the effects of LITA upon delivery to three independent colon cancer tumour models *in vivo*. Analysis of tumour growth and metabolism was determined by calliper and bioluminescence activity, as well as the use of molecular analysis. Significant changes in tumour size were observed with LITA treatment, together with marked changes in epigenetic markers. The potential of preferential delivery of the LITA nanoparticles to key sites of metabolic control will provide beneficial therapeutic effects in animal models of both obesity and cancer.

Chapter 2

Formulation and Characterisation of Liposomal Encapsulation of Acetate (*LITA*)

2.1 Introduction

As described in Chapter 1, supplementation with dietary fibre has been shown to ameliorate features of the metabolic syndrome and attenuate malignant growth in certain cancers [159, 160]. Component carbohydrates are fermented by the microflora of the large intestine, producing short-chain fatty acids (SCFA), such as acetate, propionate and butyrate [159]. Acetate is a key metabolic intermediate in several ubiquitous cellular processes and has multiple beneficial effects [125].

In order to avoid the harmful side effects of pure acetate administration [115] or volume of dietary consumption [159], a safe and effective method of delivery is required. A nanoparticle delivery system was resolved to be the solution to this problem, specifically the liposome. Liposomal encapsulation of therapeutic agents addresses a number of these issues by improving bio-availability, extending treatment effects and reducing dosing [177]. This chapter is intended to confirm that a liposome is a multi-purpose, artificially prepared vesicle composed of a lipid bilayer which can be loaded with small molecules, such as acetate.

2.1.1 Aims of Studies

To formulate and characterise a nanoparticle that has the capacity to encapsulate the short chain fatty acids: acetate, butyrate and propionate. This will develop a novel delivery system of short-chain fatty acids with the capacity to tailor the design of the nanoparticle to target organs of interest.

To assess the bio distribution over time and in real time of the nanoparticle *in vivo*. This will help to develop a profile of distribution *in vivo* and can determine the effectiveness of delivery of the acetate encapsulated liposome.

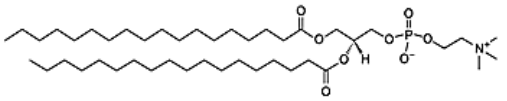
2.2 Methods

2.2.1 Materials

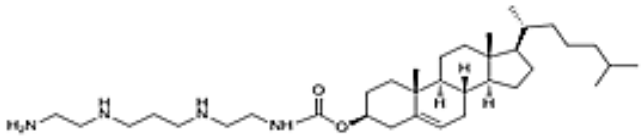
2.2.1.1 Lipids

The cationic lipid incorporated into the liposomal bilayer was CDAN (N^1-cholesteryloxycarbonyl-3,7-diazanonane-1,9-diamine, $C_{35}H_{64}N_4O_2$). One isoform of CDAN used in this study is DDAB (Dimethyldioctadecylammonium, C38H80NBr). DSPC (1,2-distearoyl-*sn*-glycero-3-phosphocholine, $C_{44}H_{88}NO_8P$) was added for membrane structure. Two isoform of DSPC was also tested: DOPE(1,2-dioleoyl-*sn*-glycero-3-phosphoethanolamine, $C_{41}H_{78}NO_8P$) and DLPC (1,2-dilauroyl-*sn*-glycero-3-phosphocholine, $C_{32}H_{64}NO_8P$). The lipid used to increase blood-half life and bioavailability within *in vivo* circulation was 1,2-distearoyl-*sn*-glycero-3-phosphoethanolamine-N-[methoxy(polyethylene glycol)-2000] (ammonium salt) (DSPE-PEG^{2000}). The helper lipid cholesterol (3β-Hydroxy-5-cholestene, 5-Cholesten-3β-ol, $C_{27}H_{46}O$) was included in order to increase fusogenicity and stability of the liposomal lipid bilayer. One isoform of cholesterol was also testsed, DC cholesterol (3ß-[N-(N',N'-dimethylaminoethane)-carbamoyl]cholesterol hydrochloride, $C_{32}H_{57}N_2O_2Cl$). To increase transfection efficiency of the liposome DOPE-Rhodamine (1,2-dioleoyl-sn-glycero-3-phosphoethanolamine-N-(lissamine rhodamine B sulfonyl), $C_{68}H_{109}N4O_{14}PS_2$) was included, which also carried a fluorescence label to allow *ex vivo* histological corroboration. For *in vivo* MRI visualisation of the liposomes, the formulation included a second label containing the lipid gadolinium (III) or Gd.DOTA.DSA (2-[4,7-bis-carboxymethyl-10-[(N,N-distearylamidomethyl-N′-amidomethyl]-1,4,7,10-tetraazacyclododec-1-yl], $C_{55}H_{109}N_6O_8Gd$). All lipids were stored as stock solutions in the anhydrous organic solvent chloroform ($CHCl_3$) at -20^oC. All chemicals were of analytical grade or best available grade and purchased from Sigma-Aldrich (Dorset, UK) or Avanti Polar Lipids (Alabaster, USA). The structures of the primary lipids introduced in the formulations of the liposome can be seen in Figure 2.1. Accessory lipid structures are found in Appendix I.

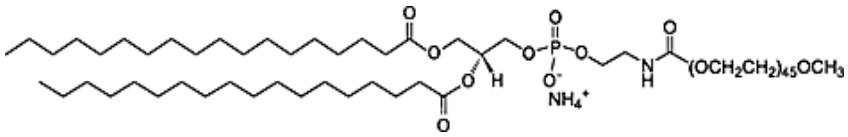
A) DSPC



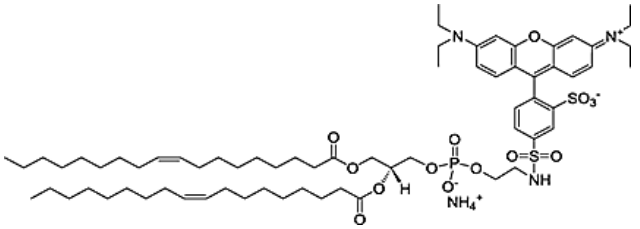
B) CDAN



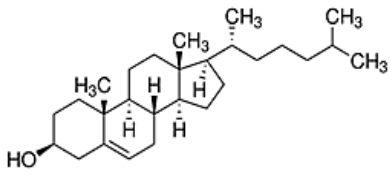
C) DSPE-PEG^{2000}



D) DOPE-Rhodamine B



E) Cholesterol



F) Gd.DOTA.DSA

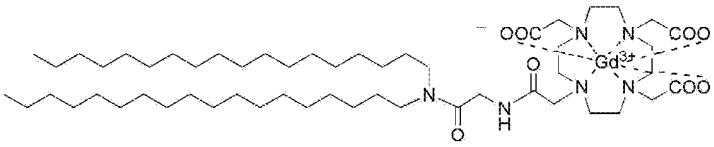


Figure 2.1 Chemical structures of the lipids incorporated into the liposomal bilayer

These chemical structures represent the lipids used to formulate the described liposomes. Lipids included **(A)** DSPC, **(B)** CDAN, **(C)** DSPE-PEG^{2000}, **(D)** DOPE-Rhodamine B, **(E)** Cholesterol and **(F)** Gd.DOTA.DSA (Gadolinium).

2.2.2 Study 1: Liposome Preparation and Formulation

2.2.2.1 Lipid incorporation

In order to determine the ideal liposome formulation for this study, a number of variable lipids and molarity components were tested. Liposomes were formulated with a defined molar ratio of individual lipids based on the desired *in vivo* application (Table 2.1). Appropriate volumes of each lipid stock were placed in a 5mL round bottom flask and the solvent slowly removed *in vacuo* at 30°C using a rotary evaporator (Bucchi, UK) until all liquid was completely evaporated to ensure production of an even lipid film [213].

2.2.3 Study 2: Short-Chain Fatty Acid Encapsulation

2.2.3.1 Liposomal encapsulation of acetate and dialysis

The lipid film following rotary evaporation was re-hydrated with either the membrane impermeable control buffer 4-(2-hydroxyethyl)-1-piperazineethanesulfonic acid (HEPES) (4mM, NaCl 135mM, pH 6.5) or the short-chain fatty acid (SCFA) (1M, CH_3COOH, pH 2.0). The first SCFA tested was acetate; following the establishment of a robust formulation and protocol, butyrate and propionate were tested. In order to form liposomes of an appropriate size of 100nm, the resulting solution was sonicated using a sonicating water bath (Grant Instruments, Cambridge, UK), for one hour at 30ºC in the dark, The pH of the liposomal suspension was determined by a pH measurement device (Camlab Ltd., UK) and was adjusted to 7.0 by the addition of sodium hydroxide (NaOH, pH 12.0) or hydrochloric acid (HCL, pH 2.0) (Sigma-Aldrich, UK). The formulated liposomes with encapsulated SCFA or HEPES then required a dialysis process to filter any excess material from the external liposome environment. To achieve this, formulated liposomes were transferred into the Float-A-lyzer G2 (Spectrum labs, USA). The column was then suspended into a beaker of

100mL sterile deionised water on a stir plate and set to the slowest speed for 18 hours. Water was replaced every 4-5 hours to ensure the external environment of the liposome was clear of any impurities, as displayed in Figure 2 [214].

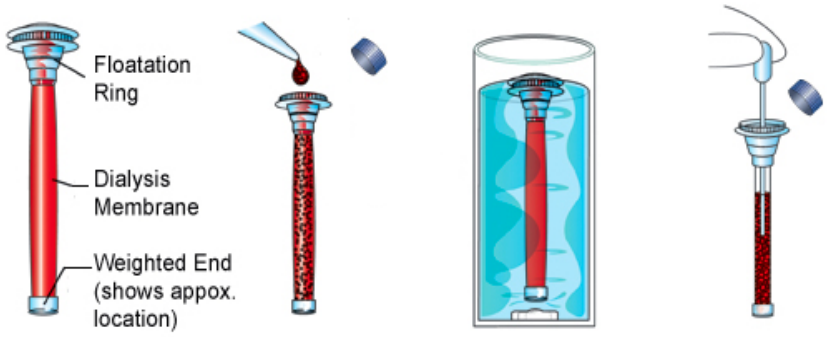


Figure 2. 2 Illustration of the Float-A-lyzer G2 column

Dialysis column used to filter the liposomal nanoparticles after formulation to rid any impurities from the solution, which is not encapsulated within the liposome. The filer and placed into a beaker of 100mL sterile deionised water on a stir plate and set to the slowest speed. The red colour in the column represents the nanoparticle solution.

2.2.4 Study 3: Liposome Characterisation

2.2.4.1 Liposome sizing and stability confirmation

Quality control of the liposome was carried out to ensure particles were fully formulated and filtered; the size and stability of the particles were determined after each formulation using a Zetasizer Nano ZA (Malvern Instruments Ltd, UK), which is an automatized light scattering instrument commonly used to measure the size of liposomal nanoparticles. Particle sizing was evaluated by measuring the average liposomal hydrodynamic diameter (nm). Particle

stability was evaluated by measuring the polydispersity index (PDI), which represents the purity in the liposomal solution as a result of the dialysis process. All measurements were taken in triplicate and at 25°C. The preparation and filtration protocol used in this study were adapted from previous liposomal studies and a commercially available filtration system.

2.2.4.2 ^{1}H NMR spectroscopy of encapsulated acetate in liposomes

To confirm and ensure encapsulation of acetate within the liposomes had occurred, NMR was carried out on the particles immediately following formulation of the LITA particle, described above using formulation 1 from Table 2.1. Albumin (4g) was added to the LITA solution, as the molecule is too large to enter the liposome.

^{1}H NMR spectra was acquired on a Bruker Biospin scanner (Bruker, USA) with a 5mm inverse mode BBI probe at the following parameters: 500.13MHz, sweep width 12ppm (6009Hz), data points 32k, acquisition time 2.726 seconds, relaxation delay 3 seconds (overall recycle delay 5.726 seconds), pulse width 6μs (corresponding to a 55 degree pulse), 64 averages and temperature of 298K. The free induction decay (FID) signal was apodized to reduce noise and fourier transformed. The obtained spectra were baseline corrected, referenced and integrated using the Mest-ReC software (Santiago, Spain).

2.2.4.3 ^{1}H NMR spectroscopy quantitation of encapsulated acetate in liposomes

^{1}H NMR spectroscopy was carried out to quantitatively identify the encapsulated SCFA concentration in 200ul (LITA formulation, as previously described in 2.2.1). To act as a reference peak, lactate (5.2mg) (Sigma-Aldrich, UK) was added to 200μL of liposomes. The SCFA encapsulated liposomes and lactate solution were combined in a chilled 50mL conical tube and placed into a freeze drier (BOC Edwards, USA) overnight at -20ºC. Once solution

was in freeze-dried form, the crystals were resuspended in 1.0mL deuterium oxide (D_2O) and analysed with ^1H NMR spectroscopy. Parameters for ^1H NMR scan were described previously in 2.2.2.1. Baseline correction was carried out using a spline function and peaks were integrated for relative quantification of acetate.

2.2.5 Study 4: Liposomal Bio Distribution and *in vivo* Optimisation

2.2.5.1 Ex vivo *liposomal detection using fluorescence microscopy imaging*

For *in vivo* monitoring and imaging of the liposomes three methods were applied to examine bio-distribution at different stages. For visual identification and *in vivo* optimisation of the liposomes within the organ at a determined time point, fluorescence microscopy was carried out using the LITA-Rhd nanoparticle (Table 2.2, formulation A). For quantitative identification of the liposomes within the organ at a determined time point, MRI was carried out using the LITA-Gd nanoparticle (Table 2.2, formulation B). In order to monitor the liposomal bio-distribution in real-time, PET/CT was applied using the LITA nanoparticle (Table 2.2, formulation 3) and encapsulating the radioactive isotope [^{18}F]FDG.

2.2.5.1.1 Histological evaluation of LITA-Rhd at differing concentrations of acetate and peripheral injection comparison

In order to determine the ideal *in vivo* dosage and injection method of the liposomes, a number of *ex vivo* bio-distribution studies were executed using histological methods to positively identify the presence of the liposome in organs of interest. WT male C57BL/6 mice were used for all histological studies. Four different concentrations of acetate were encapsulated; 100μM, 1mM, 10mM and 1M as well as control HEPES using formulation A, LITA-Rhd (Table 2.2). Animals received a single 200μL injection either intraperitoneally (i.p.) or intravenously (i.v.) at each concentration and culled at 2hr (n=4/group). The organs of

interest were frozen on dry ice immediately after sacrifice and either continued onto histological evaluation or stored at -80ºC. Organs of interest such as the liver, kidneys, heart, brain, spleen and lungs were cut into 7µm sections using a Cryostat (Leica, UK) and cell membranes were stained with the DNA nuclear stain, 1µL 4',6-diamidino-2-phenylindole (DAPI). Microscopy images of the organs of interest were obtained using an Olympus 251 (Soft Imaging Solutions GmbH, Germany). Three different filters were used to confirm liposomes presence. A red filter identified the rhodamine embedded into the lipid bi-layer. A green filter identified any background noise and a blue filter used ultraviolet (UV) light to identify the DAPI stain thus confirming the liposomes were in fact being identified within tissue.

2.2.5.1.2 Histological evaluation of LITA-Rhd at differing time points after injection

In order to determine the ideal *in vivo* delivery of liposomes to organs of interest over time, WT male C57BL/6 mice received a single 200µL injection intraperitoneally (i.p.) at and culled at 2, 16, 24 and 48 hours post injection of LITA-RhD (Table 1). Organs of interest such as the liver, spleen, kidney, lungs, heart, brain, muscles, and pancreas were evaluated using the same protocol as described in 2.2.4.1.1 (n=4/group).

2.2.5.2 *In vivo* liposome detection using MRI and T1 measurements

To monitor bio distribution of liposome accumulation *in vivo* at a particular time point, LITA-Gd (Formulations B) and LITA (Formulation C) from Table 1 were used in this study. Both sets of liposomes were encapsulated with acetate (1M); the only difference in groups was the lipid composition. Formulation B, LITA-Gd contained Gadolinium (Gd), which is an MRI contrast agent which when taken up by the tissues decreases the relaxation time of the tissue therefore increasing the signal from the tissue. Formulation C, LITA, contained no gadolinium and was used as a control liposome.

Animals were anesthetized with 4-3% isoflurane oxygen mix, placed in a birdcage coil and maintained at 2-2%. A breathing pad was used to monitor the breathing rate and a rectal probe for the body temperature which was maintained at 37ºC.

Following shimming on the water signal of the whole mouse, a scout image was obtained. This was used to plan the axial slices covering the whole animal. An array of a fast spin echo sequence with TR 8500msec, TEeff 20msec, ETL 8, k zero at 2, FOV 50x50 mm2, matrix 256x256, one average, 40 slices of 2mm thickness, with TI 50, 100, 500, 1000 and 5000msecs was obtained. Array of 5 TI image volumes was 22 minutes with the total scan time per animal about 30 minutes. Animals were then recovered in a heating box.

After the baseline scan was finished animals received 200µL of acetate liposomes either with or without Gd, intraperitoneally. The scans were repeated 2, 16, 24 and 48 hours post-injection. For each time point and each TI, signal intensities were measured in ROIs placed in the following organs, liver, brain, heart, fat and kidney using Image J. These were fitted into the equation 1 to determine the T_1 values using Graphad Prism.

$$Y=abs\ [M_0 \times (1+e^{8500/T1}-2e^{TIT1})]$$

Equation 2.1 T_1 values were averaged as mean ± SEM. Unpaired t-test was carried out for statistical analysis.

2.2.5.3 Real-time biodistribution assessment by PET/ CT fusion

Positron Emission Tomography (PET) and x-ray Computed Tomography (CT) were used in combination to monitor liposomal bio-distribution in real-time and *in vivo*. Images acquired from both PET and CT were taken sequentially in the same imaging session and combined

into a single superposed (co-registered) image. Liposomes were formulated (as described in 3.1.1) using formulation C, LITA and encapsulated with fluorodeoxyglucose ([^{18}F]FDG). The volume administered was 200μL in order to monitor the exact dosage given during the study. The encapsulation of [^{18}F]FDG was calculated to ensure at the end of the required filtration time, there would be an activity of 10 MBq per dosage. Once formulation was completed, 200μL (10 MBq) [^{18}F]FDG encapsulated liposomes were injected into the mice either intraperitoneally (i.p.) or intravenously (i.v.).

Immediately following injection of liposomes, mice were anesthetized with 2-2.5% isoflurane 1/min oxygen and placed prone into the scanner. Once the animal was placed into the scanner, a CT scan without contract was performed which lasted 10 minutes and the PET scan followed immediately. During the scan animals were maintained at 1-2% isoflurane-oxygen mix and body temperature maintained at 37ºC.

Images of entire body of the mouse were acquired using a 30-minute acquisition program. The micro PET/CT (Siemens) scanner operates in a 3-dimensional volume imaging acquisition mode. The CT had an X-ray source of 80kVp and 500μA with an exposure time of 200ms and isotropic resolution of 103μm. The scan consisted of 3 bed positions with a 20% overlap. Small animals were laser aligned at the centre of the scanner field of view (FOV) for subsequent imaging. To minimize any errors between PET and CT, mice were scanned in a chamber, which kept positioning to minimal errors [215].

Images were analysed using Inveon Research Workplace Version 3, the software provided by Siemens. The PET data acquired were list-mode data then sorted into 3D sonograms with a span of 3-ring difference of 79 and converted into 2D sonograms by Fourier rebinning.

Images with matrix size 128x128, pixel size 0.776mm^2 and slice thickness 0.796mm were reconstructed from the 2D sonogram by 2D filtered back projection using a ramp filter with a nyquist frequency of 0.5. Dynamic framing was used in reconstruction with 20 3s frames, 8 30s frames, 5 60s frames and 10 300s frames. All regions of interest (ROI) were defined on fused PET/CT images to ensure reproducible positioning and accuracy. Reconstructed PET images were registered onto the CT images and ROIs were drawn on the desired organs using the CT images. PET signals on the desired ROI were obtained over the scan period. The intensity of [^{18}F]FDG uptake was quantified using the mean standard uptake value (SUV) over the desired ROI by Equation 2 and expressed as area under the curve (AUC).

SUV= Regional radioactivity (MBq/kg)/ (Injected radio activity (MBq)/ body weight (g))

Equation 2.2 Standard Uptake Value (SUV) to obtain uptake of [^{18}F]FDG from PET/CT acquired image

2.3 Results

2.3.1 *Study 1: Liposome Preparation and Formulation*

First objective was to determine an ideal liposome formulation that would encapsulate acetate. To do this, both the lipid type and molarity percentage incorporated into the liposome were tested. The foundation of the liposome was selected to contain four primary lipids: DSPC, cholesterol, DSPC-PEG^{2000} and CDAN. From those lipids, I tested substitute lipids to determine the best formulation for a LITA nanoparticle. Following the lipid selection, molarity percentage differences were tested. Table 2.1 shows the 14 different liposome formulation variables (n=3/group).

Molar component (%) Lipid variable	DSPC	DOPE	DLPC (C12)	DLPC (C20)	CDAN	DDAB	Cholesterol	DC Cholesterol	DSPE-PEG^{2000}	DSPE-PEG^{500}	DSPE-PEG^{10000}
1) Formulation 1	32				32		35		1		
2) DSPC ↔ DOPE	-	32	-	-	32	-	35	-	1	-	-
3)DSPC ↔ DLPC (C12)	-	-	32		32	-	35	-	1	-	-
4)DSPC ↔ DLPC (C20)	-	-	-	32	32	-	35	-	1	-	-
5)DSPC ↔ 10% DSPC	10	-	-	-	44	-	45	-	1	-	-
6)DSPC ↔ 50% DSPC	50	-	-	-	25	-	24	-	1	-	-
7)Cholesterol ↔ DC chol	32	-	-	-	35	-	-	32	1	-	-
8)Cholesterol ↔ 10% chol	45	-	-	-	45	-	10	-	1	-	-
9)Cholesterol ↔ 50% chol	24.5	-	-	-	24.5	-	50	-	1	-	-
10)PEG^{2000} ↔ PEG^{500}	32	-	-	-	32	-	35	-	-	1	-
11)PEG^{2000} ↔ PEG^{10000}	32	-	-	-	32	-	35	-	-	-	1
12)CDAN ↔ DDAB	32	-	-	-	-	32	35	-	1	-	-
13)CDAN ↔ 10% CDAN	45	-	-	-	10	-	45	-	1	-	-
14)CDAN ↔ 50% CDAN	24.5	-	-	-	50	-	24.5	-	1	-	-

Table 2.1 Percentage molar and lipid components of potential liposome formulations

Formulation variables of liposomes generated to produce the most stable and appropriately sized liposome which will encapsulate acetate for *in vivo* delivery.

Once the formulation and rehydration was carried out, liposomes were sized. Sizes of the formulated liposomes were determined by using a Zetasizer Nano (Malvern, UK). Size is expressed in nanometers (nm) and the difference in size within the liposome solution is expressed as the poly distribution index (PDI). Figure 2.3 shows two diagrams that show the size distribution of the liposome solution before (Figure 2.3 A) and after (Figure 2.3 B) dialysis via the Float-A-Lyzer. This comparison of sizing confirms that after dialysis is carried out all the excess material, unformed lipids and any other unwanted material is cleared from the liposome solution and is appropriately sized and purity for *in vivo* application. The green and red colour recordings in each graph refer to technical replicates to confirm sizing reproducibility. Once this method was developed, it was applied to the panel of liposome variables to quantitatively assess each formulation.

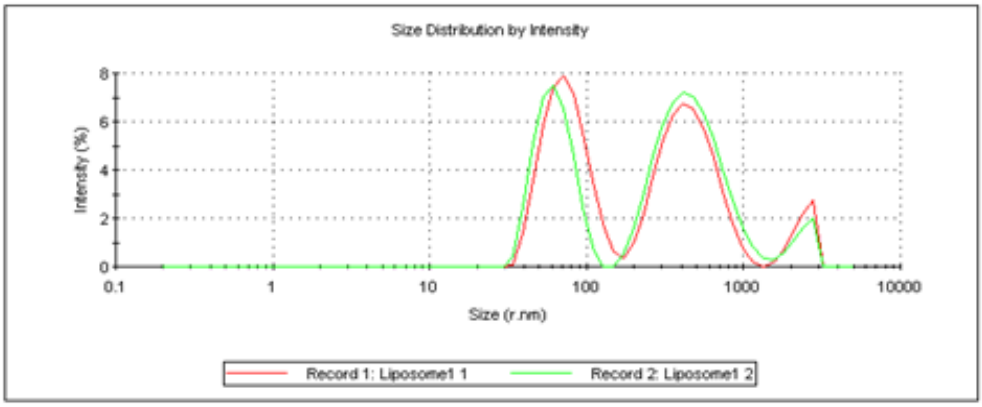
DSPC was substituted with isoform lipids: DOPE, DLPC (carbon 12) and DLPC (carbon 20) (Figure 2.4 A-C). DOPE, DLPC (C12) and DLPC (C20) lipids formulated a bit below than the desired 100mn. The molarity of DSPC was tested at 10% and 50% molarity to determine stability and formulation abilities (Figure 2.4 D-E). Both molarity percentages formulated appropriate, especially 50% DSPC where the average size 100mn; however 10% DSPC averaged well below that.

Cholesterol was substituted with the isoform lipid, DC cholesterol (Figure 2.5 A), which formulated slightly smaller than the target 100mn however had a precise range of size. The molarity of cholesterol was tested at 10% and 50% molarity to determine stability and formulation abilities (Figure 2.5 B-C), neither of which formulated properly and had an excess of lipids in the solution which did not form into liposomes.

DSPE-PEG^{2000} was substituted with isoform lipids of varying PEG length but at the same 1% molarity: DSPE-PEG^{500} and DSPE-PEG^{10000} (Figure 2.6). A shorter PEG length formed a liposome of appropriate size; however a longer PEG chain caused a formulation size below the ideal 100mn.

CDAN was substituted with the isoform lipid, DDAB (Figure 2.7), which was unable to formulate a liposome. The molarity of CDAN was tested at 10% and 50% molarity to determine stability and formulation abilities (Figure 2.10). At 10% CDAN the formulated liposome size was too small, from 10-120nm; whereas 50% CDAN formulated the correct average size however had too high a range. Out of all the formulation tested, Formulation 1 had the most exact sizing profile at 100mn. A quantitative summary of these formulates is shown in Table 2.2.

A)



B)

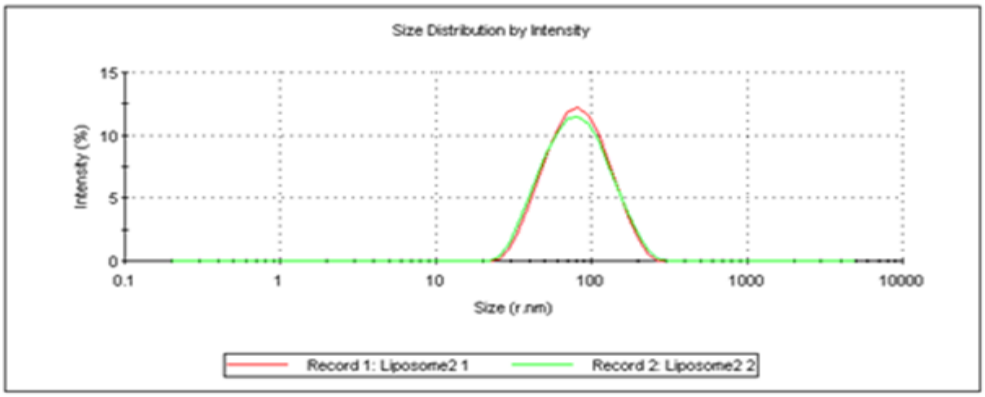
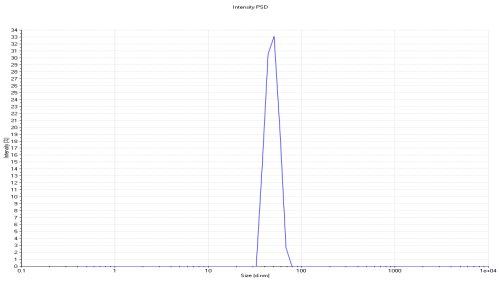


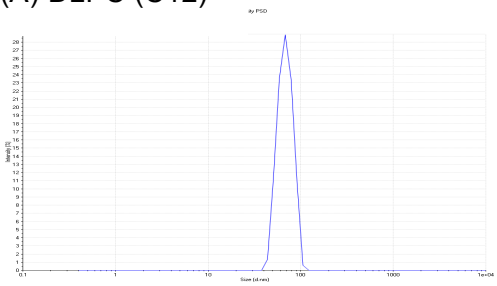
Figure 2.3 Liposomal nanoparticle profiles before and after dialysis

Size distribution of LITA nanoparticles **(A)** before and **(B)** after filtration in the Float-A-Lyzer. The x-axis is the size distribution of the particles measured in the solution and the y-axis is the intensity of the particles. This particular formulation is notated as Formulation 1 in Table 2.1. The green and red colour recordings refer to technical replicates.

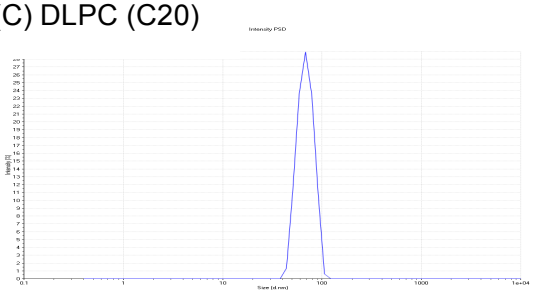
(A) DOPE



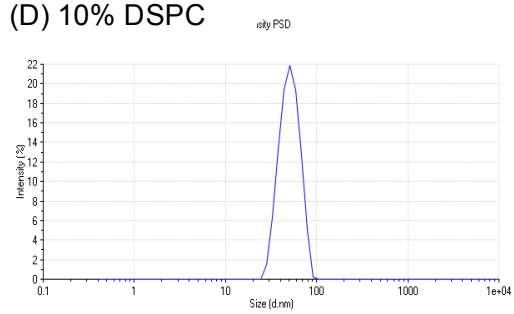
(A) DLPC (C12)



(C) DLPC (C20)



(D) 10% DSPC



(E) 50% DSPC

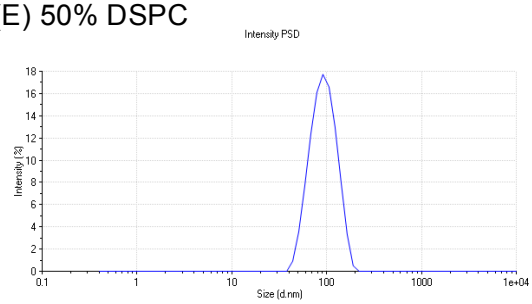
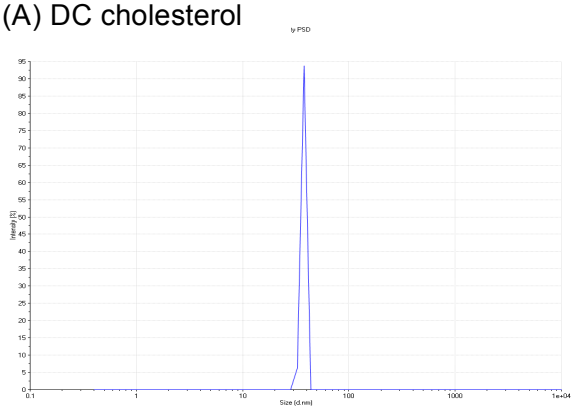


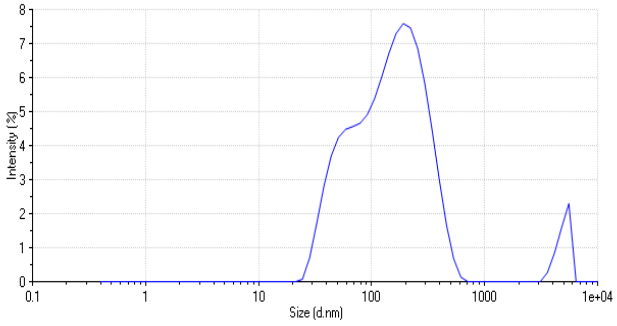
Figure 2.4 Size of liposomes after formulation and dialysis- target lipid: 1,2-distearoyl-sn-glycero-3-phosphocholine (DSPC)

The LITA-nanoparticle was formulated and sized by varying DSPC lipid of either: **(A)** DOPE, **(B)** DLPC (C12) or **(C)** DLPC (C20). Liposomes were formulated at varying molarities of **(C)** 10% or **(D)** 50% DSPC.

(A) DC cholesterol



(B) 10% cholesterol PSD



(C) 50% cholesterol SD

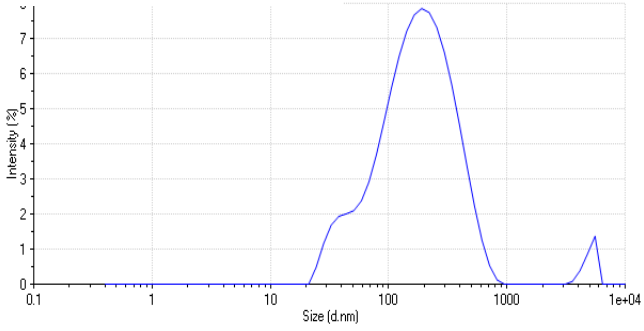


Figure 2.5 Size of liposomes after formulation and dialysis- target lipid: 3β-Hydroxy-5-cholestene, 5-Cholesten-3β-ol (cholesterol)

The LITA-nanoparticle was formulated and sized by varying the cholesterol lipid of **(A)** DC cholesterol. Liposomes were formulated at varying molarities of either **(B)** 10% or **(C)** 50% cholesterol.

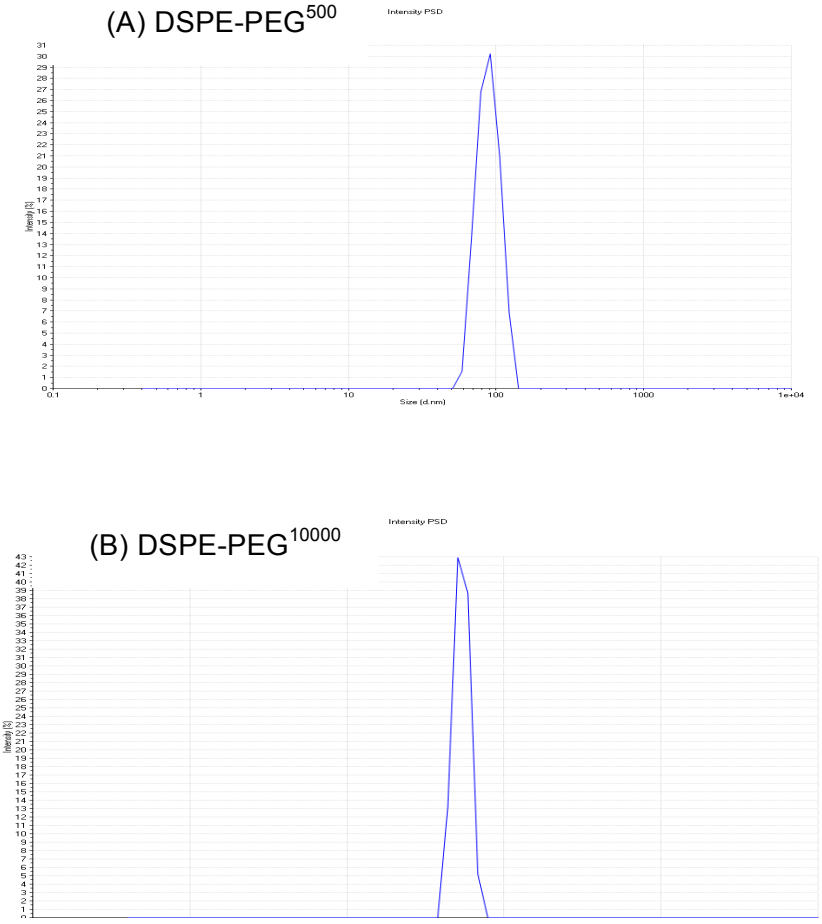


Figure 2.6 Size of liposomes after formulation and dialysis- target lipid: 1,2-distearoyl-sn-glycero-3-phosphoethanolamine-N-[methoxy(polyethylene glycol)-2000] (DSPE-PEG^{2000})

The LITA-nanoparticle was formulated and sized by varying the cholesterol lipid of either **(A)** DSPE-PEG^{500} or **(B)** DSPE-PEG^{10000}. Both formulations were had the same 1% molarity incorporated into the liposomes.

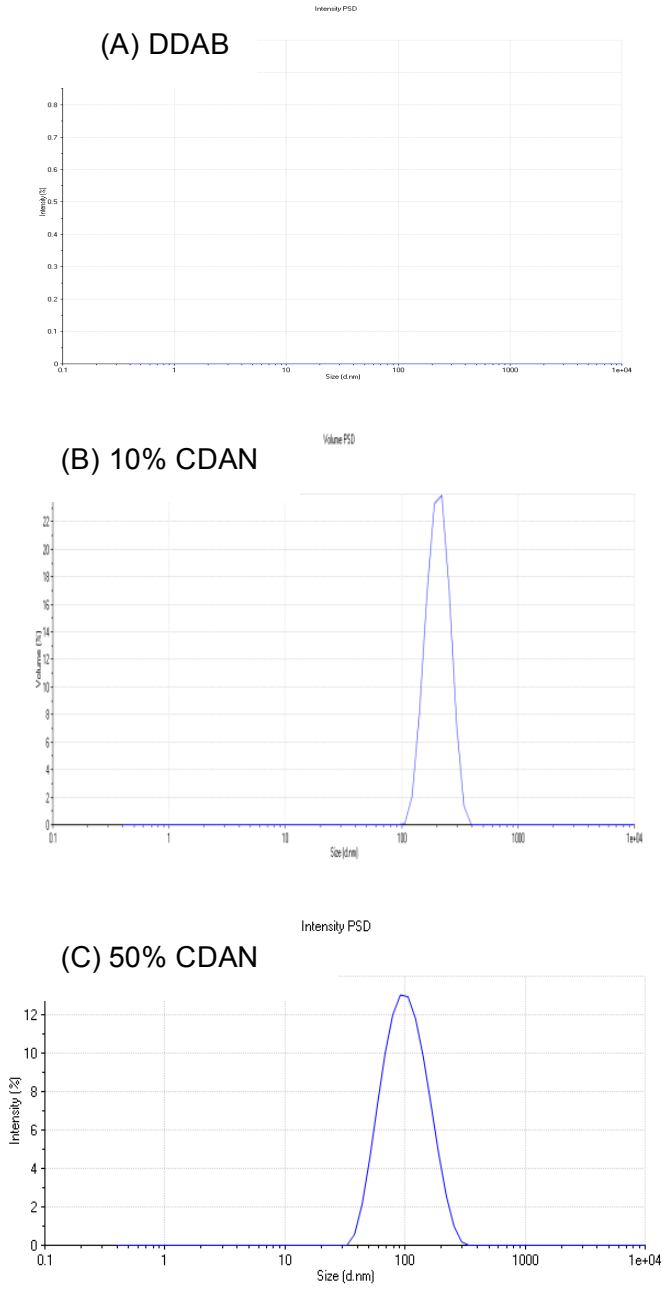


Figure 2.7 Size of liposomes after formulation and dialysis- N1-cholesteryloxycarbonyl-3,7-diazanonane-1,9-diamine lipid (CDAN)

The LITA-nanoparticle was formulated and sized by varying the cholesterol lipid of **(A)** DDAB. Liposomes were formulated at varying molarities of either **(B)** 10% or **(C)** 50% CDAN.

Lipid	Lipid variation	Size (nm)
Formulation 1	DSPC (32); Chol (35); DPSE-Peg^{2000} (1); CDAN (32)	80-110
DSPC	DOPE	35-80
	DLPC (C12)	35-150
	DLPC (C20)	30-110
	10% DSPC	15-100
	50% DSPC	30-110
Cholesterol	DC Cholesterol	25-45
	10% Cholesterol	20-1000
	50% Cholesterol	20-160, 1000+
DSPE-PEG^{2000}	DSPE-PEG^{500}	50-150
	DSPE-PEG^{10000}	35-80
CDAN	DDAB	2.4x10^{4}
	10% CDAN	100-300
	50% CDAN	20-200

Table 2.2 Quantitative summary from formulation with varying molarities and incorporated lipids

A panel of lipids and varying molarities were incorporated into numerous liposome formulations, filtered through dialysis and measured for characterisation of each formulation. This lipid selection was from each foundation lipid selected to incorporate into the liposome: DSPC (Figure 2.4), cholesterol (Figure 2.5), DSPC-PEG^{2000} (Figure 2.6) and CDAN (Figure 2.7). The formulation with the best performance was Formulation 1.

2.3.2 *Study 2: ^{1}H NMR Spectroscopy of Encapsulated Acetate in Liposomes*

^{1}H NMR spectroscopy was performed to confirm the encapsulation of acetate within liposomes and determine the resulting concentration. Firstly, a baseline scan of pure acetate solution (4mM) was carried out and a visible acetate peak was observed at 2.03ppm (Figure 2.8, A). The acetate signal suppressor molecule, albumin (4g), was added to the liposome solution and the same scan was repeated. The ^{1}H NMR signal from acetate was completely suppressed; (Figure 2.8, B). This established a model to confirm the encapsulation of acetate within the liposome. The nanoparticle, specified as Formulation 1, underwent a baseline scan and a visible acetate peak was observed at 2.03ppm (Figure 2.9, A). Addition of albumin reduced the acetate signal significantly (Figure 2.9, B). The albumin bound to the acetate present in the solution which was external of the liposomes, thus the internal acetate could be measured and quantified.

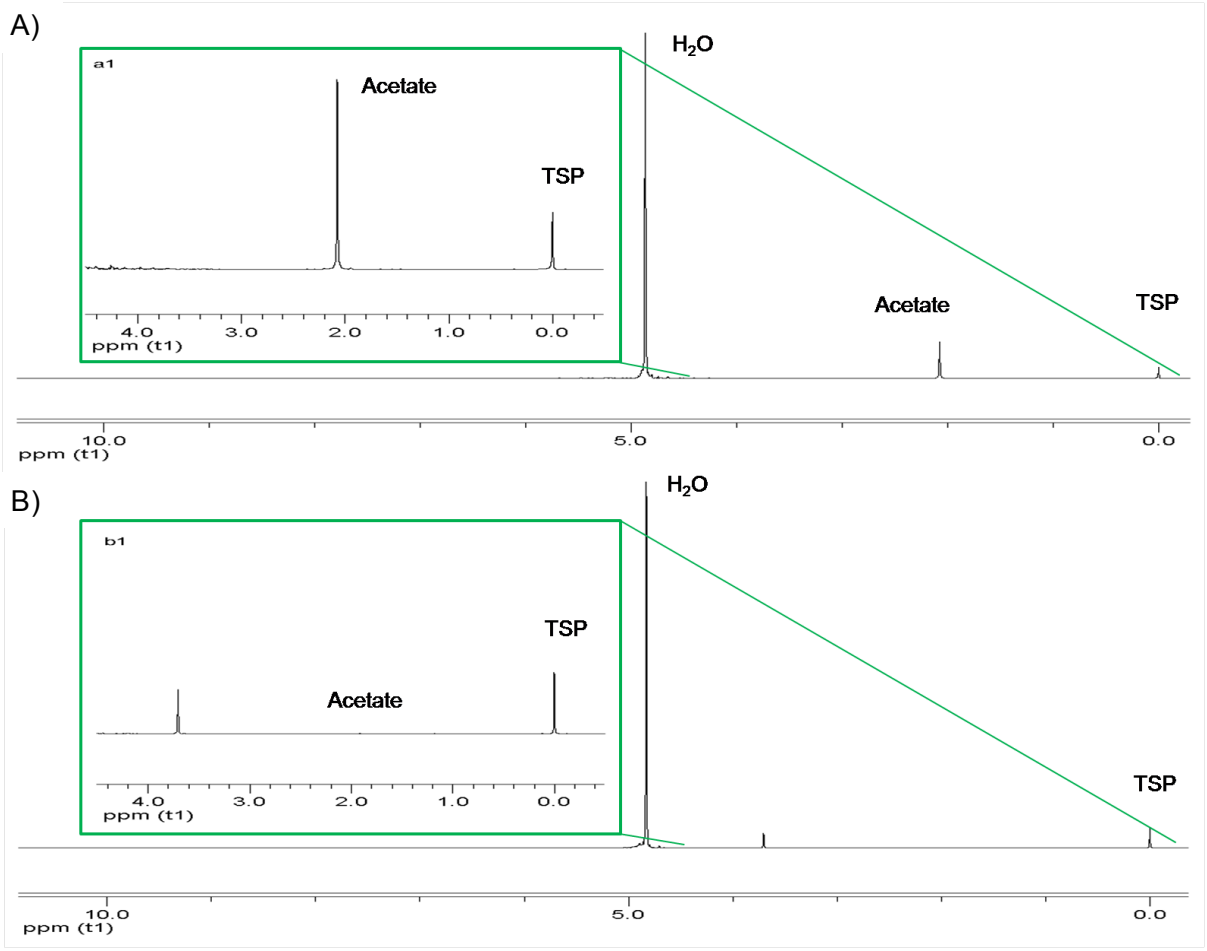


Figure 2. 8 ^{1}H NMR spectra of acetate with added albumin

^{1}H NMR spectra of **(A)** 4mM acetate solution and **(B)** 4mM acetate solution with 4g of albumin. The highlighted green boxes are expanded sections of the spectra from 4.5 to -0.5ppm; the peak for acetate is normally observed at 2.03ppm.

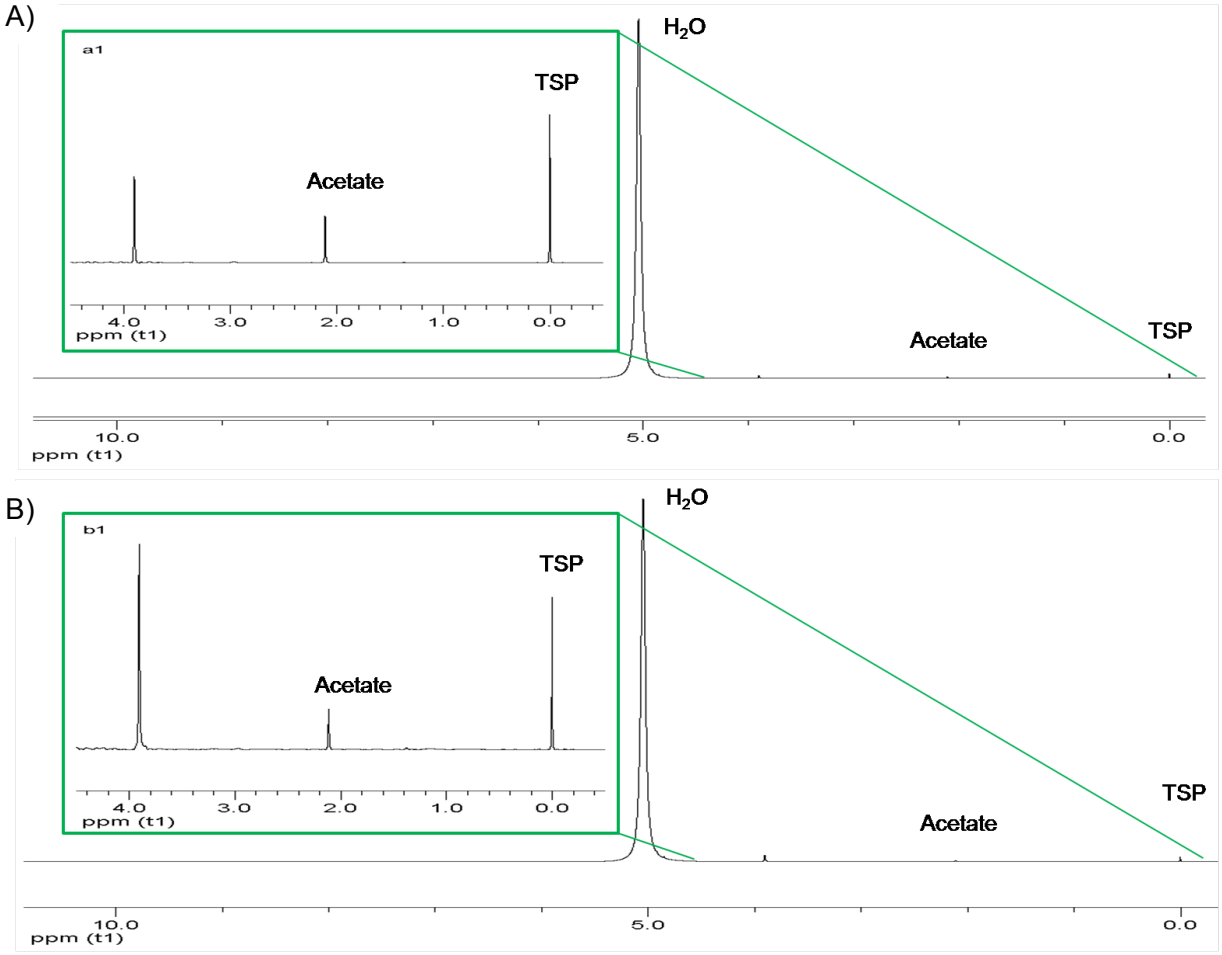


Figure 2.9 ^{1}H NMR spectra of acetate encapsulated liposomes with added albumin

^{1}H NMR spectra of **(A)** LITA solution and **(B)** LITA solution with albumin added (4g). Trimethylsilyl propionate (TSP) provides a reference at 0ppm. The highlighted green boxes are expanded sections of the spectra from 4.5 to -0.5ppm; the peak for acetate is normally observed at 2.03ppm.

2.3.3 *Study 3: Liposome Characterisation ^{1}H NMR Spectroscopy to Determine Encapsulated Acetate Concentration*

Once a formulation was determined, the amount of acetate encapsulated was measured. Figure 2.10 shows the ^{1}H NMR spectra of 200µL LITA nanoparticles formulated with 1M acetate and the composition of Formulation 1 for a baseline profile. Figure 2.11 shows the same ^{1}H NMR spectra following the addition of sodium lactate (5.2mg) added in prior to being freeze-dried.

Based on the integrated peak of lactate and acetate, the concentration of acetate in 200µl was determined to be 52.9µg (4.41mM). Each liposomal particle was calculated to contain 4.41×10^{-14}mmol of acetate, based on the concentration of nanoparticles in a known concentration of liposome solution (10^{11} in 1mL).

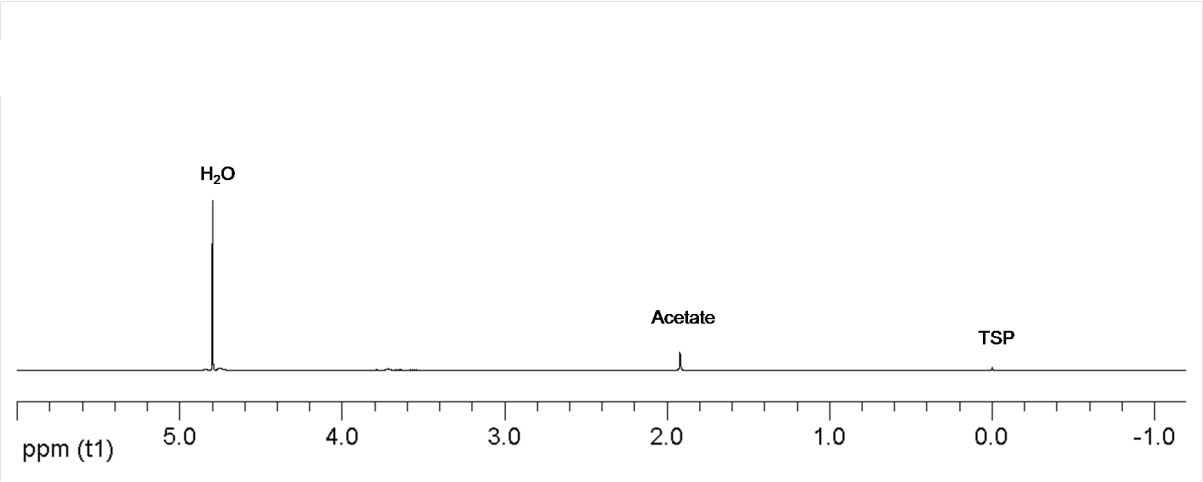


Figure 2.10 ^{1}H NMR spectra of LITA formulated with 1M acetate

^{1}H NMR spectra exhibits the fingerprints of 200μL of LITA (1M). Peak at zero is the reference peak; the peak at 2.03ppm is acetate.

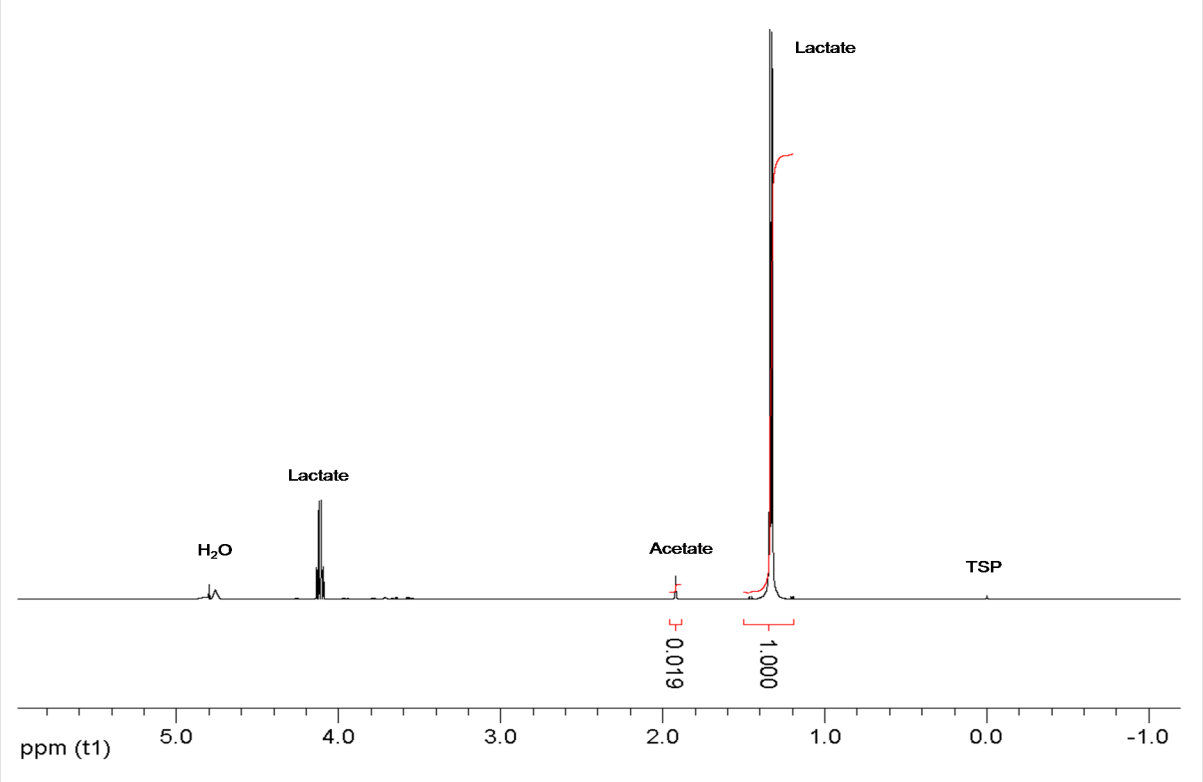


Figure 2.11 ^{1}H NMR spectra of LITA nanoparticles and sodium lactate

^{1}H NMR spectra of freeze-dried LITA nanoparticles encapsulated with 1M acetate and added sodium lactate (5.2mg) to act as a reference. Peak at zero is the reference peak; peak at 1.3ppm is sodium lactate whereas the peak at 2.03ppm is acetate. Values underneath the peaks (shown in red) are the calculated integrals of the peaks

2.3.3.1 Liposome characterisation 1H NMR spectroscopy to determine encapsulated acetate concentration of formulation candidates

Once a protocol was developed and confirmed to identify acetate concentration encapsulated within the liposome, this same method was applied to the 13 other liposome formulations to determine the best candidate for *in vivo* application (n=3). For formulation specifics, refer to Table 2.1.

DSPC was substituted with isoform lipids: DOPE, DLPC (carbon 12) and DLPC (carbon 20), which encapsulated a varying range of acetate per formulation (Figure 2.12 A-C). DOPE and DLPC (C12) encapsulated approximately the same amount of acetate (1mM), whereas DLPC with a higher carbon chain (C20) encapsulated only half that amount of acetate (0.58mM). The molarity of DSPC was tested at 10% and 50% molarity and had differing encapsulation concentrations; 10% of DSPC contained 4.19mM whereas 50% contained 0.51mM of acetate (Figure 2.12 D-E).

Cholesterol was substituted with the isoform lipid, DC cholesterol (Figure 2.13 A), which failed to encapsulate a detectable amount of acetate. The molarity of cholesterol was formulated with 10% and 50% molarity (Figure 2.13 B-C). The liposome embedded with 10% cholesterol into the lipid bilayer encapsulated 2.79mM of acetate, whereas 50% cholesterol failed to encapsulate a detectable amount of acetate.

DSPE-PEG^{2000} was substituted with isoform lipids of varying PEG length but at the same 1% molarity: DSPE-PEG^{500} and DSPE-PEG^{10000} (Figure 2.14). A shorter PEG length failed to formulate a liposome which had a detectable amount of acetate; however a longer PEG chain caused the high amount of encapsulated acetate found in this study (6.13).

CDAN was substituted with the isoform lipid, DDAB (Figure 2.15 A), which detected a trace of acetate encapsulated within the liposome (0.03mM). The molarity of CDAN was tested at 10% and 50% molarity (Figure 2.15 B-C); at 10% CDAN the formulated liposome encapsulated 1.28mM of acetate, whereas 50% CDAN encapsulated a minimal 0.04mM of acetate. Out of all the formulation tested, Formulation 1 had the second highest amount of acetate encapsulated within the liposome (4.41mM). A quantitative summary of these formulates is shown in Table 2.3.

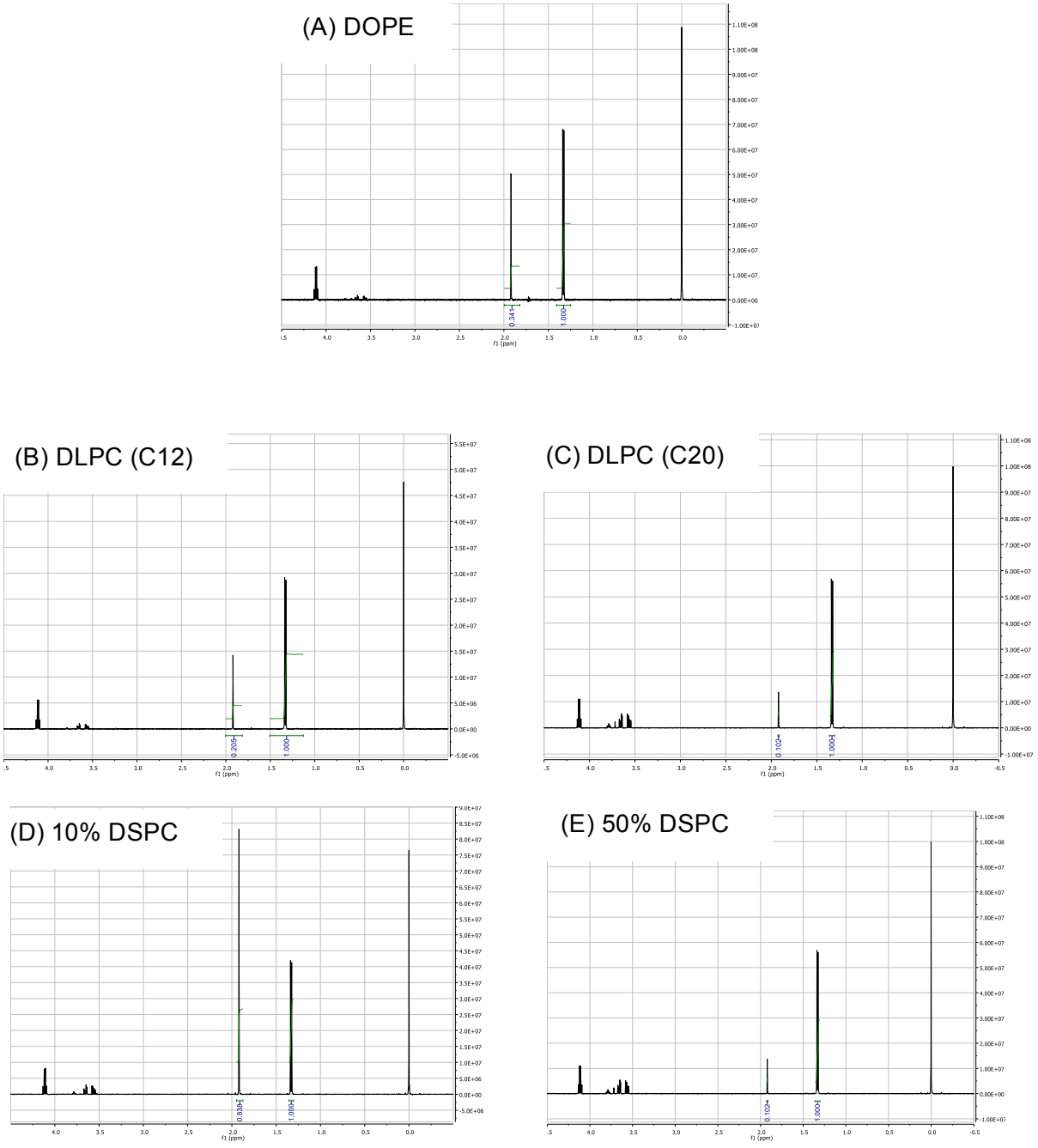
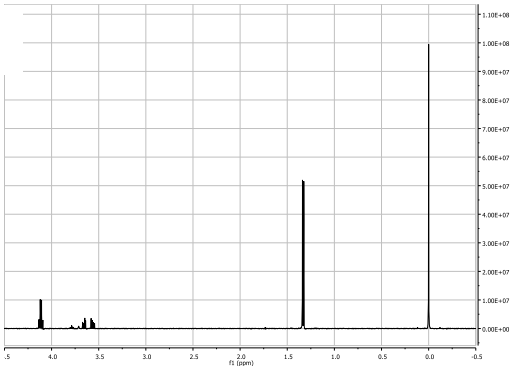


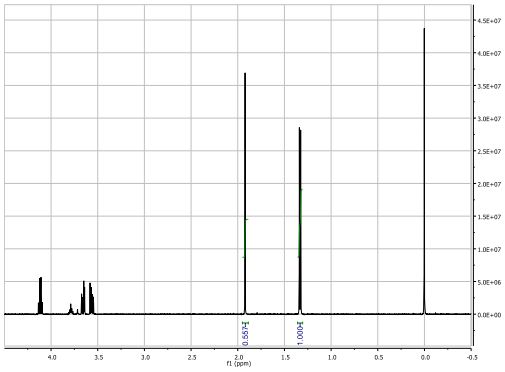
Figure 2.12 Acetate encapsulated within the liposomes and measured by 1H MRS - target lipid: 1,2-distearoyl-sn-glycero-3-phosphocholine (DSPC)

The LITA-nanoparticle was formulated and sized by varying DSPC lipid of either: **(A)** DOPE, **(B)** DLPC (C12) or **(C)** DLPC (C20). Liposomes were formulated at varying molarities of **(C)** 10% or **(D)** 50% DSPC.

(A) DC cholesterol



(B) 10% cholesterol



(C) 50% cholesterol

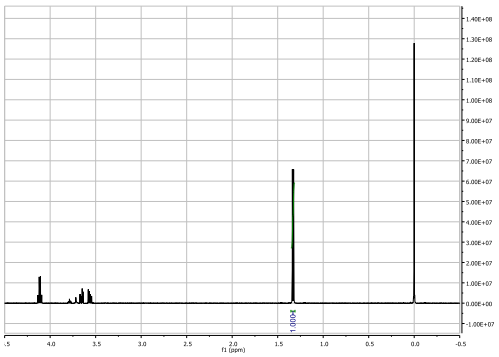


Figure 2.13 Acetate encapsulated within the liposomes and measured by 1H MRS - target lipid: 3β-Hydroxy-5-cholestene, 5-Cholesten-3β-ol (cholesterol)

The LITA-nanoparticle was formulated and sized by varying the cholesterol lipid of **(A)** DC cholesterol. Liposomes were formulated at varying molarities of either **(B)** 10% or **(C)** 50% cholesterol.

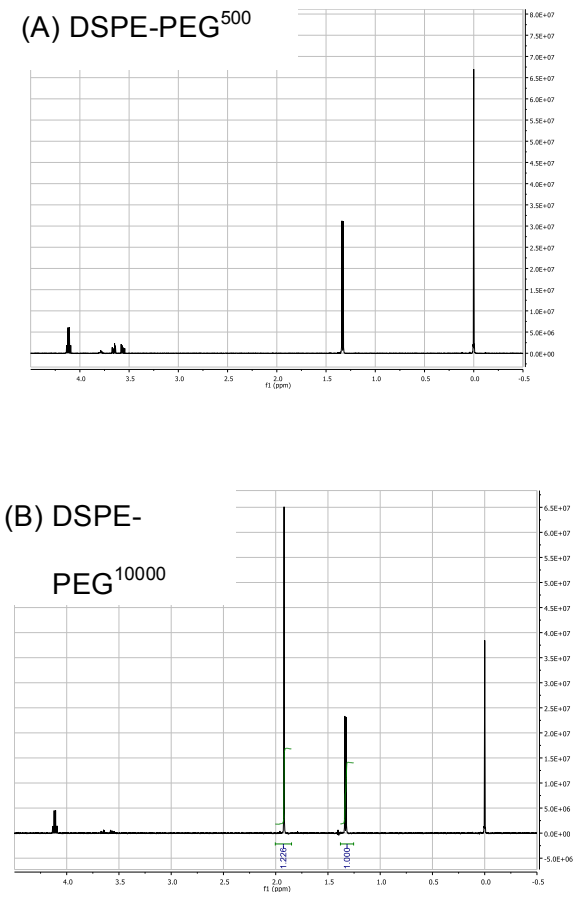


Figure 2.14 Acetate encapsulated within the liposomes and measured by ^{1}H MRS – target lipid: 1,2-distearoyl-sn-glycero-3-phosphoethanolamine-N-methoxy(polyethylene glycol)-2000] (DSPE-PEG^{2000})

The LITA-nanoparticle was formulated and sized by varying the cholesterol lipid of either **(A)** DSPE-PEG^{500} or **(B)** DSPE-PEG^{10000}. Both formulations were had the same 1% molarity incorporated into the liposomes.

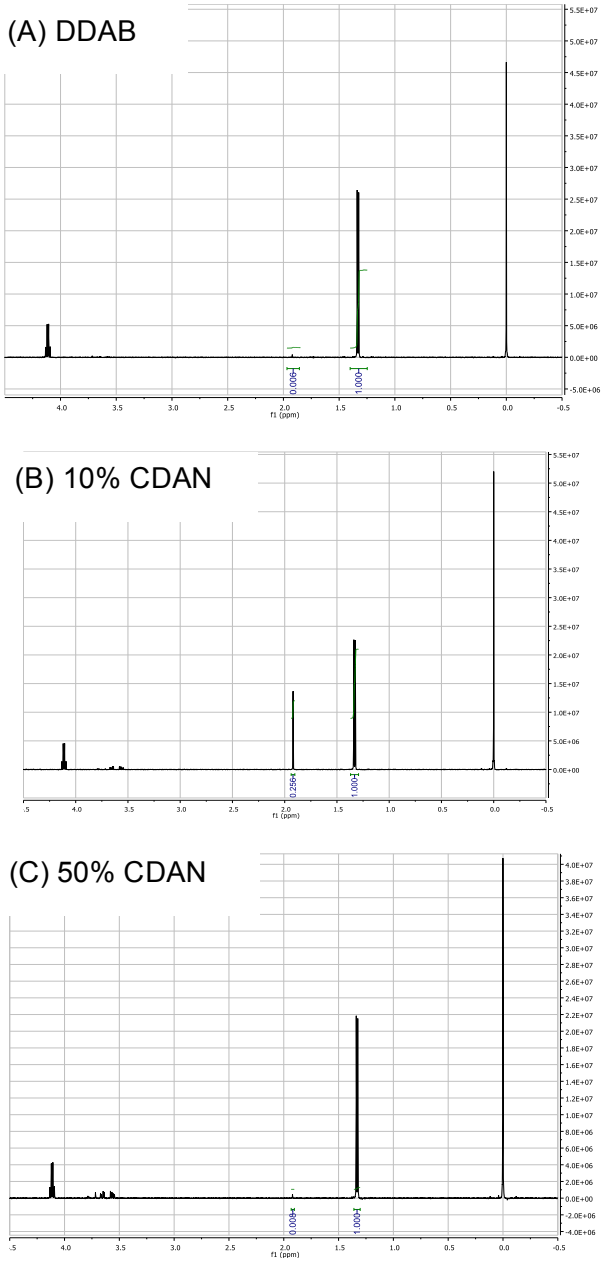


Figure 2.15 Acetate encapsulated within the liposomes and measured by 1H MRS - N1-cholesteryloxycarbonyl-3,7-diazanonane-1,9-diamine lipid (CDAN)

The LITA nanoparticle was formulated with varying the cholesterol lipid of **(A)** DDAB and varying molarities of either **(B)** 10% or **(C)** 50% CDAN, and amount of acetate encapsulated measure.

Lipid	Lipid variation	Acetate encapsulated (mM)
Formulation 1	DSPC (32); Chol (35); DPSE-PEG^{2000} (1); CDAN (32)	4.41
DSPC	DOPE	1.70
	DLPC (C12)	1.02
	DLPC (C20)	0.58
	10% DSPC	4.19
	50% DSPC	0.51
Cholesterol	DC cholesterol	0.00
	10% Cholesterol	2.79
	50% Cholesterol	0.00
DSPE-PEG^{2000}	DSPE-PEG^{500}	0.00
	DSPE-PEG^{10000}	6.13
CDAN	DDAB	0.03
	10% CDAN	1.28
	50% CDAN	0.04

Table 2.3 Quantitative summary of acetate encapsulated within the liposomes and measured by ^{1}H MRS

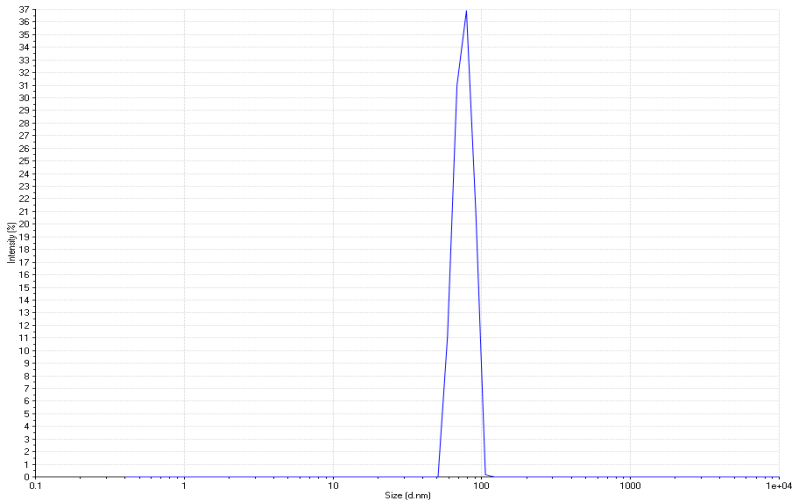
A panel of lipids and varying molarities were incorporated into numerous liposome formulations, filtered through dialysis and measured for characterisation of each formulation. This lipid selection was from each foundation lipid selected to incorporate into the liposome: DSPC (Figure 2.12), cholesterol (Figure 2.13), DSPC-PEG^{2000} (Figure2.14) and CDAN (Figure 2.15). The formulation with the highest amount of acetate was with DSPE-PEG^{10000}.

2.3.3.2 Liposome characterisation spectroscopy to determine encapsulated acetate concentration of formulation parameters

From the previous characterisation experiments carried out examining various liposome formulations, one was chosen (Formulation 1, encapsulated with 1M acetate) which had the ideal size, stability and acetate encapsulated. Moving forward, this formulation was applied with varying concentrations of acetate in order to determine maximum capacity of payload within the liposome.

LITA was formulated with varying ranges of acetate was hydrated and measured by ^{1}H NMR to determine acetate potential dosage in one administration of 200µl. LITA nanoparticles that were hydrated with 1mM encapsulated a total of 0.62mM (Figure 2.16). LITA nanoparticles that were hydrated with 10mM encapsulated a total of 0.30mM (Figure 2.17). LITA nanoparticles that were hydrated with 100mM encapsulated a total of 0.84mM (Figure 2.18). LITA nanoparticles that were hydrated with 10M encapsulated a total of 0.12mM (Figure 2.19).

A)



B)

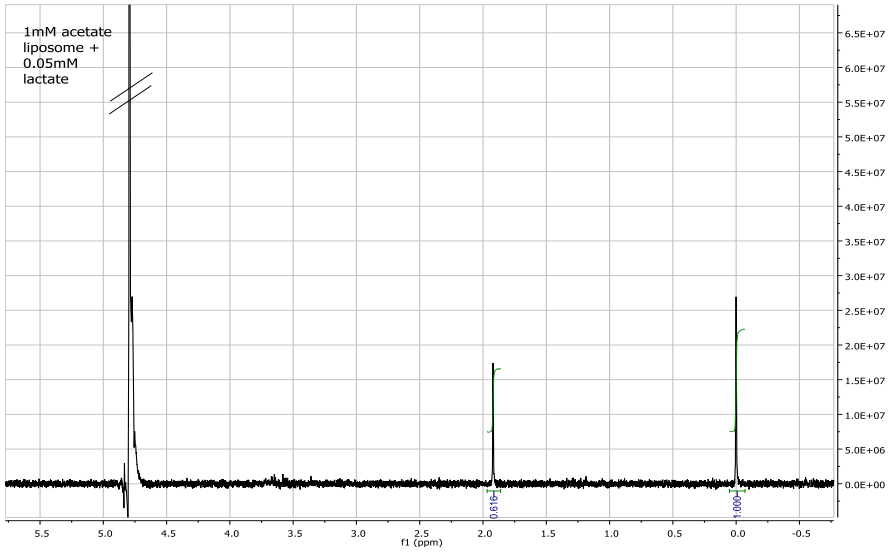
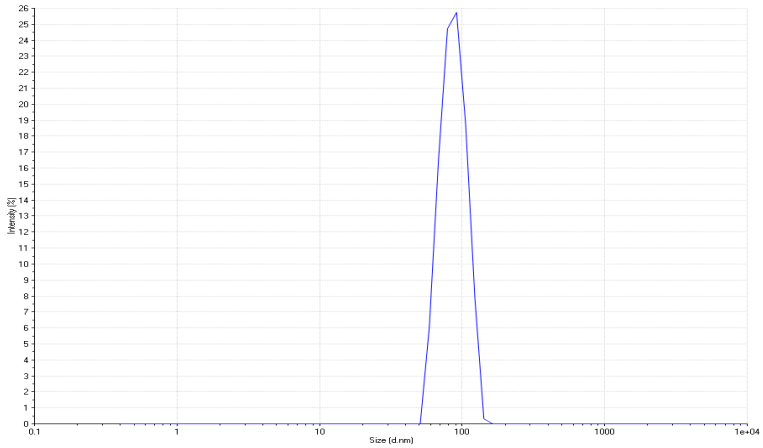


Figure 2.16 LITA nanoparticle characterisation- size and payload formulated with 1mM acetate

LITA nanoparticle was formulated as previously described and rehydrated with 1mM acetate. **(A)** Size and stability were measured revealing a stable nanoparticle. **(B)** Encapsulated acetate was 0.62mM.

A)



B)

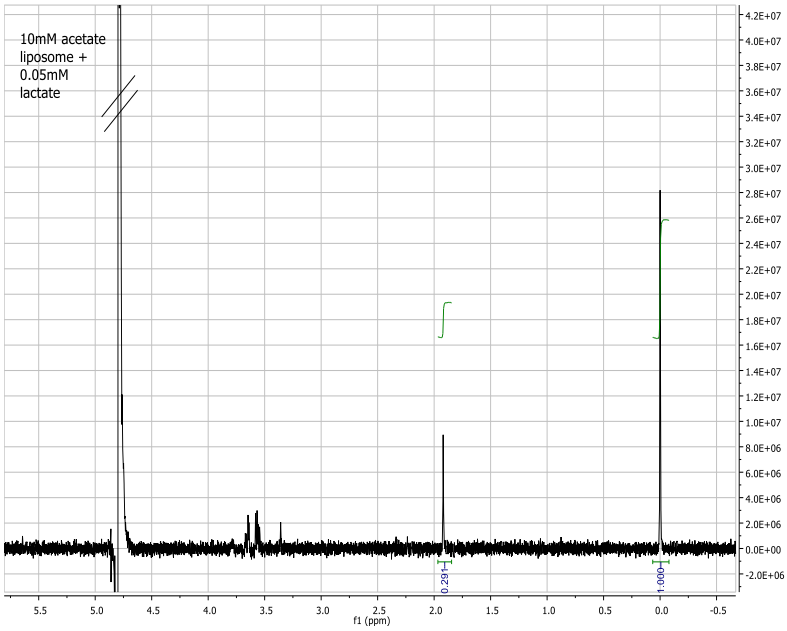
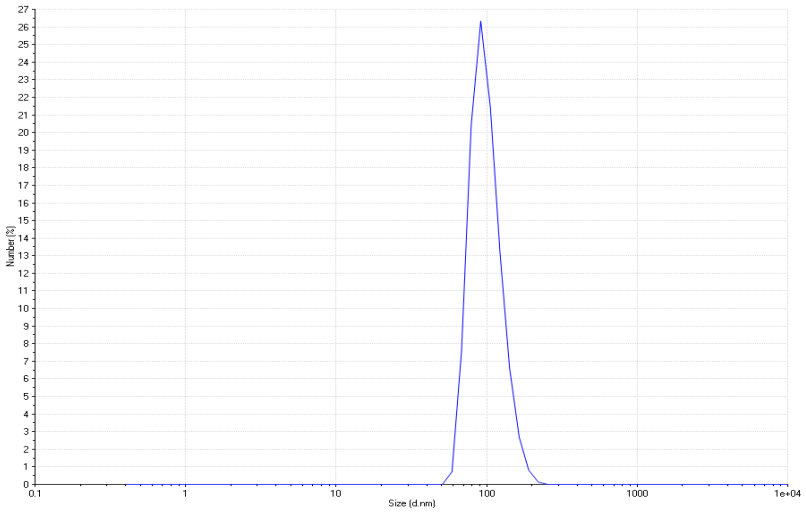


Figure 2.17 LITA nanoparticle characterisation- size and payload formulated with 10mM acetate

LITA nanoparticle was formulated as previously described and rehydrated with 10mM acetate. **(A)** Size and stability were measured revealing a stable nanoparticle. **(B)** Encapsulated acetate was 0.30mM.

A)



B)

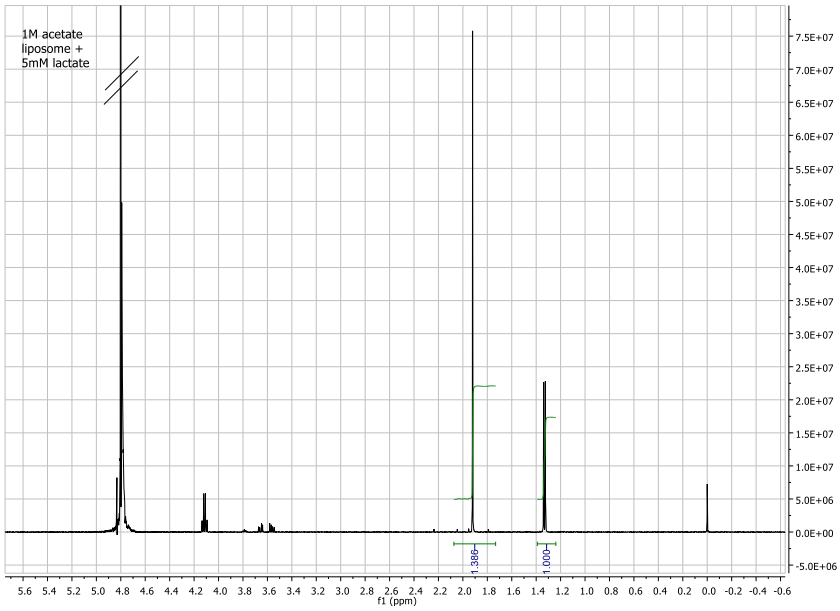
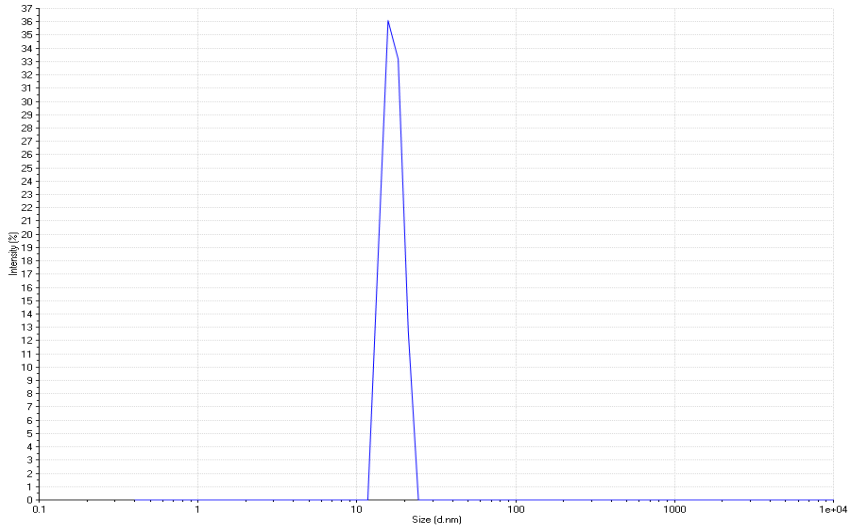


Figure 2. 18 LITA nanoparticle characterisation- size and payload formulated with 100mM acetate

LITA nanoparticle was formulated as previously described and rehydrated with 100mM acetate. **(A)** Size and stability were measured revealing a stable nanoparticle. **(B)** Encapsulated acetate was 0.84mM.

A)



B)

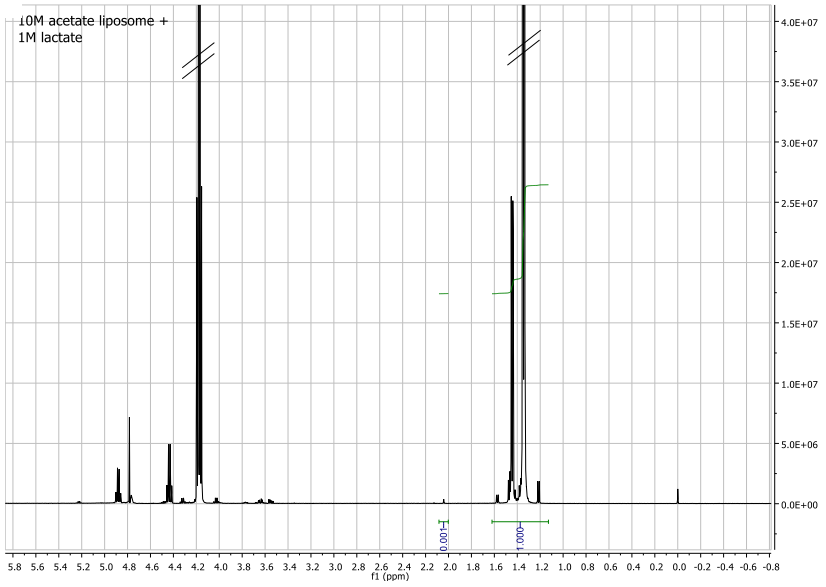


Figure 2.19 LITA nanoparticle characterisation- size and payload formulated with 10M acetate

LITA nanoparticle was formulated as previously described and rehydrated with 10M acetate. **(A)** Size and stability were measured revealing a stable nanoparticle. **(B)** Encapsulated acetate was 0.12mM.

2.3.3.2 LITA Characterisation for *in vivo* application

Once a formulation was chosen, characterisation of the LITA nanoparticle was carried out. Table 2.4 describes the formulation for the five separate liposome formulations applied in the studies discussed in this thesis. (A) LITA-Rhd contains Rhodamine (Rhd), a fluorescent lipid used for biodistribution via histological investigation using fluorescence microscopy. (B) LITA-Gd contains gadolinium (Gd) for use in MRI biodistribution analysis. (C) LITA: liposomes conjugation used for the encapsulation of [^{18}F] FDG, acetate or HEPES. (D) LITA-xenograft, used for *in vivo* delivery to xenograft tumours, contains increased DSPE-PEG^{2000}. (E) LITA-Rhd-xenograft contains Rhd for histological analysis targeted to the xenograft. Figure 2.20 is a schematic for the chosen formulation including the lipids used for incorporation.

Figure 2.21 A-B shows the reproducibility of liposome in batch-to-bath formulations was evaluated, the LITA nanoparticles typically formulated slightly larger in size though there was no statically significant difference between groups (control: 93.82 ± 5.642, n=6; LITA: 105.4 ± 5.998, n=6; p=0.1905). The single peak in each graph represents the size distribution of a single reading of the liposomes from the Zetasizer. In the example used here, the PDI of HEPES was 0.175 (Figure 2.21 C) and the PDI of LITA was 0.475 (Figure 2.21 D).

Molar component (%) Application	DSPC	CDAN	DSPE-PEG^{2000}	Cholesterol	DOPE-Rhodamine B	Gd.DOTA DSA
A) LITA-Rhd	32	32	1	34	1	-
B) LITA-Gd	32	32	1	34	-	1
C) LITA	32	32	1	35	-	-
D) LITA-xenograft	32	32	5	31	-	-
E) LITA-Rhd-xenograft	32	32	5	30	1	-

Table 2.4 Percentage molar components of liposome formulations

Four separate liposome formulations were conjugated for this study. **(A)** LITA-Rhd: liposomes to contain 1% of Rhodamine (Rhd), a fluorescent lipid used for histology analysis; **(B)** LITA-Gd: liposomes to be conjugated with 1% gadolinium (Gd) for use in MRI bio-distribution analysis; **(C)** LITA: liposomes conjugation used for the encapsulation of [18F] FDG, acetate or HEPES; **(D)** LITA-xenograft: liposomes to contain 5% DSPE-PEG2000 for increased *in vivo* circulation; DSPC: 1,2-distearoyl-sn-glycero-3-phosphocholine; CDAN: N1-cholesteryloxycarbonyl-3,7-diazanonane-1,9-diamine; DSPE-PEG^{2000}: 1,2-distearoyl-sn-glycero-3-phosphoethanolamine-N-methoxy (polyethylene glycol)-2000; DOTA: gadoterate meglumine; DSA: digital subtraction angiography; DOPE – Rhodamine B:1,2-dioleoyl-sn-glycero-3-phosphoethanolamine-N- (lissamine rhodamine B sulfonyl); **(E)** LITA-Rhd-xenograft: liposome contains 1% less cholesterol in order to allow for Rhd incorporation for histological analysis targeted to the xenograft.

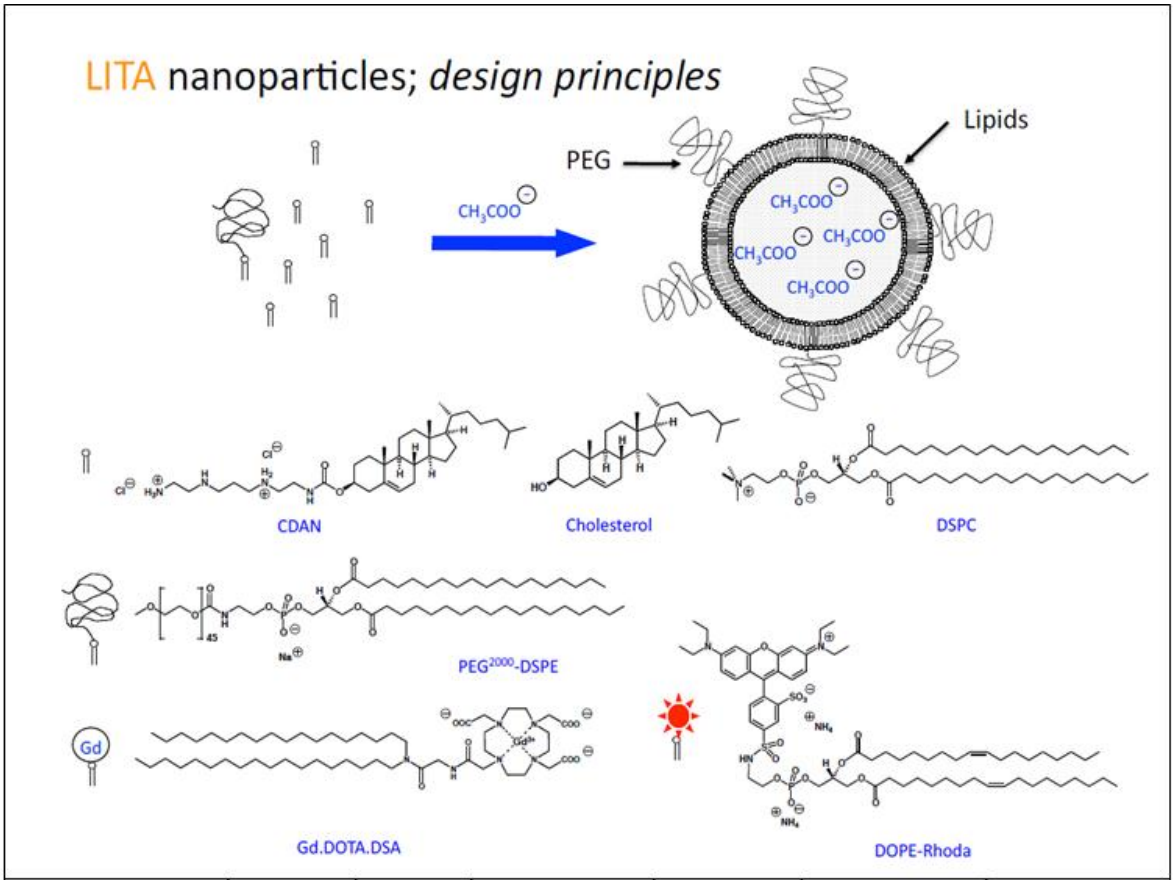


Figure 2.20 LITA nanoparticle design principles

An overview of the nanoparticle formulation process, including chemical structures of the key bilayer components. LITA: Liposomal encapsulated acetate; DSPC: 1,2-distearoyl-sn-glycero-3-phosphocholine; CDAN: N1-cholesteryloxycarbonyl-3,7-diazanonane-1,9-diamine; DSPE PEG^{2000}: 1,2-distearoyl-sn-glycero-3-phosphoethanolamine-N-methoxy (polyethylene glycol)-2000; DOTA: gadoterate meglumine; DOPE - Rhodamine:1,2-dioleoyl-sn-glycero-3-phosphoethanolamine-N- (lissamine rhodamine B sulfonyl); DSA: digital subtraction angiography.

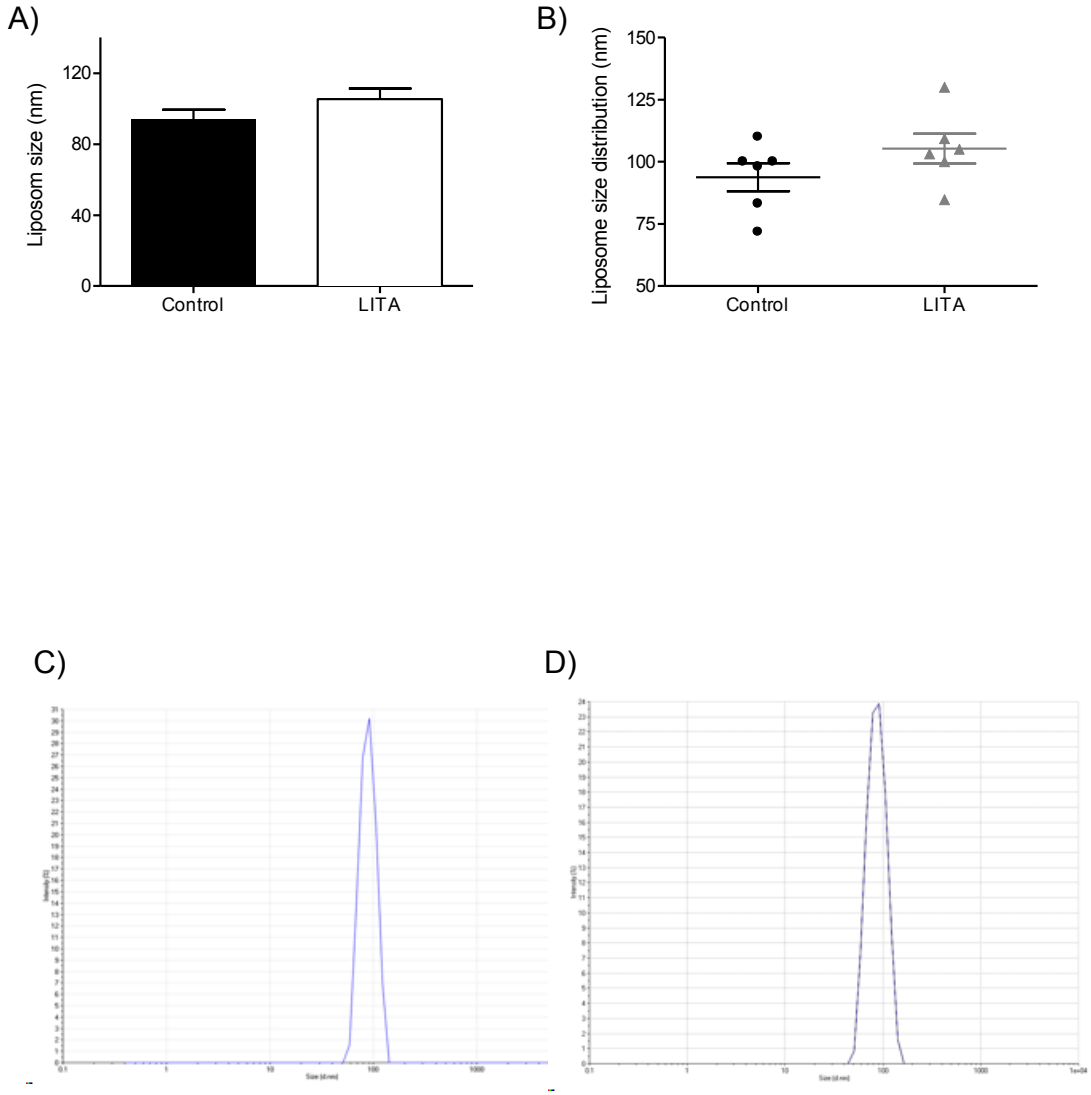


Figure 2.21 Liposomal nanoparticle sizing method after completed formulation

The **(A)** formulated liposome size, data shown as mean ± SEM and **(B)** size distribution between groups showed no statistical significance between groups or batch-to-batch formulation (n=6/group). **(C)** Sizing peaks of control (containing HEPES) and **(D)** LITA (liposome encapsulated acetate) respectively. The x-axis represents the size (nm) of the nanoparticle and the y-axis represents the number (%) of liposomes.

2.3.4 *Study 4: Liposomal Biodistribution and* in vivo *Optimisation*

2.3.4.1 *Ex vivo* liposomal detection using fluorescence microscopy imaging

Bio-distribution of LITA-Rhd was achieved by histological investigation using fluorescence microscopy to visually identify the bi-layer incorporated lipid, rhodamine (Rhd). For *in vivo* optimisation, a panel of LITA-Rhd was formulated with varying concentrations of acetate (control of 0, 1mM, 10mM or 1M) and administered two different routes (i.v. or i.p.) with a dosage volume of 200µL. Organs of interest were extracted and observed 2 hours post injection (Table 2.5). For all concentrations of loaded acetate and injection methods, no visible adverse side effects were observed on the animal during or post injection. The high concentration of LITA-Rhd was observed in the liver (Figure 2.22) and spleen (Figure 2.23). A much lower visible presence of LITA-Rhd was observed in the kidneys (Figure 2.24) and almost no LITA-Rhd was observed in the heart (Figure 2.25).

A control lens was first used to confirm there was no artefact that would generate a false positive identification of the LITA-Rhd (Figures 2.22- 2.25 A). A nuclear stain (DAPI) was then allied to the microscope slide to ensure the region being observed was tissue (Figures 2.22- 2.25 B). A rhodamine-specific filter was used to observe the same slide for LITA-Rhd visualisation and confirmation of delivery to the tissue of interest (Figures 2.22- 2.25 C). Red in images represents the fluorescent rhodamine embedded into the liposome membrane.

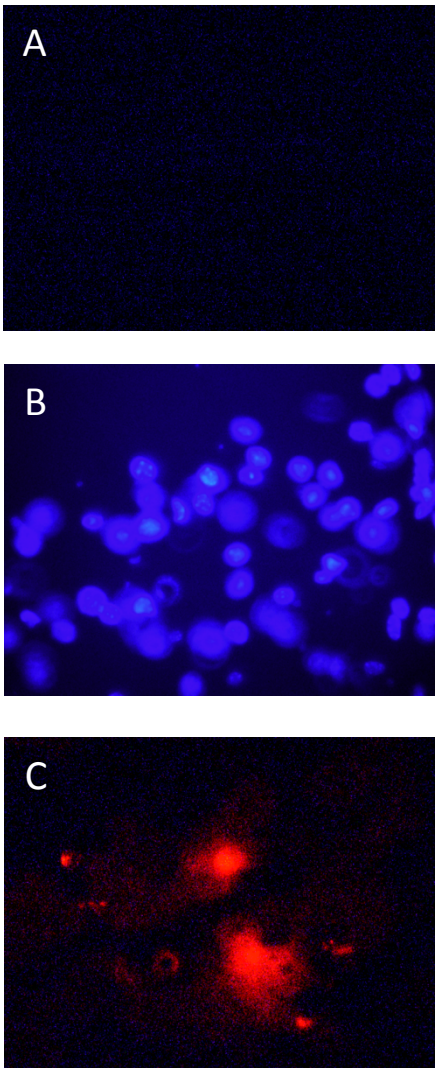


Figure 2.22 LITA nanoparticle tumour localisation LITA-Rhd identification in the liver by histological fluorescence imaging

Images obtained from the liver of a murine which received LITA-Rhd i.p. administration (**A**) control, (**B**) nuclear stain (DAPI), (**C**) rhodamine-specific filter visualisation. Red in images represents the fluorescent rhodamine embedded into the liposome membrane.

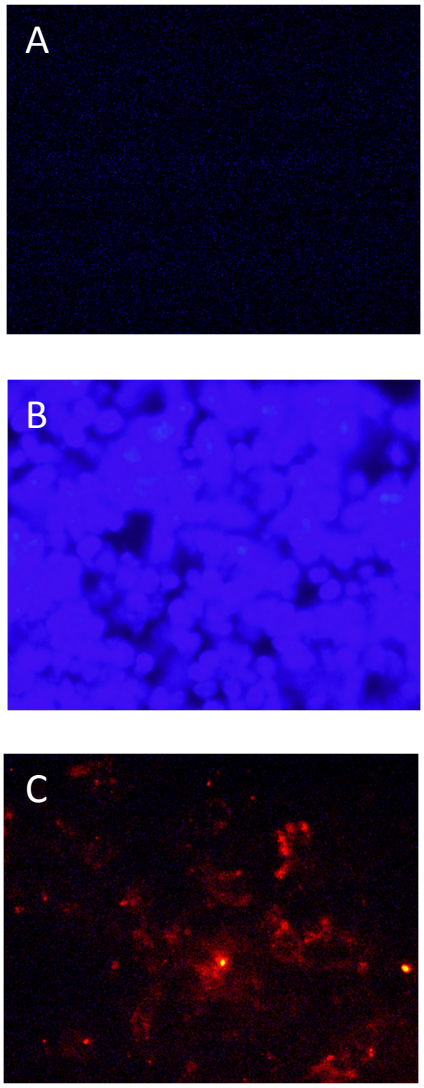


Figure 2.23 LITA nanoparticle tumour localisation LITA-Rhd identification in the spleen by histological fluorescence imaging

Images obtained from the spleen of a murine which received LITA-Rhd i.p. administration **(A)** control, **(B)** nuclear stain (DAPI), **(C)** rhodamine-specific filter visualisation. Red in images represents the fluorescent rhodamine embedded into the liposome membrane.

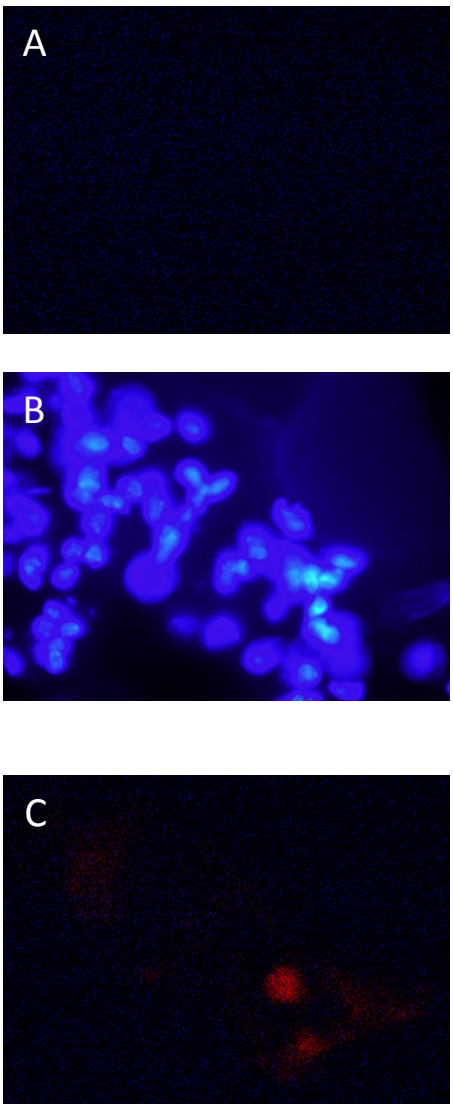


Figure 2. 24 LITA nanoparticle tumour localisation LITA-Rhd identification in the kidney by histological fluorescence imaging

Images obtained from the kidney of a murine which received LITA-Rhd i.p. administration **(A)** control, **(B)** nuclear stain (DAPI), **(C)** rhodamine-specific filter visualisation. Red in images represents the fluorescent rhodamine embedded into the liposome membrane.

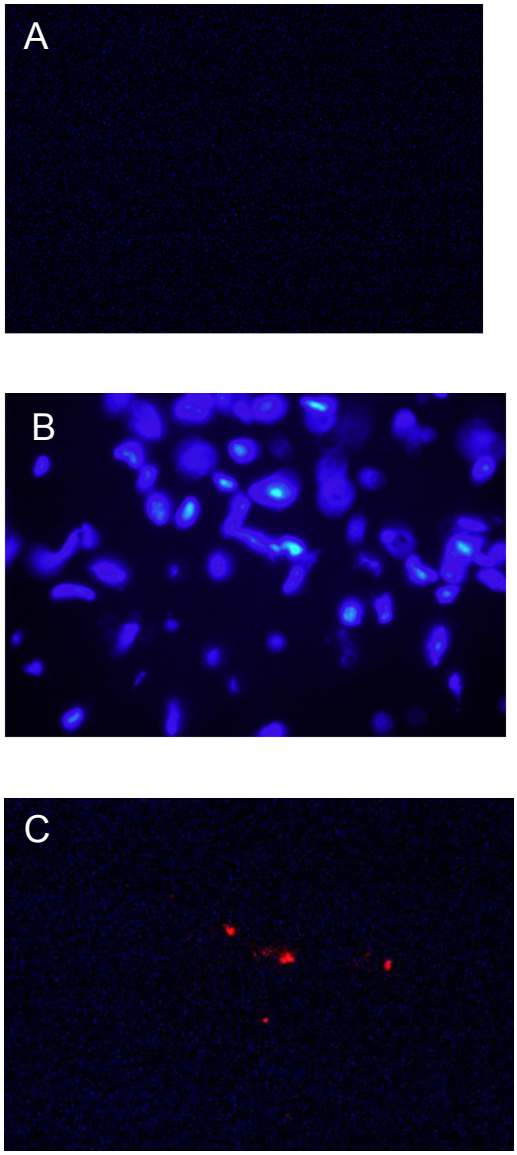


Figure 2.25 A nanoparticle tumour localisation LITA-Rhd identification in the heart by histological fluorescence imaging

Images obtained from the heart of a murine which received LITA-Rhd i.p. administration (**A**) control, (**B**) nuclear stain (DAPI), (**C**) rhodamine-specific filter visualisation. Red in images represents the fluorescent rhodamine embedded into the liposome membrane.

variables / Organs	Control		1mM		10mM		1M	
	i.v.	i.p.	i.v.	i.p.	i.v.	i.p.	i.v.	i.p.
Liver	✓	✓	✓	✓	✓	✓	✓	✓
Spleen	✓	✓	✓	✓	✓	✓	✓	✓
Kidneys	✓	✓	✓	✓	✓	✓	✓	✓
Heart	--	✓	✓	✓	✓	--	--	✓
Lungs	--	✓	✓	✓	✓	✓	✓	✓

Table 2.5 Histological evaluation of LITA-Rhd at differing acetate concentrations and injection methods

Histology was carried out in the organs of interest and examined for the presence of LITA-Rhd, 2 hours after administration of the 200μL dosage volume. A range of acetate concentrations was loaded into the liposome and administered either i.v. or i.p. Select filtering organs were investigated for LITA-Rhd presence (n=3/group).

2.3.4.1.2 Histological evaluation of LITA-Rhd at differing time points after injection

Animals were assessed at 16, 24 and 48 hours after LITA-Rhd i.p. injection (Table 2.6). Following peripheral injection, LITA-Rhd nanoparticles were present in the highest concentrations in the liver and spleen with lower concentrations observed in the kidneys at the earliest time point, which was consistent with the first histological study. No detectable signals from LITA-Rhd were observed in the skeletal muscle or lungs. Signal for LITA-Rhd was detected in the brain at all three time points, but not in the heart after the earliest time point of 16 hours (Figure 2.25).

	Liver	Spleen	Kidney	Lungs	Heart	Brain	Muscle	Pancreas
2h	✓	✓	✓	✓	✓	✓	-	✓
16h	✓	✓	✓	-	✓	✓	-	✓
24h	✓	✓	✓	-	-	✓	-	✓
48h	✓	✓	-	-	-	✓	-	-

Table 2.6 Histology time course of LITA-Rhd in selected organs

Histology was carried out in select filtering organs of interest and examined for the presence of LITA-Rhd at 2, 16, 24 and 48 hours post injection (i.p.) of the 200μL dosage volume. The table indicated the presence of (✓) or absence (-) of rhodamine at these time points.

2.3.4.2 *In vivo* liposome detection using MRI and T_1 measurements

This experiment was carried out to profile the accumulation of LITA *in vivo* with and without Gadolinium in respect to tissue delivery over time. Gadolinium (Gd) is an MRI contrast agent which when taken up by the tissue decreases the relaxation time of the tissue and therefore increasing the T_1 signal. Changes in T_1 signal were assessed in: brain, liver, subcutaneous fat and kidney (Figure 2.26 A-D). At 24 hours the T_1 values of the liver with LITA-Gd were significantly different from LITA (804.10 ± 81.81 msec; $p<0.05$). At 48 hours post administration of these was significant decreases in the liver T_1 (495.90 ± 37.36 and 502.80 ± 65.89msec, respectively) compared to the T_1 pre-administration (807.80 ± 76.59 msec; $p<0.05$). No changes in the T_1 value were observed in hypothalamus, subcutaneous fat or kidney. Results for all T_1 measurements can be seen in Table 2.7.

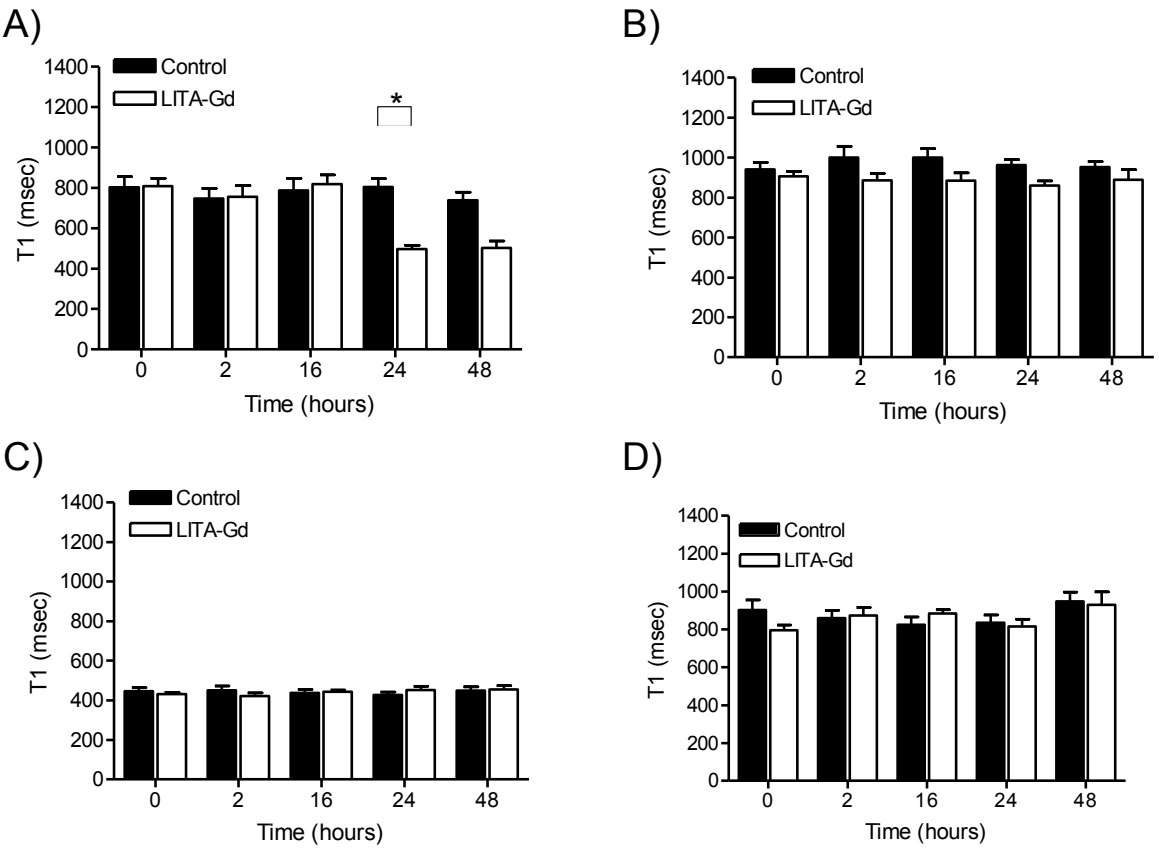


Figure 2.26 T1 measurement following administration of LITA nanoparticle conjugated with gadolinium (LITA-Gd)

In vivo assessment of T1 values following peripheral delivery of LITA or LITA-Gd conjugated liposomes in the **(A)** liver, **(B)** brain, **(C)** subcutaneous fat and **(D)** kidney. Measurements were taken at 0, 2, 16, 24 and 48 hours post i.p. injection of LITA-Gd or LITA. T1 values in the liver were significantly reduced at 24 and 48 hours following LITA-Gd injection. No significant differences were observed between LITA-Gd and control groups in any other ROI at any time point. Data analysed by two-way ANOVA. Results are shown as mean ± SEM, n=4/group.

	Before (mean ± sem)	2 hours (mean ± sem)	16 hours (mean ± sem)	24 hours (mean ± sem)	48 hours (mean ± sem)	p value
Liver LITA	802.30 ± 106.70	746.80 ± 99.01	786.60 ± 122.50	804.10 ± 81.81	737.70 ± 80.10	p<0.05
LITA-Gd	807.80 ± 76.59	755.60 ± 110.60	818.00 ± 90.96	495. 90 ± 37.26	502.80 ± 65.89	p<0.05
Brain LITA	941.00 ± 69.98	1000.00 ± 111.70	1000.00 ± 91.47	963.00 ± 52.99	952.20 ± 53.52	NS
LITA-Gd	905.70 ± 49.12	886.60 ± 68.42	884.80 ± 77.33	860.40 ± 44.04	890.10 ± 98.50	NS
Subcut LITA	446.20 ± 36.09	451.40 ± 43.24	437.60 ± 35.10	427.80 ± 26.44	449.80 ± 37.85	NS
LITA-Gd	432.30 ± 16.61	422.00 ± 32.26	442.90 ± 38.55	451.90 ± 38.66	454. 90 ± 38.75	NS
Kidney LITA	902.60 ± 106.60	858.90 ± 84.32	825.30 ± 81.07	836.40 ± 81.81	949.50 ± 93.74	NS
LITA-Gd	796.50 ± 52.88	873.50 ± 86.73	814.40 ± 78.34	814.40 ± 78.43	930.00 ± 136.00	NS

Table 2.7 T1 measurements post administration of LITA nanoparticle conjugated with gadolinium (LITA-Gd)

In vivo assessment of T1 values following peripheral delivery of LITA or LITA-Gd conjugated liposomes in the liver, brain, subcutaneous fat and kidney. Measurements were taken at 0, 2, 16, 24 and 48 hours post i.p. injection of LITA-Gd or LITA. No significant differences were observed between LITA-Gd and control groups in any other ROI at any time point. Data analysed by two-way ANOVA. Results are shown as mean ± SEM, n=4/group.

2.3.4.3 Real-time bio distribution assessment by PET/ CT fusion

Bio distribution of the LITA nanoparticle in real-time was measured by PET/CT. Post injection are shown in Figure 2.27. Images are independently acquired during both the (A) PET, (B) CT scan and (C) fused PET and CT scans taken over 30 minutes.

For liposomal distribution profiling, the mean intensity of [^{18}F]FDG alone or encapsulated within the nanoparticle was taken and standardized uptake values (SUV). To determine uptake over time, the area under the curve (AUC) over the 30-minute acquisition time was calculated using the previously described SUV values. There was significant uptake of LITA encapsulated [^{18}F]FDG when compared to the control [^{18}F]FDG in the muscle (SUV $p<0.01$; AUC: $p<0.05$) (Figure 2.28), heart (SUV: $p<0.01$; AUC: $p<0.05$) (Figure 2.29) and brain (SUV: $p<0.01$; AUC: $p<0.001$) (Figure 2.30). There was no significant uptake difference in [^{18}F]FDG uptake in the liver (Figure 2.31) or kidney (Figure 2.32).

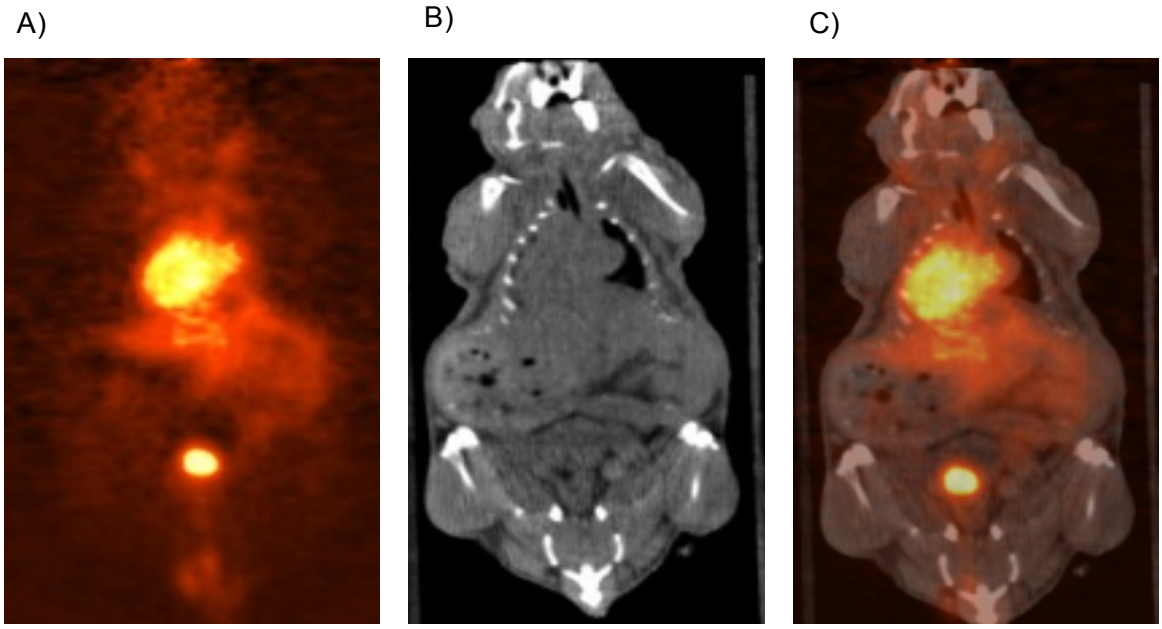


Figure 2.27 PET/CT fused image after injection with [^{18}F]FDG conjugated liposomes

Representative **(A)** PET, **(B)** CT and **(C)** PET/CT fusion imagines 30 minutes after i.v. of 200µL [^{18}F]FDG conjugated liposomes. The bright regions in the **(A)** PET and **(C)** PET/CT images represent [^{18}F]FDG uptake.

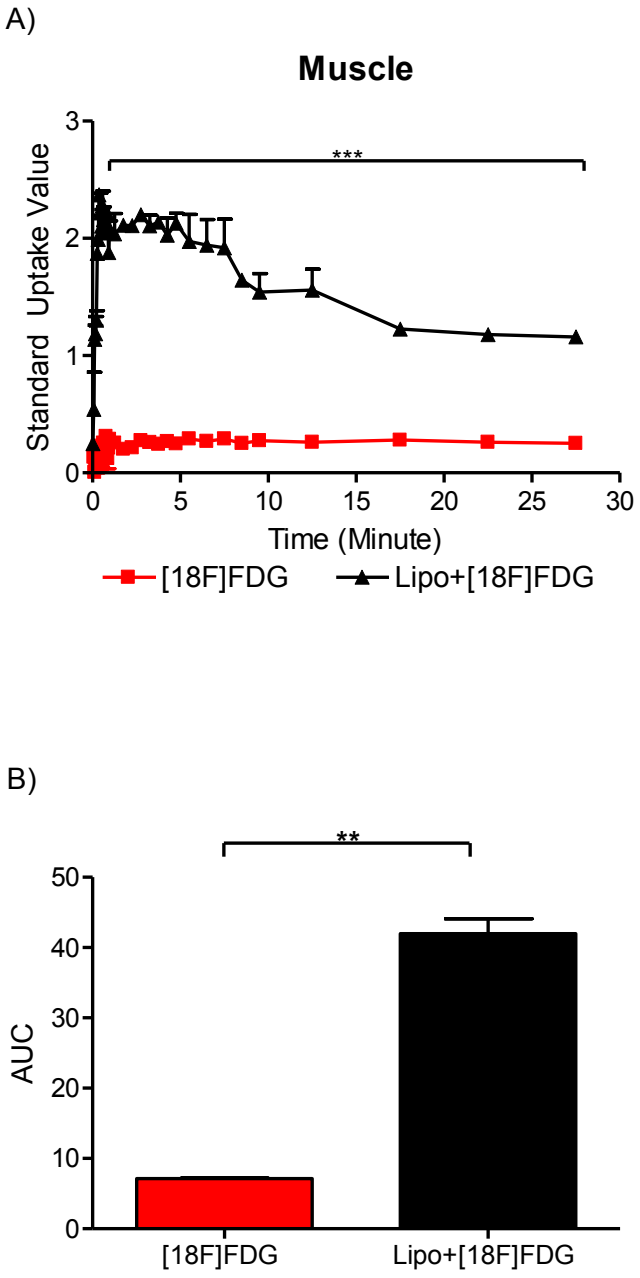


Figure 2.28 Standard Uptake Value (SUV) and Area under the curve (AUC) from muscle for 30min post-injection of [18F]FDG or [18F]FDG conjugated liposomes

In vivo assessment of bio distribution following peripheral delivery of [^{18}F]FDG or [^{18}F]FDG conjugated liposomes over 30 minute acquisition time post i.v. injection in the muscle. **(A)** SUV was significant (*** = $p<0.001$). Data is presented as mean ± SEM and analysed as two-way ANOVA. **(B)** AUC were significant ($p<0.01$ vs. control). Data is presented as AUC ± SEM and analysed as unpaired t-test; n=4/group.

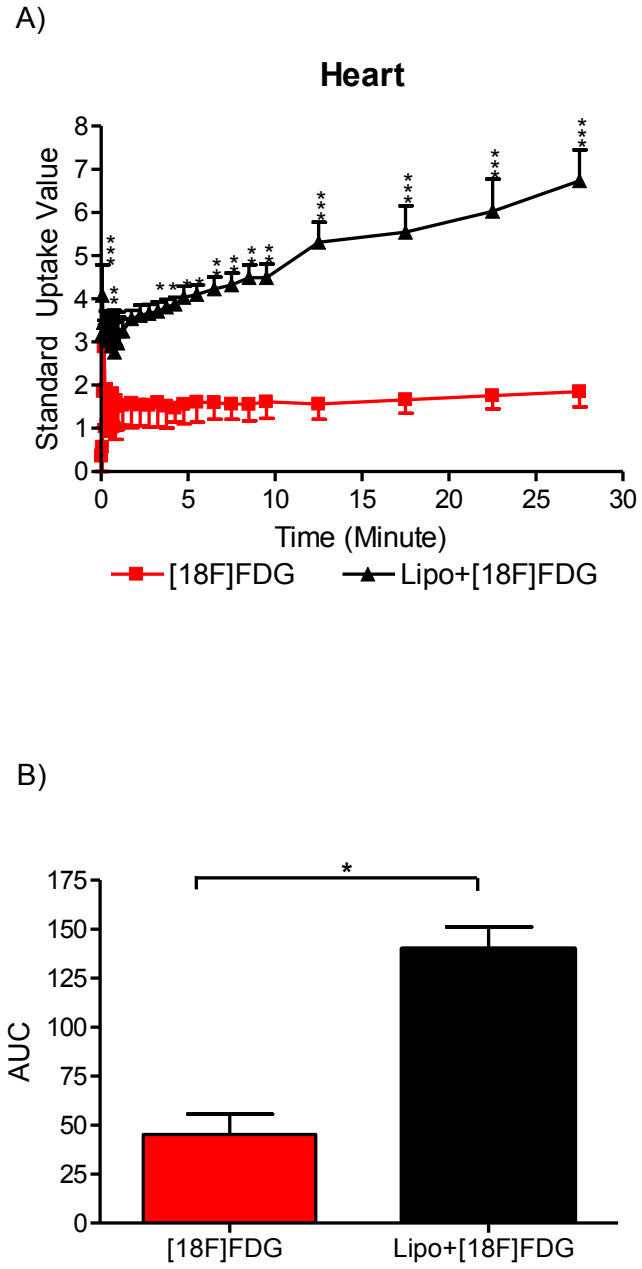


Figure 2.29 Standard Uptake Value (SUV) and Area under the curve (AUC) from heart for 30min post-injection of [^{18}F]FDG or [^{18}F]FDG conjugated liposomes

In vivo assessment of bio distribution following peripheral delivery of [^{18}F]FDG or [^{18}F]FDG conjugated liposomes over 30 minute acquisition time post i.v. injection in the heart. **(A)** SUV was significant (* = p<0.05, ** = p<0.01 and *** = p<0.001). Data is presented as mean ± SEM and analysed as two-way ANOVA. **(B)** AUC were significant (p<0.05 vs. control). Data is presented as AUC ± SEM and analysed as unpaired t-test; n=4/group.

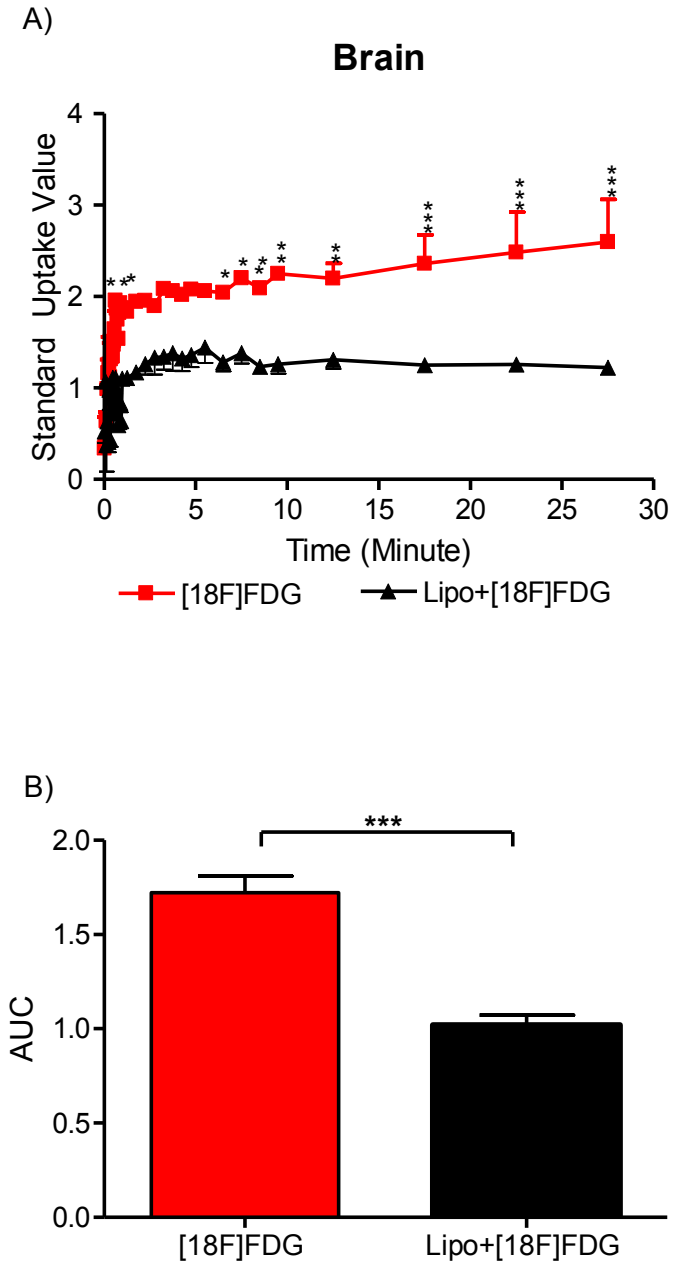


Figure 2.30 Standard Uptake Value (SUV) and Area under the curve (AUC) from brain for 30min post-injection of [18F]FDG or [18F]FDG conjugated liposomes

In vivo assessment of bio distribution following peripheral delivery of [^{18}F]FDG or [^{18}F]FDG conjugated liposomes over 30 minute acquisition time post i.v. injection in the brain. (A) SUV was significant (* = p<0.05, ** = p<0.01 and *** = p<0.001). Data is presented as mean ± SEM and analysed as two-way ANOVA. (B) AUC were significant (p<0.001 vs. control). Data is presented as AUC ± SEM and analysed as unpaired t-test; n=4/group.

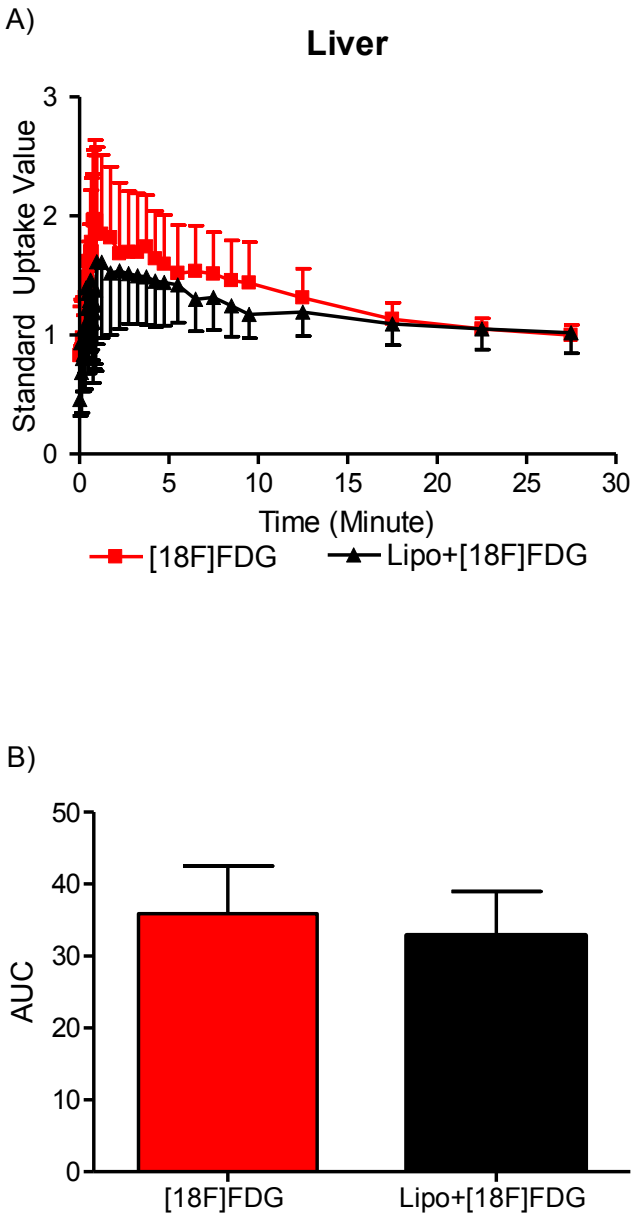


Figure 2. 31 Standard Uptake Value (SUV) and Area under the curve (AUC) from liver for 30min post-injection of [18F]FDG or [18F]FDG conjugated liposomes

In vivo assessment of bio distribution following peripheral delivery of [^{18}F]FDG or [^{18}F]FDG conjugated liposomes over 30 minute acquisition time post i.v. injection in the brain. **(A)** SUV did not reach significance. Data is presented as mean ± SEM and analysed as two-way ANOVA. **(B)** AUC did not reach significance. Data is presented as AUC ± SEM and analysed as unpaired t-test; n=4/group.

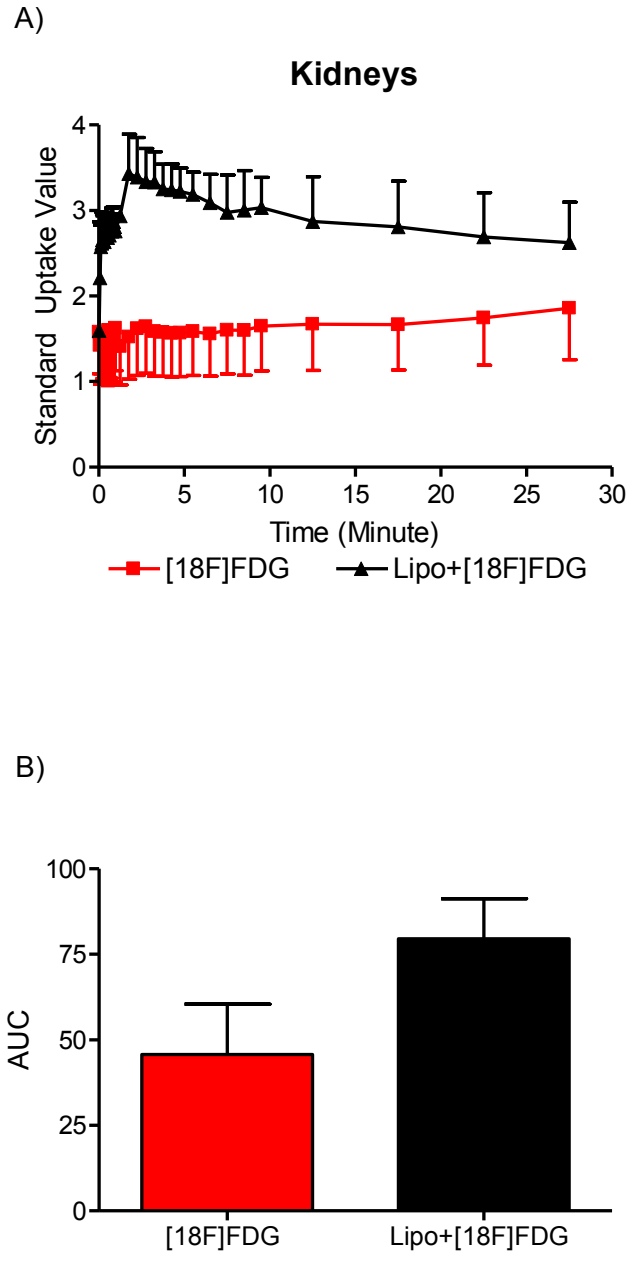


Figure 2.32 Standard Uptake Value (SUV) and Area under the curve (AUC) from kidneys for 30min post-injection of [18F]FDG or [18F]FDG conjugated liposomes

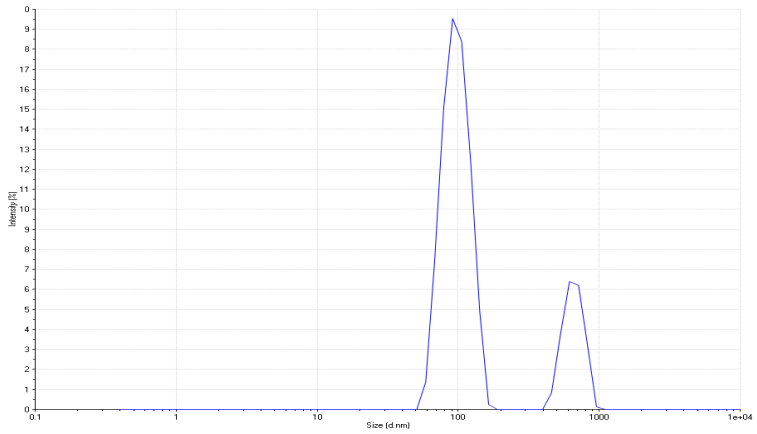
In vivo assessment of bio distribution following peripheral delivery of [^{18}F]FDG or [^{18}F]FDG conjugated liposomes over 30 minute acquisition time post i.v. injection in the kidneys. **(A)** SUV did not reach significance. Data is presented as mean ± SEM and analysed as two-way ANOVA. **(B)** AUC did not reach significance. Data is presented as AUC ± SEM and analysed as unpaired t-test; n=4/group.

2.3.4 *Study 5: Liposomal Encapsulation of Butyrate and Propionate*

Once acetate was encapsulated and characterised, butyrate and propionate were encapsulated independently. Figure 2.33 show the size of liposomes encapsulated with butyrate (1M) and amount of butyrate encapsulated within 200µl of liposome solution. The size of the liposome revealed two peaks, one within size range of a normal liposome and another peak at too large a size to be a liposome, indicating an excess of lipids which did not formulate properly. ^{1}H NMR revealed no amount of butyrate was encapsulated, indicating the formulation did not occur properly.

Figure 2.34 shows the size of liposomes encapsulated with propionate (1M) and amount of butyrate encapsulated within 200µl of liposome solution. The size of the liposome revealed two peaks, one within range of a normal sized liposome and another peak of similar size, though not within range of a formulated liposome. ^{1}H NMR revealed no amount of propionate was encapsulated, indicating the formulation did not occur properly.

A)



B)

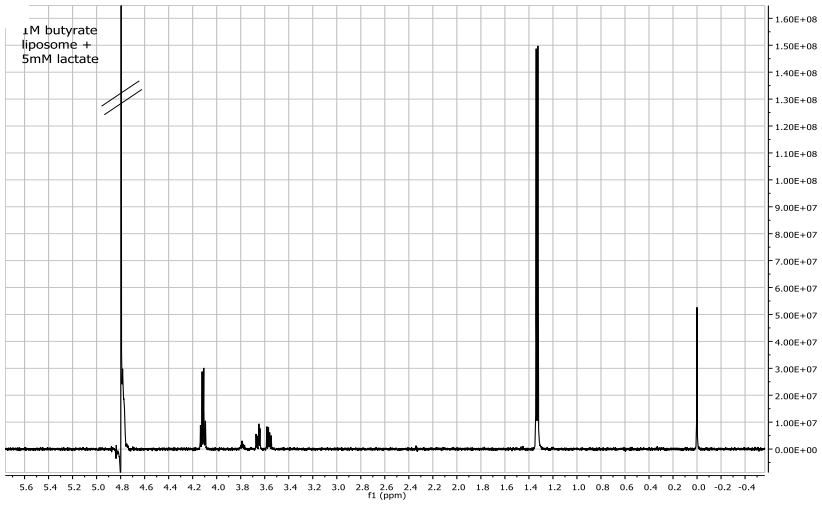


Figure 2.33 Butyrate encapsulated liposomal formulation and characterisation

Formulation of butyrate encapsulated liposomes was attempted and characterised using the LITA formulation. **(A)** The liposome was sized using a zetasizer which did not form liposomes of appropriate size after formulation and dialysis. **(B)** ^{1}H NMR analysis revealed no detection of butyrate was encapsulated within the liposomes.

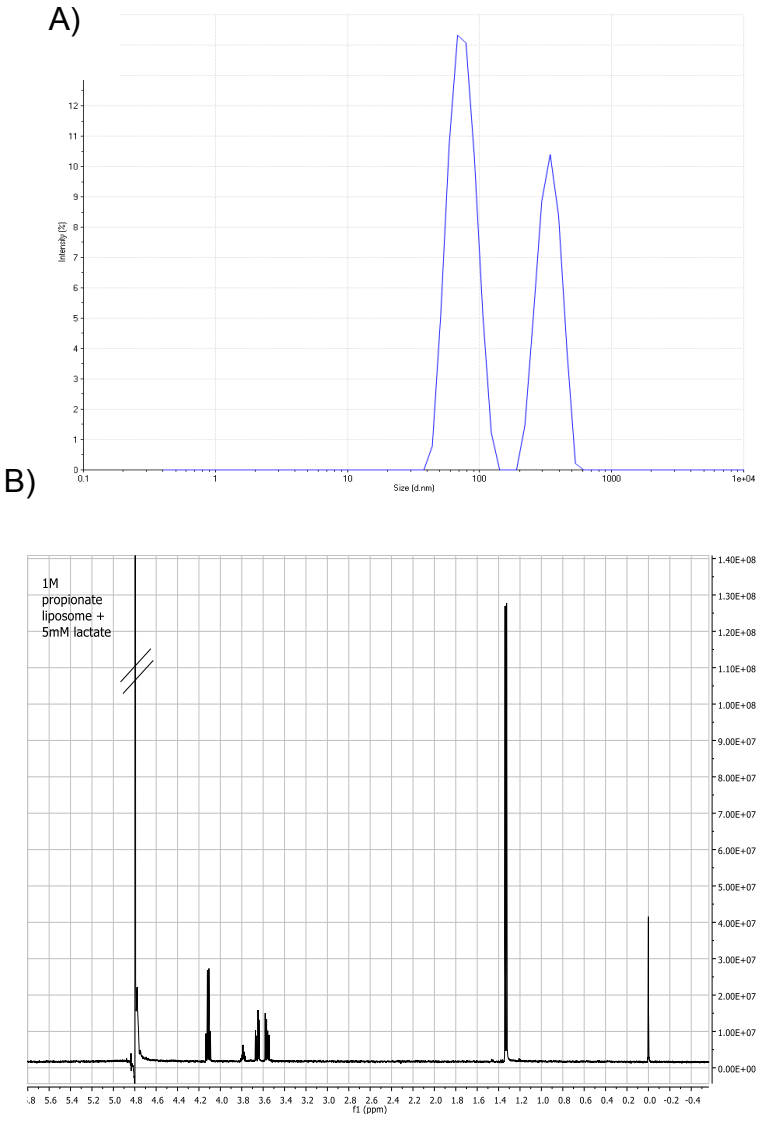


Figure 2.34 Propionate encapsulated liposomal formulation and characterisation

Formulation of propionate encapsulated liposomes was attempted and characterised using the LITA formulation. **(A)** The liposome was sized using a zetasizer which did not form liposomes of appropriate size after formulation and dialysis. **(B)** ^{1}H NMR analysis revealed no detection of propionate was encapsulated within the liposomes.

2.4 Chapter Discussion

The chosen method delivery of SCFA, specifically acetate, was a lipid-based nanoparticle known as a liposome. Liposomes are a preferential vehicle for therapeutic delivery due to the ability to overcome biological barriers to reach a desired organ of interest. In this study, a select composition of lipids were incorporated based on their properties to encapsulate and deliver such a small molecule, such as acetate, and in parallel act as an imaging agent for *in vivo* monitoring.

One advantage of using the liposome is the modification capabilities and versatile lipids that can be incorporated into the formulation to specify the exact purpose. The characteristics of liposome formulation, including particle size, surface change properties and encapsulated small molecule/lipid ratio possess an influential effect on the cellular uptake. The formulation specificity for the LITA nanoparticle was two-fold, one objective was to formulate a particle with high payload of a very small molecule and the other was to ensure it reached the organ of interest. To achieve both objectives, the lipids of choice were rigid enough to form a tight bilayer and have an external environment in order to control circulation time *in vivo*. The first set of experiments was to determine the ideal formulation for a liposome which is stable, a functional size, contains contrast agents for *in vivo* monitoring, encapsulates acetate and reaches the organ of interest. From previous work carried out in this lab [216], four main lipids were chosen as the foundation lipids: CDAN, DSPC, DSPE-PEG^{2000} and cholesterol.

The purpose of the CDAN was to increase uptake within the cell. CDAN are cationic lipids which enhance liposomal uptake into the cellular membrane [217]. The isoform, DDAB, did not perform as well as the initial CDAN most likely because of the strong cationic properties. DSPC is a good building block for liposomes due to a long chain of lipids to encourage a higher encapsulation efficiency and stability [218]. The key is the PC (phosphatidylcholine)

part; DS stands for di-stearoyl (di-C18 saturated alkanoyl chains). Therefore any PC variants being used as alternatives to DSPC, containing the same or different alkanoyl chains between C12 and C20 in length, saturated and unsaturated were tested. Length chains <C12 and >C20 were proven less likely to formulate stable nanoparticles. Secondly I exchange the DSPC with potential alternatives, including DOPE and DLPC, which did not formulate as well as the DSPC lipid. There are two components of the DSPE-PEG^{2000}; the DSPE is a cholesterol lipid which anchors the PEG lipid securely into the external membrane of the liposome. Variation in the size of the molecular weight of the PEG lipid was carried out, using PEG of PEG^{500} to PEG^{10000}. The ideal size of PEG length was confirmed to be 2000, which is consistent with most PEG literature [219, 220]. The PEG lipid causes a negative peripheral charge, which has a 'stealth-like' effect of macrophages in the bloodstream and therefore increases circulation time of the liposome within the body [191]. Cholesterol is an important structural lipid which strengthens the bilayer of the liposome increasing the amount of acetate that can be contained within, and also decreasing the rate at which acetate leaks out [221]. There are no real structural variations possible here; however we have tested the use of Dimethylaminoethane-carbamoyl cholesterol (DC cholesterol), to assess if there is any difference compared to normal cholesterol, which did inhibit formulation of the liposome.

Again, for each lipid, a formulation was carried out which had a varied molarity of select lipids. Based on size and acetate encapsulation, the best formulation of choice was: DSPC (32%); Cholesterol (35%); DPSE-Peg2000 (1%); CDAN (32%). The additional lipids used for bio distribution studies were used for identification purposes only and did not have any effect on the liposome to our knowledge [216, 222]. Liposomes in this study were approximately 100nm to avoid macrophage uptake and have the ability to fit through the artery walls in order to be taken up by organ tissue [223].

The yielded liposome from this process was shown to indeed encapsulate acetate by ^{13}C NMR spectroscopy confirmation. This was achieved by the use of albumin, which is a relatively large molecule that has been shown to bind to anionic molecules such as acetate [224]. The binding of albumin to acetate causes a reduction in the NMR signal of the compound and thus hinders any acetate signal that was not encapsulated within the nanoparticle [225].

Addition of albumin to a liposome free acetate solution had a significant effect on the NMR signal intensity of the latter, reducing its presence in the spectra significantly and demonstrating albumin macrostructure does interact with the acetate molecule. No such effect was observed with the liposomes encapsulated acetate solution. Having a remaining peak after the addition of albumin to the LITA nanoparticle solution indicates that the acetate molecules are protected from albumin interaction within the liposomal structure. These data indicate that acetate is encapsulated within the confines of the nanoparticle to which albumin does not have access. Once it was confirmed acetate was in fact encapsulated within the liposome, the concentration of encapsulated acetate was determined using ^{1}H NMR spectroscopy. A known amount of lactate was added to the LITA solution once the formulation was complete and the combination of solutions was freeze-died. The released acetate from within the liposomes was compared to the concentration of the lactate added and by using the ratio between lactate and acetate.

A range of concentrations of acetate was encapsulated into liposomes to determine the maximum amount of payload. Five concentrations were attempted, of which the maximum acetate was found to be encapsulated when the liposome was formulated with 1M of acetate (4.41mM). Concentrations lower than 1M had a concentration dependent gradient of

encapsulated acetate. Concentrations higher than 1M did encapsulated only traces of acetate, most likely because of the rehydrated solution was overly acidic.

After the LITA nanoparticle was confirmed to formulate appropriately and encapsulate acetate, the bio distribution profile came into question. Histology, MRI T_1 measurements and PET/CT in real time were employed to demonstrate that LITA reach the organs of interest or the desired frame of time. Histology was conducted to examine accumulation of the LITA embedded within the multiple organs across a panel time points, injection methods and acetate concentrations. Though histology is a reliable method for liposomal detection, there are limitations regarding the bio distribution over time and the uptake of the material encapsulated within the liposome. For these reasons, I turned to two other methods of bio distribution to access the LITA nanoparticle: MRI and PET/CT. MRI was used to measure LITA accumulation within the tissue over a 24 hour period; however the limitations of sensitivity and indication of encapsulated material release encourage me to carrying out PET/CT in parallel. The study examining PET/CT allowed me to monitor liposomal bio distribution within the first 30 minutes and accumulation of the material encapsulated within the liposome, which I was unable to do with either MRI or histology. With these three different methods, I was able to determine the bio distribution profile, time frame and deposited payload of the LITA nanoparticle.

Histology visually confirmed the presence of liposomes within the tissue and was carried out by incorporating the lipid rhodamine into the liposome formulation (LITA-Rh), which is a fluorescent lipid easily identifiable by microscopy. Confirmation of LITA-Rhd is a reflection of visual identification of a red colour generated by the fluorescent rhodamine lipid. The ensuing two images serve as controls eliminating the possibility of any false positive of background artifacts and confirming the LITA-Rhd identification is in fact located within the

tissue. The fluorescence pattern observed from the liver sections of the LITA-Rhd can be explained by the "endothelial massage" theory put forward by Wisee and McCucky [226]. This theory describes the movement of fluid and small particles in and out of the Space of Disse, which is the area located between the endothelial lining of the hepatic sinusoid and the hepatocytes. It has also been shown that Kupffer cells take up far more liposomes per cell than other cell types, which may explain the strong fluorescence observed in Figure 2.9.

After histology confirmed the delivery of liposomes, the next step was to investigate the bio distribution profile *in vivo*. MRI was employed to measure T_1 of the liposome in circulation. Liposomes (LITA-Gd) were formulated containing a gadolinium lipid, which is a paramagnetic ion that increases the signal in the tissue it is absorbed into [227, 228]. Although histology confirmed the presence of liposomes in multiple organs, T_1 change was only observed in the liver. This is more likely related to the lower accumulation of liposomes in these tissue compare with the liver. A significant T_1 reduction was observed in the liver, 16 and 24 hours post injection of Gd liposomes [213].

Bio distribution in real time was conducted *in vivo* using PET/CT with the metabolic tracer [^{18}F]FDG to assess whether uptake is altered between [^{18}F]FDG or [^{18}F]FDG conjugated liposomes. Previous studies have been carried out using [^{18}F]FDG with liposomes [229], however this is the first to my knowledge that encapsulated the tracer instead of incorporating it into the bi-lipid membrane of the liposome. This study allowed a number of questions to be answered, such as the distribution profile of the liposome, a secondary confirmation of encapsulation of a small molecule and the duration of encapsulation. It was determined previously that the LITA did have the ability to encapsulate small molecules, however we did not have a method to analyse uptake behaviour in real time.

The results from this study reveal there a difference uptake profiles between the [^{18}F]FDG and [^{18}F]FDG conjugated liposomes, confirming the encapsulation of [^{18}F]FDG within the LITA. The distribution pattern fit within our expectations of liposomal uptake, especially with the filter organs such as the liver.

2.4.3 Conclusion

In this chapter, a select composition of lipids were incorporated based on their ability to encapsulate and deliver such a small molecule, such as acetate, and in parallel act as an imaging agent for *in vivo* monitoring. The formulation specificity for the LITA nanoparticle was two-fold, one objective was to formulate a particle with high payload (4mM) of acetate and the other was to ensure it reached the organ of interest, which in this case was the liver. For this thesis, the desired liposomal size was approximately 100nm and the lipids used had specific purposes including a labelling mechanism, a layer to sterically inhibit uptake in the plasma, and lipids of rigid formation to ensure the encapsulation of such a small molecule. Encapsulated acetate was measured by ^{1}H NMR, which quantitatively confirmed that a single treatment of 200µl of LITA would contain 52.9µg of deliverable acetate.

Histology, MRI T_1 measurements and PET/CT in real time were employed to demonstrate the LITA reach the organs of interest in within the desired frame of time. Histology confirmed the presence of the LITA-Rhd nanoparticle in the tissue when examined at varying time, injection method and acetate concentrations. All of these methods yielded the biodistribution profile of the nanoparticle and confirmed delivery to the liver.

Chapter 3

In Vivo Biological Evaluation of liposome encapsulated acetate nanoparticles (LITA)

3.1 Introduction

As discussed in detail in Chapter 1, the increasing prevalence of obesity has created an urgent need to understand its aetiology and that of the metabolic syndrome associated morbidities in order to develop effective novel treatments. Relevant here, epidemiological studies have indicated that nutritional supplementation with dietary fibre ameliorates several features of the metabolic syndrome by promoting reductions in body weight, total body fat and blood glucose levels [91, 159, 230, 231]. In fibre, component carbohydrates are resistant to amylase digestion in the small intestine, but are subject to fermentation by microflora in the large intestine, producing short-chain fatty acids (SCFA) such as acetate, propionate and butyrate [159, 232]. Of these SCFAs, acetate in particular has been suggested to mediate beneficial effects on features of the metabolic syndrome including reductions in fat mass, IHCL, inflammation and improvements in insulin sensitivity, as a dietary supplement [90, 230, 233].

In Chapter 2, I showed the encapsulation of acetate within a liposomal nanoparticle which could deliver up to 4.41mM of acetate per injection dose of 200μL. The biodistribution of the liposomes through histological evaluation, T_1 measurements and PET/CT confirmed the potential delivery to organs of interest, specifically the liver. Thus, the acetate encapsulated liposomes provide a viable, passively targeted vector for delivering SCFAs to key sites of metabolic control.

3.1.1 Aims of Studies

To investigate the metabolic effects of chronic administration of the LITA nanoparticle in mice and on a high fat diet. This study will assess the *in vivo* phenotypic and metabolic effects chronically administered liposomes encapsulated with acetate in a high fat model environment. A model of obesity will be established by placing mice a high fat diet and once an obese state is established, control or LITA nanoparticles will be administered to determine if an introduced SCFA will change the obesogenic state or have an effect on liver metabolism and assess for phenotypic and molecular changes.

To investigate metabolic effects of LITA nanoparticles using indirect calorimetry in mice on a normal fat diet. This will establish the metabolic profile of the LITA *in vivo* after a 7 day administration period using the CLAMS cages. This may indicate how the LITA is being metabolized and if there are any changing in gas exchange or activity in mice with control or LITA nanoparticle treatment. The diet used in this study will be a normal fat diet to determine the metabolic effects of LITA in a non-obese environment.

3.2 Methods

3.2.1 Materials

3.2.1.1 Animals

Male WT C57BL/6 mice (specific pathogen free (SPF), Harlan, UK) were maintained in individually ventilated cages (IVC) under controlled conditions of temperature (21-23°C) and light (12 hrs light, 12 hrs dark, lights on at 7am) with access to food and water *ad libitum*. All work with IVC animals was carried out under a ventilated fume hood. All experiments were carried out in compliance with Animals (Scientific Procedure) Act 1986 under the project licence 70/6656.

3.2.1.2 Diets

For mice placed on a normal fat diet (NFD), a 16**%** kCal diet (RM3) was used. For mice placed on a high fat diet (HFD), a 60% kCal fat diet (EF D12402) was used. Both diets were used independently and in specific models that are outlined in the following text. Dietary details are outlined in Table 3.1. Details of each diet were provided by SSNIFF (England, UK), the company from which these diets were purchased.

Ingredients	Normal fat diet	High fat diet
Crude fat	4.25	34.0
Crude protein	22.39	24.1
Starch	33.92	2.2
Sugar	5.75	22.4
Energy	11.36 MJ/kg	21.4 MJ/kg

Table 3.1 Ingredients of diets used in feeding studies

The normal fat diet (RM3) used was composted of 4.25% crude fat with a level of energy that could be metabolised containing 11.36MJ/kg. The high fat diet (EF D12402) used was composed of 34% crude fat. The level of energy that could be metabolised from the high fat diet contained 21.4 MJ/kg.

3.2.2 *Study 1: Chronic LITA Nanoparticle Administration on an Obesogenic Background*

Pre-clinical relevance of the liposomal therapy was carried out using an *in vivo* model over a 15 week period. At 5 weeks of age, mice were placed on a high fat diet for 5 weeks, during which time food intake and weight gained were monitored at least 3 times a week. At 10 weeks of age the mice underwent a ^{1}H MRS of the liver to establish a baseline for intrahepatocellular lipid (IHCL) content prior to liposomal therapy. After which, the mice received chronic delivery of either LITA or the control nanoparticles by i.p. injection every 2 days for 5 weeks. The injection volume was 200µL, which contained approximately $5x10^{8}$ liposomes per injection. Mice remained on the high fat diet for the duration of the liposomal therapy. At the end of study, MRS was repeated in order to determine the effects of liposomal therapy on IHCL. The timeline of the process can be seen in Figure 3.1.

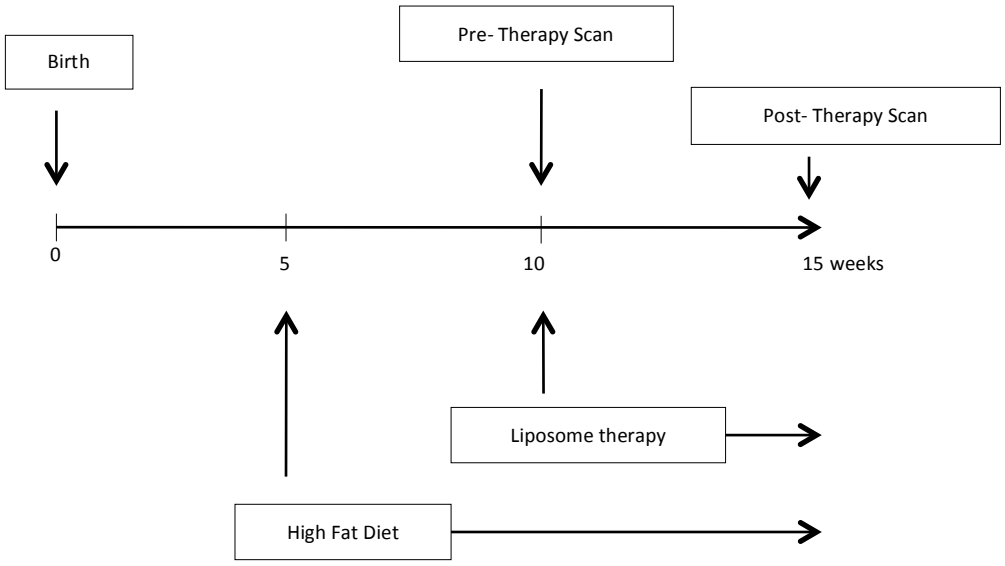


Figure 3.1 Timeline of the model carried out for liposomal therapeutic study

At 5 weeks of age the mice were placed on a high fat diet, which they consumed for the duration of the study. At 10 weeks of age, ^{1}H MRS of the liver was carried out for the pre-therapy scan prior to the initiation of liposomal injections. At 15 weeks of age, the ^{1}H MRS was repeated as a post-study scan before animals were sacrificed.

3.2.2.1 Whole body ^{1}H MRS scanning parameters

Mice were placed on a high fat diet to induce a fatty liver development and localised ^{1}H liver MRS scans were performed to access IHCL content before and at the end of treatment. Prior to the scans, animals were fasted overnight for 16-18 hours. For the scan, mice were anaesthetised with 2 – 3% isoflurane 2/min oxygen, placed prone into the RF coil with the liver at the centre of the coil and scanned on a 4.7T Unity Inova MR scanner (Varian Inc, USA). During the scan, a breathing pad was used to monitor respiration rate and a rectal probe was used to measure core temperature, which was maintained at 37° C with a warm air blower.

The field homogeneity was optimised by shimming on the water signal of the whole mouse. A three plane scout image was taken in order to plan a series of contiguous axial slices over the mouse abdomen to give full liver coverage. Localised ^{1}H liver MRS was performed using a PRESS sequence with a voxel 2x2x2mm3 placed using whole body MRI with the following parameters: repetition time (TR) 10s, echo delay time (TE) 9ms, averages 64 and spectral width 20,000Hz. Total scanning time was approximately 30 minutes per animal. Statistical analysis for determining IHCL using ^{1}H liver MRS was carried out using MestRe-C software.

3.2.2.2 Tissue collection and glucose measurement

Anaesthesia was induced with a 3% oxygen-isofluorane and approximately 1mL of blood was collected by cardiac puncture, at which point the animal was then culled and dissected. Subcutaneous, epididymal, retroperitoneal and mesenteric white adipose tissue was collected, along with brown adipose tissue, liver, pancreas, spleen, kidneys, and heart tissues were collected. All tissue samples were frozen in dry ice and kept at -80°C until used for further analysis. Glucose was also measured during organ collection by a glucose meter (Boots, UK).

3.2.2.3 Adipocyte isolation and counting

During dissection, samples from the epididymal and subcutaneous fat depots collected were used to isolate and measure adipocyte numbers and size. Dulbecco's Modified Eagle Medium (DMEM) solution (glucose 1g/mL) was prepared with 4% albumin. Collagenase solution was made up by adding 1mg/mL of collagenase to the DMEM solution with 4% albumin. Wash buffer solution was prepared with trypsin inhibitor 1mg/mL of 4% albumin DMEM solution. The tissue was rinsed in DMEM solution 4% albumin and then added to a bijou tube along with 1mL of prepared collagenase solution per 0.5g of tissue. The tissue was finely minced with scissors and kept in a vibrating water bath at 140 cycles/min and 37°C for 75-90 minutes. The cell suspension was then filtered through a polypropylene mesh (250μm) in order to separate the adipocytes from undigested tissue into a clean bijou tube. To stop any further digestion separated adipocytes were washed thoroughly with wash buffer. The tube was left out of the water bath till a cell suspension was formed. Then using a blunt needle, the wash buffer was sucked up from underneath the cells. More wash buffer was added to the tubes and left until the cell suspension was formed again.

After the second wash, the wash buffer was removed and the cells were transferred to a universal tube. DMEM solution (5mL DMEM, glucose 1g/mL and 4% albumin) was added to the universal tube and this was left in the water bath at 120 cycles/min and 37°C for 30-60 minutes. The adipocytes were then sized using MultisizerTM 4 Coulter Counter (Beckman Coulter, USA).

3.2.2.4 Serum analysis

Blood was collected via cardiac puncture during dissections and treated with 10% Aprotinin (100000KIU) at the collection time, allowed to clot on a rocker for at least 30 minutes and then centrifuged at 4000rpm for 10 minutes. Serum was removed and kept at -80°C until

used. These samples were used for analysis of cholesterol, triglycerides, HDL and LDL, albumin, free fatty acids and adiponectin were measured using 2-site electrochemical luminescence immunoassays from MesoScale Discovery (Gaithersburg, USA). Free fatty acids were measured using the Non- Esterified Free Fatty Acid kit (Roche). Creatinine, ALT, AST, alkaline phosphate, triglyceride, HDL and cholesterol were measured on the Dimension RXL autoanalyser (Siemens Healthcare).

3.2.2.5 Protein extraction

Tissues were weight and placed into an Eppendorf, which contained 250µl per gram of tissue of homogenisation buffer (50mM Tris, 5mM sodium pyrophosphate, 50mM sodium fluoride, 1mM EDTA and 0.25M Sucrose) supplemented with protease inhibitors (1 tab per 5mL, Roche). Samples were briefly homogenised while maintaining a constant temperature of 4°C and 20µl of 10% Triton X-100 added and left to incubate on ice for 10 minutes, centrifuged at 14,000rpm for fifteen minutes at 4°C. From the supernatant aliquot, the concentration of protein homogenates was measured immediately with BCA protein assay (Thermo Scientific, USA). Protein homogenates were kept at -80°C until the next use and precipitated residues were kept at -80°C for histone extraction. Protein expression levels were analysed with Western blotting as described in 3.2.3.6.

3.2.2.6 Western blot analysis

Equal amounts of protein homogenates (50µg) were resolved by SDS-PAGE on a 4-12% bis-tris gel (Invitrogen, UK) and transferred to an Immobilon transfer membrane (Millipore, UK). After transfer, the membrane was blocked in 5% non-fat dry milk in 1x TBST (50mM Tris, 150mM sodium chloride and Tween-20) for 1 hour at room temperature. Following the blocking step, the membrane was incubated with purified primary antibodies, targeted to various proteins, raised in rabbit or mouse (AbCam, UK) overnight at 4°C on a shaking

platform. TBS was diluted from 10X TBS (24.2g Tris base, 80g NaCl in 1 litre H_2O, pH was adjusted to 7.6 with HCl) and washed in TBS-tween three times, 5 minutes each, and incubated in horseradish peroxidase-conjugated secondary anti-mouse antibodies, diluted 1:2000 in TBST (Santa Cruz Biotechnology, USA), anti-rabbit (1:10000, Sigma-Aldrich) in 5% non-fat milk in TBS-tween at room temperature for one hour on a shaking platform. The secondary antibodies were removed and the membrane was washed with TBST. The membrane was further washed three times with 1x phosphate buffered saline (PBS) the same way and the proteins were visualised using enhanced chemiluminescence (GE Healthcare, UK). Optical densities of individual bands were measured and protein expression was standardized to β-actin (mouse monoclonal, 1:10000, Sigma-Aldrich). Image acquisitions were carried out by Image J; statistical analysis was carried out by calculating the relative intensity using the described housekeeper.

3.2.2.7 RNA isolation and cDNA synthesis

Total RNA was isolated from 30~100mg of liver tissue and homogenized as described in 3.2.3.5 and then centrifuged at 12,000 g for 5 minutes at 4°C. The supernatant was discarded and pellet was resuspended in 100µL of TE buffer and combined with pre-cooled 75% (v/v) ethanol. The supernatant and ethanol solution was loaded into a RNA isolation column (Sigma-Aldrich, USA) and isolated according to manufactures guidelines. To remove the potential genomic DNA all RNA samples were further treated with DNase using TURBO DNA-free™ Kit (Ambion, USA) according to manufacturer's guidelines. All RNA samples were measured for concentration and quality on a nanodrop (Thermo Scientific, USA) and stored at -80 °C until use.

Total RNA (500ng), 1µL 250ng primer oligo(dT)16 and 1µL 10mM dNTP mix (10 mM each dATP, dGTP, dCTP and dTTP at neutral pH) were mixed with dH2O and pre-heated to 70°C

and then cooled on ice for cDNA synthesis. 20µl of reagents, containing 4µl 5X first-strand reaction buffer (250mM Tris-HCl, 375mM KCl, 15mM MgCl2), 1µl 0.1M DTT and 1µl of Super-script III Reverse Transcriptase (Invitrogen, UK), were incubated at 25ºC for a 5 min annealing step, followed by an extension step at 42°C for one hour followed by a final step at 70ºC for a 15 min heat-inactivate step.

3.2.2.8 Quantitative real-time polymerase chain reaction

Expression of mRNA was quantified by TaqMan real-time RT-PCR with a GeneAmp 7500 Fast System (Applied Biosystems, USA). Each reaction mixture contained 1x SYBR Green PCR master mix, 1µl cDNA (normalized to represent the equal amount of reverse-transcribed total RNA in each sample), 0.4µM each TaqMan primer and RNase-free water (Qiagen). A 10-fold dilution of RT reaction for each sample was analysed using TaqMan Gene Expression Assays (Applied Biosystems, USA) with commercially available specific primer-probes. Real-time PCR reactions were set following the manufacture instructions: one initial step at 95ºC for 10 minutes for holding, followed by a 40-cycle step, which was 15 seconds at 95°C for denaturation and one minute at 60°C for annealing or extension. The fluorescent dye ROX was used as an internal reference for normalisation of SYBR Green fluorescence. A dissociation protocol ranging from 60°C to 90°C was performed to investigate the specificity of the primer and the presence of primer dimers after the final amplification cycle. Threshold cycle (Ct) values obtained for each gene were converted to the linear form using the term $^{2-\blacktriangle\blacktriangle}$Ct as a value directly proportional to the copy number of mRNA 237, where $^{\blacktriangle\blacktriangle}$Ct was the Ct value normalized to GAPDH and referenced to the values obtained for each gene under normoxic conditions.

3.2.2.9 Histone extraction

Tissue residues from protein extraction were washed twice with ice-cold PBS containing 5mM sodium butyrate to retain levels of histone acetylation. Lysis buffer (10mM Tris 6.5 pH, 50mM sodium bisulphate, 10mM MgCl2, Sacarose 8.6%, 1% Triton X-100) was added to samples on ice and left to incubate on ice for 10 minutes, centrifuged at 14,000rpm for fifteen minutes at 4°C. After thorough homogenation, the supernatants were removed and the pellets washed with Tris-EDTA (10mM Tris 7.4 pH, 13mM EDTA) and centrifuged at 14,000rpm for 15 minutes at 4°C. Precipitated nuclei were resuspended in 50µl of ice-cold dH2O. 50µl 0.4M sulfuric acid was added to the samples, vortexed, and kept on ice overnight. Following centrifuge at 15,000rpm for another one hour, histone was precipitated as white pellets in 1mL acetone at -20°C overnight. Dry pellets were resuspended in dH2O for measurements of histone concentration with Bradford assay (Bio-Rad, UK). Histone expression levels were analysed with Histone acetylation assessment as described in 3.2.2.9.1.

3.2.2.9.1 Histone acetylation assessment

Histone acetylation was assessed with Western blotting. Equal amounts of histone extracts (10µg) were resolved by SDS-PAGE on a 12% bis-tris gel (Invitrogen, UK) and transferred Immobilon transfer membrane (Millipore, UK). After transfer, the membranes were blocked in 5 % non-fat dry milk in TBS-tween with agitation for one hour and then incubated with purified rabbit polyclonal antibodies against human acetyl-histone H3 (1:20000), acetyl-histone H3 lysine9 (acH3K9, 1:20000), acetyl-histone H4 (1:2000) and acetyl-histone H4 lysine12 (acH4K12, 1:2000, Millipore) in 5% BSA in TBS-tween overnight at 4°C on a shaking platform. After washed in TBS-tween three times, 5 minutes each, they were incubated in HRP-conjugated secondary antibodies against rabbit (1:10000, Sigma-Aldrich) in 5% non-fat milk in TBS-tween for one hour at room temperature on a shaking platform. The membranes were then washed three times again, 5 minutes each, and the proteins

were detected by chemiluminescence (Amersham GE Healthcare, UK). Optical densities of individual bands were measured and acetyl-histone expression was standardized to total histone H3 (rabbit polyclonal, 1:10000, Millipore) or total histone H4 (rabbit polyclonal, 1:2000, Millipore), which were executed on parallel gels as loading control. The data were presented as ratio of acetyl-histone over total histone.

3.2.2.10 Microarray

A genome wide expression analysis with DNA microarray was carried out on liver samples from LITA and control nanoparticle groups at the end of the 10 week study (n=5/group). GeneChip Mouse Gene 2.0 ST Array was used to examine the whole-transcript of the liver, which contain 35,240 probe sets. Total RNA, was extracted from frozen liver specimens using the miRNeasy Mini Kit (Qiagen). RNA quality and integrity was assessed with the RNA 6000 Nano Assay on the Agilent 2100 Bioanalyzer (Agilent Technologies, USA). Samples selected for further analysis had integrity factors (RIN) in the range of 7.0–7.6. Total RNA (500ng) was transcribed *in vitro* with an RNA amplification fit and IVT reagents (Affymetrix, USA) to label cDNA synthesis with nucleotides coupled to a fluorescent dye was prepared following Alexa Fluor 555 and Alexa Fluor 647 (Invitrogen) Kit protocols. Labelled RNA quality was again assessed with an Agilent Bioanalyser. Hybridization and scanning was carried out at the MRC microarray centre (Hammersmith Hospital, London, UK). The hybridization array was washed and scanned and data was extracted from the scanned image using Feature Extraction (FE) version 10.2 (Agilent technologies).

Raw microarray data (cel files) were imported into R using the software package Bioconductor (R Development Core Team). An MA plot was carried out in the initial data set to determine if there was a need to correct any of the individual samples for differences that were not due to the biological data. The MA-plot distributes the intensity ration (M) plotted by

the average intensity (A). One to adjust for differences in labelling intensities and hybridization identified from the MA plot, a global normalization was conducted by aligning signal intensities of data arrays across the medians. Only probe sets that had a signal intensity distribution profile similar to the sample set carried through to analysis; in this case, 4 arrays were analysed, giving a raw dataset of 16,321 probe sets. Raw data were normalized with a log2 transform with median stabilization. Suppression of controls, normalization, filtering and expression summary was carried out with the moderate t-test Linear Models for MicroArray (LIMMA) in the R-package LIMMA [234]. The parameters *m* and *v* are treated as known and set equal to the estimated values, and the Bayesian modelled t-test. LIMMA provided functions to summarize the results as (log) fold change in a linear model.

3.2.3 *Study 2: Chronic LITA Nanoparticle Administration in Metabolic Cages*

For metabolic chamber experiment, male WT C57BL/6 mice were assigned to a treatment group randomly and received i.p. injections of control or LITA nanoparticles (prepared as described in Chapter 2), daily for 7 days prior to being placed in the metabolic cages. The injection volume was 200μL, which contained approximately $5x10^8$ liposomes per injection. Mice were housed 1 per cage with access to normal fat diet food (Table 2.1) and water *ad libitum* (n=8/group).

For metabolic measurements, mice were housed in a climate-controlled metabolic chamber designed for mouse studies, the Comprehensive Lab Animal Monitoring System (CLAMS; Columbus Instruments, USA). The open-circuit indirect calorimetry system chambers were maintained at 2-22°C on a 12-hour light/12-hour dark cycle with lights on at 7am. Mice remained on the same food and water as in the week during the nanoparticle administration.

Each animal was housed individually in an airtight cage where oxygen consumption (VO_2) and carbon dioxide expiration (VCO_2) was measured by high-speed gas sensors on a continuously monitored for 48 hours in a 24 chamber open circuit Oxymax. Mice were acclimated to their metabolic cages for 5 hours before data was acquired. Samples were obtained electronically hourly and recorded during the 30-second sampling period. Other metabolic measurements such as food intake, locomotor activity and core temperature were also acquired.

3.2.4 Statistical Analysis

All the results are presented as mean ± standard error of the mean (SEM) or mean ± standard deviation (SD). Statistical analysis was performed by GraphPad Prism version 4 (GraphPad Software, USA). One-way ANOVA was applied for data of multiple group comparisons, whereas Two-way ANOVA was applied for data when there was more than one independent variable with multiple observation periods. For comparison between two groups, unpaired nonparametric t-test with Mann- Whitney modification was used. Any other analysis method is mentioned in the specified text. Significance was accepted at the level of $p < 0.05$ (*), $p < 0.01$ (**), or $p < 0.001$ (***).

3.3 Results

3.3.1 *Study 1: Chronic LITA Nanoparticle Administration on an Obesogenic Background*

Liposomes described in Chapter 2 were applied for an *in vivo* passive targeting system with 4mM of acetate loaded within the aqueous core of the vesicle. Preliminary biodistribution studies confirmed the acetate encapsulated liposomes does reach the circulatory system intact. Moving forward, the liposomal encapsulated acetate nanoparticle, or LITA, was applied to an *in vivo* model for observations in an obese state.

3.3.1.1 Food Intake and body weight

No statistically significant difference in average food intake between groups was observed (control: 18.04 ± 0.999; LITA: 15.29 ± 1.216, p=0.6170) (Figure 3.2 A). No statistically significant difference in cumulative food intake between groups at any week for the duration of the 10 week study was observed (p=0.978) (Figure 3.2 B).

Figure 3.3 shows the weight gain measured weekly over the 10 week study (n=8/group). The LITA group show an increase in body weight compared to the control (two-way AONVA, $p<0.01$ vs. Control). Similar changes were observed in cumulative body weight (two-way AONVA, $p<0.05$ vs. Control) for the last four weeks of the study (Figure 3.3 A-B). However there was no observed statistically significant difference when we comparing change in body weight (Control: 6.586 ± 0.8983; LITA: 7.075 ± 0.6310; unpaired t-test), or cumulative change in body weight between groups (two-way ANOVA) (Figure 3.3 C-D).

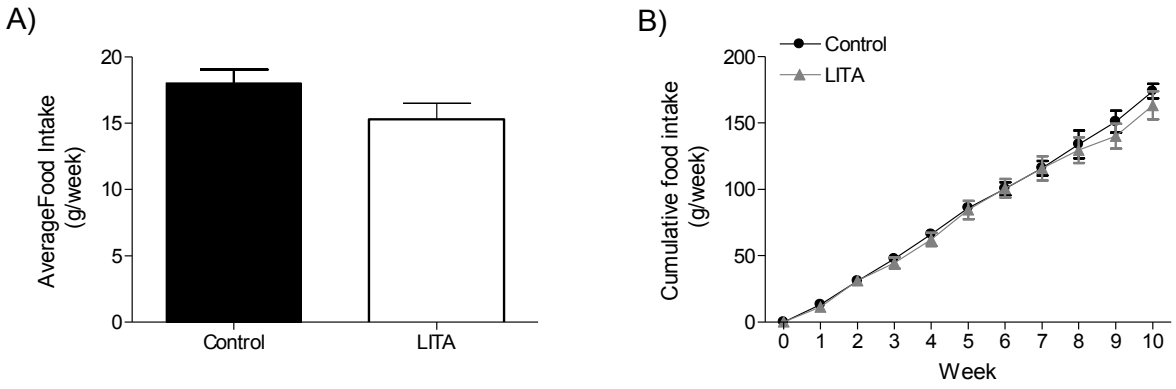


Figure 3. 2 Effects of average and cumulative food intake of chronic i.p. injections of control to LITA nanoparticles in ad libitum fed mice on high fat diet

Food intake of *ad libitum* fed mice on high fat diet was measured weekly after i.p. injections of control or LITA nanoparticles. **(A)** Average food intake showed no significant difference between groups. Data analysed by unpaired t-test. **(B)** Cumulative food intake showed no significant difference between groups. Data analysed by two-way ANOVA. Results are shown as mean ± SEM; n=8/group.

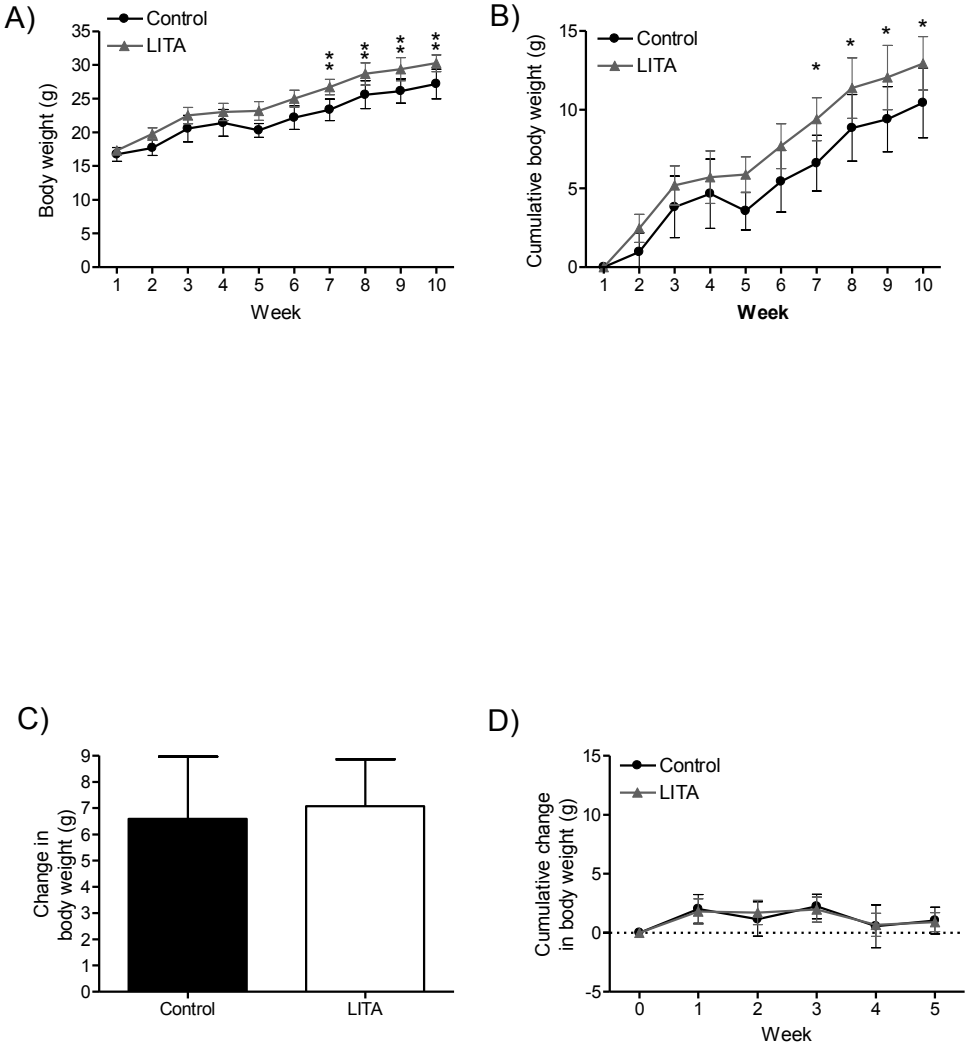


Figure 3.3 Effects on body weight of chronic i.p. injections of control to LITA nanoparticles in mice on high fat diet

Body weight of mice on high fat diet was measured weekly after i.p. injections of control or LITA nanoparticles. **(A)** Average body weight showed a significant increase in LITA group when compared to the control. Data analysed by two-way ANOVA. **(B)** Cumulative body weight showed a significant increase in LITA group when compared to the control. **(C)** Overall change in body weight showed no significant difference between groups (data analysed by student t-test) and **(D)** also showed no significant difference in LITA group when compare to the control group. Data analysed by two-way ANOVA. Results are shown as mean ± SEM, n=8/group

3.3.1.2 Whole body ^{1}H adiposity

The effect of LITA on whole body adiposity was determined by *in vivo* magnetic resonance spectroscopy (MRS). Whole body adiposity was similar pre-treatment in both the control liposomes (0.295 ± 0.041) and LITA treated (0.317 ± 0.041) groups (p=0.781) (Figure 3.4 A). Following the 5-week administration (Figure 3.4 B) a reduction in whole body adiposity content were observed in the LITA group (0.333 ± 0.033) compared to the control group (0.628 ± 0.126) (p=0.0423). Change of whole body adiposity between pre and post liposomal administration showed a significant reduction in the LITA group compared to the control group (CTRL: 0.400 ± 0.089, LITA: 0.090 ± 0.068; p=0.020), as shown in Figure 3.5 (n=8/group).

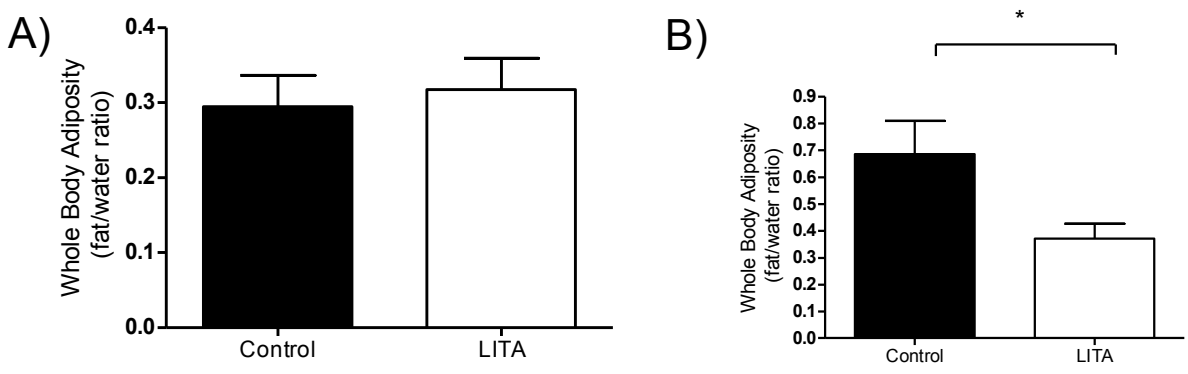


Figure 3.4 Whole body adiposity before and after control or LITA administration measured *in vivo* by MRS

Whole body lipid adiposity relative to water content was measured by MRS in mice to measure the effects of control and LITA administration in the obesogenic model. A baseline scan was taken **(A)** before nanoparticle treatment at 10 weeks of age (p= 0.7081) and **(B)** after nanoparticle treatment at 15 weeks of age (p=0.0423). * = $p<0.05$ vs. control group; n=8/group. Data is presented as mean ± SEM and analysed by unpaired t-test.

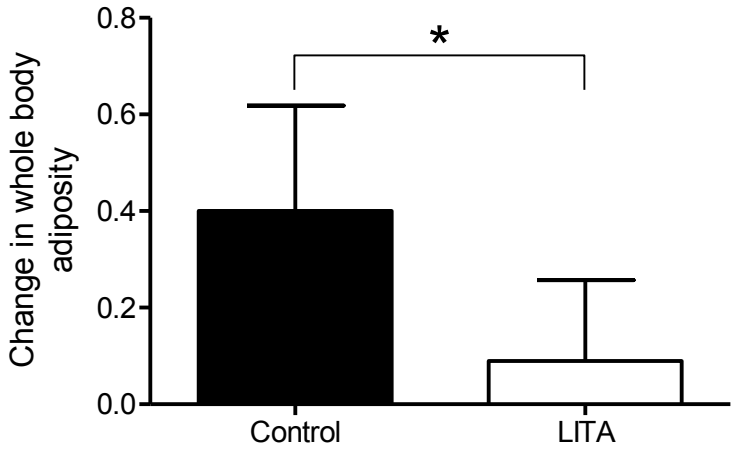


Figure 3.5 Whole body adiposity change after control and LITA administration measured *in vivo* by ^{1}H MRS

Whole body lipid adiposity relative to water content was measured by MRS in mice before and after control and LITA administration and decreased in the LITA treated group ($p=0.020$). * = $p<0.05$ vs. control group. Data is presented as mean ± SEM and analysed by unpaired t-test; n=8/group.

3.3.1.3 Whole body adiposity measured *ex vivo* by dissections

At the end of the study, white adipose tissue (WAT) was collected by means of dissection. Total WAT was calculated by summing the subcutaneous, epididymal, retroperitoneal and mesenteric adipose fat depots. There was a slight decrease in total white adipose tissue weight in the LITA group ($p=0.3726$ (Figure 3.6 A)). The regional decrease shown in total WAT is itemised in Figure 3.6 B, whereas the epididymal and retroperitoneal fat depots show a significant decrease ($p<0.05$ vs. control) and the subcutaneous ($p=0.2874$) and mesenteric ($p=0.3726$) shows a trending decrease in the LITA treated group. Results for all white adipose tissue recovered from dissections can also be seen in Table 3.2. Continuing on with the varying fat depot analysis, when the total WAT to subcutaneous ratio is examined is significantly reduced in the LITA group ($p<0.05$ vs. control (Figure 3.6 C)). However, when calculating total WAT over body weight, there is a significant reduction in the LITA group ($p<0.05$ vs. control (Figure 3.6 D)).

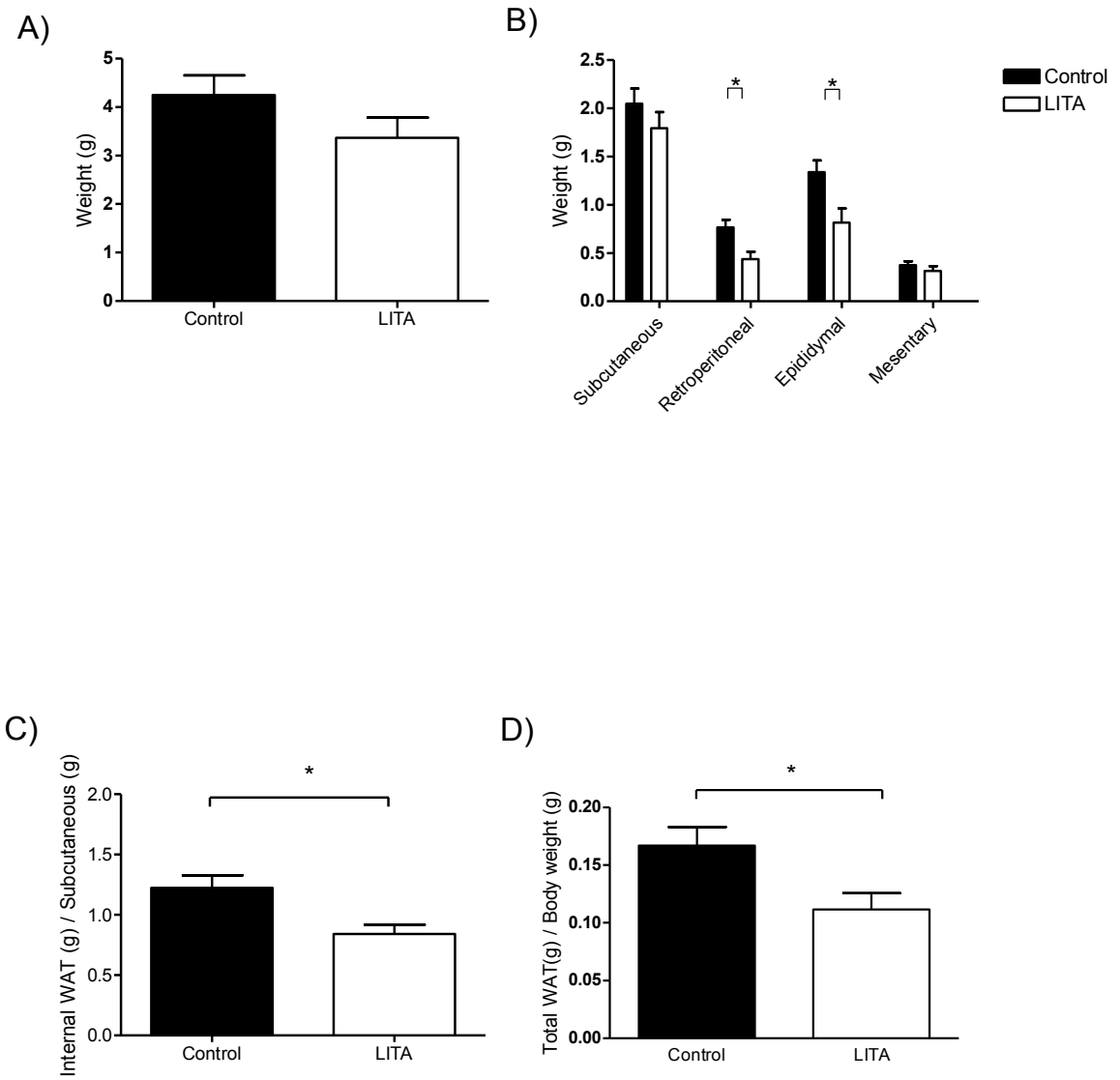


Figure 3.6 Fat distribution in mice after 10 week study on high fat diet with either control or LITA nanoparticle administration

Mice were dissected at the end of the 10 week study of chronic administration of either control or LITA nanoparticles. **(A)** Total white adipose tissue is decreased in LITA group when compared to the control group and **(B)** differences in fat distribution between the control and LITA groups with a statically significant decrease in the retroperitoneal and epididymal depots (*p = <0.05). **(C)** Internal WAT in relation to subcutaneous fat and **(D)** total WAT in relation to body weight. Data is presented as mean ± SEM and analysed by unpaired t-test; n=8/group.

	Control (mean ± SEM)	LITA (mean ± SEM)	p value
Total white adipose tissue	0.376 ± 0.038	0.316 ± 0.0499	0.3726
Subcutaneous	2.049 ± 0.154	1.795 ± 0.166	0.2874
Epididymal	1.339 ± 0.123	0.814 ± 0.148	**p<0.05**
Retroperitoneal	0.764 ± 0.081	0.437 ± 0.078	**p<0.05**
Mesenteric	0.376 ± 0.038	0.316 ± 0.049	0.3726

Table 3.2 Total white adipose tissue extracted by dissection in mice after 10 week study on high fat diet with either control or LITA nanoparticle administration

Mice were dissected at the end of the 10 week study of chronic administration of either control or LITA nanoparticles and white adipose tissue was dissected. Total WAT was calculated by summing the subcutaneous, epididymal, retroperitoneal and mesenteric adipose fat depots. Data is presented as mean ± SEM and analysed by unpaired t-test, n=8/group.

3.3.1.4 Adipocyte size and number

Results show the adipocyte isolation from the epididymal and subcutaneous fat depots from both the control and LITA treated animals at the end of the 10 week study. The total number of cells was measured for a range of 20-120μm to disregard non-cellular debris. The total mean number in the subcutaneous (p=0.1801) and in the epididymal (p=0.4417) fat depot showed no significant difference between groups (Figure 3.7 A-B). The total cell number of cells per gram showed no difference between groups in the subcutaneous (p=0.8997) fat depot however there was a slight but not significant decrease in epididymal (p=0.1143) fat depot (Figure 3.7 C-D).

Both the mean total cell volume in the epididymal (p=0.4417) fat depot and the subcutaneous (p=0.4754) fat depots showed no significant difference between the control and LITA groups (Figure 3.8 A-B). Again, the mean surface area showed no different in the epididymal (p=0.8119) and the subcutaneous (p=0.1801) showed a non-significant increase in the LITA group when compared to the control (Figure 3.8 C-D). Results for all adipocyte cell isolation can be seen in Table 3.3.

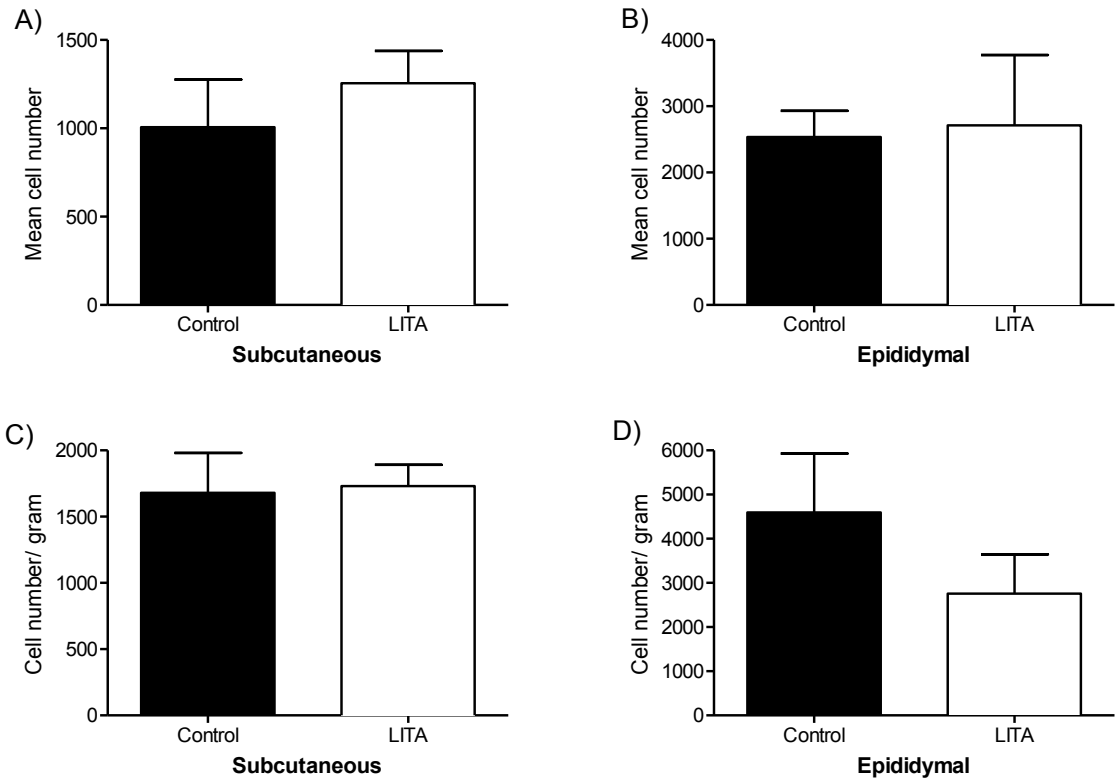


Figure 3.7 Adipocyte cell number in mice after 10 week study with either control or LITA nanoparticle administration

Mice were dissected at the end of the 10 week study of chronic administration of either control or LITA nanoparticles and white adipose tissue was dissected out and the adipocytes were counted in the epididymal and subcutaneous fat depots. **(A)** The mean number of cells in the subcutaneous tissue had a slight increase in the LITA group and **(B)** the mean number of cells in the epididymal fat depot showed no difference between groups. **(C)** Total cell number per gram of subcutaneous tissue had no difference in cell number between groups and **(D)** Total cell number per gram of epididymal tissue is decreased in LITA group when compared to the control group. Data is presented as mean ± SEM and analysed by unpaired t-test.

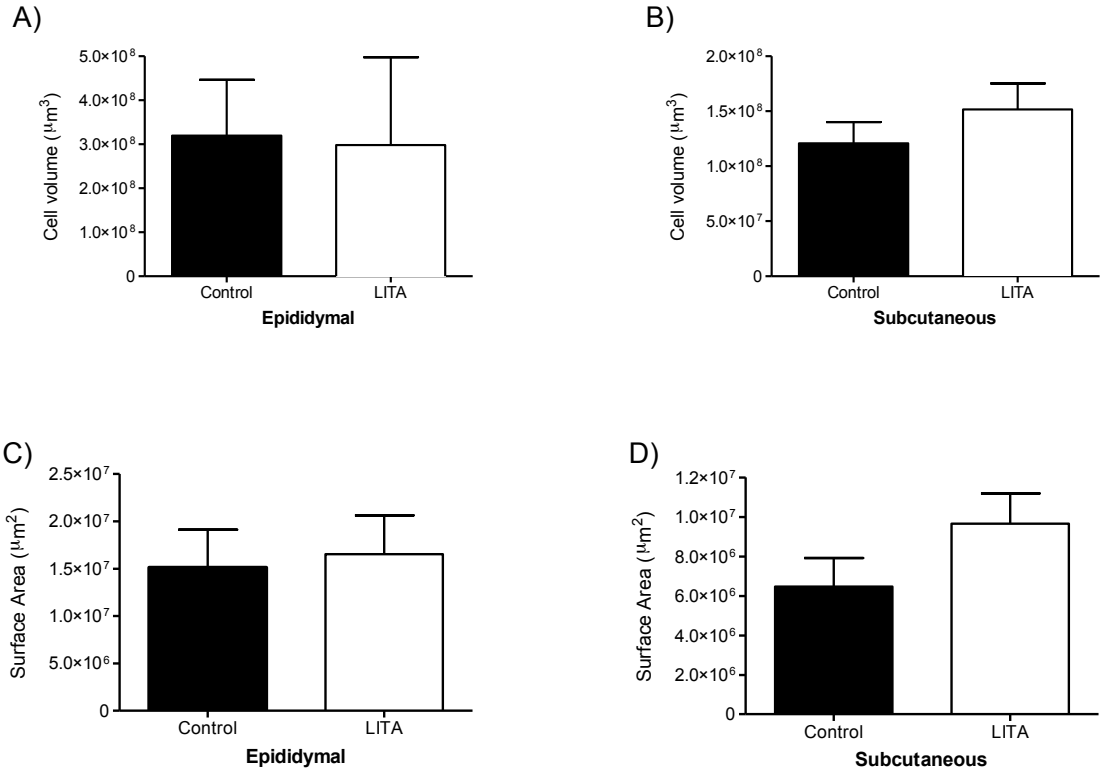


Figure 3.8 Adipocyte cell dimensions in mice after 10 week study with either control or LITA nanoparticle administration

Mice were dissected at the end of the 10 week study of chronic administration of either control or LITA nanoparticles and white adipose tissue was dissected out and the adipocytes were counted in the epididymal and subcutaneous fat depots. Both the **(A)** total cell volume in the epididymal fat depot and **(B)** the subcutaneous fat depots showed no significant difference in cell volume between the control and LITA groups. **(C)** Surface area showed no different in the epididymal and the **(D)** subcutaneous showed a non-significant increase in the LITA group when compared to the control. Data is presented as mean ± SEM and analysed by unpaired t-test, n=8/group.

		Control (mean ± SEM)	LITA (mean ± SEM)	p value
Mean number	Subcutaneous	1007 ± 270.2	1255 ± 183.2	0.4754
	Epididymal	2537 ± 396.4	2711 ± 1064	0.4417
Number/ gram	Subcutaneous	1681 ± 299.8	1731 ± 161.7	0.8997
	Epididymal	4597 ± 1335	1335 ± 890.3	0.1143
Volume (μm^3)	Subcutaneous	120700000 ± 19320000	151700000 ± 23650000	0.3535
	Epididymal	319300000 ± 126900000	298200000 ± 199500000	0.465
Surface area (μm^2)	Subcutaneous	6478000 ± 1437000	9665000 ± 1534000	0.1801
	Epididymal	15130000 ± 4009000	16550000 ± 4110000	0.8199

Table 3.3 Adipocyte cell isolation in mice after 10 week study with either control or LITA nanoparticle administration

Mice were dissected at the end of the 10 week study of chronic administration of either control or LITA nanoparticles and white adipose tissue was dissected out and the adipocytes were counted in the epididymal and subcutaneous fat depots. Number, number per gram, volume and surface are displayed. Data is presented as mean ± SEM and analysed by unpaired t-test, n=8/group.

3.3.1.5 Intrahepatocelluar lipid content

^{1}H MRS revealed no significant difference between groups in intrahepatocellular lipid (IHCL) content at baseline scans (control: 0.224 ± 0.362, LITA: 0.242 ± 0.037; p= 0.7398) (Figure 3.9 A). Figure 3.9 B shows the change after the 5-weeks of liposomal administration, there was a significant decrease in IHCL in the LITA treat when compared to the control group (CTRL: 0.333 ± 0.629, LITA: 0.111 ± 0.024, p=0.0074) (** = p<0.01 vs. control group; n=8/group).

IHCL content differences at the end of the 5-week study comparing pre and post IHCL levels (Figure 3.10). The control group had an increase in IHCL content (0.236 ± 0.089). Whereas, the LITA treated had a significant decrease in IHCL content (-0.106 ± 0.256). The difference between the control and LITA treated groups reached statistical significance (*** = p<0.001 vs. control group; n=8/group).

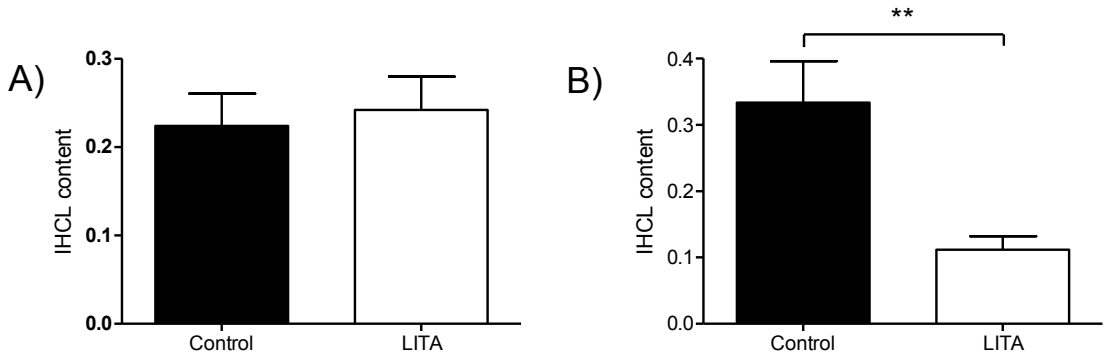


Figure 3.9 Lipid content in the liver before (A) and after (B) control and LITA administration as determined by ^{1}H MRS

Intrahepatocellular lipid content relative to water was measured by ^{1}H MRS in mice. Before control or LITA nanoparticle administration baseline MRS scan, the mice had been on a HFD for 5 weeks to establish a fatty liver. After LITA or control administration the scan was repeated after 5 weeks of administrations and remaining on the HFD. **(A)** Prior to injections a baseline scan was taken of each mouse in both designated treatment groups (p= 0.7398). **(B)** After administration there was a decrease in IHCL when comparing control and LITA treated groups (p=0.0074). ** = p<0.01 vs. control group. Data is presented as mean ± SEM and analysed by unpaired t-test; n=8/group.

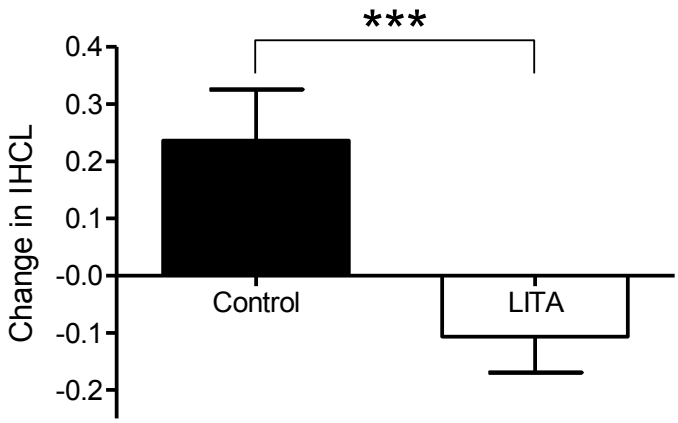


Figure 3. 10 Change in lipid content in the liver as an effect to chronic i.p. control or LITA administration as determined by ^{1}H MRS

The change in intrahepatocellular lipid content relative to water was measured by MRS in mice. Change shown was calculated from an initial baseline scan with an established fatty liver as a result of 5 weeks on a HFD and after 5 weeks of receiving either control or LITA nanoparticles whilst remaining on a HFD during injections. The IHCL significantly decreased in the LITA group when compared to the control group. *** = $p<0.001$ vs. control group. Data is presented as mean ± SEM and analysed by unpaired t-test; n=8/group.

3.3.1.2 Organ size

Organ weights were recorded upon dissection at the end of the 10 week study (Figure 3.11, Table 3.4). A statically significant decrease in liver (*$p<0.05$ vs. control) and a trending decrease in the pancreas ($p=0.056$) and kidneys ($p=0.050$) following LITA treatment. An increase in the muscle in the LITA treated group was observed but did not reach significance ($p=0.2394$). No other differences were observed between (n=8/group). When examining the organ mass in relation as a percentage of body weight, the LITA groups had a significant increase in the muscle (**$p<0.01$ vs. control) and BAT (*$p<0.05$ vs. control (Figure 3.12, Table 3.5)) compared to control.

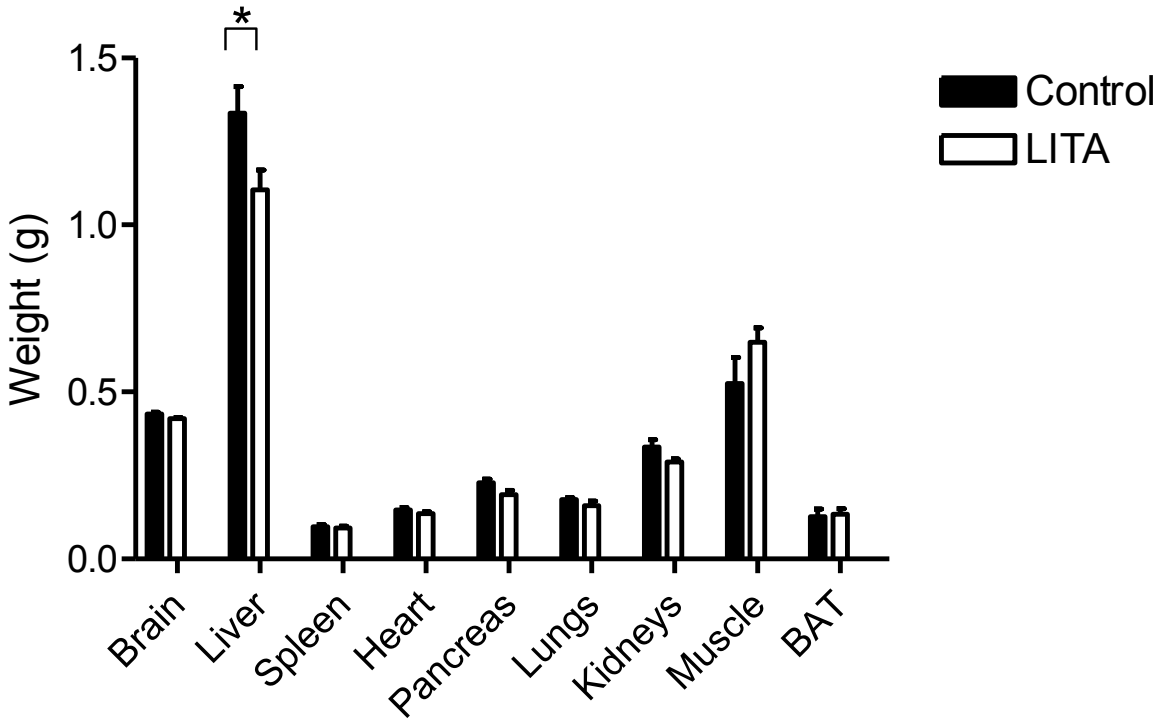


Figure 3.11 Organ weight following chronic i.p. injections of either control or LITA nanoparticles during 10 week study

Organ weight recorded at the of the 10 week study for control and LITA treated groups. The liver had a statistically significant decrease in weight (* = $p<0.05$). The muscles had a trending increase in mass but did not reach significance. Results are mean ± SEM and analysed by unpaired t-test; n=8/group.

	Control (mean ± SEM)	LITA (mean ± SEM)	p value
Brain	0.434 ± 0.004	0.421 ± 0.003	0.0807
Liver	1.335 ± 0.080	1.106 ± 0.058	**p<0.05**
Spleen	0.097 ± 0.007	0.093 ± 0.006	0.7115
Heart	0.147 ± 0.007	0.135 ± 0.005	0.2504
Pancreas	0.228 ± 0.012	0.193 ± 0.012	0.0568
Lungs	0.177 ± 0.005	0.159 ± 0.013	0.2437
Kidneys	0.336 ± 0.021	0.291 ± 0.009	0.0503
Muscle	0.526 ± 0.077	0.649 ± 0.043	0.2394
Brown Adipose Tissue	0.127 ± 0.240	0.134 ± 0.018	0.6032

Table 3.4 Organ weight following chronic i.p. injections of either control or LITA nanoparticles during 10 week study

Organ weight recorded at the of the 10 week study for control and LITA treated groups. The only organ showing a statistically significant different between the control and LITA group was the liver. Data is presented as mean ± SEM and analysed by unpaired t-test; n=8/group.

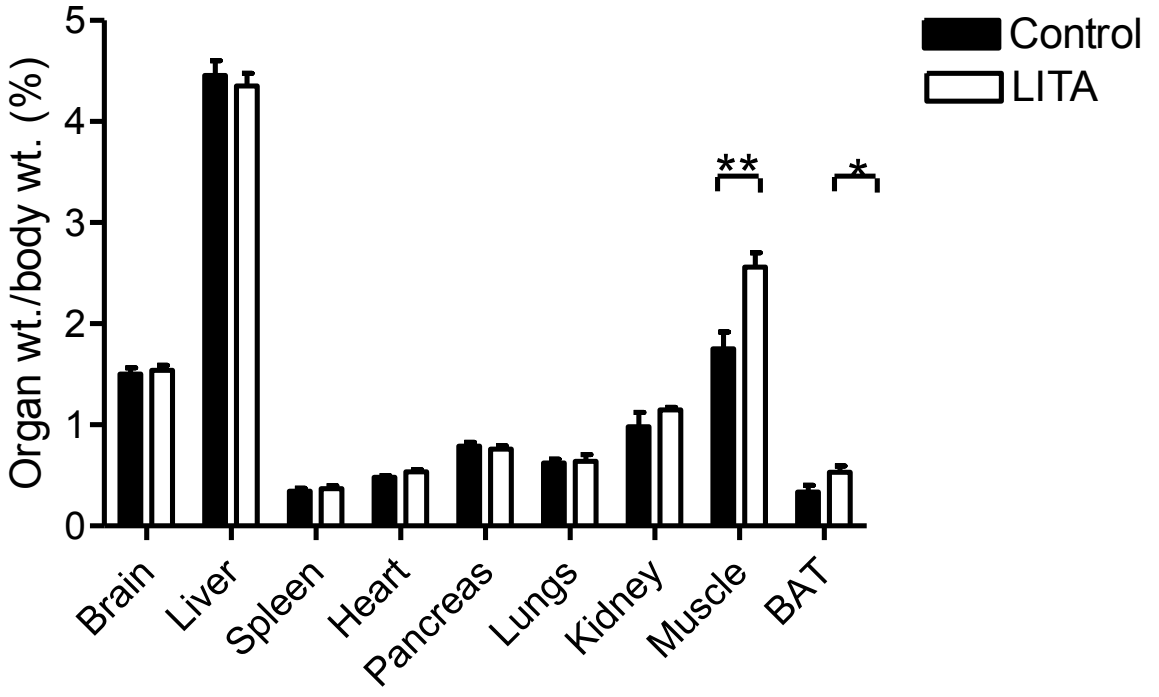


Figure 3.12 Organ weight to total body weight ratio in mice following chronic i.p. injections of either control or LITA nanoparticles during 10 week study

Organ weight to total body weight ratio recorded at the of the 10 week study for control and LITA treated groups. The muscle and BAT were statistically significant (* = $p<0.05$, ** = $p<0.01$). Results are mean ± SEM and analysed by unpaired t-test; n=8/group.

	Control (mean ± SEM)	LITA (mean ± SEM)	p value
Brain	1.503 ± 0.061	1.538 ± 0.050	0.715
Liver	4.458 ± 0.145	4.351 ± 0.127	0.5878
Spleen	0.341 ± 0.029	0.369 ± 0.027	0.4957
Heart	0.481 ± 0.015	0.535 ± 0.020	0.0573
Pancreas	0.789 ± 0.036	0.759 ± 0.032	0.5489
Lungs	0.622 ± 0.036	0.641 ± 0.063	0.7997
Kidneys	0.981 ± 0.142	1.149 ± 0.024	0.2686
Muscle	1.750 ± 0.167	2.560 ± 0.142	**p<0.01**
Brown Adipose Tissue	0.335 ± 0.066	0.532 ± 0.062	**p<0.05**

Table 3. 5 Organ weight to total body weight ratio following chronic i.p. injections of either control or LITA nanoparticles during 10 week study

Organ weight to total body weight recorded at the of the 10 week study for control and LITA treated groups. The organs showing a statistically significant different between the control and LITA group were the muscle and BAT. Data is presented as mean ± SEM and analysed by unpaired t-test; n=8/group.

3.3.1.7 Serum analysis

Serum samples were collected via cardiac puncture at the end of the study and in order to investigate metabolic markers of obesity. The LITA treatment group showed a significant reduction in triglycerides ($p<0.05$), leptin ($p<0.05$) and free fatty acids (FFA) ($p<0.05$) (Figure 3.7, Table 3.6)). There was a trending increase in adiponectin ($p=0.0748$) and lipase ($p=0.0770$) levels, although did not reach significance.

Similarly, keratinocyte chemoattractant/ GRO-alpha (KC/GRO) was significantly decreased (*$p<0.05$ vs. control). There was a trending increase of interleukin-2 ($p=0.1854$), interleukin-4 ($p=0.1342$) and interleukin-10 ($p=0.265$) in the LITA treated group though none were significant. Other inflammatory factors such as TNK- α ($p=0.678$), IFN- γ (0.751), interleukin-1β (0.996) and interleukin-5 (0.898) had almost no change between control or LITA nanoparticle treated groups. (Figure 3.8, Table 3.6)). (n=5-8/group).

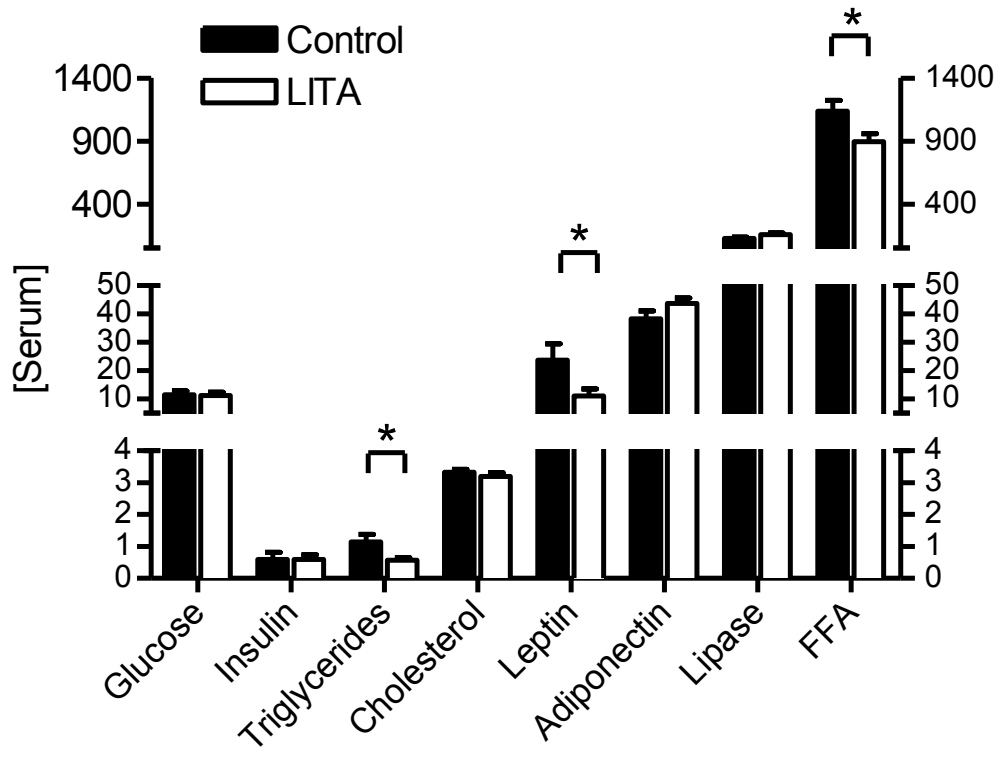


Figure 3.13 Serum analysis of metabolic marker of obesity in control and LITA groups

Serum samples were collected via cardiac puncture at the end of the study to investigate the effects of LITA and control in obesogenic mice model. A statically significant reduction was observed in triglycerides, leptin and free fatty acid (* = $p<0.05$). Results are mean ± SEM and analysed by unpaired t-test; n=5-8/group.

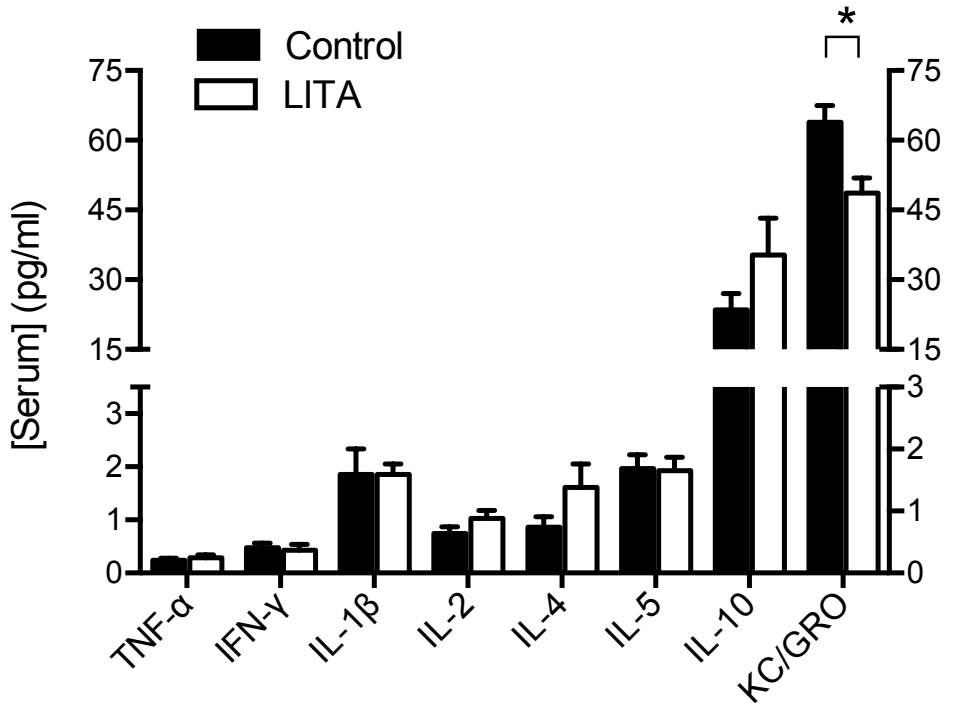


Figure 3.14 Serum analysis of inflammatory marker of obesity in control and LITA groups

Serum samples were collected via cardiac puncture at the end of the study to investigate the effects of LITA and control in obesogenic mice model. A statically significant reduction was observed in KC/GRO (* = $p<0.05$). Results are mean ± SEM and analysed by unpaired t-test; n=5-8/group.

		Control (mean ± SEM)	LITA (mean ± SEM)	p value
Metabolic markers	Glucose	11.53 ± 1.358	11.26 ± 1.218	0.4416
	Insulin	0.394 ± 0.054	0.592 ± 0.149	0.3102
	Triglycerides	1.214 ± 0.254	0.556 ± 0.286	**p<0.05**
	Cholesterol	3.300 ± 0.152	3.229 ± 0.0944	0.6978
	Leptin	23.82 ± 5.617	11.20 ± 2.549	**p<0.05**
	Adiponectin	38.26 ± 2.835	43.68 ± 1.944	0.0748
	Lipase	127.6 ± 11.15	158.7 ± 10.75	0.0770
	FFA	1138 ± 85.73	896.8 ± 61.41	**p<0.05**
Inflammatory markers	TNF-α	0.25 ± 0.050	0.284 ± 0.056	0.6785
	IFN-γ	0.474 ± 0.086	0.430 ± 0.108	0.7513
	IL-1β	1.859 ± 0.481	1.861 ± 0.203	0.9966
	IL-2	0.742 ± 0.125	1.025 ± 0.156	0.1854
	IL-4	0.860 ± 0.199	1.609 ± 0.445	0.1342
	IL-5	1.963 ± 0.261	2.010 ± 0.240	0.8987
	IL-10	25.74 ± 3.615	35.44 ± 7.908	0.265
	KC/GRO	63.87 ± 3.635	48.64 ± 3.284	**p<0.05**

Table 3.6 Serum analysis from 10 week obesogenic study in mice receiving either chronic LITA or control nanoparticles administration

Results obtained after 10 week chronic control and LITA nanoparticle treated groups on HFD from serum samples were collected via cardiac puncture. A significant decreased was observed in triglycerides, free fatty acids Data is presented as mean ± SEM and analysed by unpaired t-test; n=5-8/group.

3.3.1.8 Western blot analysis

Liver tissue and brown adipose tissue were examined using western blot for proteins of interest. Liver was examined for a panel of histone deacetylase proteins and BAT was examined for thermogenic activity changes.

3.3.1.8.1 Histone deacetylase protein changes in liver tissue

Analysis of western blotting of liver samples revealed a significant increase in select HDACs from class I, HDAC2 (control: 0.7213 ± 0.1106; LITA: 1.257 ± 0.05781, $p<0.01$) and HDAC3 (control: 0.8597 ± 0.004951; LITA: 1.316 ± 0.06639, $p<0.05$). A non-significant decrease was seen in HDAC 1. When examining HDACs from class IIA, the only significantly decreased protein was HDAC7 (control: 1.427 ± 0.1787; LITA: 0.7555 ± 0.07421, $p<0.001$) in the LITA treated group compared to control groups (Figure 3.26). Other class IIA HDACs that did not have a significant difference was HDAC4 with a decrease and an increase in HDAC5 in the LITA group when controlled to the control group. Bands from western blot can be seen in Figure 3.27 (n=5-6/group).

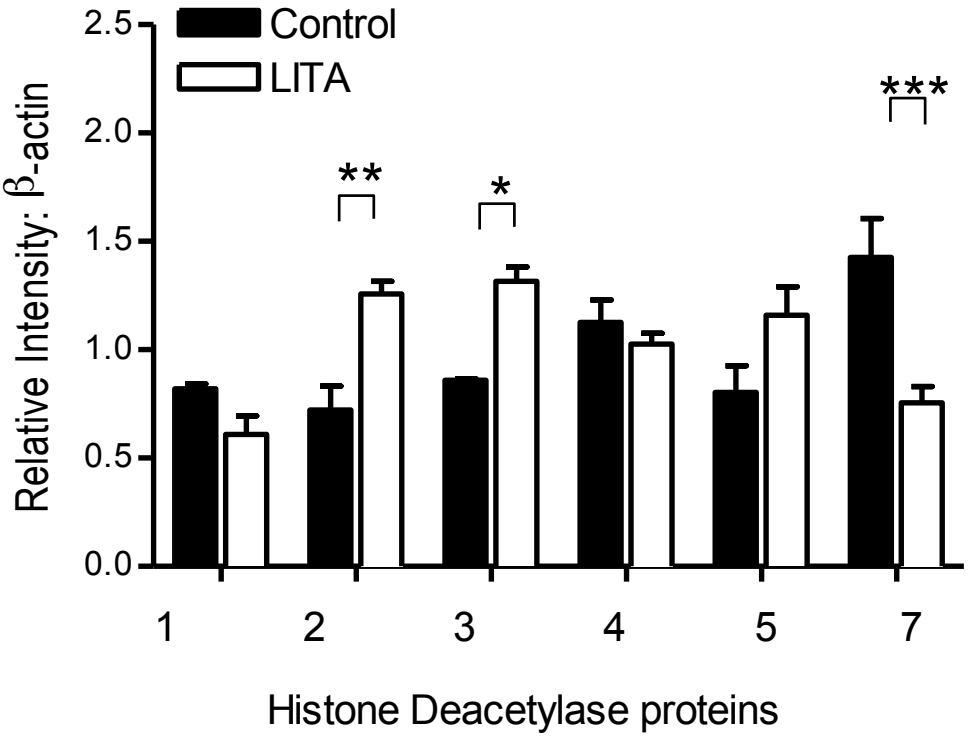


Figure 3.15 Quantitative relative intensity of western blot examining histone deacetylase (HDACs) in total proteins isolated from liver tissue after 10 week obesogenic study in mice receiving either control or LITA administration

Western blot determined no change in expression of histone deacetylase total protein in the liver tissue in mice at the end of the study between the control and LITA group (n=5-6/ group). Significant increase of expression was observed in HDAC 2 and 3 with a reduction in HDAC 7. HDAC 1 and 4 had trending decrease of expression and HDAC 5 had a non-significant increase. Relative intensity was measured and compared to the reference protein β-actin. Data is presented as mean ± SEM and analysed by unpaired t-test.

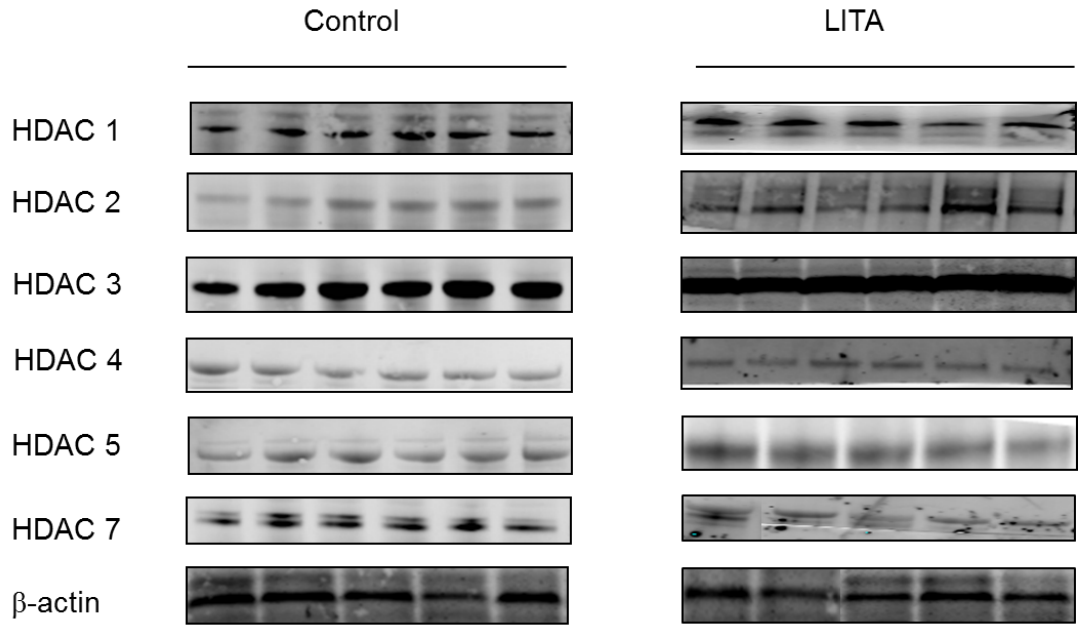


Figure 3.16 Western blot bands of histone deacetylase (HDACs) in total proteins isolated from liver tissue after 10 week obesogenic study in mice receiving either control or LITA administration

Western blot determined no change in expression of histone deacetylase total protein in the liver tissue in mice at the end of the study between the control and LITA group (n=5-6/ group). To serve as a control β-actin staining was conducted in parallel. Intensity of staining (darkness of band) is related to the amount of protein present.

3.3.1.8.2 Uncoupling Protein-1 changes in brown adipose tissue

The protein expression level of uncoupling protein-1 (UCP-1) was examined in the brown adipose tissue (BAT) extracted from the mice at the end of the 10 week study. No significant difference between the control (14.17 ± 1.998) and the LITA (14.44 ± 3.061) group was observed (Figure 3.28).

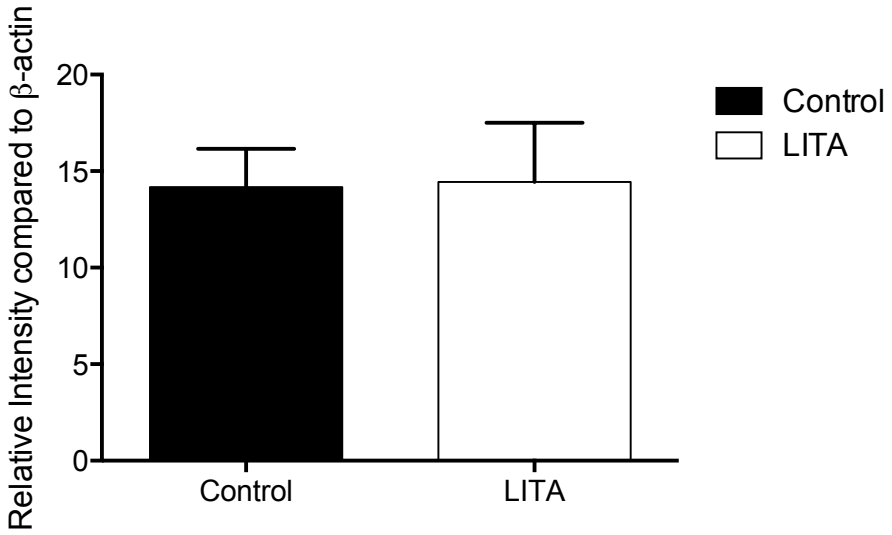


Figure 3.17 Quantitative relative intensity of western blot examining uncoupling protein-1 in brown adipose tissue after 10 week obesogenic study in mice receiving either control or LITA administration

Western blot determined no change in expression of uncoupling protein-1 in the brown adipose tissue in mice at the end of the study between the control and LITA group. The bands probing for UCP-1 from the western blot can be seen in Figure 3.18 and the analysis of relative intensity compared to the control protein β-actin. Data is presented as mean ± SEM and analysed by unpaired t-test; n=7/group.

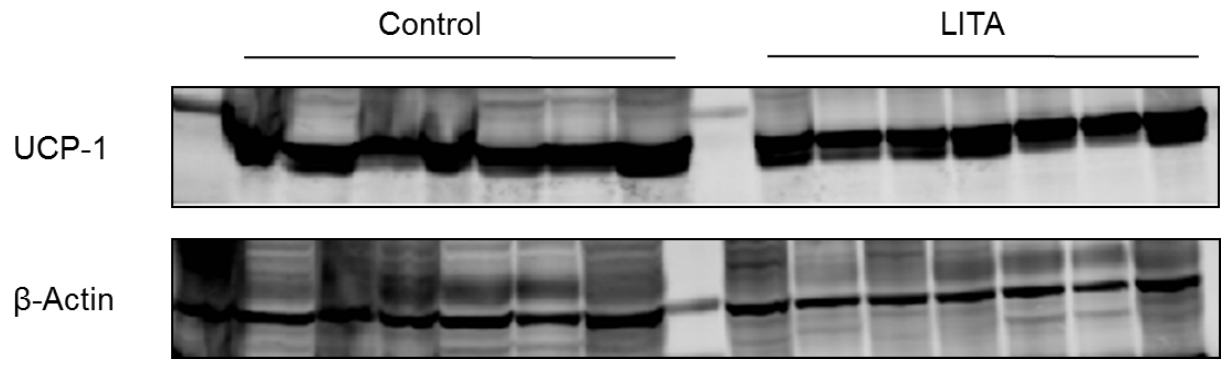


Figure 3.18 Western blot bands of uncoupling protein-1 in brown adipose tissue after 10 week obesogenic study in mice receiving either control or LITA administration

Western blot was conducted to measure protein levels of uncoupling protein-1 in the brown adipose tissue of mice at the end of the study between the control and LITA group (n=7/ group). To serve as a control β-actin staining was conducted in parallel. Intensity of staining (darkness of band) is related to the amount of protein present. Results show no change in UCP-1 expression between groups.

3.3.1.9 Microarray analysis

Fluorescence intensity was acquired, normalised and analysed for genes up- and down regulated in cDNA extracted from liver tissue in order to compare to the control to the LITA nanoparticle treated group. Two preliminary analysis methods were conducted to examine the quality of each individual sample, and the range of fluorescence intensity detected; firstly, the MA plot showed the non-linear dependence between ratios and fluorescence of each sample, showing two samples varied in ratio when compared to the other samples (Figure 3.20). When the samples were plotted as a boxplot for signal intensities (Figure 3.21), it was confirmed that array 05 and array 10 were outliers and were removed from the samples in the final analysis.

Analysis parameters removed outlier genes, leaving 2028 genes available for group comparison analysis. Colour scheme represents intensity of fluorescence. Data shown is the remaining 2028 genes, analysed using LIMMA in R; n=4/group. A heat map was generated to give visualization between signal intensities in the most effected genes (x-axis) across the 8 samples (y-axis) (Figure 3.22).

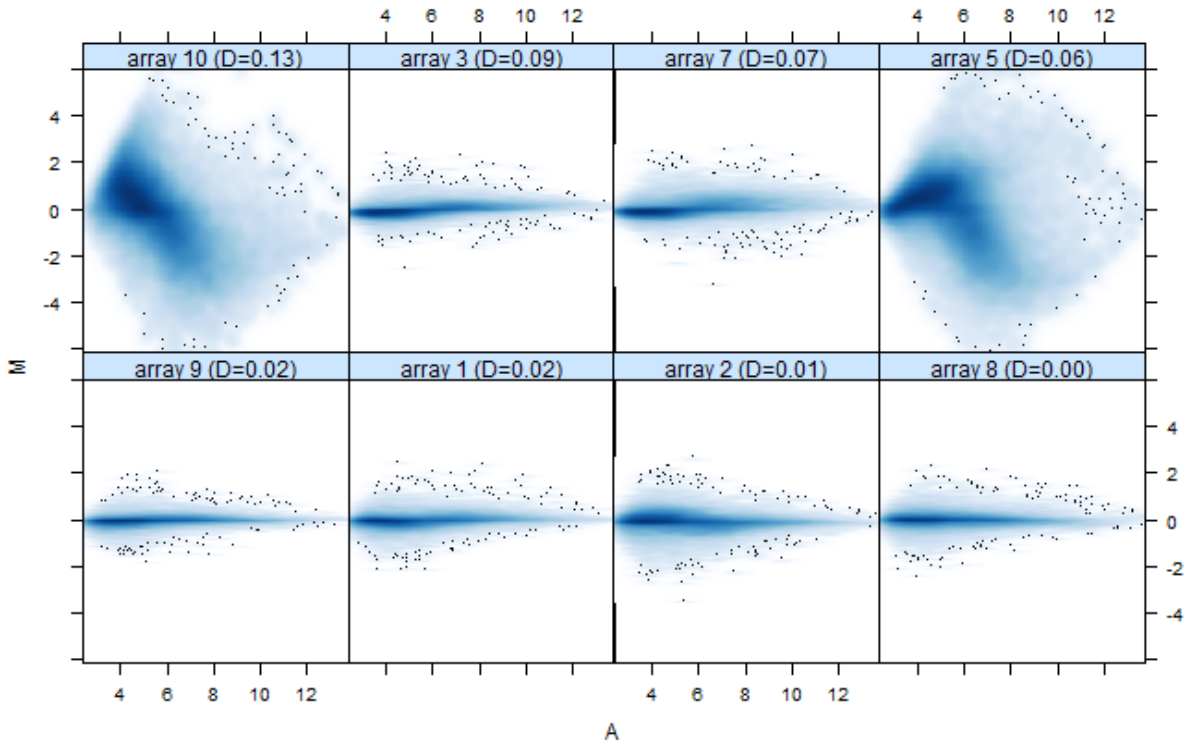


Figure 3.19 MA plots of signal intensity for outlier detection and quality control of samples post 10 week chronic study of either LITA or control nanoparticle administration for final analysis

Outlier detection was performed in R by computing Hoeffding's statistic Da on the joint distribution of A and M for each array. Shown are the 4 arrays with the highest value of Da (top row), and the 4 arrays with the lowest value (bottom row). The value of Da is shown in the panel headings. 0 arrays had Da >0.15 and were marked as outliers. Outlier samples were identified as array 5 and array 10 and removed from final analysis; n=5/group.

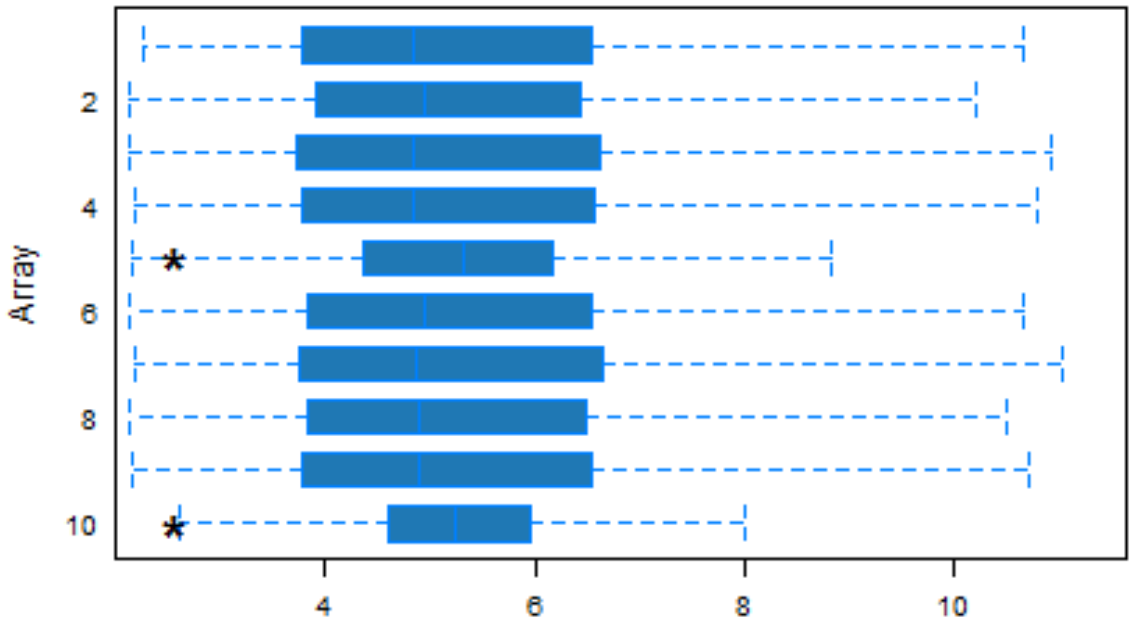


Figure 3.20 Microarray intensity distributions of samples post 10 week chronic study of either LITA or control nanoparticle administration

Boxplots representing signal intensity distributions of the sample arrays. Each box corresponds to one array. Outlier detection was performed by computing the Kolmogorov-Smirnov statistic Ka between each array's distribution and the distribution of the pooled data. This confirms array 05 and array 10 are outliers; n=5/group.

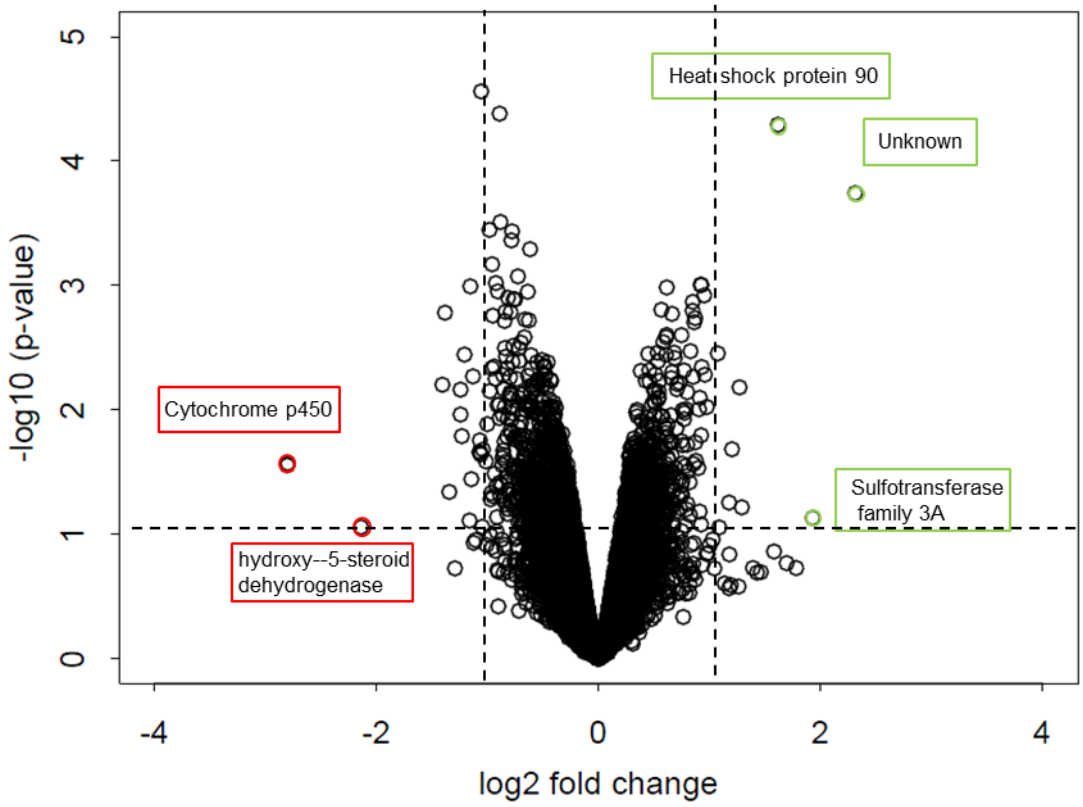


Figure 3.21 A volcano plot of differentially expressed genes in liver tissue from 10 week study of chronic i.p. administration of either LITA or control nanoparticles

Fluorescence intensity is acquired, normalised and analysed for genes up- and down regulated when compared to the LITA treated group. Each point represents a gene from the microarray experiment. The log2 ratio of expression is shown on the x-axis and the log10 p-value of the ANOVA significance test is shown on the y-axis. Analysis parameters removed outlier genes, leaving 2028 genes available for group comparison analysis. Data shown is the remaining 2028 genes, analysed using LIMMA in R; n=4/group.

3.3.1.9 Gene expression analysis

Gene expression was carried out to examine a number of genes of interest using qRT-PCR to analyse effects of control versus LITA nanoparticles at the end of a 10 week study in liver tissue. A statically significant decrease was observed in UCP-2 (***p>0.01 vs. control), however no change in PPARα (p= 0.866) (Figure 3.22). When looking at β-oxidation changes, ACOX1 (p=0.4423) was up regulated and CPT1A (p=0.0613) was down regulated though neither change was significant. The fatty acid synthesis gene, ACC, was slightly down regulated when compared to the control group however the difference was not significant. The enzyme family of histone deacetylases analysed showed a significant decrease in HDAC 1 expression (***p>0.01 vs. control) and a trending decrease in HDAC 2. Data is also displayed in Table 3.6.

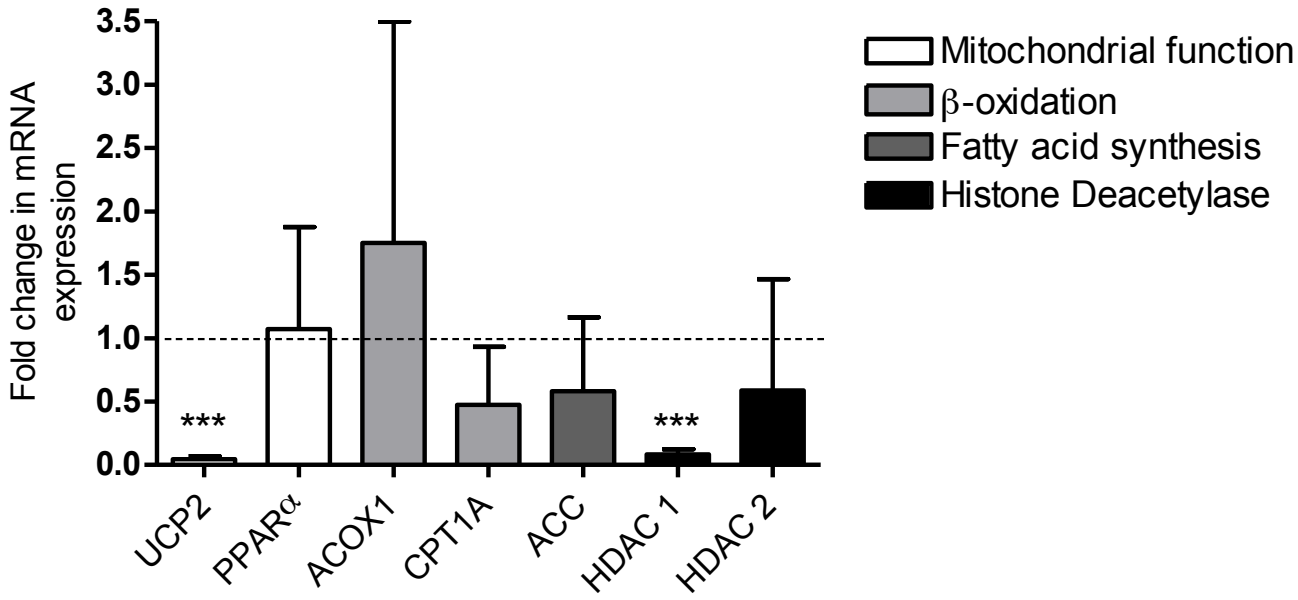


Figure 3.22 qRT-PCR analysis of gene expression fold changes in mRNA isolated from the liver as a result of chronic LITA treatment in obesogenic model

Gene expression changes at the end of a 10 week study of chronic LITA or control nanoparticle administration in a HFD model. The mitochondrial function classification of genes showed a significant decrease in UCP2 and no change in PPARα. The β-oxidation and fatty acid synthesis classification of genes showed no significant changes. There was a down regulation of HDAC1, which was not observed in HDAC 2. *** = $p<0.001$ vs. control group. All expression changes were compared to the control nanoparticles set to 1.0 and in relation to the housekeeper gene, GAPDH. Data is presented as mean ± SD and analysed by unpaired t-test (n=5-8/group).

Gene of interest	LITA (mean ± SD)	p value
ACC	0.583 ± 0.583	0.1102
UCP-2	0.044 ± 0.025	**p<0.001**
PPAR-α	1.071 ± 0.805	0.8661
ACOX1	1.751 ± 1.748	0.4236
CPT1A	0.475 ± 0.456	0.0613
HDAC 1	0.083 ± 0.040	**p<0.001**
HDAC 2	0.588 ± 0.807	0.4117

Table 3.7 Summary of qRT-PCR analysis of gene expression fold changes in mRNA isolated from the liver as a result of chronic LITA treatment in obesogenic model

Gene expression changes presented as mean ± SD at the end of a 10 week study of chronic LITA or control nanoparticle administration in a HFD model. All gene expression changes were compared to the control nanoparticles set to 1.0 and in relation to the housekeeper gene, GAPDH. *** = p<0.001 vs. control group; n=5-8/group. Data is analysed by unpaired t-test.

3.3.1.10 Histone acetylation assessment

Histone protein expression was determined *ex vivo* by western blot at the end of the 10 week study to analyse effects of control and LITA nanoparticle administration in histones isolated from liver tissue (n=4/group). The histone residue acH3K9 showed a decrease in the LITA group when compared to the control group (control: 1.349 ± 0.129, LTA: 0.913 ± 0.109; p=0.0622). Another histone examined, M^2H3K9 showed no significant difference between treatment groups (control: 0.929 ± 0.158, LITA: 1.271 ± 0.206; p=0.260) group. The histone residue acH4K12 did show a significant increase in expression in the control group when compared to the LITA treated group (control: 1.291 ± 0.130; LITA: 0.688 ± 0.101, p=0.0220), Data in graph format can be seen in Figure 3.23 and blots from experiment can be seen in Figure 3.24. (*p<0.05 vs. control, n=4/group).

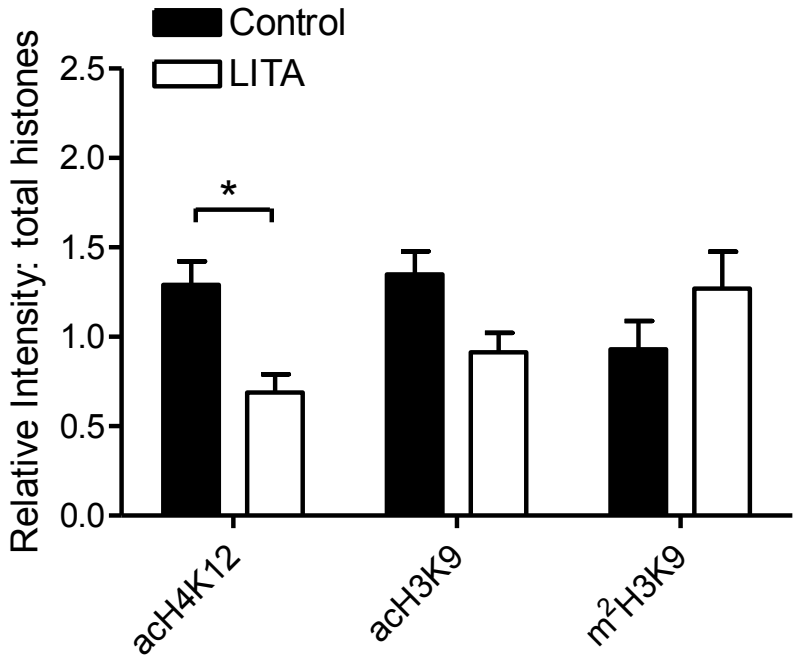


Figure 3.23 Quantitative relative intensity of western blot examining histone residues in histones isolated from liver tissue after 10 week obesogenic study in mice receiving either control or LITA administration

Western blot determined a reduction was seen in acH4K12 at the end of the study between the control and LITA group (n=4/ group). Relative intensity was measured and compared to the reference protein total histone 3 or 4 depending on which target protein of interest was being investigated. Both histones acH3K9 and M^2H3K9 showed only trending changes, however a significant difference was seen in acH4K12. * = $p<0.05$ vs. control group; data is presented as mean ± SEM and analysed by unpaired t-test.

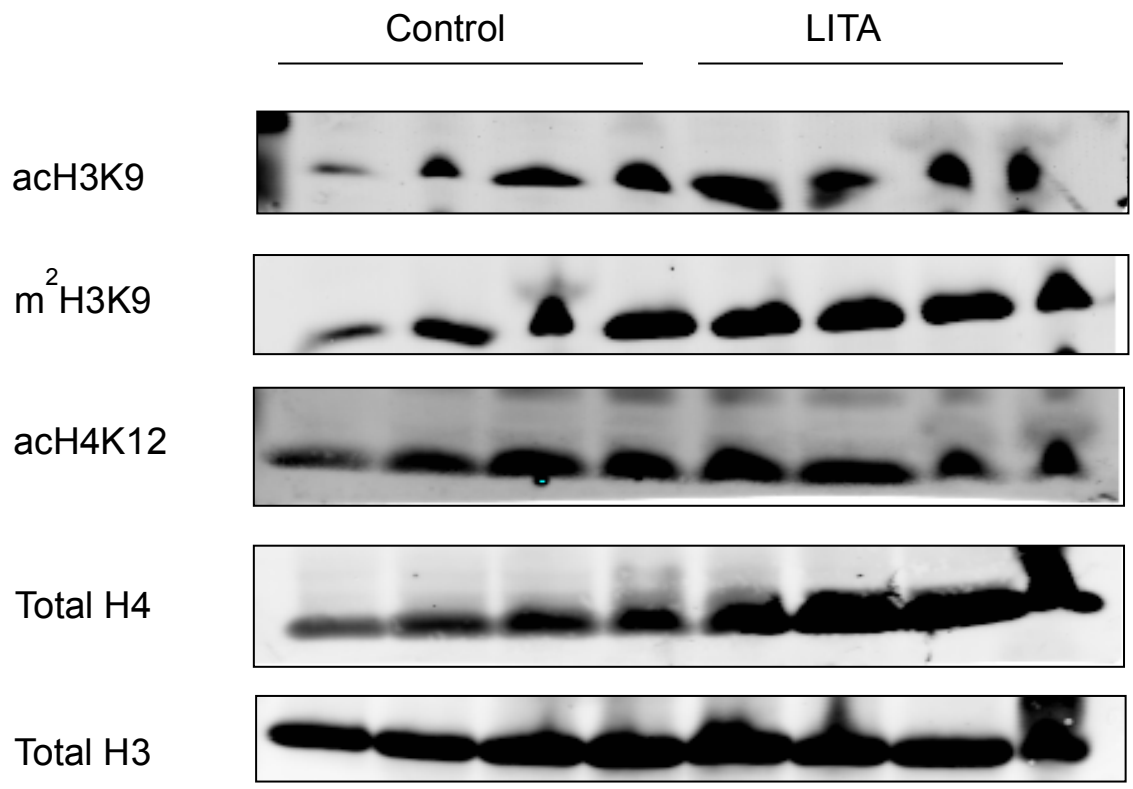


Figure 3.24 Western blot bands of histone residue proteins in histones isolated from the liver after 10 week obesogenic study in mice receiving either control or LITA administration

Western blot was conducted to measure histone protein levels in the histones isolated from the liver of mice at the end of the study between the control and LITA group (n=4/ group). To serve as a control either total histone 3 or 4 staining was conducted in parallel depending on the target protein of interest. Intensity of staining (darkness of band) is related to the amount of protein present.

3.3.2 *Study 2: Chronic LITA Nanoparticle Administration in Metabolic Cages*

To explain some of the observation made during Study 1, a monitoring of acute motor and metabolic activity was investigated. Mice received chronic i.p. injections of either control of LITA nanoparticles for 7 days prior to being placed in the metabolic cages for 48 hours. Day/ nights are represented in the following figures by the white/black bars along the x-axis of all graphs.

Feeding profile while housed in the metabolic cages is shown in Figure 3.25. No significant difference in day/night feeding profile (p=0.8550), cumulative food intake (p=0.1941) (Figure 3.25 B) or cumulative water intake (p=0.8204) (Figure 3.25 C) between groups (Figure 3.25 A).

Gas exchange showed no different between control or LITA groups when specifically looking at VO_2 (p=0.8614) (Figure 3.26 A) and VCO_2 (p=0.8911) (Figure 3.26 B) during the 48 hour examination period. Heat was slightly increased however not significant in the LITA group when compared to the control group (p=0.8741) (Figure 3.27 A). The respiratory exchange ratio (RER) had no significant difference between groups (p=0.9169) (Figure 3.27 B).

Motor activity of mice within the metabolic cages showed no statistical significance between the control or LITA treated groups in either XAMB (p=0.8948) (Figure 3.28 A) or the XTOT (p=0.8471) (Figure 3.28 B) directional movements. There was no significance in the ZTOT beam breaks, between the control group and LITA treated group (p=0.5568) (Figure 3.28 C).

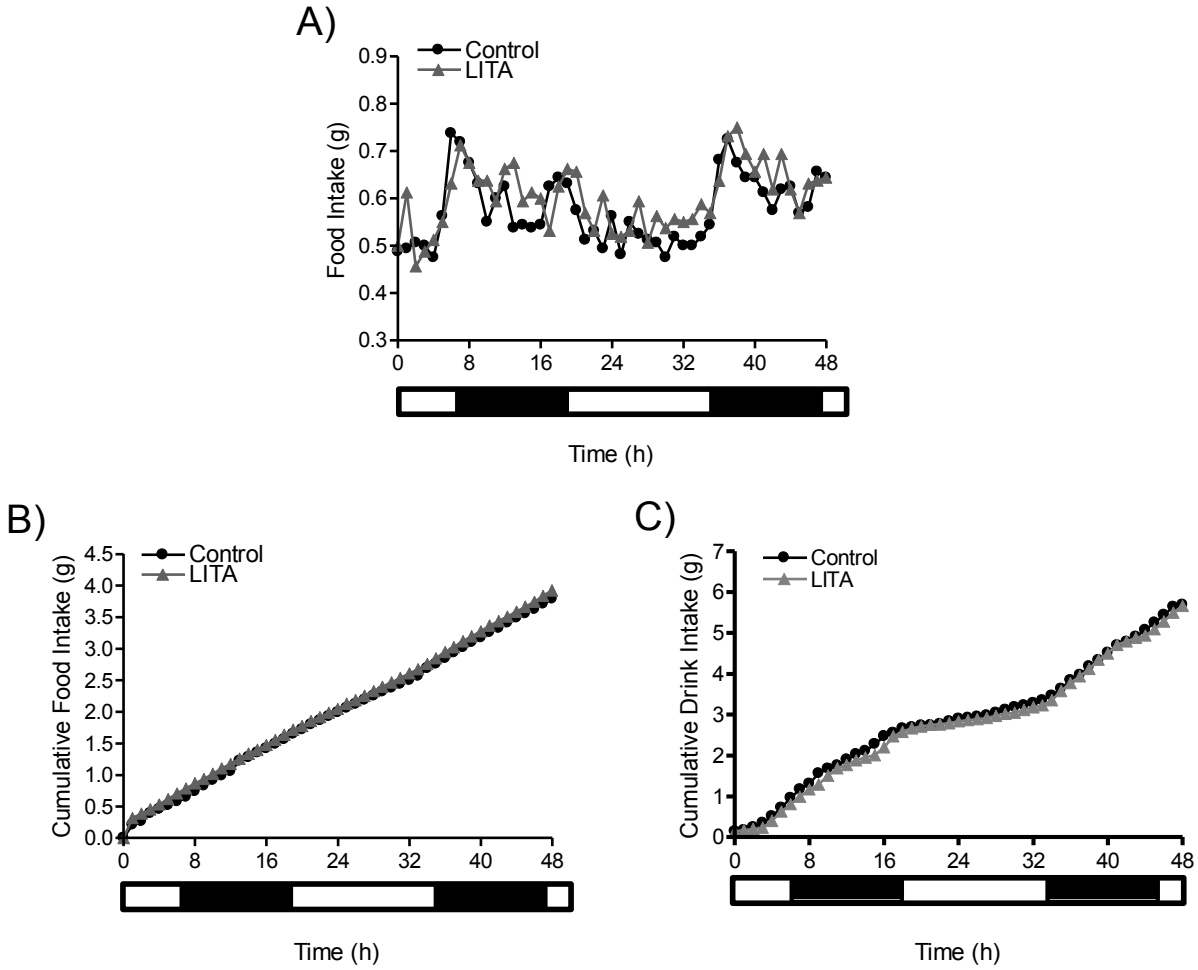


Figure 3.25 Metabolic cage monitoring of mice after 7 day LITA or control nanoparticle administration- Food and drink intake

The effects of 200µL LITA or control liposomes i.p. daily for 7 days on food and drink intake in mice housed in metabolic cages **(A)** Day/Night feeding profile (p=0.8550), **(B)** cumulative food intake (p=0.1941) and **(C)** water intake (p=0.8204) during the 48 hour study. White and black bars along x-axis indicate day/night cycle. Results are mean ± SEM, statistical differences between treatment groups were determined using 2-way ANOVA, n=8/group.

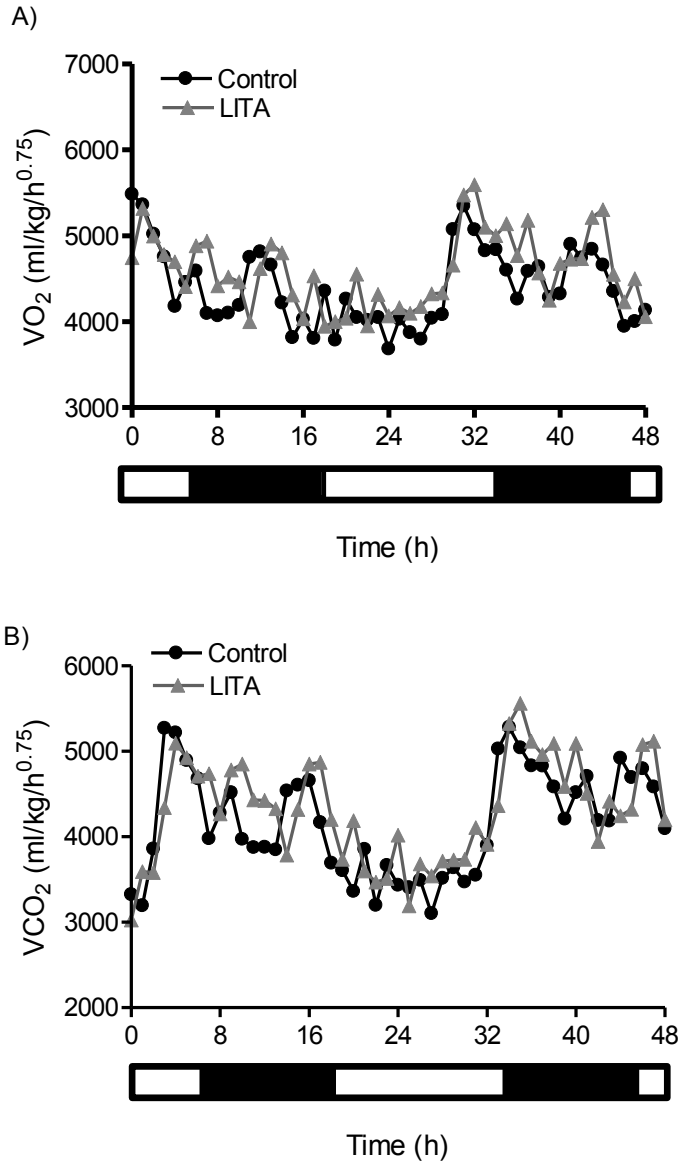


Figure 3.26 Metabolic cage monitoring of mice after 7 day LITA or control nanoparticle administration- VO_2 and VCO_2

The effects of 200µL LITA or control liposomes i.p. daily for 7 days on gas exchange in mice housed in metabolic cages. **(A)** VO_2 (p=0.8614) and **(B)** VCO_2 (p=0.8911) were monitored during the 48 hour study. White and black bars along x-axis indicate day/night cycle. Results are mean, error bars removed from clarity. Statistical differences between treatment groups were determined using 2-way ANOVA, n=8/group.

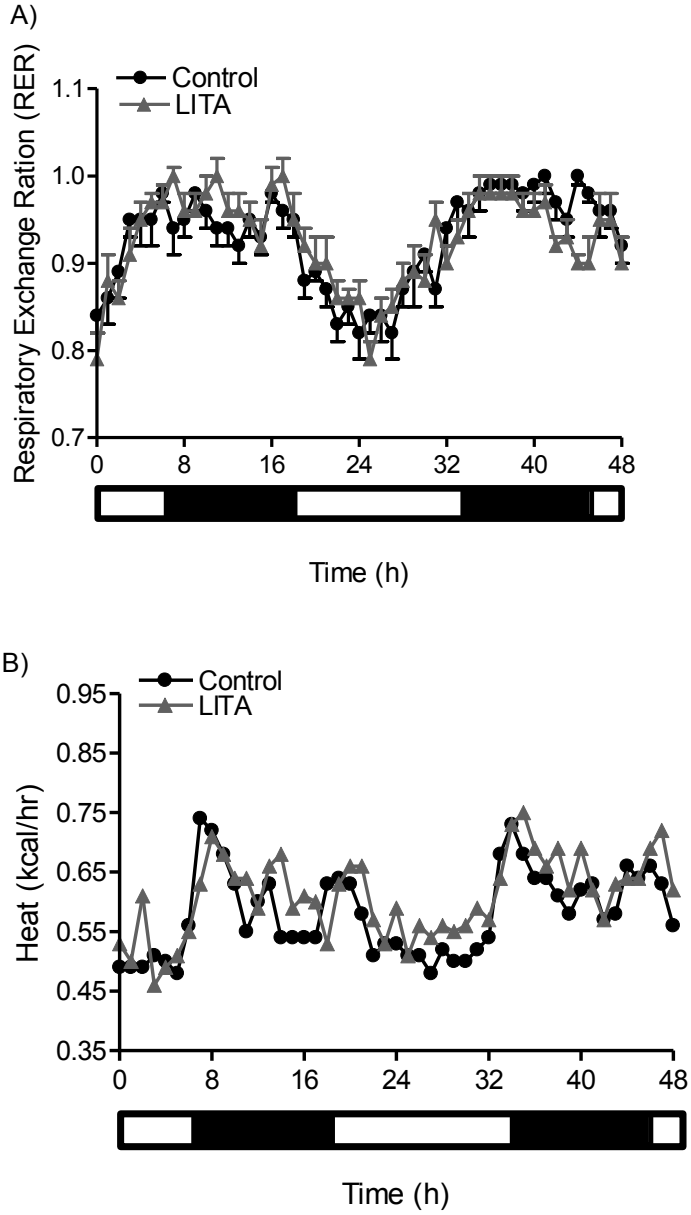


Figure 3.27 Metabolic cage monitoring of mice after 7 day LITA or control nanoparticle administration- RER and heat

The effects of 200µL LITA or control liposomes i.p. daily for 7 days on gas exchange in mice housed in metabolic cages. **(A)** RER (p=0.9169) and **(B)** heat (p=0.8741) was monitored during the 48 hour study. White and black bars along x-axis indicate day/night cycle. Results are mean, error bars removed from clarity. Statistical differences between treatment groups were determined using 2-way ANOVA, n=8/group

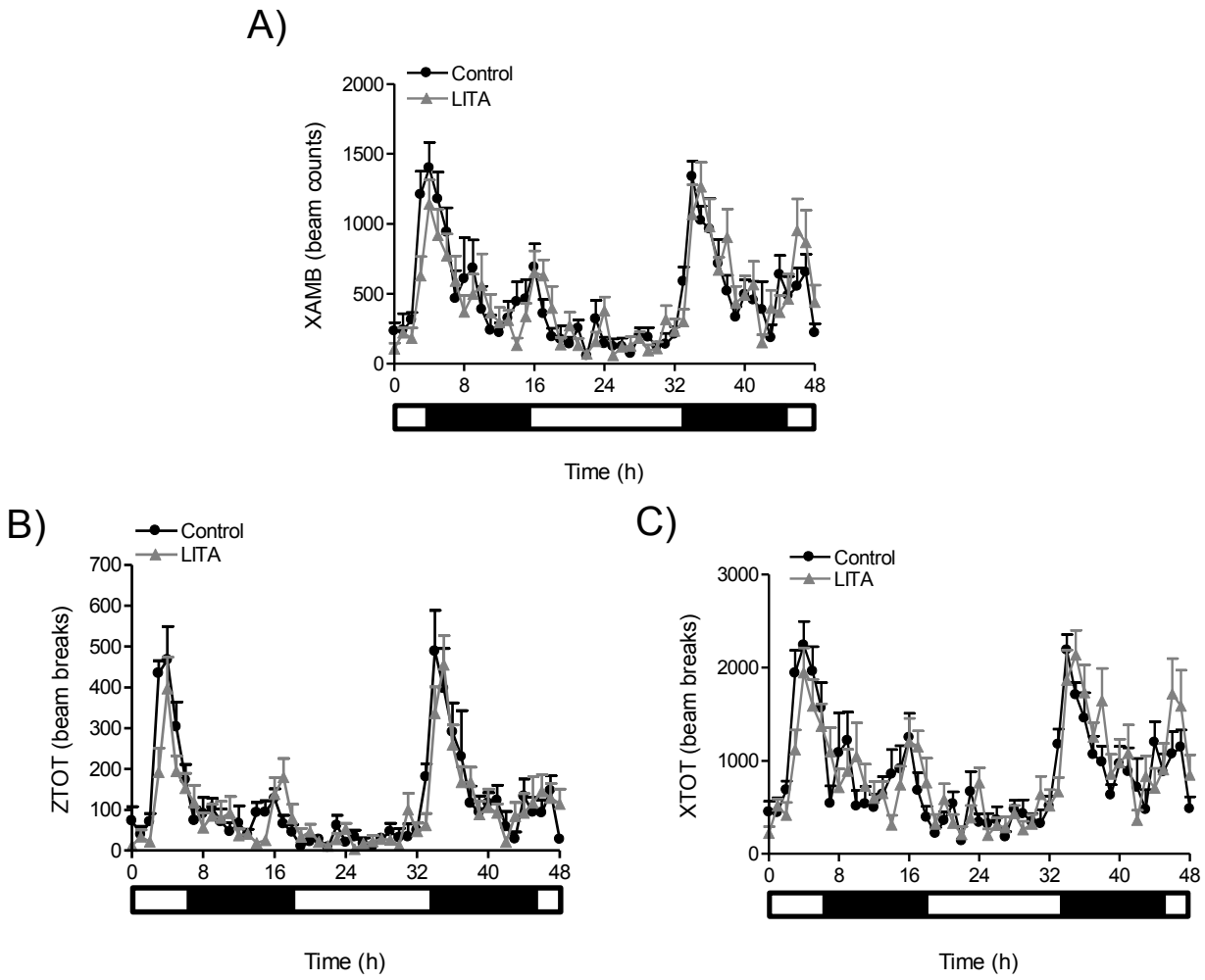


Figure 3.28 Metabolic cage monitoring of mice after 7 day LITA or control nanoparticle administration- XAMB, XTOT and ZTOT

The effects of 200µL LITA or control liposomes i.p. daily for 7 days on activity in mice housed in metabolic cages. **(A)** XAMB (p=0.8948), **(B)** XTOT (p=0.8471) and **(C)** ZTOT (p=0.5568) during the 48 hour study. White and black bars along x-axis indicate day/night cycle. Results are mean ± SEM, statistical differences between treatment groups were determined using 2-way ANOVA, n=8/group.

3.4 Chapter Discussion

Previous studies have shown that fermentable carbohydrates can have a positive effect on body composition, weight, and insulin sensitivity [118, 235]. The combination of increased food (energy) in the form of a high fat diet provides a complex model of obesity and fatty liver syndromes. In the first study, an obesogenic background was established by placing C57BL/6 mice on a high fat diet (HFD) for 5 weeks. Mice subsequently received i.p. injections of LITA or control (HEPES) nanoparticles (n=8/group) every 3 days for an additional 5 weeks, while maintained on a HFD. In the second study, I attempted to monitor the metabolic behaviour of the mice based on data reported in Study 1. In order to assess the effects of LITA nanoparticle administration on respiratory outcomes, metabolic activity and motor behaviour, metabolic cage analysis was performed. Following a week of daily day administration of LITA or control injections (n=8/group), mice were monitored over a period of 48 hours in CLAMS metabolic cages.

LITA treated animals did not have a significant difference in food intake, however did show a significant increase in body weight. No differences in cumulative food intake over the course of this study was observed, if anything a minor, though not significant, decrease in cumulative food intake was observed in the LITA treated group during week 9 and 10. The main increase in body weight in the LITA group occurred in weeks 7, 8, 9 and 10. Studies done previous by Kondo et al have shown a decrease in body weight with acetate [125]. This difference may be related to the mode of administration, Kondo et al administered acetate orally (water), thus none targeted which may contribute to appetite regulation and therefore decrease in food intake [125]. In my study the use of LITA may have avoid this effect and the changes observed may be related to increase in muscle mass, given that I the LITA treated group shows a significant decrease in some body fat depots. Thus acetate may have an anabolic effect, a process that may require further investigation.

To further investigate the metabolic phenotype of LITA treated animals, I used calorimetric cages. In this study, animals were treated for 7 days with either LITA or control nanoparticles whilst consuming a normal fat diet and placed in a metabolic cage for 48 hours. Metabolic cage studies revealed that LITA nanoparticle treated mice were slightly hyperphagic compared with their controls nanoparticle group. In fact they ate a significant amount more ($p>0.05$) when adjusted for total body weight. This is in contrast to what one would expect considering it was hypothesized that an energy source would be coming from the acetate encapsulated within the nanoparticles. However, the food intake increases the most during the last day, potentially after the acetate has been metabolised. There was no difference between groups when looking at cumulative drink intake.

Core temperature was considerably higher in LITA treated mice, though not significant. The increased heat could be explained in part by the input of acetate causing an increase in potential energy. Oxygen consumption showed no significant difference between groups. RER levels were similar overall. However, during the first dark period, RER levels were increased in LITA treated mice, which may reflect increased carbohydrate utilization. The second dark period had a period of symmetry with the control group and later with a decrease in RER in the LITA group, which would indicate a difference in carbohydrate-to-protein ratio utilization difference.

Motor activity was acquired as three different functions; XAMB (horizontal beam breaks) and XTOT (total x-axis ambulation) had similar day/night motor patterns between groups. This was a surprising result because in Study 1 there was a trending increase in muscle mass in the LITA group when compared to the control group. However, 48-hour surveillance did not

answer why that was observed. Potentially the monitoring process of Study 2 would require a longer observational period to justify the finding in Study 1.

In general, the metabolic profile of the LITA animals showed an altered response to control nanoparticles, showing an increase in caloric intake whilst not changing in motor activity. There was a trending increase in heat production, which has previously been shown in rodent models on ketogenic diets [236]. A shift away from carbohydrate metabolism might be also expected to result in altered respiratory outcomes in LITA-injected animals. However, I observed no differences following metabolic cage analysis, with only non-significant trends towards reduced RER, and increased oxygen consumption and heat production in LITA-injected animals. These results are in accord with several papers that demonstrate energy expenditure is maintained following acetate infusion, as acetate replaces fat as an oxidative fuel [237-239]. Determining the cellular pathways responsible for a compensatory shift from fat to acetate metabolism, with a focus on additional aspects of hepatic beta-oxidation, will be required to fully elucidate the mechanisms of LITA nanoparticle action.

LITA treatment induced a significant change in total body fat, as measured by MRS. Kondo et al., has previously reported a similar decrease in total fat mass as a result of acetate administration [240]. However, using dissections to look at different fat depots, a significant decrease was only observed in epididymal and retroperitoneal fat, with subcutaneous fat depot showing a trend to decrease, while the mesenteric fat depot showed no difference. The reason for this discrepancy is unclear, but it may be related to the fact that with *in vivo* MRS all fat can be detected, which cannot be done regularly with MRI or by dissection. The localised effect of LITA on epididymal and retroperitoneal fat depots is unclear. The *in vivo* distribution profile of the LITA nanoparticle, as assessed by PET, showed no difference in uptake between fat depots, suggesting that other factors, including metabolic susceptibility to

acetate may play a role. For example adipose tissue lipase, the enzyme associated lipid breakdown [241] , showed a slight increase in the LITA treated group when compared to the control group although it did not reach significance. Differential effects on this and other process by acetate may lead to differences in fat content in different fat depots.

Size and number of adipocytes are known to be directly associated with adipose tissue metabolism, so epididymal and subcutaneous adipocytes were isolated and measured. These depots were chosen as they were differentially affected by LITA. The total mean number of adipocytes in the subcutaneous and in the epididymal fat depot showed no significant difference between groups. The total cell number of cells per gram showed no difference between groups in the subcutaneous fat depot however there was a slight but not significant decrease in epididymal fat depot. The decrease in the epididymal fat cell number per gram of tissue was consistent with the decrease in weight reported during after dissections. There was no significant difference in surface area or cell volume between groups in the epididymal and subcutaneous adipocytes. This suggests that any effect of LITA on these fat depots may be related to lipid oxidation and deposition rather than changes in cell number [242, 243].

Chronic LITA administration significantly reduced IHCL. This was confirmed by a decrease in liver weight and size. An increased IHCL level is associated with an increase in overall mass of this organ [244]. These changes occurred independently of the potentially confounding effects of a reduced food intake or body weight changes. Importantly, more than merely slowing accumulation, LITA delivery actively reduced IHCL. Hepatic lipid accumulation represents a key intermediary in a succession of increasingly debilitating liver conditions and is strongly associated with the development of insulin resistance and diabetes [245, 246]. The mechanism by which the effects of LITA on IHCL take place are unclear but may include

increases in beta-oxidation and/or decrease TG uptake from the circulation. Indeed, LITA treatment leads to a decrease in circulating FFA and triglycerides. These findings are consistent with previous studies showing a fall in FFA and triglyceride circulating levels following chronic acetate administration [125, 170]. The reduced levels of FFA and triglycerides indicate that liver function is being directly targeted by the LITA and not just the adipose tissue. Decreased circulating FFA is consistent with other models examining the effect of acetate, including those in which animals were fed fermentable carbohydrates. Fernandes J., et al recently reported that administered acetate results in a reduction in plasma FFA concentrations [247]. Yamashita et al., has also shown a reduction in plasma lipids following chronic acetate administration [170]. These changes were attributed to the protective behaviour of acetate, causing an inhibition from accumulation of lipids in the liver. Thus LITA-induced reduction in IHCL suggests our nanoparticle therapy is not only capable of preventing NAFLD, but may also modulate subsequent progression to HCC [246, 248, 249].

Leptin, a sensor of energy storage and regulator of appetite and metabolism at the level of the brain, was significantly decreased in the LITA group when compared to the control. Circulation levels of leptin have been reported to directly correlate with body fat, which would be consistent with the changes in body fat in the LITA group [250]. Glucose is an important regulator of leptin in humans and rodents [251, 252], which had no difference between groups, thus glucose does not appear to be the catalyst for the decrease in circulating leptin levels. A slight increase was observed in circulating adiponectin levels. Adiponectin is produced mainly from internal body fat depots and is involved with multiple metabolic processes such as regulation of glucose and fatty acid oxidation [253]. Adiponectin levels

have been shown to have an inverse correlation with body fat, which again correlates with the effects of LITA on this organ

Cytokine balance within the immune system has been correlated with obesity in humans and animals [254]. Examination of inflammation markers in the plasma showed a significant decrease in KC/GRO in the LITA treated group when compared to the control group. KC/GRO (chemokine gro-alpha/ growth-related protein) plays an essential role in the phagocytosis and removal of pathogens entering the liver via the portal-venous blood [255, 256]. KC has a direct hepatotoxic effect and regulating liver inflammation, which would indicate a decrease in toxicity in the livers of LITA treated mice [257]. As expected from a decrease in KC/GRO, levels of TNF-α and IFN-γ in the LITA treated group were not increased, confirming a decreased state of proinflammatory mediators [256]. TNF-α was one inflammatory factor of interested, as it increase the risk of cancers including breast and colon [258, 259]. However, there were some other inflammatory markers that were non-significantly increased from the interleukin family, specifically IL-4 and IL-10. IL-4, a prominent cytokine released during activation of B-cells [260] and lipoprotein receptor pathways [261]. IL-10, an anti-inflammatory cytokine produced by several cell types within multiple organs, is an important factor in counteracting inflammatory responses. An increase in IL-10 indicates an attempt to inhibit continued proinflammatory cytokine production [262, 263]. The slight increases in inflammatory markers is thought to be attributed to the obese state of the mice and believe that if the LITA administrations continued, the inflammation would decrease as the obese state decreased.

In order to investigate identify potential target genes and/or metabolic pathway as a result of LITA administration, a microarray analysis of liver tissue was carried out. For quality control purposes, a M vs. A plots [264] was carried out to view ratios of fluorescence intensities at

the same time. This analysis of the samples is meant to identify spot artefacts and detect intensity dependent patters in the log ratios before and after quantitative normalisation. Once outliers were removed the quantitative analysis programme of LIMMA was conducted revealing a handful of genes affected by LITA treatment, including genes associated with detoxification and heat-activated protein and genes whose metabolic functions have not been fully identified. The results of the microarray unfortunately did not shed light on one specific pathway. This may arise from the fact that acetate may metabolise very fast having rather small effect on gene activity levels. Alternatively, the number of samples used is this part of the *in vivo* study was rather limited, thus 'biological noise' masking any true change. Indeed, cell work with SCFA has shown an extensive number of genes being altered by acetate, which I could not reproduce in my study. I therefore carried out qPCR to examine genes of interest associated with lipid metabolism.

To investigate the phenotypic changes at the genetic level, a panel of select genes were investigated at the mRNA level. The present studies provide *in vivo* evidence that LITA administration decrease uncoupling protein 2 (UCP-2) mRNA expression in hepatocytes. Similar effects have been reported previously; the groups conducting the research found that acetate administration resulted in a decrease in UCP-2 [125]. Elevated UCP-2 expression has been previously reported as an adaption to the obese state, wherein mitochondria exhibit an increased rate of proton leakage which disrupts the membrane potential and decreases efficiency [265]. The mitochondria are an important component of the metabolic landscape due to the adaptive response of oxidation that takes place in hepatic cells [266]. Previous studies have shown an increase in UCP-2 expression during obesity due to the overly abundant cellular energy supply exceeding hepatocytes requirements [267].

Surprisingly no change in mRNA expression was seen in the peroxisome proliferator-activated receptor alpha (PPARα), a transcription receptor which plays a critical role in the control of obesity-induced chronic inflammatory response and regulator of lipid metabolism in the liver [267, 268] . Targets genes of PPARα, including peroxisomal acyl-coenzyme A oxidase 1 (ACOX1), Carnitine palmitoyltransferase 1 (CPT1) and Acetyl-CoA carboxylase (ACC) were investigated. CPT1A, a mitochondrial enzyme associated with the transport of long-chain fatty acids across the mitochondrial membrane, had a non-significant decrease in mRNA expression. ACC, an enzyme important in the regulation of fatty acid metabolism, showed a decrease in mRNA expression however did not reach significance [269]. It has been shown that an increase in acetyl-CoA can reduce glycolysis and net hepatic glycogen breakdown. One study which supports these findings, reported that rats fed a cholesterol rich diet supplemented with acetic acid also had reduced concentrations of in ACC [270]. ACC and CPT1A are two of the three main enzymes that regulate the synthesis of malonyl-CoA, which is the principal inhibitor of fatty-acid entry into the mitochondria for β-oxidation. This decrease of activity indicates the potential of decreased lipid uptake into the mitochondria and therefore decreasing the rate of β-oxidation. However, ACOX1 which plays a key role in the fatty acid β-oxidation pathway was shown to increase following LITA treatment. An increase in ACOX1 expression is associated with increased oxidation and lean body phenotype. These effect contrasts with those observed with ACC and CPT1A which would reduce lipid oxidation. Clearly more work is required to unravel the underlying mechanism by which LITA decreases IHCL observed in my study.

In parallel to the above experiment, I looked at the potential effects of LITA HDACs protein modification. Butyrate, another of the SCFA produced in the colon is a well-known HDAC inhibitor (HDAC) [271, 272]. Moreover, suppression of HDAC (class 2) has been shown in murine models of obesity [273, 274]. Thus, I examined HDAC protein level and activity by acetate. Inhibition HDAC expression is carried out by the removal the acetyl group from

protein substrate, such as histone proteins [165, 275]. Previous studies have suggested that acetate contributed minimally to HDAC inhibition [276, 277]. Indeed, I observed a significant inhibition in HDAC 7 and trending inhibition in HDAC 1. I also observed an increase in expression of the HDAC proteins 2, 3 and 5. The trending decrease in HDAC 1 protein is consistent with the decreased mRNA level, confirming HDAC 1 is affected by LITA administration. These changes were accompanied by a hypoacetylation of the liver histone H4K12. This raises an important question about the epigenetic mechanism by which acetate may work as an epigenetic modulator. For example butyrate regulates histone acetylation and contributes of the Warburg effect as a by-product of the acetyl-CoA/HAT mechanism [278]. This involves the metabolism of butyrate to acetyl-CoA, which in turn stimulates HAT activity by functioning as a HAT cofactor and acetyl-group donor, representing an additional cascade of regulatory elements [160]. This mechanism of HDAC inhibition is more prevalent because studies are now looking into lower doses of butyrate-induces histone acetylation, whereas the HDACi is only a by-product rather than a direct effect of acetate arising from butyrate. In the case of acetate arising from LITA, it does not require the metabolic process seen with butyrate, thus it is likely that acetate is directly shuttle into mitochondria avoiding accumulation in the cytoplasm. Much more work is required to clearly define the downstream effectors of epigenetic modification. Figure 3.30 shows a global view of LITA administration and how HDACs are potentially modified by the introduction of acetate. Interestingly, it important to mention that 5mM dose of butyrate *in vitro* is physiologically relevant because it is routinely found at this concentration in the lumen of the colon [115], thus the administration of a similar dose via nanoparticle delivery would have the potential for nuclear access and for manipulating metabolic pathways epigenetically. I must also point out that the production of butyrate-containing liposome is not as straight forward as LITA and further work is required to obtain stable nanoparticles with longer SCFAs.

Increasing fatty acid availability, as observed in this model by the lack of accumulation in the liver, results in the upregulation of fatty acid oxidation while concomitantly reducing endogenenous rates of fatty acid oxidation and glucose metabolism, consistent with the Randle hypothesis [156, 279]. However, an unresolved question remains how increased extracellular fatty acid availability could lead to this “feed-forward” activation of fatty acid metabolism. One mechanism to explain the effects of acetate is adenosine monophosphate-activated protein kinase (AMPK), a crucial sensor of cellular energy status, in particular fatty acid circulating levels alike AMP, resulting in allosteric activation leading to the phosphorylation and activation by an increase in the AMP/ATP ratio [280]. This multi-substrate enzyme is considered to be a cell’s “low fuel warning system” since it is activated by the low concentrations of ATP (Figure 3.29) [281, 282].

Sakakibara et al. reported activation of AMPK and reduced hyperglycemia after feeding acetic acid to obsess mice [283, 284]. Additional studies have reported that in muscle cells the “feed-forward” activation of fatty acid oxidation by fatty acids is completely dependent on AMPK signalling [285]. This suggests an important mechanism by which muscle responds to alterations in substrate availability, which could potentially identify the reason I saw an increase in muscle mass dissected from the chronic HFD model. AMPK is also responsible for gluconeogenesis via phosphorylation and nuclear exclusion of HDACs 4, 5 and 7 in the liver, which coincides with the significant inhibition in HDAC 7 I am reporting [273]. This may explain the increase in HDAC 3 I found, due to the heighted recruiting process that occurs during AMPK pathway activation in the liver.

Acetyl-CoA leads to an increased formation of AMP, which increases the AMP/ATP ratio and causes the phosphorylation of AMPK [170]. AMPK induces transcription of PPARα gene, which was slightly increased in expression level when compared to the control group PPARα

has downstream effects on two upregulating fatty acid oxidation enzymes examined, CPT-1A, and UCP-2 [286]. Activation of AMPK has also been shown to suppress the activity of lipogenic enzymes, including the transcription of ACC, which is consistent in these findings [287]. Other lipogenic enzymes to investigate in my future work will consist of sterol regulatory element binding protein (SREBP-1) and downstream of SERBP-1 fatty acid synthase (FAS) [288]. However, acetate affects may go beyond direct regulation of metabolic signalling.

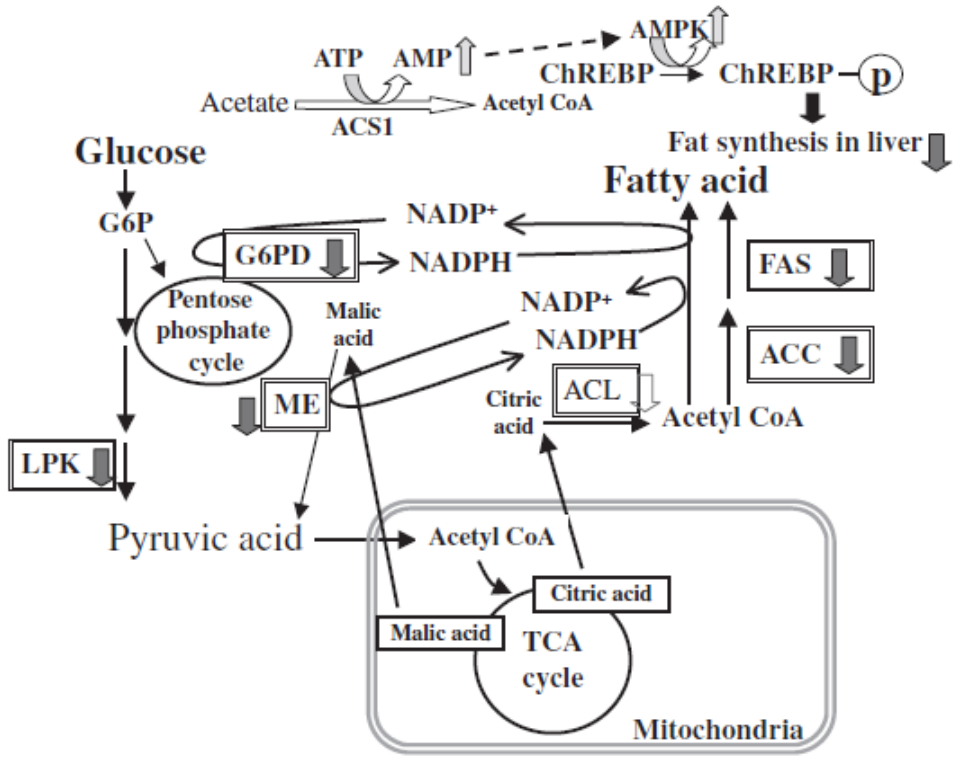


Figure 3.29 Proposed mechanisms on fatty acid synthesis following hepatic delivery

A proposed mechanism of effect of acetate on fatty acid synthesis in liver is shown in the figure. Acetate through activation of AMPK, inhibits fat synthesis in the liver. Fatty acids are synthesized from excess glucose in the liver. Glucose is turned into pyruvic acid which goes into TCA cycle. Once citrate is formed it generates cytosolic acetyl-CoA and malonyl-CoA which then forms fatty acids. Figure from Yamashita et al., 2007.

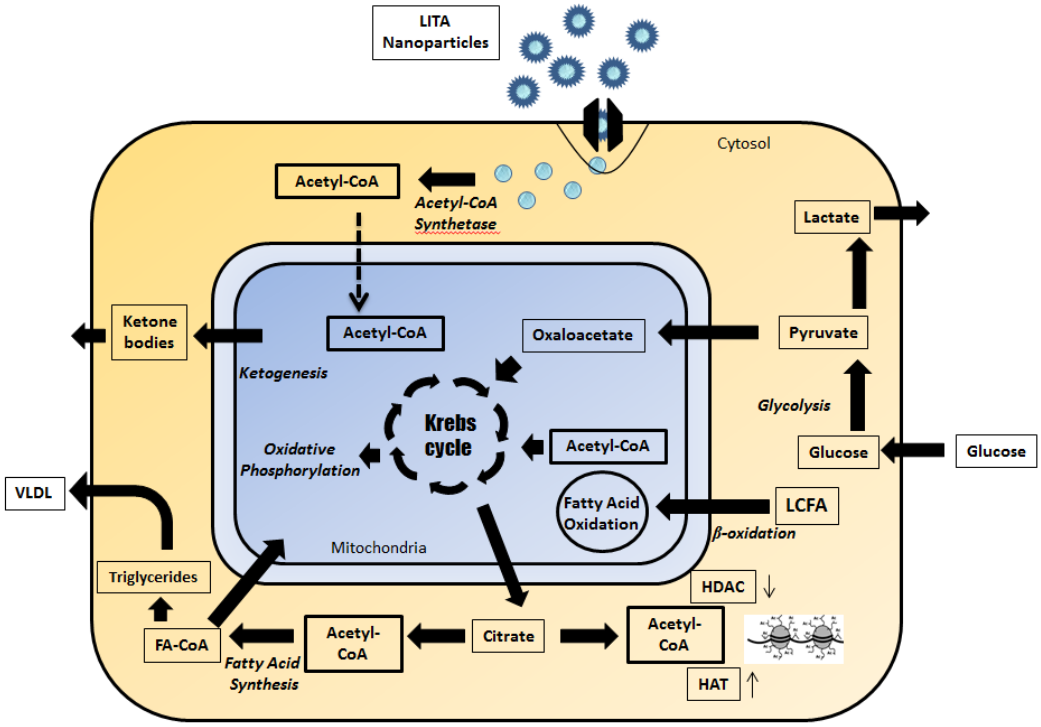


Figure 3.30 Proposed mechanism of global LITA activity following hepatic delivery

The effects of LITA nanoparticles (●) on key cellular pathways in the cytoplasm and mitochondria of a hepatocyte are shown. LITA nanoparticle administration leads to cellular uptake of acetate (blue circles) followed by mitochondrial accumulation of acetyl-CoA. Acetyl-CoA then enters the TCA, or Krebs Cycle, to yield citrate. Citrate, an intermediate in the TCA cycle, is then transported out of the mitochondria via the citrate shuttle and converted to acetyl-CoA. Acetyl-CoA in the cytosol has the availability for lipid biosynthesis. Acetyl-CoA is also transported into the nucleus and regulates histone acetylation. This model also includes glucose-induced signal transduction that upregulates acetyl-CoA activity (via phosphorylation of the enzyme conversion of acetyl-CoA and citrate) which makes it susceptible to being regulated by the Warburg effect. Black coloured arrows indicate the up-regulation effects of LITA delivery. LCFA: Long chain fatty acids; VLDL: very low density lipoprotein.

3.4.4 Conclusion

The present work looking at the reparative effects of a HFD with LITA nanoparticle has shown to have an improved state of the liver and the overall metabolic profile *in vivo*.

In both sets of experiments, chronic injections of liposomes did not seem to cause any side effects and overall animal behaviour appeared normal. Overall, LITA administration resulted in a comprehensive improvement in metabolic profile in animal models of obesity; including amelioration of a wide range of metabolic syndrome associated outcomes, including reductions in IHCL, body fat, serum insulin, FFA and inflammatory tone. More work will be required to fully elucidate the numerous, interconnected metabolic pathways underpinning these effects. However, these results present LITA administration as a promising therapy for the positive modulation of obesity transformation *in vivo*.

In conclusion, my results support a mechanism by which the LITA-induced mitochondrial accumulation of acetyl-CoA, the end-product of SCFA catabolism, caused changes that are consistent with the Randle hypothesis; whereby the availability of acetate as a fuel source generates metabolic signals that impair the use of glucose through inhibition of glycolytic and gluconeogenic pathways [289]. This shift in substrate oxidation reduced lipid uptake, lipogenesis and hepatic glucose uptake, whilst observing no net change in energy balance [290]. Further work is required to unravel the full metabolic effects that transpired during LITA treatment of metabolic dysfunction.

Together, these results support a mechanism by which the LITA-induced mitochondrial accumulation of acetyl-CoA, the end-product of SCFA catabolism, inhibits β-oxidation and subsequently reduce lipid uptake, lipogenesis and hepatic uptake. Furthermore, the changes observed are consistent with the Randle hypothesis; whereby the availability of acetate as a fuel source generates metabolic signals that impair the use of glucose through inhibition of glycolytic and gluconeogenic pathways [289]. A shift away from carbohydrate metabolism might be expected to result in altered respiratory outcomes in LITA-injected animals yet observed no differences following metabolic cage analysis. However, these results are in accord with several papers that demonstrate energy expenditure is maintained following acetate infusion, as acetate replaces fat as an oxidative fuel [237, 239].

Chapter 4

In Vivo Biological Evaluation of LITA-xenograft in Tumour Models

4.1 Introduction

As discussed in Chapter 1, impaired cellular energy metabolism is a defining characteristic of a number of diseases, including cancer. Supplementation with dietary fibre, or by-products of its subsequent colonic breakdown, such as acetate, propionate and butyrate has been shown to ameliorate features of the metabolic syndrome and attenuate malignant growth in certain cancers [159, 160, 230, 231, 291, 292]. Acetate plays a central role in cellular metabolism, functioning as a key intermediate in the synthesis of fatty acids and cholesterol in the liver. Furthermore, oxidation of acetate derived from carbohydrates, fats and proteins is the initial step in the tricarboxylic acid (TCA) cycle, a fundamental energy producing pathway in all aerobic organisms [293]. Oxidative phosphorylation generates the majority of energy required for cellular function in normal differentiated cells. In contrast, cancer cells rely primarily on aerobic glycolysis**,** a metabolic shift termed the Warburgh effect that comprises attenuation of energy production via mitochondrial beta-oxidation [152]. **I**n malignant cells the inhibition of glucose uptake and metabolism by products of SCFA breakdown is thought to preferentially inhibit aerobic glycolysis and supress the uncontrolled cellular proliferation [162, 294].

In Chapters 2 and 3, I demonstrated that LITA nanoparticles are a viable vector for the non-targeted delivery of SCFAs to key sites of metabolic control. Liposome based therapeutics have found their way to the clinic over the last few decades as drug delivery systems in cancer therapy. In this chapter, colorectal cancer (CRC) was examined based on previous studies which had a similar metabolic approach of SCFA [295] or acetate isoforms as a CRC therapeutic.

4.1.1 Aims of Studies

To optimise and measure LITA-xenograft nanoparticle uptake in an *in vivo* colorectal cancer model. Nanoparticle formulation requires the appropriate ratio of lipids to allow for prolonged circulation and tumour accessibility, and a reliable method for detectability post-delivery. This will develop a delivery system of acetate with the capacity to tailor the design of the nanoparticle to reach the xenograft tumour.

To evaluate therapeutic effects of LITA-xenograft nanoparticles in colorectal cancer xenograft models *in vivo*. I will examine the effects of LITA-xenograft nanoparticles on tumour growth in three different colorectal cancer cell lines. Longitudinal phenotypic changes will be monitoring at a two-fold level, using a standardly used calliper and the activity of the tumour by bioluminescent optical imaging. Downstream molecular investigations will also be examined for mechanistic changes to mirror any phenotypic changes and determination of pathways involved for any growth changes, specifically the Warburg effect and deacetylation changes.

4.2 Methods

4.2.1 Materials

4.2.1.1 Animals

Male Bulb-c nude/nude mice (SPF, Harlan, UK) were housed in IVC cages under the same controlled conditions of temperature and light as above. Diet and water was autoclaved (RMI diet, Special diet Services, Ltd, Essex, UK) with *ad libitum* access. All experiments were carried out in compliance with Animals (Scientific Procedure) Act 1986 under the project licence 70/6656.

4.2.1.2 *In vivo* cancer cell lines

Three different cancer cell lines were investigated to explore the therapeutic potential of the LITA nanoparticle. A xenograft model of three varying colorectal cancer cell line models were independently carried out *in vivo* with the specified nanoparticle formulation that was specific to tumour delivery. Three different CRC cell lines were used in this study with different metabolic profiles: HT-29 with a mutated state of p53, HCT 116 with p53 (+/+) and HCT 116 without p53 (-/-).

4.2.2 *Study 1: Liposome Preparation, Formulation and Characterisation for Xenograft Model Application*

4.2.2.1 LITA-xenograft preparation and formulation

Liposomes were formulated with a defined molar ratio of individual lipids based on the desired *in vivo* application of delivery to the xenograft tumour *in vivo*. Liposomes were prepared as described in 2.2.2 and 2.2.3 for anticipation of xenograft delivery, therefore used formulation LITA-xenograft. To achieve the 'stealth' state introduced earlier, the LITA-xenograft was formulated with a higher percentage molarity of 5% DSPE-PEG^{2000} (Table 2.2), rather than the LITA molarity of 1% DSPE-PEG^{2000}, to increase circulation time of the particle allocating passive localization within the solid tumour. As shown in the Table 2.2, 4% decrease in cholesterol was used in the LITA-xenograft formulation to compensate for the increase in DSPE-PEG^{2000}. For *in vivo* histological analysis, (E) LITA-Rhd-xenograft was used for 1% of rhodamine incorporation and 30% cholesterol.

4.2.2.1 Liposome tumour specificity and characterisation

Xenograft delivery on small animal models of cancer has been made possible through specific formulations tailored to the angiogenic environment of a solid tumour. To determine delivery of the nanoparticle to the xenograft tumour, *ex vivo* bio-distribution studies were executed using histological studies. Similarly described in 2.2.5.1.1, the LITA-Rhd-xenograft formulation was examined for delivery after a single 200μL injection intraperitoneally (i.p.) to bulb-c nude/nude mice which had established xenograft tumours from HT-29 cells (n=4).

4.2.2 *Study 2: LITA effects in a Colorectal Cancer Xenograft Model*

4.2.2.1 Cellular

The desired cells line was seeded at $2.5x10^5$ cells per T-25 flask (Nunc, USA) and grown as a monolayer in Dulbecco's Modified Eagle Medium (DMEM) (Sigma-Aldrich, UK), supplemented with 10% fetal calf serum (FCS) (Sigma-Aldrich, UK) in an incubator at 37°C with 5% CO_2. Cells were maintained every 3-5 days while never exceeding 15 passages. Once the cells were approximately 80% confluent, the media was removed, they were harvested by removal of the media, washing with PBS, and followed by the addition of trypsin (Sigma-Aldrich, UK) for approximately 5 minutes. The media was removed and cells were washed with PBS three times and re-suspended in serum-free DMEM and centrifuged at 1,000 RPM for 5 minutes. The media was removed and cells were counted on a haemocytometer.

4.2.2.2 Luciferase-stable CRC cell lines HCTp53+/+ and HCTp53-/-

HCT 116 wild-type p53 (HCT 116 p53+/+) and HCT 116 isogenic knocked-down p53 (HCT 116 P53-/-) were maintained at 37°C in Dulbecco's modified Eagle's medium (Sigma-Aldrich, USA) supplemented with 10% fetal bovine serum (FBS; Sigma), 1% L-glutamine, 1% and penicillin/streptomycin in the presence of 5% CO_2. For generating luciferase-stable clones from HCT 116 p53+/+ and HCT 116 p53-/-, each cell line was cultured in a 10 cm dish until the cells reach 60-70% confluency. The transfection was carried out with Polyethylenimine (PEI) polymers mixed with the pGL4.20 [luc2/Puro] Vector from Promega in ratio 4:1, and the mixture was completed to 200 µL with Opti-MEM media. Then the mixture was dropped over the cells covered with the minimum amount of Dulbecco's modified Eagle's medium. Two days after the transfection, the stable clones from each cell line (HCT 116 p53+/+ and HCT 116 p53-/-) were selected in Puromycin for two weeks. To

confirm the success of our stable clones and to check the luciferase expression levels, Steady-Glo® Luciferase Assay System (Promega, USA) was used. Cells were finally resuspended at $1x10^7$ cells per mL of serum-free DMEM for injections into the mice.

4.2.2.3 *In Vivo* tumour model development

Tumourigenicity was achieved by preparing cells as described in 4.2.2.1 and injecting into balb/c nude mice subcutaneously into the right flank with $5x10^6$ cells in 100µl of serum-free media, using a 25 gauge needle. Mice were divided into groups bearing tumours from three cell lines of the colon cancer origin: Group 1 (n=6/group) consisted of mice bearing tumours from HT-29; Group 2 (n=6/group) consisted of mice bearing tumours from HCT 116+/+; Group 3 (n=6/group) consisted of mice bearing tumours from HCT 116-/-. At the initial identification of the xenograft tumour, a baseline measurement was obtained using the two growth assessment techniques, described in 4.2.2.4. After baseline measurements, mice were stratified into 2 groups. In the first group, mice will be treated with the control HEPES liposome. The second group will be treated with the LITA-xenograft nanoparticles in parallel. For the duration of the study, injections were administered three times a week i.p. of 200 µl per injection. Xenograft tumour growth was monitored on a weekly basis by two different methods, the calliper and IVIS Spectrum.

4.2.2.4 Tumour growth assessment by size and by bioluminescent imaging luciferase

For an in-depth assessment of tumour growth and development, a multi-mode approach was employed by using both bioluminescence imaging and by calliper. Tumour volume was measured by calliper assuming an ellipsoid shape using the following equation:

$$\text{Volume} = \text{length} \times \text{width} \times \text{depth} \times \pi/6$$

Equation 4.1 Volume equation used to measure tumour from calliper

For visualization by luminescence, the Xenogen IVIS 2000 small-animal *in vivo* imaging system (Xenogen Corp., USA) was used. Briefly, an IVIS 200 cooled CCD camera system was used for emitted light acquisition and Living Image software (Xenogen Corp., USA) for data analysis as an overlay on IGOR software (Wavemetrics Corporation, USA). Animals received a 100uL intraperitoneal injection of D-luciferin (Gold Biotechnology, USA.) at a concentration of 15 mg/mL under 1-2% inhaled isoflurane anaesthesia. An average of 10 kinetic bioluminescent acquisitions will be collected between 0 and 30 minutes after substrate injection to confirm a peak photon emission recorded as maximum photon efflux per second. Data analyses and background correction was be carried out by using total photon flux emission (photons/s) in an ROI covering the entire xenograft tumour region.

4.2.2.5 Xenograft mouse tumour tissues processing

At the end of the study, animals were sacrificed and the tumours were carefully excised, making sure that the samples did not contain any surrounding normal tissue. Tumours were weighed and portioned to either formalin solution (Sigma-Aldrich, UK) for histological evaluation or snap frozen in liquid nitrogen and stored at -80°C for subsequent extraction of mRNA. Homogenisation of the tissue was performed as described in 3.2.3.7 and mRNA levels were measured as described in 3.3.1.8.

4.2.2.6 Statistical analysis

All statistical analyses were performed using GraphPad Prism (San Diego, CA), unless otherwise noted. Data are presented as means ± standard deviation (SD) or standard error mean (SEM). Statistical significance was calculated with Student's t test, two-way ANOVA with Bonferroni post-hoc test for multiple comparisons. Significance was accepted at the level of * = $p<0.05$, ** = $p< 0.01$, *** = $p<0.001$.

4.3 Results

4.3.1 Study 1: Liposome Preparation, Formulation and Characterisation for Xenograft Model Application

Liposomes formulated in Chapter 2 were applied for an *in vivo* passive targeting system with 4mM of acetate loaded within the aqueous core of the vesicle. Preliminary biodistribution studies confirmed the acetate encapsulated liposomes does reach the circulatory system intact and does have multiple effects on the metabolism of an obesogenic state. Moving forward, the question turned to altering the metabolism of cancer *in vivo*. In order for a liposome to reach a xenograft tumour, a longer circulation time of the LITA-xenograft was required than the original LITA nanoparticle. These formulation changes were achieved by increasing the molarity of the DSPE-PEG^{2000} lipid from the 1% in the LITA formulation to 5%.

4.3.1.1 Liposome preparation and formulation

Liposomes were formulated with a defined molar ratio of individual lipids based on the desired *in vivo* application (Table 2.1 D-E). LITA-xenograft: liposomes contain 5% DSPE-PEG^{2000} for increased *in vivo* circulation; DSPC: 1,2-distearoyl-sn-glycero-3-phosphocholine; CDAN: N1-cholesteryloxycarbonyl-3,7-diazanonane-1,9-diamine; DSPE-PEG^{2000}: 1,2-distearoyl-sn-glycero-3-phosphoethanolamine-N-methoxy (polyethylene glycol)-2000; DOPE – Rhodamine B:1,2-dioleoyl-sn-glycero-3-phosphoethanolamine-N- (lissamine rhodamine B sulfonyl). LITA-Rhd-xenograft: liposome contains 1% less cholesterol in order to allow for Rhd incorporation for histological analysis targeted to the xenograft.

4.3.1.2 Liposome sizing and stability confirmation

Confirmation of the size of the formulated liposomes was determined by using a Zetasizer Nano (Malvern, UK). Size is expressed in nanometers (nm) and the difference in size within

the liposome solution is expressed as the poly distribution index (PDI). Figure 4.1 A-B shows the reproducibility of liposome in batch-to-bath formulations was evaluated, the LITA nanoparticles typically formulated slightly larger in size though there was no statically significant difference between groups (control: 100.7 ± 2.071, n=10; LITA-xenograft: 108.2 ± 3.338, n=10; p=0.0740). The single peak in each graph represents the size distribution of a single reading of the liposomes from the Zetasizer. In the example used here, the PDI of HEPES was 0.892 (Figure 4.1 C) and the PDI of LITA-xenograft was 0.591 (Figure 4.1 D).

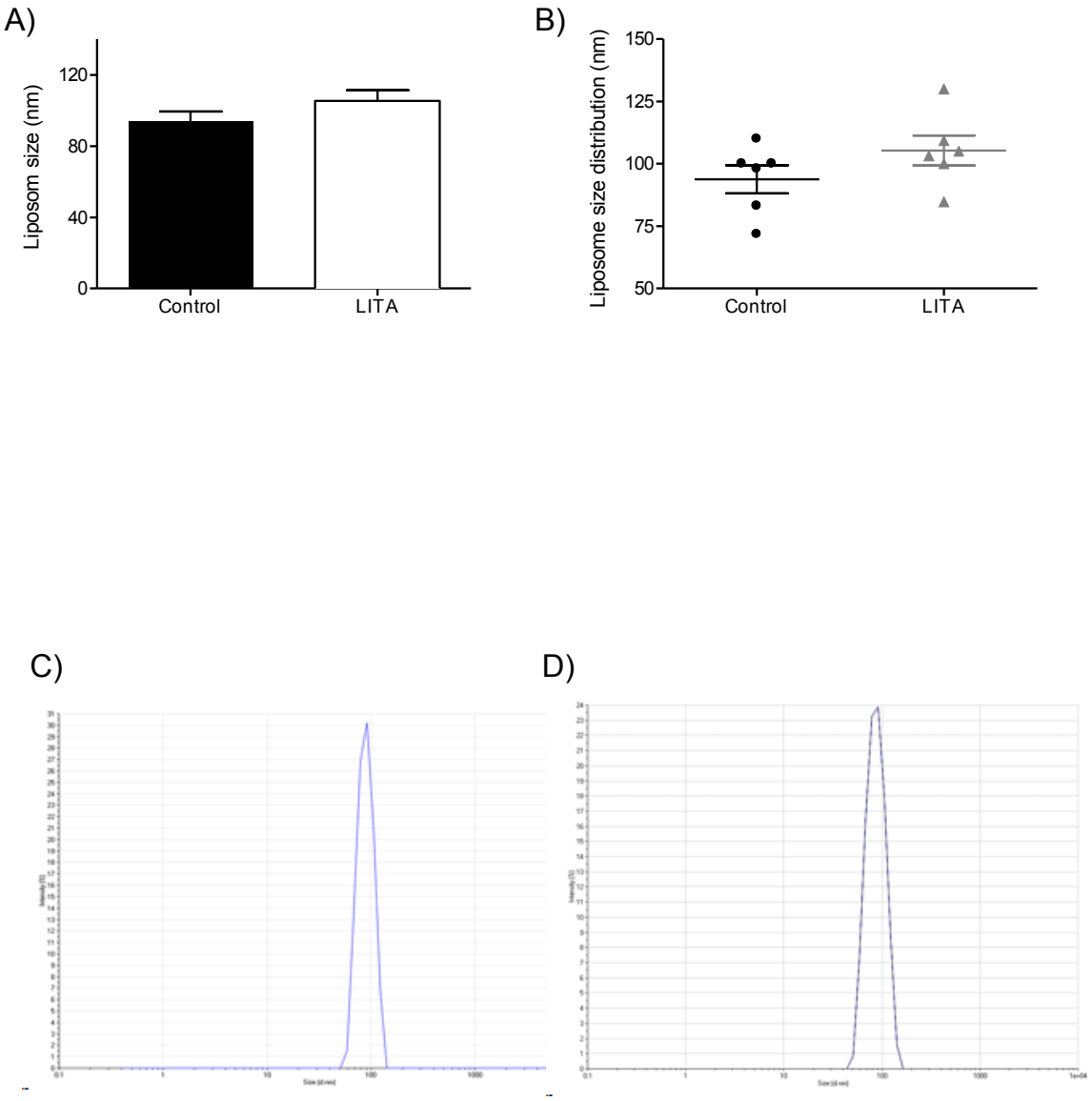


Figure 4.1 Liposomal nanoparticle sizing method after completed formulation

The **(A)** formulated liposome size, data shown as mean ± SEM and **(B)** size distribution between groups showed no statistical significance between groups or batch-to-batch formulation (n=10/group). **(C)** Sizing peaks of control (containing HEPES) and **(D)** LITA-xenograft respectively. The x-axis represents the size (nm) of the nanoparticle and the y-axis represents the number (%) of liposomes.

4.3.1.2.1 Liposomal tumour specificity using fluorescence microscopy imaging *ex vivo*

Once sizing and stability of the LITA-xenograft was concurrent with the original LITA formulation, biodistribution was tested. The specific cell line used for this study was HT-29. For *in vivo* detection of xenograft tumour delivery, LITA-Rhd-xenograft was formulated with 5% DSPC-PEG^{2000} encapsulated with 1M acetate and 200μL was administered i.p. Bio-distribution of LITA-Rhd-xenograft was assessed by histological investigation using fluorescence microscopy to visually identify the bi-layer incorporated lipid, rhodamine (Rhd). Figure 4.2 shows the xenograft tumour extracted and observed 2 hours post injection. The red in Figure 4.2 C confirms presence of LITA-Rhd-xenograft within the tumour tissue.

A control filter was first used to confirm there was no artefact that would generate a false positive identification of the LITA-Rhd-xenograft (Figure 4.2 A). A nuclear stain (DAPI) was then allied to the microscope slide to ensure the region being observed was in fast tissue (Figure 4.2 B). A rhodamine-specific filter was used to observe the same slide for LITA-Rhd-xenograft visualisation and confirmation of delivery to the tissue of interest (Figure 4.2 C). Red in images represents the fluorescent rhodamine embedded into the liposome membrane.

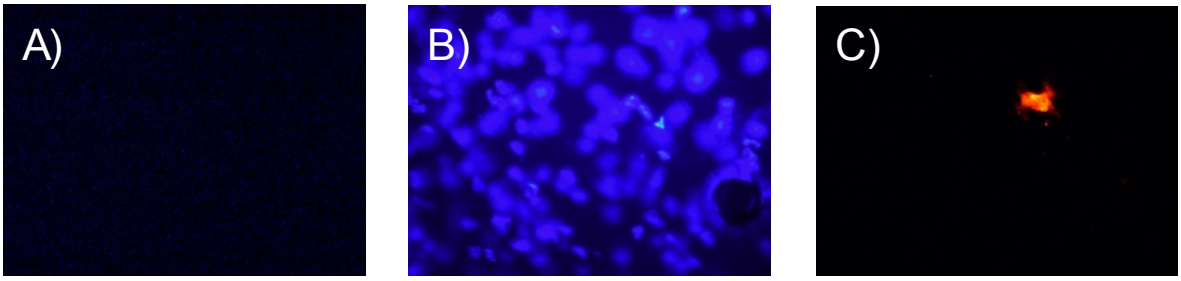


Figure 4.2 LITA-Rhd-xenograft nanoparticle tumour localisation LITA-Rhd-xenograft identification in the xenograft tumour by histological fluorescence imaging

Images obtained from xenograft tumour 2 hours post LITA-Rhd-xenograft i.p. administration (**A**) control, (**B**) nuclear stain (DAPI), (**C**) rhodamine-specific filter visualisation. Red in images represents the fluorescent rhodamine embedded into the liposome membrane.

4.3.2 *Study 2: LITA-xenograft effects in a Colorectal Cancer Xenograft Models*

4.3.2.1 HT-29 colorectal cancer cell line tumour model

The HT-29 colorectal cancer cell line was used for the xenograft inoculation, of which tumour take up rate was 50% and tumours appeared within the expected time of 14 days. Time 0 references when the tumour was palpable and large enough to measure by calliper, at which point injections of either control or LITA-xenograft nanoparticles were administered. The chronic administration of LITA-xenograft nanoparticles led to a significant reduction in growth as measured by calliper at the end of the 4 week study (LITA-xenograft: 98.20 ± 25.34mm^3, Control: 107.2 ± 46.71 mm^3, p=0.490) (Figure 4.3 A). During the first 2 weeks, tumour size between groups does not have much variability, however going into week 3 showed a rate of growth difference that reached significance over the 4 week period. Weekly growth values can be seen in Figure 4.3 B and quantitative values in Table 4.1.

At the end of the study, there was a reduction in the LITA group in size of the tumour weight (LITA-xenograft: 0.05 ± 0.03mg, Control: 0.33 ± 0.04mg, $p<0.01$) compared to controls (Figure 4.4 A). The image of a xenograft tumour extracted at the end of the study from each treatment group, the LITA and the control (Figure 4.4 B).

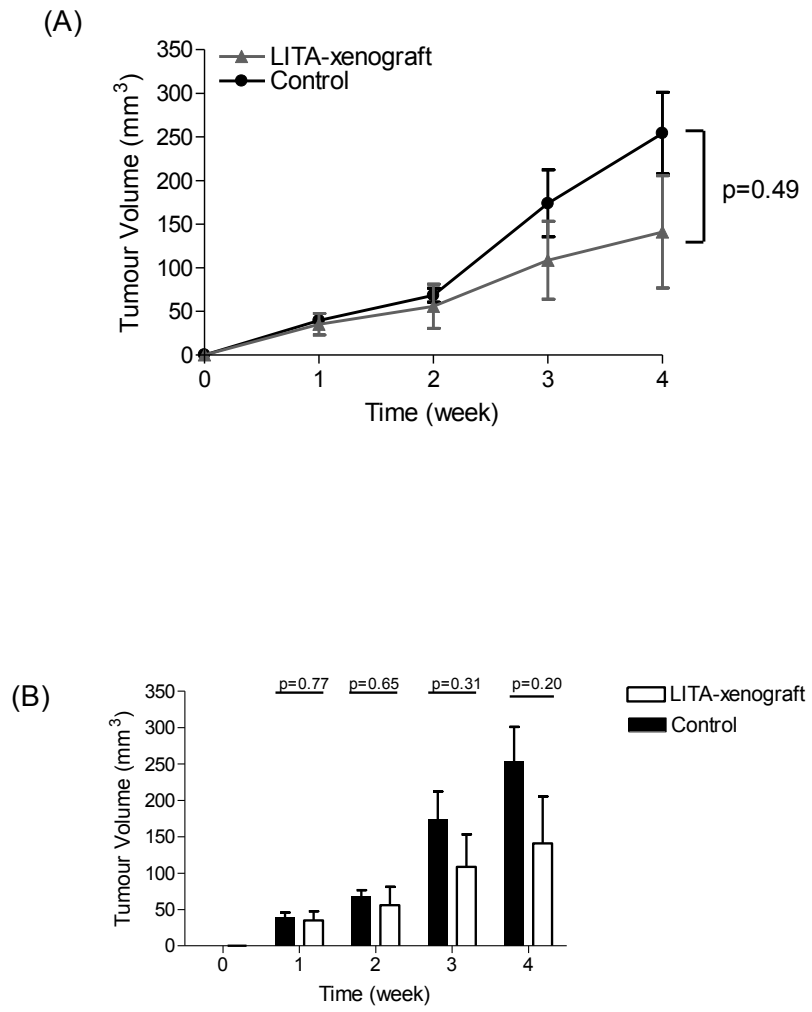


Figure 4.3 Effects of LITA-xenograft nanoparticles in murine HT-29 colorectal tumour growth

Mice were inoculated with HT-29 colorectal cancer cells and were injected every three days with either control or LITA-xenograft nanoparticles for 4 weeks, once tumour was confirmed palpable. Tumour volume was measured weekly using the standard calliper method. **(A)** Tumour growth over the 4 weeks had a significant decrease in growth in the LITA-xenograft treated group, with particular growth difference shown at week 4 **(B)**. Data is presented as mean ± SEM and analysed by two-sample *t* test with Wilcoxon test; n=6/group.

Week	Control (mean ± sem)	LITA-xenograft (mean ± sem)	p value
0	00.00 ± 00.00	00.00 ± 00.00	---
1	39.40 ± 6.467	32.83 ± 9.891	0.7777
2	68.46 ± 8.088	48.79 ± 20.82	0.6525
3	173.8 ± 38.27	254.2 ± 46.80	0.3103
4	108.9 ± 34.54	122.9 ± 53.09	0.2053

Table 4.1 Effects of LITA-xenograft nanoparticles in murine HT-29 colorectal tumour growth

Mice were inoculated with HT-29 colorectal cancer cells and were injected every three days with either control or LITA-xenograft nanoparticles for 4 weeks, once tumour was confirmed palpable. Tumour volume was measured weekly using the standard calliper method. Tumour growth over the 4 weeks had a significant decrease in growth in the LITA-xenograft treated group, with particular growth difference shown at week 4. Data is presented as mean ± SEM and analysed by two-sample *t* test with Wilcoxon test; n=6/group.

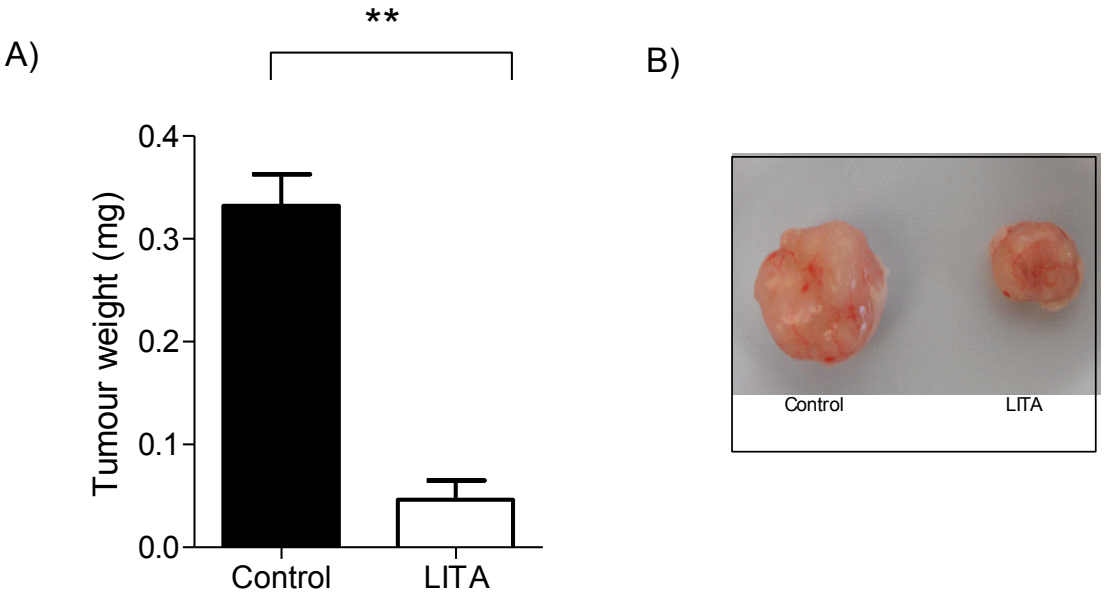


Figure 4.4 Effects of LITA nanoparticles in murine HT-29 colorectal tumours

Mice were inoculated with HT-29 colorectal cancer cells and were injected every three days with either control or LITA-xenograft nanoparticles for 4 weeks. (**A**) Tumour weight (mg) and (**B**) the represented in the tumour grafts from control on the left side and LITA on the right side. Data is presented as mean ± SEM and analysed by unpaired t-test (n=6/group); ** = $p<0.01$.

4.3.2.1.1 HT-29 Colorectal Cancer Cell Line Tumour Gene Expression Analysis

Quantitative RT-PCR was carried out on isolated mRNA from a HT-29 xenograft model, chronically treated with either control to LITA-xenograft nanoparticles for 4 weeks. Gene expression analysis revealed a significant decrease in Class I of the HDACs genes in LITA-xenograft injected animals when compared to the control group; HDAC 1 ($p<0.05$), HDAC 2 ($p<0.05$), HDAC 3 ($p<0.001$) and HDAC 4 ($p<0.01$). SiRT1 mRNA was also significantly reduced in LITA-xenograft injected animals ($p<0.05$) and SirT2 had an increase in expression though did not reach significance (Figure 4.5). All expression changes were compared to the control nanoparticles set to 1.0 and in relation to the housekeeper gene, GAPDH Data is also displayed in Table 4.2.

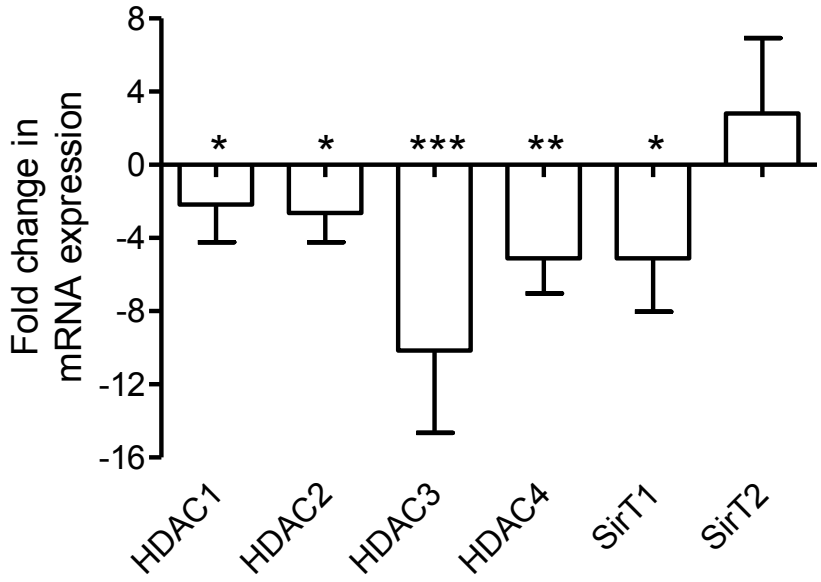


Figure 4.5 Effects of LITA-xenograft nanoparticles in murine HT-29 colorectal tumours at the end of the study

Mice were inoculated with HT-29 colorectal cancer cells and were injected every three days with either control or LITA-xenograft nanoparticles for 4 weeks. Quantitative mRNA changes in xenograft tumour after chronic LITA-xenograft administration normalized to control liposomes. A significant decrease in expression was observed in all HDACs in class I and SirT1, however SirT2 had a non-significant increase. All expression changes were compared to the control nanoparticles set to 1.0 and in relation to the housekeeper gene, GAPDH. Data is presented as mean ± SD analysed by Student's t-test (n=6/group); * = $p<0.05$, ** = $p<0.01$, *** = $p<0.001$.

	LITA (mean ± SD)	p value
HDAC 1	-2.178 ± 1.183	**p<0.05**
HDAC 2	-3.039 ± 1.319	**p<0.05**
HDAC 3	-8.117 ± 1.399	**p<0.001**
HDAC 4	-5.106 ± 1.930	**p<0.01**
SirT1	-5.100 ± 2.937	**p<0.05**
SirT2	1.106 ± 0.250	0.8305

Table 4.2 Summary of qRT-PCR analysis of gene expression fold changes in mRNA isolated from the tumour as a result of chronic LITA-xenograft treatment in HT-29 colorectal cancer xenograft model

Gene expression changes presented as mean ± SD at the end of a 4-week study of chronic LITA-xenograft or control nanoparticle administration in a CRC xenograft model. All gene expression changes were compared to the control nanoparticles set to 1.0 and in relation to the housekeeper gene, GAPDH; n=6/group. Data is analysed by unpaired t-test.

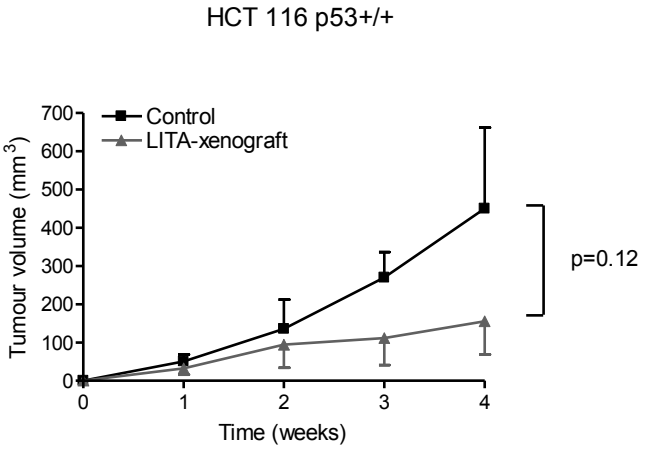
4.3.2.2 HCT 116 colorectal cancer cell line tumour model

To examine whether the results from the LITA-xenograft in the HT-29 xenograft model was a cell line specific response, the same model was established with another line of CRC, HCT 116. The difference between the two CRC lines is the active state of p53; in HT-29 the p53 is in a mutated form, whereas HCT 116 is functioning without mutation. In order to determine if p53 was a determining factor in a tumour growth patterns, a xenograft model was established with a p53 knockout HCT 116 cell line. Thus, first a normal functioning HCT 116 p53+/+ CRC cell line was used followed by a HCT 116 p53-/- using the same model and method as carried out before with HT-29.

4.3.2.2.1 HCT 116 p53+/+ colorectal cancer cell lines tumour model

The HCT 116 p53+/+ colorectal cancer cell line had less than a 50% take rate after inoculation and successfully xenotransplanted tumours appeared within the expected time of 14 days. Time 1 refers to when the tumour was palpable and large enough to measure by calliper, at which point injections of either control or LITA-xenograft nanoparticles were initiated. Figure 4.6 A-B shows the chronic administration of control or LITA-xenograft nanoparticles over the course of 4 weeks led to a trend reduction in tumour size however did not reach significance (control: 449.9 ± 211.8, LITA-xenograft: 155.5 ± 87.19; p= 0.1250). During the first 2 weeks, tumour size between groups does not have much variability, however going into week 3 showed a rate of growth difference that reached significance over the 4 week period. Weekly growth values can be seen in Figure 4.6 B and quantitative values in Table 4.3.

A)



B)

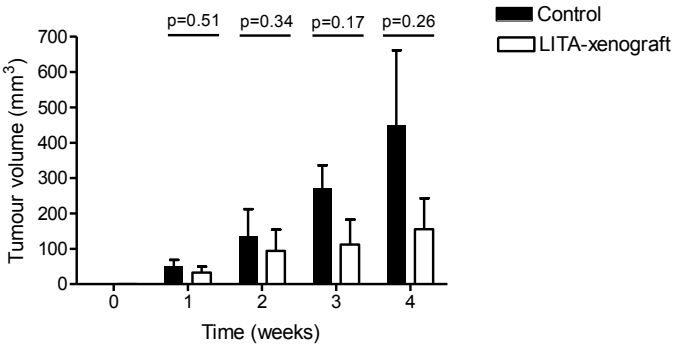


Figure 4.6 Effects of LITA-xenograft nanoparticles in HCT116 p53+/+ colorectal tumour growth

Xenograft tumour volume growth curve in control or LITA-xenograft treated groups for the duration of a 4-week study in the colorectal cancer cell line HCT116 p53+/+. **(A)** Tumour growth showed a decreased growth rate in LITA-xenograft treated group when compared to the control group, however neither reached significance; a particular growth rate difference shown at week 4 (p=0.125) **(B)** Data is presented as mean ± SEM and analysed by two-sample *t* test with Wilcoxon test; n=6/group.

Week	Control (mean ± sem)	LITA-xenograft (mean ± sem)	p value
0	00.00 ± 00.00	00.00 ± 00.00	---
1	50.26 ± 18.05	32.59 ± 16.8	0.513
2	135.7 ± 76.11	94.23 ± 60.05	0.345
3	269.6 ± 66.38	111.7 ± 70.86	0.179
4	449.9 ± 211.7	155.5 ± 87.18	0.268

Table 4.3 Effects of LITA-xenograft nanoparticles in murine HCT116 p53+/+ colorectal tumour growth

Mice were inoculated with HCT116 p53+/+ colorectal cancer cells and were injected every three days with either control or LITA-xenograft nanoparticles for 4 weeks, once tumour was confirmed palpable. Tumour volume was measured weekly using the standard calliper method. Tumour growth over the 4 weeks had a trending decrease in growth in the LITA-xenograft treated group, with particular growth difference shown at week 4. Data is presented as mean ± SEM and analysed by two-sample *t* test with Wilcoxon test; n=6/group.

4.3.2.2.1.1 Bioluminescence imaging for HCT 116 p53+/+ colorectal cancer cell lines tumour model

For a secondary way to follow tumourigenesis and proliferation activity, luciferase stable cell lines HCT 116 p53+/+ was generated and transplanted into nude mice and non-invasive spatiotemporal visualization was used based on a bioluminescent molecular imaging system. The activity of the tumour groups showed a trending decrease in the LITA-xenograft treated groups when compared to the control groups in both cell lines. The images for control and LITA treated mice in HCT 116 p53+/+ is represented in Figure 4.7 (group=6/group). Graph for luminescence output is shown in Figure 4.8 and quantitative results Table 4.4.

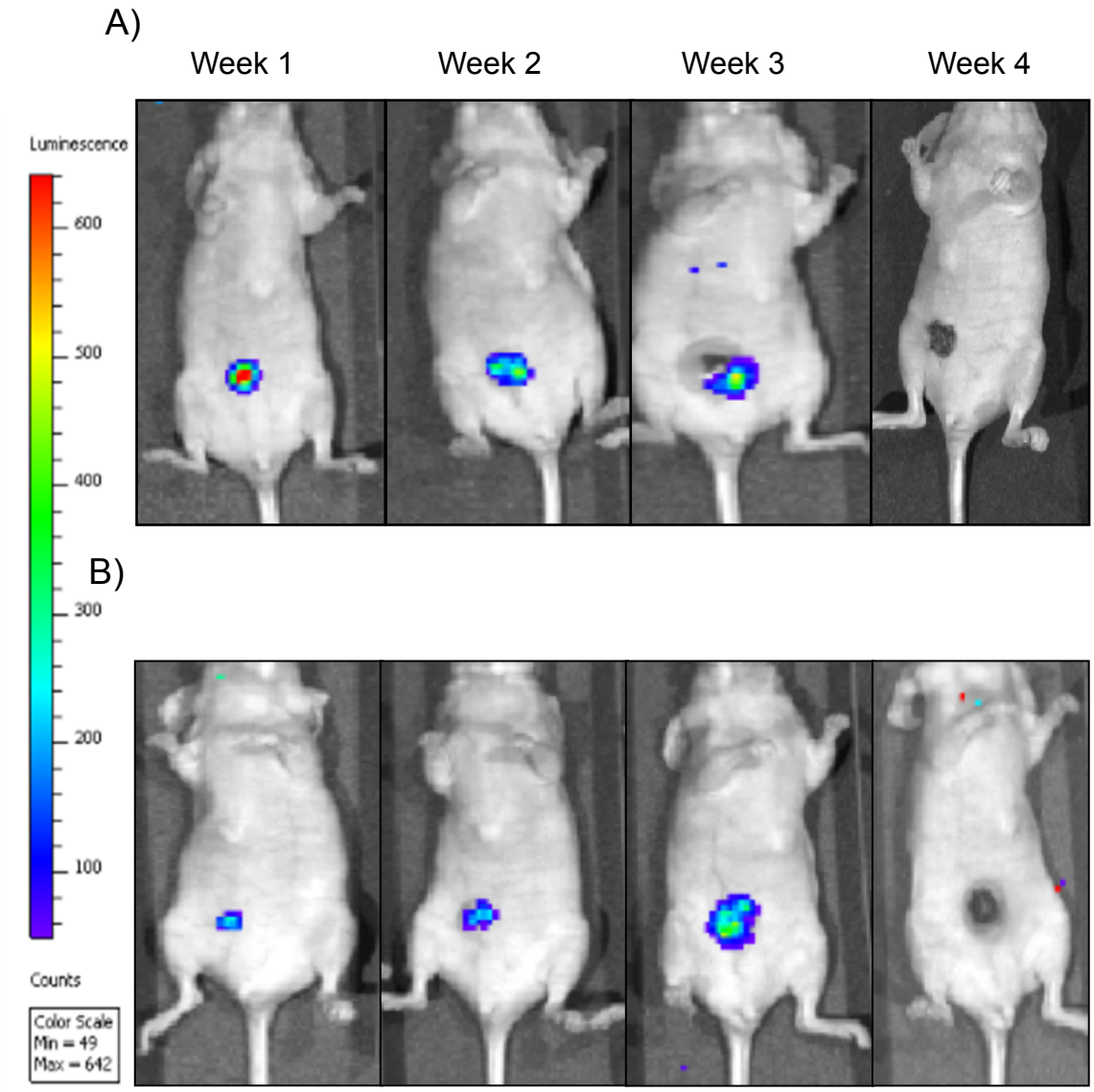


Figure 4.7 Bioluminescence imaging for control or LITA-xenograft treated HCT 116 p53+/+ colorectal cancer cell lines tumour model

Images of the murine xenograft model of HCT 116 p53+/+ after 3 weeks of having chronic control nanoparticle i.p. injections. (**A**) Control and (**B**) LITA-xenograft treated groups represent the luciferase activity quantified by the bioluminescent imaging system. Colour indicates luciferase activity which is correlated in counts given in the scale.

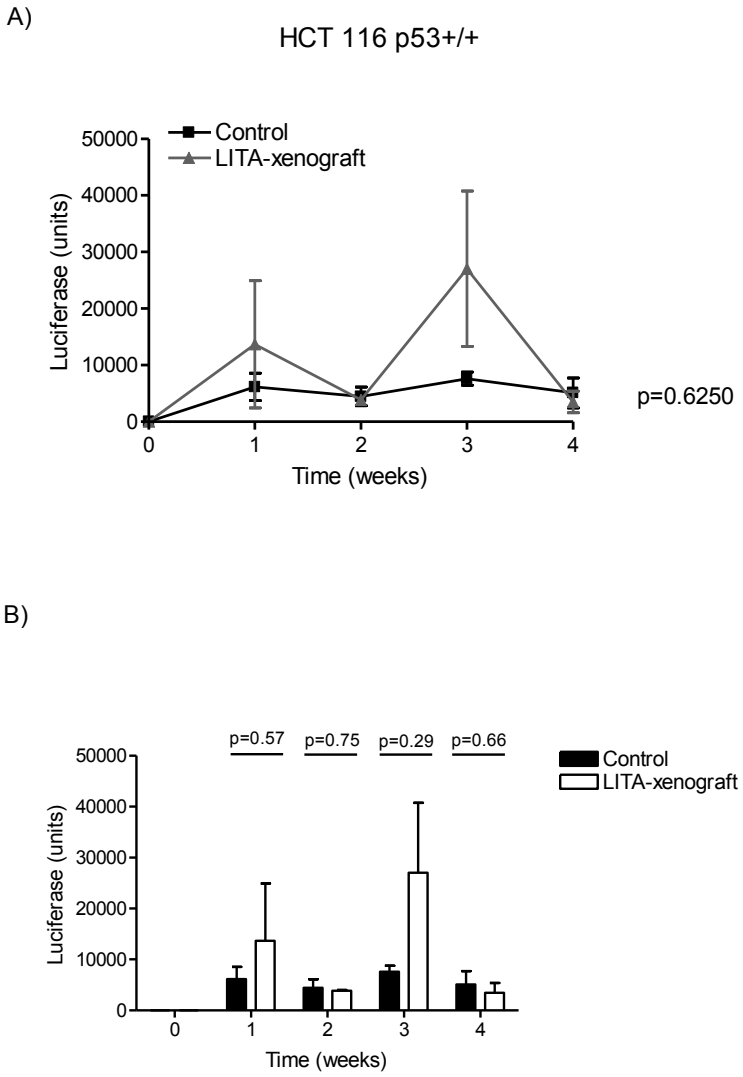


Figure 4.8 Bioluminescence imaging for control or LITA-xenograft treated HCT 116 p53+/+ colorectal cancer cell lines tumour model

Mice were inoculated with HCT 116 p53+/+ colorectal cancer cells. Once tumours were confirmed palpable, mice were injected every three days with either control or LITA-xenograft nanoparticles for 4 weeks. Data is presented as mean ± SEM and analysed by two-sample *t* test with Wilcoxon test; n=6/group.

Week	Control (mean ± sem)	LITA-xenograft (mean ± sem)	p value
0	00.00 ± 00.00	00.00 ± 00.00	---
1	6139 ± 2422.8	13697.5 ± 11250.5	0.578
2	4458.1 ± 1652.4	3864.7 ± 161.6	0.755
3	7602.8 ± 1152.6	27038.8 ± 13730.8	0.293
4	5100.2 ± 2643.4	3476.6 ± 1934.4	0.669

Table 4.4 Bioluminescence imaging for HCT 116 p53+/+ colorectal cancer cell lines tumour model

Mice were inoculated with HCT116 p53+/+colorectal cancer cells and were injected every three days with either control or LITA-xenograft nanoparticles for 4 weeks, once tumour was confirmed palpable. Tumour metabolic activity was measured weekly using the standard calliper method. Tumour growth over the 4 weeks had a trending decrease in growth in the LITA-xenograft treated group, with particular growth difference shown at week 3. Data is presented as mean ± SEM and analysed by two-sample *t* test with Wilcoxon test; n=6/group.

4.3.2.2.2 HCT 116 p53-/- colorectal cancer cell lines tumour model

The HCT 116 p53-/- colorectal cancer cell line had less than a 50% take rate after inoculation and successfully xenotransplanted tumours appeared within the expected time of 14 days. Time 0 refers to when the tumour was palpable and large enough to measure by calliper, at which point injections of either control or LITA-xenograft nanoparticles were initiated. Figure 4.9 shows the chronic administration of control or LITA-xenograft nanoparticles over the course of 4 weeks led to a trend reduction in tumour size however did not reach significance (control: 216.1 ± 75.47, LITA-xenograft: 132.9 ± 48.06, p= 0.2500). During the first 3 weeks, tumour size between groups does not have much variability, however going into week 4 showed a rate of growth difference that reached significance over the 4 week period. Weekly growth values can be seen in Figure 4.9 B and quantitative values in Table 4.5.

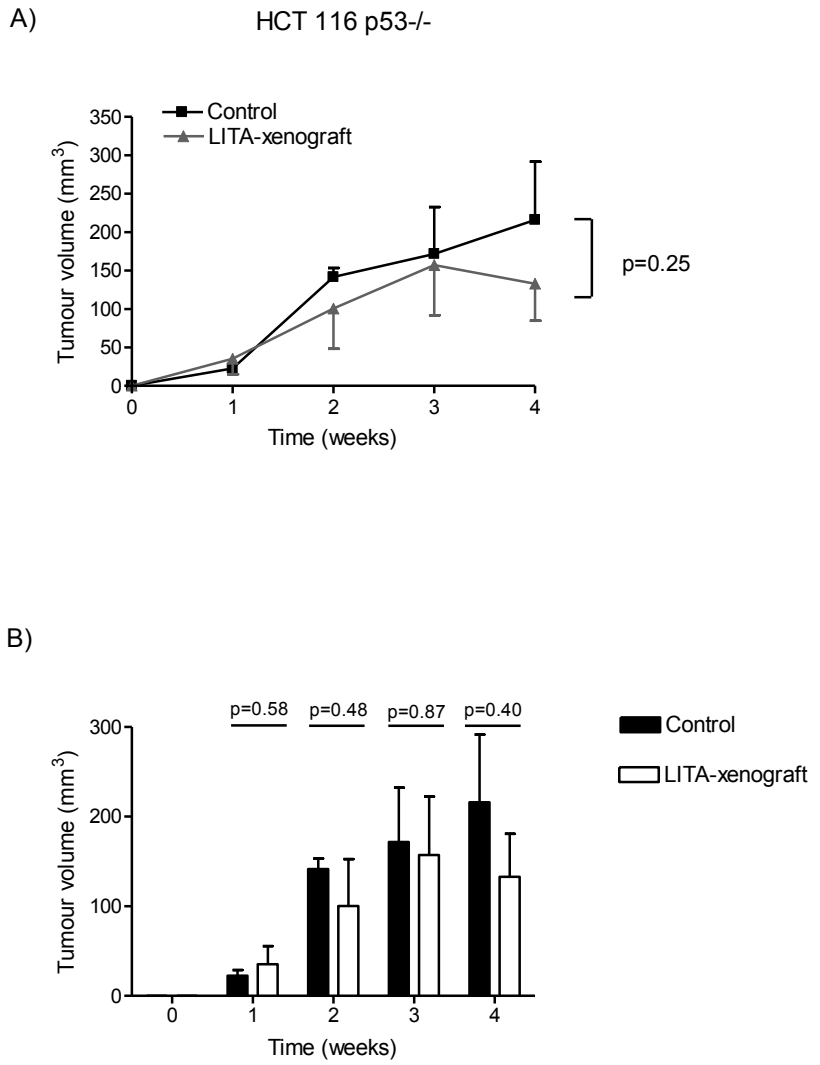


Figure 4.9 Effects of LITA-xenograft nanoparticles in HCT116 p53-/- colorectal tumour growth

Xenograft tumour volume growth curve in control and LITA-xenograft treated groups for the duration of a 4-week study in HCT116 p53-/- colorectal cancer cell lines. **(A)** Xenograft cell line growth showed a decrease in LITA-xenograft treated group, however neither reached significance. **(B)** Tumour growth over the 4 weeks had a trending decrease in growth over the 4 week period, with particular growth difference shown at week 4 (p=0.250). Data is presented as mean ± SEM and analysed by two-sample *t* test with Wilcoxon test or student's unpaired t-test; n=6/group.

Week	Control (mean ± sem)	LITA-xenograft (mean ± sem)	p value
0	00.00 ± 00.00	00.00 ± 00.00	---
1	22.58 ± 6.338	35.25 ± 20.34	0.584
2	141.6 ± 11.7	100.3 ± 52.19	0.483
3	171.7 ± 60.74	157 ± 65.39	0.877
4	216 ± 75.46	132.8 ± 48.05	0.405

Table 4.5 Effects of LITA-xenograft nanoparticles in murine HCT116 p53-/- colorectal tumour growth

Mice were inoculated with HCT116 p53-/- colorectal cancer cells and were injected every three days with either control or LITA-xenograft nanoparticles for 4 weeks, once tumour was confirmed palpable. Tumour volume was measured weekly using the standard calliper method. Tumour growth over the 4 weeks had a trending decrease in growth in the LITA-xenograft treated group, with particular growth difference shown at week 4. Data is presented as mean ± SEM and analysed by two-sample t test with Wilcoxon test; n=6/group.

4.3.2.2.2.1 Bioluminescence imaging for HCT 116 p53-/- colorectal cancer cell lines tumour model

For a secondary way to follow tumourigenesis and cellular proliferation, luciferase stable cell line HCT 116 p53-/- was generated and transplanted into nude mice and non-invasive spatiotemporal visualization was used based on a bioluminescent molecular imaging system. The activity of the tumour groups showed a trending decrease in the LITA-xenograft treated groups when compared to the control groups in both cell lines. The images for control and LITA treated mice in HCT 116 p53-/- is represented in Figure 4.10 (n=6/group). Graph for luminescence output is shown in Figure 4.11 and quantitative results Table 4.6

.

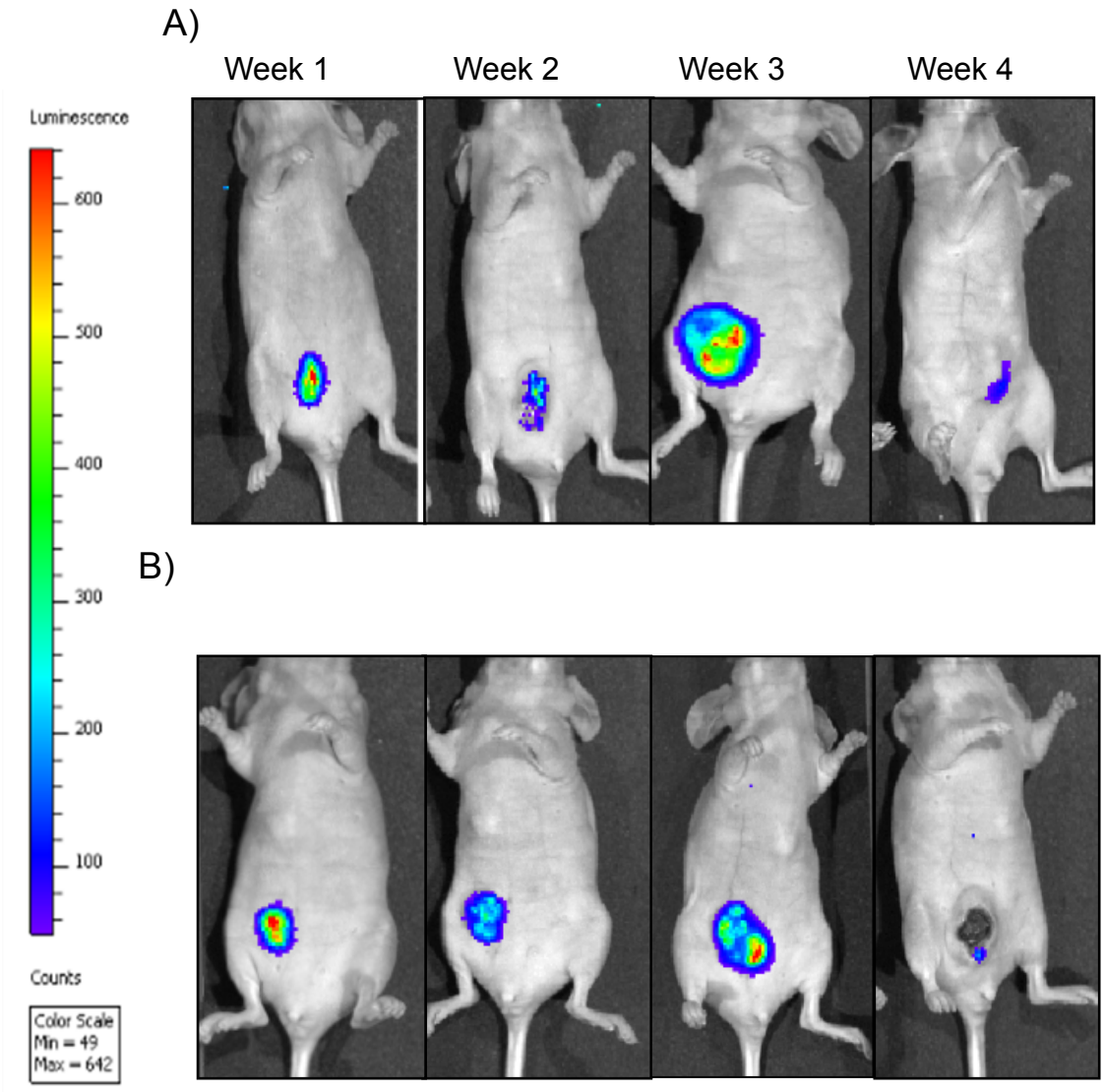


Figure 4.10 Bioluminescence imaging for control or LITA-xenograft treated HCT 116 p53-/- colorectal cancer cell lines tumour model

Images of the murine xenograft model of HCT 116 p53-/- after 3 weeks of having chronic control nanoparticle i.p. injections. (**A**) Control and (**B**) LITA-xenograft treated groups represent the luciferase activity quantified by the bioluminescent imaging system. Colour indicates luciferase activity which is correlated in counts given in the scale.

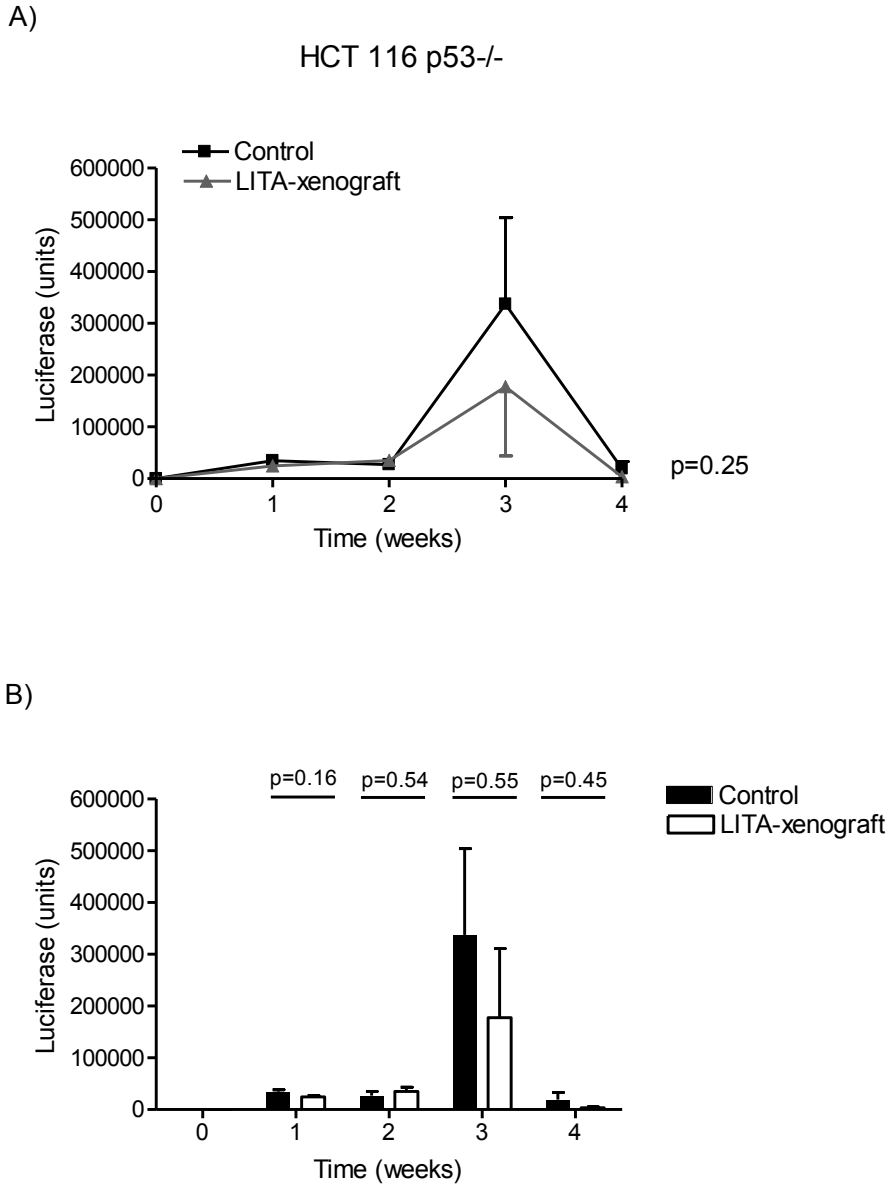


Figure 4.11 Bioluminescence imaging for control or LITA-xenograft treated HCT 116 p53-/- colorectal cancer cell lines tumour model

Mice were inoculated with HCT 116 p53-/- colorectal cancer cells. Once tumours were confirmed palpable, mice were injected every three days with either control or LITA-xenograft nanoparticles for 4 weeks. **(A)** Luciferase activity had no significance difference between control or LTIA-xenograft treated groups (p=0.25), **(B)** despite having a difference in luciferase activity at week 3. Data is presented as mean ± SEM and analysed by two-sample *t* test with Wilcoxon test or student's t-test; n=6/group.

Week	Control (mean ± sem)	LITA-xenograft (mean ± sem)	p value
0	00.00 ± 00.00	00.00 ± 00.00	---
1	34562.5 ± 3815.3	24949.2 ± 2414.3	0.164
2	27418.9 ± 7800.6	35295.5 ± 7879.5	0.547
3	337165 ± 167318.1	177838.5 ± 133426.5	0.550
4	19274 ± 14065.9	3818.5 ± 1592.5	0.458

Table 4.6 Bioluminescence imaging for HCT 116 p53-/- colorectal cancer cell lines tumour model

Mice were inoculated with HCT116 p53-/- colorectal cancer cells and were injected every three days with either control or LITA-xenograft nanoparticles for 4 weeks, once tumour was confirmed palpable. Tumour metabolic activity was measured weekly using the standard calliper method. Tumour growth over the 4 weeks had a trending decrease in growth in the LITA-xenograft treated group, with particular growth difference shown at week 3. Data is presented as mean ± SEM and analysed by two-sample t test with Wilcoxon test or student's t-test; n=6/group.

4.4 Discussion

In this Chapter I have designed a tumour-directed LITA particle for the uptake and treatment to three murine xenograph models of colorectal cancer *in vivo*, HT-29, HCT116 -/- and HCT116 +/+. HT-29 xenograft tumour showed a decreased growth rate and a decreased mRNA expression in HDAC 1, 2, 3 and 4 and Sirtuin 1 with an increase in Sirtuin 2. LITA administration caused a decrease in growth in HCT116 -/- and HCT116 +/+ by calliper measurements, however not by bioluminescent imaging.

An important factor in the design of a drug delivery system is the efficiency with which it comes in contact with the desired tissue, in this case the tumour tissue. The LITA nanoparticle formulated and tested in this study is categorised as a passively targeted, cationic liposome. This formulation was chosen as positively charged lipids lead to favourable interaction with surfaces of cells which are normally negatively charged. Liposome-tumour endothelial cells interactions is strongly governed by the degree of surface cationic charge, which is in turn determined by the amount of cationic lipid used in the formulation of the liposomal bilayer [213, 217]. Thus in the case of my LITA formulation the cationic lipid content was 32%mol. Krasnici et al. have previously shown that intravenously applied cationic liposomes preferentially accumulated in a xenograft tumour *in vivo*, in comparison with normal surrounding tissue [296]. Interestingly, this preferential accumulation of cationic liposomes in the solid tumour is thought to cause binding of the liposomes to angiogenic tumour microvessels. It would therefore be interesting to assess if the LITA nanoparticles develop here undergo a similar binding process.

Many studies have focused on elucidating the optimal concentration of the polymer polyethylene-glycol (PEG) that should be incorporated in the liposomal membrane to provide liposomes with long-circulating characteristics. Abu Lila et al. showed that PEG-coated

cationic liposomes had a 2-3 fold higher accumulation in tumour tissue than PEG-coated neutral liposomes [297]. Levchenko et al demonstrated that for a xenograft model *in vivo*, PEG concentrations of ≥6 mol% shield the electric surface of potential cationic liposomes, while higher concentrations (≥15%mol) were found to cause unfavourable structural changes in the liposome bilayer that enhanced the rapid clearance of liposomes from circulation[186]. In agreement, Cambell et al proposed a concentration range of PEG-lipid incorporation to be approximately 4-9% for ideal xenograft delivery [298] . This is also in accordance with my previous work [216], with an increased molarity percentage of DSPE-PEG^{2000} in the liposome membrane led to a preferential accumulation of liposomes in tumour tissue. Here, 5%mol of PEG lipid was incorporated into the liposome bilayer and created a long-circulating characteristic and allowed accumulation within the xenograft tumour.

As a verification of accumulation of LITA within the tumour, *ex vivo* fluorescence microscopy was performed. As with the previously validated LITA-Rhd nanoparticles in Chapter 3, the inclusion of the fluorescent DOPE-Rhodamine lipid in the liposome formulation allowed for post-mortem analysis. Confirmation of the LITA-Rhd is based on visual identification to determine presence of liposome and comparison of uptake between organs. The fluorescence pattern observed for the LITA-Rhd-xenograft nanoparticles appear to be more localised within the tissue than in previous histological evaluations carried out in the HFD model. The distribution profile of the nanoparticle was different in tumours versus organs; passively targeted tumours have a high accumulation in filter organs such as the liver or kidneys, thus the LITA-Rhd allowed visualisation of the vascular structure as well as tissue distribution (Chapter 3, Figures 2.9-2.12). Tumour growth does not have this vascular organisation and so the LITA-Rhd-xenograft appears bright in only one location within the histology slice as a result of liquid accumulation. It is also a factor of distribution over time, and the initial 2-hour time point does not allow for such cross organ comparison. Nomure et al. have previously demonstrated that tumour accumulation of liposomes tended to increase

up to 24 hours after injection and remained at this level for 48 hours [299]. The time point of 2 hours was merely used to confirm the delivery of the LITA nanoparticles to the tumour and therefore does not fully reflect the overall uptake of these nanoparticles by the tumour. This clearly needs further investigation. Fluorescence microscopy was carried out *ex vivo* in HCT116 cells lines, however with a different panel of small molecules thus is not included in this thesis, however it was confirmed liposomal delivery in achievable all cell lines used in this study.

Following the renewed interest in the 'Warburg effect', it has become clear that alterations in metabolism should be included among the essential characteristics of tumour cells, as described earlier. To investigate cancer dysregulated metabolism, acetate encapsulated nanoparticles were chronically delivered to xenograft inoculated mice, investigating colorectal cancer (CRC) cell lines with varying metabolic profiles. These CRC cell lines were HT-29 and HCT116 derived from two widely used colon carcinoma models. The latter consisted of a wild-type p53 (HCT116 3 (+/+)) and a p53-knockout (HCT116 without p53 (-/-)). Furthermore, HT-29 bears a mutation in one allele of p53 and is therefore characterised by altered p53 protein [300, 301]. The tumour suppressor p53 integrates intracellular signals and induces the transcription of target genes and interacts with a wide array of pathways to help determine cell fate and promote cell arrest, senescence or apoptosis. Indeed, p53 has been recently associated with the control of cancer cell metabolism [302, 303].

All cell lines underwent to same inoculation and treatment protocol leading to visible xenographs. HT-29 cell lines were only measure by calliper as no luciferase cloned cell line was available. HT-29 showed a decrease in tumour volume in the LITA group by the end of the study. However, both groups had similar growth patterns for the first two weeks. This apparent discrepancy could be due to the lack of acetate reaching the tumour and/or the fact

that acetate requires to be present for a significant period of time before cellular response can take place. Thus, the increase in acetate delivery over time may have curved the metabolism by saturating the tumour environment. Consistent with the decrease in the tumour growth curve, the volume and mass were also both significantly decreased in the LITA-xenograft treated group. A noticeable difference in tumour volume versus tumour mass was observed at the end of the study. One potential confounding factor could be the dense microenvironment of the tumour, which is included in the calliper measurement but is dissected out when removing and isolating the tumour itself. Another factor that could contribute to the discrepancy between volume and mass changes may be the growth pattern of the tumours; some tumour appeared to have significant necrosis, being hollowed centre filled with liquid instead of cellular tissue.

Calliper based measurements were also carried out for HCT116 p53+/+ and HCT116 p53-/- cell lines, which showed a reduction in tumour volume in the LITA-xenograft group, though neither reached significance. The growth rate of HCT116 p53+/+ appeared much more aggressive than HCT116 p53-/- and the HT-29, though they all showed a reduction when treated with the LITA nanoparticle. Interestingly, the protocol of treatment was the same for all models, yet the growth response was different between cell lines. It has been previously shown *in vitro* that HCT116 p53+/+ grows at a higher rate than HT-29 cells, but both are faster than the HCT116 p53-/- [304, 305]. Furthermore, the HT-29 and HCT116+/+ had a more pronounced response to the LITA administrations than HCT116-/-, possibly indicating a role for p53 in the mechanism of action of acetate [306].

Bioluminescence imaging is a broadly applicable technology for assessing biological process *in vivo*. Luciferase activity provides a read-out of increases or decreases in transcription of the reporter gene *in vivo*. Thus, bioluminescent imaging was carried out in addition to calliper

to measure tumour activity. It is important to point out; the intensity of the signal measured by *in vivo* may depend on various factors, including D-luciferin absorption through the peritoneum, cell membrane permeability, availability of co-factors, blood flow, intracellular pH and transparency of overlying tissue, in addition to the amount of luciferase that is able to reach the location of interest [307]. Luciferase activity and calliper measurements did not appear to correlate at any point over the 4 week study in the HCT 116+/+ cell line. Calliper measurements showed an increase over the 4 week study; however the luciferase activity did follow the same pattern. Indeed, luciferase activity and calliper measurement only correlated in the HCT 116-/- tumour growth at week 3. While in the first two weeks the calliper measured group showed tumour growth in both groups at relatively the same rate, the luciferase groups appears to have no change over time or between groups. Week 2 in particular had low luciferase activity which most likely was a result of the assay more than the tumour. This inconsistency between methods may arise from the fact that changes in tumour architecture may limit the supply of either substrate or enzyme activity, thus leading to a diminished bioluminescence despite having tumour growth. Moreover, at the alter stage of the study; tumour necrosis may play a significant role in the bioluminescence measurements. Thus, although the luciferase activity could have delivered important data on tumour activity *in vivo* the more accurate and consistent measurements from calliper will be referred to when discussing growth rates.

The discrepancy between calliper and bioluminescence presented a difference in recorded observations. According to the tumour measurements by calliper and weight, I observed a decrease in tumour growth in the LITA group; however according to the bioluminescence pattern, I saw no difference in either group. The lack of agreement was a surprising result since this method is widely reliable. It is assumed that bioluminescence signal increases as tumour volume increases, but the relationship might have been disrupted due to hypoxia, necrosis or pH of the tumour microenvironment or the location of transplantation of the

xenograft tumour [307]. The tumour decreased in size, thus it can be assumed some portion of the LITA-xenograft nanoparticle was reaching the tumour, however the hypoxic conditions might have hindered the signal of the bioluminescence substrate that reached the tumour tissue, and impacting the interpretation.

The mechanism behind the effects of LITA-xenograft results is unclear but may take place by altering genetic or metabolic processes. SCFA have previously been investigated for activity in cell differentiation, growth arrest and/or apoptosis [308, 309]. Valproic acid, phenyl acetate and butyrate have been shown to have antigrowth properties [310, 311] . These anti-proliferation effects attributed to SCFAs have been linked to changes in activity of many enzymes and transcription factors, including HDAC enzymes, important markers that play a key role in cellular gene expression [173, 312].

LITA-xenograft treatment of HT-29 xenograft showed a reduction in tissue mRNA expression of HDACs 1, 2, 3 and 4. This would suggest a potential decrease in HDAC activity following LITA-xenograft treatment. A potential model to understand this effect would be butyrate, a well-known HDC inhibitor. It was initially proposed that butyrate inhibited HDAC activity by its accumulation in the cytoplasm, leading to its transport into the nucleus and directly affected HDAC transcription. However, Donohoe et al., have shown that butyrate might induce histone acetylation by an alternative mechanism. Metabolism of butyrate to acetyl-CoA appears to stimulate HAT activity by functioning as a HAT cofactor and acetyl-group donor. In this model, butyrate undergoes β-oxidation to acetyl-CoA inside of the mitochondria, followed by the first step of the TCA cycle to yield citrate. Citrate is then transported out of the mitochondria via the citrate shuttle and converted by the enzyme ATP citrate lyase (ACL) to acetyl-CoA and oxaloacetate, thus the butyrate is active as a result of conversation to acetyl-CoA. This model also potentially includes glucose-induced signal transduction that

upregulates ACL activity (via phosphorylation of ACL by AKT [313]), which makes it susceptible to being regulated by the Warburg effect [160]. If this is the case, then acetate may not be functioning as direct HDACi, but may be causing a decrease in expression of the same family of genes through other mechanisms.

Wellen et al also showed that post-translational modification of proteins, particularly histones, through acetylation requires acetyl-CoA, and inhibition of acetyl-CoA production can affect histone acetylation in response to growth-factor stimulation [314]. One example of this effect is the sirtuins, a class of NAD+-dependent protein deacetylases, which are important regulators of energy metabolism and stress resistance. The decreased expression of the histone deacetylase, SirT1, is of note given its established role as an inhibitor of apoptosis and promoter for tumourigenesis [315]. However, more work is required to clearly define the downstream effectors of epigenetic modification.

Dicholoracetate (DCA), an analogue of acetate, has been shown to have significant anti-tumour effects [316]. DCA appears to inhibit pyruvate dehydrogenase kinase (PDK), which leads to a shift in metabolism from glycolysis to oxidative phosphorylation, thus diminishing the 'Warburg effect' [316]. This in turn will create a substantial increase in ROS production, and subsequent cell death. Clearly the acetate from the LITA-xenograft particles would not affect PDK directly but would increase the influx of acetyl-CoA molecules into the mitochondria, thus inducing elevated ROS production and apoptosis of cancer cells. However, it is important to point out that DCA has not been universally reported to enhance apoptosis in tumour cells. Shahrzad et al (2010) showed that DCA had no effect on the apoptotic rate in tumours [317]. Interestingly, Babu et al has recently shown that DCA also act as an HDAC inhibitor when examined under identical *in vitro* conditions of 1mM [318]. This is an interest parallel to my findings where a decrease in HDAC activity, including SirT1, was observed in the HT-29 xenograft model. The lack of change in SirT2 in my model was

not surprising as *in vitro* studies also by Babu showed that after an incubation of acetate and DCA a significant decrease was only seen in SirT1 and no change to SirT2 [318]. Future work is required to clearly define the downstream effectors of the LITA-xenograft in relation to these Sirtuins.

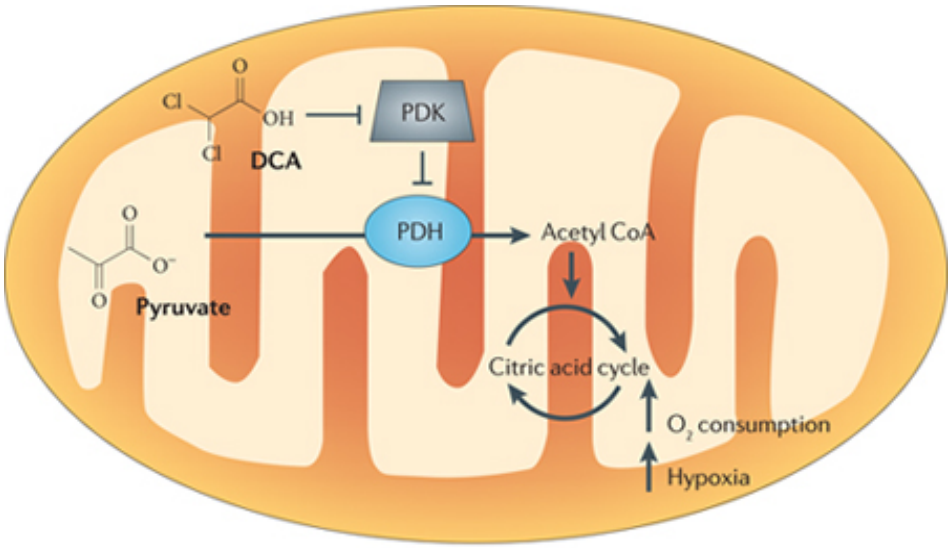


Figure 4.12 Mitochondrial responses to dichloroacetate administration

Dichloroacetate (DCA) inhibits the function of pyruvate dehydrogenase kinase (PDK) in mitochondria which in turn releases the inhibition of pyruvate dehydrogenase (PDH). PDH catalyses the conversion of pyruvate to acetyl-CoA and consequently causing hypoxia and in turn causes lethality to the tumour cell. Figure from Chan & Giaccia, 2011.

Thus, acetate may parallel the DCA mechanism when administered *in vivo*. This represents a diverse molecular abnormality in cancer that has the potential be exploited in future treatments. The Warburg Effect does explain the altered metabolism in cancer cells, though it does not define the only source or metabolic targeting. Since acetate plays a ubiquitous role in metabolism and alterations, a number of cellular pathways could feasibly contribute to

the decrease in tumour growth. A theme that is consistent amongst the proposed models of mechanism for the LITA-xenograft nanoparticle, with the mitochondria playing a pivotal role. In regards to the conflicting literature cited here, the novel approach of acetate delivery via a carrier system introduces a number of parameters that have not been examined before; the system described here was *in vivo*, whereas most data referenced was carried out *in vitro*. In addition, acetate delivery was chronically over a time course of weeks, whereas most data referenced was one single administration.

Finally, many cellular processes are highly dependent on the availability of metabolites, so metabolic reprogramming may have even more of a marked effect in cancer cells [319-321]. Cancer cells reprogram their metabolism in order to satisfy their bioenergetic and biosynthetic requirements [322-324]. Increased aerobic glycolysis has been linked to therapeutic resistance in cancer and the deregulated cancer metabolism promotes cell proliferation through increased energy production and metabolite synthesis. It is possible that the phenotypic changes observed in these cancer models may have been induced by metabolic changes brought about by the influx of excess acetate. The formation of acetyl-CoA from acetate requires ATP, thus activating AMPK [284]. This acetyl-CoA can then enter the TCA cycle modifying the generation of lactate from pyruvate [325] or by utilised for FA synthesis. These processes can in turn change the bioenergetics balance of the cell, increase ROS production leading accelerated cell death. Additionally, tumour development and progression are both accompanied by marked changes in expression and activity of pivotal enzymes in lipid metabolism including fatty acid synthesis FAS [326] . FAS catalyses *do novo* synthesis of fatty acids from acetyl-CoA, Malonyl-CoA and NADPH [327]. Furthermore, ACC is a determining factor for FAS activity can significantly affect cancer cell metabolism. Genetic manipulation of the two isoforms of ACC, ACC1 or ACC2, in cancer cells have been shown to yield different outcomes in terms of FAS and β-oxidation [328]. Based on this, one would predict that accumulation of acetate in the tumour tissue may

affect the functions of these enzymes. Once acetate is converted into acetyl-CoA, and depending on its cellular location, will activate ACC1 or ACC2 [329]. However, activation of AMPK will inhibit ACC isoforms, which would lead to a decrease in FA synthesis. This is clearly a paradox which requires further investigation, regardless, the presence of acetate in cancer cell leads to increase cell death and a reduction in tumour size Figure 4.12 gives a schematic diagram for a potential mechanism for acetate metabolism within tumour cells.

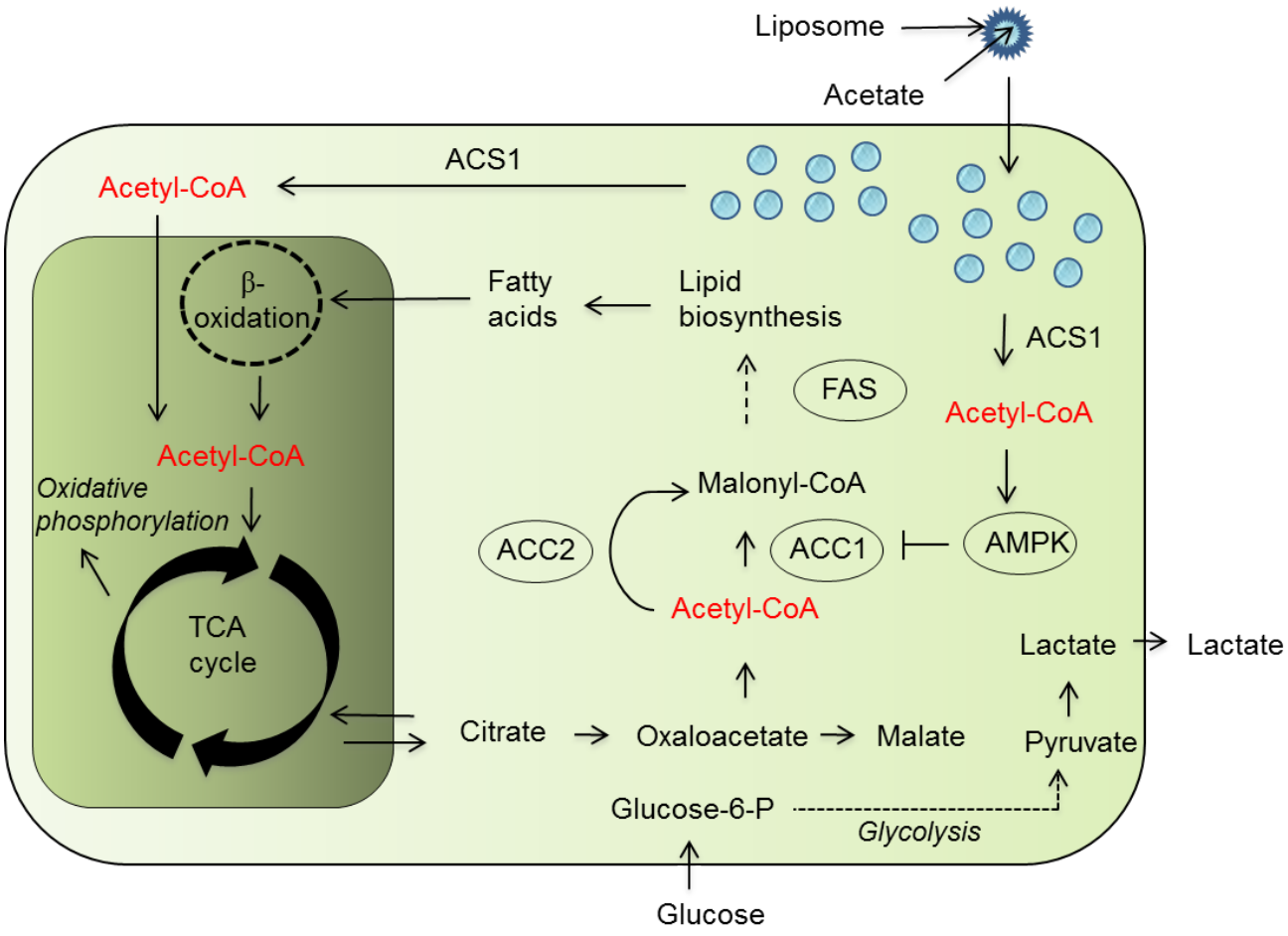


Figure 4.13 Effect of LITA-xenograft on Cancer Cell Metabolism

A schematic representation of the metabolic routes interconnected with β-oxidation. The LITA-xenograft enters the tumour tissue and is converted to Acetyl-CoA via Acetyl-Coenzyme A synthase 1 (ACS1). Central metabolism processes are depicted such as glycolysis, the TCA cycle, oxidative phosphorylation, and β-oxidation. Acetyl-CoA enters the TCA cycle, one effect of that is the production of citrate, which is exported to the cytoplasm. Dashed arrows represent indirect effects or serial reactions.

4.5 Conclusion

The combined results from my studies support the hypothesis that chronic administration of LITA-xenograft nanoparticles specifically engineered for tumour uptake leads to a reduction in tumour growth across three independent studies of colorectal cancer: HT-29, HCT116+/+ and HCT116-/-. Much of cancer treatment depends not only on the drug itself, but dosage and delivery. This study has aimed to tailor the delivery aspect in order to reach the xenograft tumour itself. Literature cited here has carried out research either *in vitro* or achieved SCFA delivery through diet, which would incorporate a system-wide change incorporating many different elements of effect on tumour growth. The data presented here is the starting point for the potential use of SCFA via liposome delivery for *in vivo* therapeutics.

Chapter 5

Final Discussion

5.1 Final conclusions

The intertwining developmental trajectories of cancer and obesity have a shared origin in impaired cellular metabolism, with mitochondrial dysfunction at their core. In order to correct the aberrant pathways associated with these conditions I have manufactured and evaluated an acetate carrying liposomal-based vector that is preferentially delivered to key sites of metabolic control. Dietary supplementation with fibre ameliorates features of the metabolic syndrome and inhibits malignant growth in certain cancer types, effects attributed to the production of short-chain fatty acids (SCFA), such as acetate. My results presented here indicate that nanoparticle encapsulated acetate acts as a multifunctional active pharmaceutical ingredient (API), capable of altering the development of pathogenic signatures indicative of both obesity and cancer.

5.2 Discussion of Methods Used

Chapter 3

Mircroarray analysis was used to investigate the profile of how acetate may change the metabolic system in a way that would be recognisable to this particular assay. Data analysis was done in conjunction of a bioinformatics platform in order to obviate any computer coding issues or misinterpretations in results. While the data does not indicate any specific mechanism or pathway, it did exploit the difficultly of using wild-type C57/BL6 mice on a HFD as a background to this assay. A more sensitive analysis method may be desirable, including qPCR.

Chapter 4

In Chapter 4, assessment of xenograft tumour *in vivo* was conducted with a two-pronged approach: calliper and bioluminescence. The use of bioluminescence was concluded to be an unreliable measurement tool in this setting. Xenograft tumour models are well-accepted methods; however my study had difficulties correlating the results between the calliper and bioluminescence. The reason for this is unclear, but growth pattern of xenograft tumours are known to have interrupted blood flow, necrosis, and varying microenvironments. These factors make longitudinal studies difficult and require further optimising. Possible improvements to the design could include an increased sample size, shorter experimental duration and potentially bi-weekly measurements instead of weekly.

While the xenograft tumour model is a widely used and accepted technique, there are many limitations to take into consideration. As previously stated, the method used for statistical analysis was the two-sample *t* test using a generalised Wilcoxon test. This selection was done with the following challenging problems in mind: 1) the numbers of animals per group were quite low, approximately 6, which introduces a wide variability between the animals as

far as tumour growth and response to treatment. 2) The loss of data from animal morbidity did occur, which causes a drop out in n number. 3) The growth behaviour of the tumour such as necrosis and tumours receding internally will impede measurements recorded.

5.3 Limitations to studies

Chapter 3

A number of interesting results were obtained with acetate encapsulated in liposomal nanoparticles. The results could have been enhanced with a prolonged treatment period beyond the 5 weeks tested here. The serum data presented here was carried out by an external company which had an unfortunate incident of corruption for assays intended for my study. This caused a decrease in n numbers, which has a potential affect to statistical power. Also, this cause a truncated selection of serum markers intended to be measured. However, the results obtained from these studies gave a good insight into the positive effects of acetate, the mechanism by which it causes these effects.

Chapter 4

While the xenograft tumour model is a widely used and accepted technique, there are many limitations to take into consideration. The selection of cell type needs to be expanded, as well as the rate of tumour growth needs to be controlled. Furthermore, different techniques to assess tumour size, activity and viability are required, including MRI and PET. The growth behaviour of the tumour is also an important issue, including necrosis and tumours receding internally which can impede proper assessment[330].

5.4 future studies

Here I have shown that LITA can be utilised to re-engineer the metabolism of dysfunctional tissues in obesity and cancer. Future work will require validating and expanding on these findings, including a larger cohort of animals, cell lines and further *in vivo* work to unravel the underlying mechanism underpinning the effect of LITA, both in obesity and cancer. Future work also includes the use of different obesogenic models, including ob/ob and other knockouts to have an better insight as to the extent of the LITA effect on the metabolic syndrome. In addition, further experiments could include comparisons with control clinically used agents such as metformin, which has been shown to reduce plasma glucose levels and improve insulin sensitivity through activation of AMPK [288].

To answer some of the multiple questions arising over the course of this research, I wanted to investigate how acetate was affecting cellular metabolism and specifically mitochondrial respiration and ATP production. Some preliminary results are shown below. Using HEPG2 cells (liver hepatocellular carcinoma); I measured the metabolic flux between oxygen consumption rate (OCR) and acid efflux (ECAR) through catabolic pathways used to generate ATP. Acetate (5mM) was found to increase ATP production ($p<0.01$) with no significant different in spare respiration between the acetate or control group (Figure 5.1). Further work is clearly required to assess the metabolism of acetate and its flux through the mitochondria and intact cells.

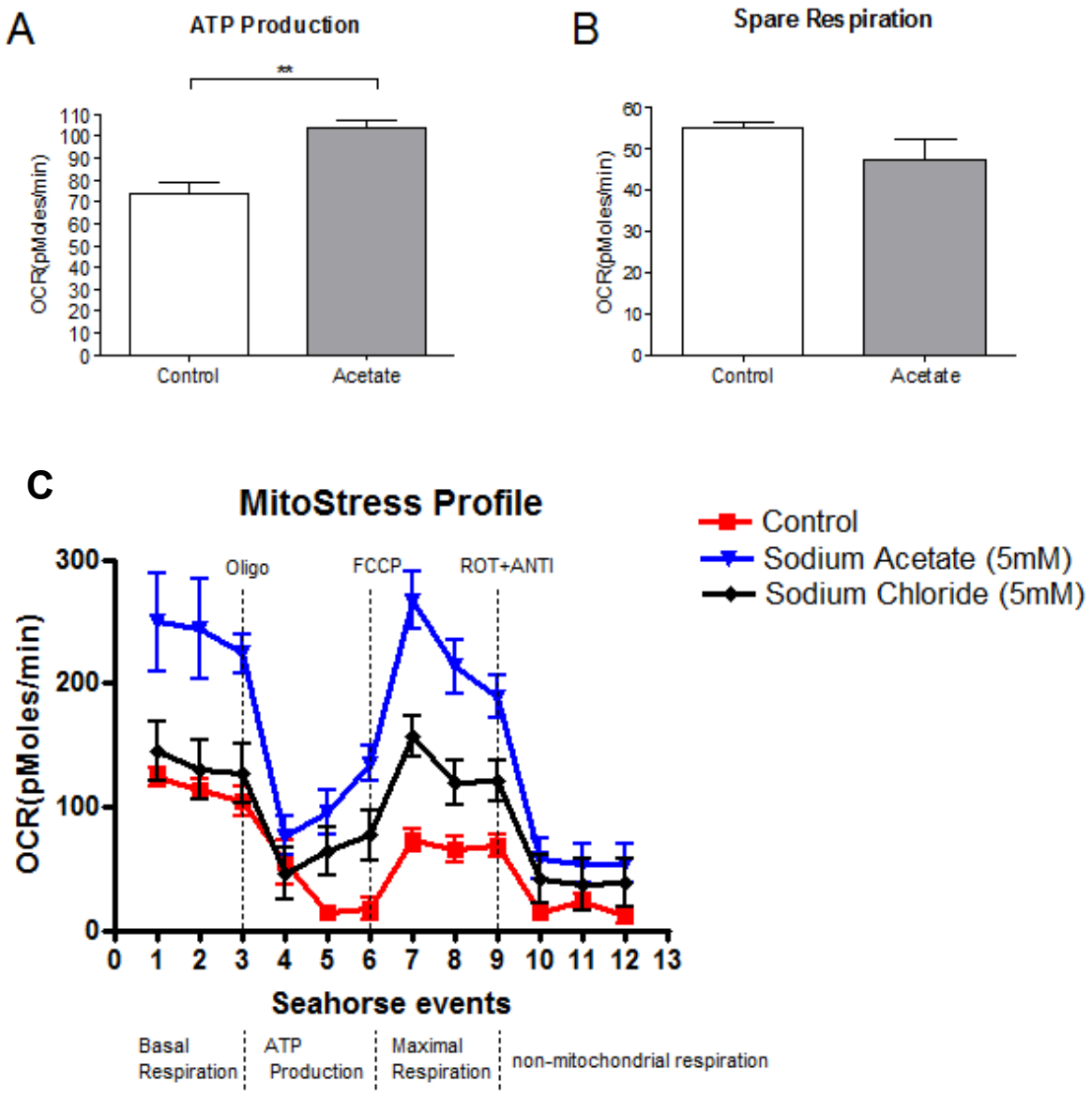


Figure 5.1 Mitochondrial calorimetry

HT-29 cells were treated with acetate (5mM) or without (Control) and assessed for ATP production by the Seahorse assay *in vitro*. **(A)** ATP production; **(B)** Spare respiration; **(C)** overall mitochondrial respiration profile; n=4/group; **=p<0.01; data analysed using student t-test (GraphPad Prism); OCR: Oxygen consumption rate.

References

1. Fernandez-Sanchez, A., et al., Inflammation, oxidative stress, and obesity. Int J Mol Sci, 2011. 12(5): p. 3117-32.

2. Ceschi, M., et al., Epidemiology and pathophysiology of obesity as cause of cancer. Swiss Med Wkly, 2007. 137(3-4): p. 50-6.

3. Choudhury, M., K.R. Jonscher, and J.E. Friedman, Reduced mitochondrial function in obesity-associated fatty liver: SIRT3 takes on the fat. Aging (Albany NY), 2011. 3(2): p. 175-8.

4. Cheng, Z. and M. Ristow, Mitochondria and Metabolic Homeostasis. Antioxid Redox Signal, 2013.

5. Savini, I., et al., Obesity-associated oxidative stress: strategies finalized to improve redox state. Int J Mol Sci, 2013. 14(5): p. 10497-538.

6. Bhandary, B., et al., An involvement of oxidative stress in endoplasmic reticulum stress and its associated diseases. Int J Mol Sci, 2012. 14(1): p. 434-56.

7. Aronne, L.J., et al., When prevention fails: obesity treatment strategies. Am J Med, 2009. 122(4 Suppl 1): p. S24-32.

8. Mingrone, G., et al., Bariatric surgery versus conventional medical therapy for type 2 diabetes. N Engl J Med, 2012. 366(17): p. 1577-85.

9. Stephanopoulos, G., Metabolic fluxes and metabolic engineering. Metab Eng, 1999. 1(1): p. 1-11.

10. Lee, S.Y., Metabolic engineering and synthetic biology in strain development. ACS Synth Biol, 2012. 1(11): p. 491-2.

11. Boghigian, B.A., et al., Metabolic flux analysis and pharmaceutical production. Metab Eng, 2010. 12(2): p. 81-95.

12. Excellence, N.I.f.H.a.C., Obesity: full guidance. 2006.

13. Alberti, K.G., et al., Harmonizing the metabolic syndrome: a joint interim statement of the International Diabetes Federation Task Force on Epidemiology and Prevention; National Heart, Lung, and Blood Institute; American Heart Association; World Heart Federation;

International Atherosclerosis Society; and International Association for the Study of Obesity. Circulation, 2009. 120(16): p. 1640-5.

14. Anderson, K.E., et al., Diabetes and endometrial cancer in the Iowa women's health study. Cancer Epidemiol Biomarkers Prev, 2001. 10(6): p. 611-6.

15. Lowell, B.B. and B.M. Spiegelman, Towards a molecular understanding of adaptive thermogenesis. Nature, 2000. 404(6778): p. 652-60.

16. Ravussin, E. and S.R. Smith, Increased fat intake, impaired fat oxidation, and failure of fat cell proliferation result in ectopic fat storage, insulin resistance, and type 2 diabetes mellitus. Ann N Y Acad Sci, 2002. 967: p. 363-78.

17. Muoio, D.M. and C.B. Newgard, Obesity-related derangements in metabolic regulation. Annu Rev Biochem, 2006. 75: p. 367-401.

18. Teusink, B., et al., Contribution of fatty acids released from lipolysis of plasma triglycerides to total plasma fatty acid flux and tissue-specific fatty acid uptake. Diabetes, 2003. 52(3): p. 614-20.

19. Oeransson, G. and T. Olivercrona, The Metabolism of Fatty Acids in the Rat. Ii. Oleic Acid. Acta Physiol Scand, 1965. 63: p. 121-7.

20. Owen, O.E., et al., Energy metabolism in feasting and fasting. Adv Exp Med Biol, 1979. 111: p. 169-88.

21. Duncan, R.E., et al., Regulation of lipolysis in adipocytes. Annu Rev Nutr, 2007. 27: p. 79-101.

22. Lumeng, C.N. and A.R. Saltiel, Inflammatory links between obesity and metabolic disease. J Clin Invest, 2011. 121(6): p. 2111-7.

23. Torres-Leal, F.L., et al., The role of inflamed adipose tissue in the insulin resistance. Cell Biochem Funct, 2010. 28(8): p. 623-31.

24. Kershaw, E.E. and J.S. Flier, Adipose tissue as an endocrine organ. J Clin Endocrinol Metab, 2004. 89(6): p. 2548-56.

25. Fruhbeck, G., Overview of adipose tissue and its role in obesity and metabolic disorders. Methods Mol Biol, 2008. 456: p. 1-22.

26. Djian, P., A.K. Roncari, and C.H. Hollenberg, Influence of anatomic site and age on the replication and differentiation of rat adipocyte precursors in culture. J Clin Invest, 1983. 72(4): p. 1200-8.

27. Pankov, Y.A., Adipose tissue as an endocrine organ regulating growth, puberty, and other physiological functions. Biochemistry (Mosc), 1999. 64(6): p. 601-9.

28. Krotkiewski, M., The effects of estrogens on regional adipose tissue cellularity in the rat. Acta Physiol Scand, 1976. 96(1): p. 128-33.

29. Berg, G., U. Troll, and U. Strunk, [The fatty acid pattern in the human depot fat]. Klin Wochenschr, 1968. 46(18): p. 997-9.

30. Gesta, S., et al., Evidence for a role of developmental genes in the origin of obesity and body fat distribution. Proc Natl Acad Sci U S A, 2006. 103(17): p. 6676-81.

31. Ashwell, M., The use of the adipose tissue transplantation technique to demonstrate that abnormalities in the adipose tissue metabolism of genetically obese mice are due to extrinsic rather than intrinsic factors. Int J Obes, 1985. 9 Suppl 1: p. 77-82.

32. Arner, P., Regional adipocity in man. J Endocrinol, 1997. 155(2): p. 191-2.

33. Frayn, K.N., Adipose tissue as a buffer for daily lipid flux. Diabetologia, 2002. 45(9): p. 1201-10.

34. Miyazaki, Y., et al., Effect of pioglitazone on abdominal fat distribution and insulin sensitivity in type 2 diabetic patients. J Clin Endocrinol Metab, 2002. 87(6): p. 2784-91.

35. Chiba, Y., et al., Relationship between visceral fat and cardiovascular disease risk factors: the Tanno and Sobetsu study. Hypertens Res, 2007. 30(3): p. 229-36.

36. Chowdhury, B., et al., A multicompartment body composition technique based on computerized tomography. Int J Obes Relat Metab Disord, 1994. 18(4): p. 219-34.

37. Hoffstedt, J., et al., Variation in adrenergic regulation of lipolysis between omental and subcutaneous adipocytes from obese and non-obese men. J Lipid Res, 1997. 38(4): p. 795-804.

38. Wajchenberg, B.L., Subcutaneous and visceral adipose tissue: their relation to the metabolic syndrome. Endocr Rev, 2000. 21(6): p. 697-738.

39. Donnelly, K.L., et al., Sources of fatty acids stored in liver and secreted via lipoproteins in patients with nonalcoholic fatty liver disease. J Clin Invest, 2005. 115(5): p. 1343-51.

40. Angulo, P., Nonalcoholic fatty liver disease. N Engl J Med, 2002. 346(16): p. 1221-31.

41. van Marken Lichtenbelt, W.D., et al., Cold-activated brown adipose tissue in healthy men. N Engl J Med, 2009. 360(15): p. 1500-8.

42. Mattson, M.P., Perspective: Does brown fat protect against diseases of aging? Ageing Res Rev, 2010. 9(1): p. 69-76.

43. Kuhn, E., N. Binart, and M. Lombes, [Brown, white, beige: the color of fat and new therapeutic perspectives for obesity...]. Ann Endocrinol (Paris), 2012. 73 Suppl 1: p. S2-8.

44. Gunawardana, S.C., Therapeutic value of brown adipose tissue: Correcting metabolic disease through generating healthy fat. Adipocyte, 2012. 1(4): p. 250-255.

45. Prentice, A.M. and S.A. Jebb, Beyond body mass index. Obes Rev, 2001. 2(3): p. 141-7.

46. Deurenberg, P. and M. Deurenberg-Yap, Validity of body composition methods across ethnic population groups. Acta Diabetol, 2003. 40 Suppl 1: p. S246-9.

47. Thomas, E.L., et al., Magnetic resonance imaging of total body fat. J Appl Physiol, 1998. 85(5): p. 1778-85.

48. Klein, S., et al., Waist circumference and cardiometabolic risk: a consensus statement from Shaping America's Health: Association for Weight Management and Obesity Prevention; NAASO, The Obesity Society; the American Society for Nutrition; and the American Diabetes Association. Am J Clin Nutr, 2007. 85(5): p. 1197-202.

49. Pouliot, M.C., et al., Waist circumference and abdominal sagittal diameter: best simple anthropometric indexes of abdominal visceral adipose tissue accumulation and related cardiovascular risk in men and women. Am J Cardiol, 1994. 73(7): p. 460-8.

50. Lean, M.E., T.S. Han, and C.E. Morrison, Waist circumference as a measure for indicating need for weight management. BMJ, 1995. 311(6998): p. 158-61.

51. Thomas, E.L., et al., Excess body fat in obese and normal-weight subjects. Nutr Res Rev, 2012. 25(1): p. 150-61.

52. Mottram, V.H., Fatty acid metabolism in the liver: Part I. A method of fatty-acid extraction. J Physiol, 1910. 40(1-2): p. 122-34.

53. Mottram, V.H., Fatty acid metabolism in the liver: II. The relation of the fatty acids in the food of plaice to those in their livers and myotomes. J Physiol, 1912. 45(5): p. 363-9.

54. Macpherson, W.E., Certain Relationships Between the Pancreas and the Liver in Carbohydrate Metabolism. Cal West Med, 1933. 39(4): p. 273.

55. Aylward, F.X., H.J. Channon, and H. Wilkinson, The liver and fat metabolism. Biochem J, 1935. 29(1): p. 169-78.

56. Feldstein, A.E., Novel insights into the pathophysiology of nonalcoholic fatty liver disease. Semin Liver Dis, 2010. 30(4): p. 391-401.

57. Franco-Bourland, R.E. and N. Mendez-Sanchez, The liver is the key organ for the development of metabolic syndrome. Ann Hepatol, 2011. 10(2): p. 216-7.

58. Hundal, R.S., et al., Mechanism by which metformin reduces glucose production in type 2 diabetes. Diabetes, 2000. 49(12): p. 2063-9.

59. Evans, J.L., J.F. Youngren, and I.D. Goldfine, Effective treatments for insulin resistance: trim the fat and douse the fire. Trends Endocrinol Metab, 2004. 15(9): p. 425-31.

60. Medina-Santillan, R., et al., Hepatic manifestations of metabolic syndrome. Diabetes Metab Res Rev, 2013.

61. Postic, C. and J. Girard, The role of the lipogenic pathway in the development of hepatic steatosis. Diabetes Metab, 2008. 34(6 Pt 2): p. 643-8.

62. Sanyal, A.J., et al., Nonalcoholic steatohepatitis: association of insulin resistance and mitochondrial abnormalities. Gastroenterology, 2001. 120(5): p. 1183-92.

63. Neuschwander-Tetri, B.A., Hepatic lipotoxicity and the pathogenesis of nonalcoholic steatohepatitis: the central role of nontriglyceride fatty acid metabolites. Hepatology, 2010. 52(2): p. 774-88.

64. Fu, S., et al., Aberrant lipid metabolism disrupts calcium homeostasis causing liver endoplasmic reticulum stress in obesity. Nature, 2011. 473(7348): p. 528-31.

65. Fabbrini, E., et al., Alterations in fatty acid kinetics in obese adolescents with increased intrahepatic triglyceride content. Obesity (Silver Spring), 2009. 17(1): p. 25-9.

66. Magkos, F., et al., Increased whole-body adiposity without a concomitant increase in liver fat is not associated with augmented metabolic dysfunction. Obesity (Silver Spring), 2010. 18(8): p. 1510-5.

67. Browning, J.D., et al., Prevalence of hepatic steatosis in an urban population in the United States: impact of ethnicity. Hepatology, 2004. 40(6): p. 1387-95.

68. Clark, J.M. and A.M. Diehl, Nonalcoholic fatty liver disease: an underrecognized cause of cryptogenic cirrhosis. JAMA, 2003. 289(22): p. 3000-4.

69. Tsochatzis, E.A., G.V. Papatheodoridis, and A.J. Archimandritis, Adipokines in nonalcoholic steatohepatitis: from pathogenesis to implications in diagnosis and therapy. Mediators Inflamm, 2009. 2009: p. 831670.

70. Fukushima, J., et al., Adiponectin prevents progression of steatohepatitis in mice by regulating oxidative stress and Kupffer cell phenotype polarization. Hepatol Res, 2009. 39(7): p. 724-38.

71. Hebbard, L. and J. George, Animal models of nonalcoholic fatty liver disease. Nature Reviews Gastroenterology & Hepatology, 2011. 8(1): p. 34-44.

72. Xu, H., et al., Chronic inflammation in fat plays a crucial role in the development of obesity-related insulin resistance. J Clin Invest, 2003. 112(12): p. 1821-30.

73. Roldan-Valadez, E., et al., Imaging techniques for assessing hepatic fat content in nonalcoholic fatty liver disease. Ann Hepatol, 2008. 7(3): p. 212-20.

74. Demetris, A.J., et al., Intraobserver and interobserver variation in the histopathological assessment of liver allograft rejection. The Liver Transplantation Database (LTD) Investigators. Hepatology, 1991. 14(5): p. 751-5.

75. Intraobserver and interobserver variations in liver biopsy interpretation in patients with chronic hepatitis C. The French METAVIR Cooperative Study Group. Hepatology, 1994. 20(1 Pt 1): p. 15-20.

76. Schrauwen, P., W.H. Saris, and M.K. Hesselink, An alternative function for human uncoupling protein 3: protection of mitochondria against accumulation of nonesterified fatty acids inside the mitochondrial matrix. FASEB J, 2001. 15(13): p. 2497-502.

77. Zhang, X., et al., Hypothalamic IKKbeta/NF-kappaB and ER stress link overnutrition to energy imbalance and obesity. Cell, 2008. 135(1): p. 61-73.

78. Shoelson, S.E., L. Herrero, and A. Naaz, Obesity, inflammation, and insulin resistance. Gastroenterology, 2007. 132(6): p. 2169-80.

79. Sethi, J.K. and A.J. Vidal-Puig, Targeting fat to prevent diabetes. Cell Metab, 2007. 5(5): p. 323-5.

80. Weisberg, S.P., et al., Obesity is associated with macrophage accumulation in adipose tissue. J Clin Invest, 2003. 112(12): p. 1796-808.

81. Ouchi, N., et al., Adipokines in inflammation and metabolic disease. Nat Rev Immunol, 2011. 11(2): p. 85-97.

82. McBride, H.M., M. Neuspiel, and S. Wasiak, Mitochondria: more than just a powerhouse. Curr Biol, 2006. 16(14): p. R551-60.

83. Campbell, K. and K. Swann, Ca2+ oscillations stimulate an ATP increase during fertilization of mouse eggs. Dev Biol, 2006. 298(1): p. 225-33.

84. Galluzzi, L., O. Kepp, and G. Kroemer, Mitochondria: master regulators of danger signalling. Nat Rev Mol Cell Biol, 2012. 13(12): p. 780-8.

85. Enerback, S., The origins of brown adipose tissue. N Engl J Med, 2009. 360(19): p. 2021-3.

86. Ord, M.J., The effects of chemicals and radiations within the cell: an ultrastructural and micrurgical study using Amoeba proteus as a single-cell model. Int Rev Cytol, 1979. 61: p. 229-81.

87. De Pauw, A., et al., Mitochondrial (dys)function in adipocyte (de)differentiation and systemic metabolic alterations. Am J Pathol, 2009. 175(3): p. 927-39.

88. Begriche, K., et al., Mitochondrial adaptations and dysfunctions in nonalcoholic fatty liver disease. Hepatology, 2013.

89. Franz, M.J., et al., Evidence-based nutrition principles and recommendations for the treatment and prevention of diabetes and related complications. Diabetes Care, 2003. 26 Suppl 1: p. S51-61.

90. Englyst, K.N., S. Liu, and H.N. Englyst, Nutritional characterization and measurement of dietary carbohydrates. Eur J Clin Nutr, 2007. 61 Suppl 1: p. S19-39.

91. McMillan-Price, J., et al., Comparison of 4 diets of varying glycemic load on weight loss and cardiovascular risk reduction in overweight and obese young adults: a randomized controlled trial. Arch Intern Med, 2006. 166(14): p. 1466-75.

92. Iscovich, J.M., et al., Colon cancer in Argentina. II: Risk from fibre, fat and nutrients. Int J Cancer, 1992. 51(6): p. 858-61.

93. Wicki, A. and J. Hagmann, Diet and cancer. Swiss Med Wkly, 2011. 141: p. w13250.

94. Abdulla, M. and P. Gruber, Role of diet modification in cancer prevention. Biofactors, 2000. 12(1-4): p. 45-51.

95. Warburg, O., On the origin of cancer cells. Science, 1956. 123(3191): p. 309-14.

96. Gatenby, R.A. and R.J. Gillies, Why do cancers have high aerobic glycolysis? Nat Rev Cancer, 2004. 4(11): p. 891-9.

97. Gatenby, R.A. and R.J. Gillies, Glycolysis in cancer: a potential target for therapy. Int J Biochem Cell Biol, 2007. 39(7-8): p. 1358-66.

98. Wu, M., et al., Multiparameter metabolic analysis reveals a close link between attenuated mitochondrial bioenergetic function and enhanced glycolysis dependency in human tumor cells. Am J Physiol Cell Physiol, 2007. 292(1): p. C125-36.

99. Yeluri, S., et al., Cancer's craving for sugar: an opportunity for clinical exploitation. J Cancer Res Clin Oncol, 2009. 135(7): p. 867-77.

100. McIntyre, A., P.R. Gibson, and G.P. Young, Butyrate production from dietary fibre and protection against large bowel cancer in a rat model. Gut, 1993. 34(3): p. 386-91.

101. Jenkins, D.J., et al., Fiber and starchy foods: gut function and implications in disease. Am J Gastroenterol, 1986. 81(10): p. 920-30.

102. Marckmann, P., Dietary treatment of thrombogenic disorders related to the metabolic syndrome. Br J Nutr, 2000. 83 Suppl 1: p. S121-6.

103. Merriam, P.A., et al., Dietary intervention targeting increased fiber consumption for metabolic syndrome. J Acad Nutr Diet, 2012. 112(5): p. 621-3.

104. Bindels, L.B., et al., Gut microbiota-derived propionate reduces cancer cell proliferation in the liver. Br J Cancer, 2012. 107(8): p. 1337-44.

105. Barth, C., M. Sladek, and K. Decker, Dietary changes of cytoplasmic acetyl-CoA synthetase in different rat tissues. Biochim Biophys Acta, 1972. 260(1): p. 1-9.

106. Hayde, V.C., et al., Non-digestible fraction of beans (Phaseolus vulgaris L.) modulates signalling pathway genes at an early stage of colon cancer in Sprague-Dawley rats. Br J Nutr, 2012. 108 Suppl 1: p. S145-54.

107. Denise Robertson, M., Metabolic cross talk between the colon and the periphery: implications for insulin sensitivity. Proc Nutr Soc, 2007. 66(3): p. 351-61.

108. Leonel, A.J. and J.I. Alvarez-Leite, Butyrate: implications for intestinal function. Curr Opin Clin Nutr Metab Care, 2012. 15(5): p. 474-9.

109. Andersen, V., et al., Interaction between interleukin-10 (IL-10) polymorphisms and dietary fibre in relation to risk of colorectal cancer in a Danish case-cohort study. BMC Cancer, 2012. 12: p. 183.

110. Zimmerman, M.A., et al., Butyrate suppresses colonic inflammation through HDAC1-dependent Fas upregulation and Fas-mediated apoptosis of T cells. Am J Physiol Gastrointest Liver Physiol, 2012. 302(12): p. G1405-15.

111. Nguyen, K.A., et al., Dietary fiber enhances a tumor suppressor signaling pathway in the gut. Ann Surg, 2006. 243(5): p. 619-25; discussion 625-7.

112. Miller, T.L. and M.J. Wolin, Fermentations by saccharolytic intestinal bacteria. Am J Clin Nutr, 1979. 32(1): p. 164-72.

113. Stjernholm, R.L., R.E. Noble, and D. Koch-Weser, Formation of methylmalonyl-CoA and succinyl-CoA by extracts of mycobacterium smegmatis. Biochim Biophys Acta, 1962. 64: p. 174-7.

114. Meng, Q., et al., Fermentation substrate and dilution rate interact to affect microbial growth and efficiency. J Anim Sci, 1999. 77(1): p. 206-14.

115. Cummings, J.H., et al., Short chain fatty acids in human large intestine, portal, hepatic and venous blood. Gut, 1987. 28(10): p. 1221-7.

116. Topping, D.L. and P.M. Clifton, Short-chain fatty acids and human colonic function: roles of resistant starch and nonstarch polysaccharides. Physiol Rev, 2001. 81(3): p. 1031-64.

117. Bergman, E.N., Energy contributions of volatile fatty acids from the gastrointestinal tract in various species. Physiol Rev, 1990. 70(2): p. 567-90.

118. Robertson, D.J., et al., Fat, fiber, meat and the risk of colorectal adenomas. Am J Gastroenterol, 2005. 100(12): p. 2789-95.

119. Roediger, W.E., Anaerobic bacteria, the colon and colitis. Aust N Z J Surg, 1980. 50(1): p. 73-5.

120. Cook, S.I. and J.H. Sellin, Review article: short chain fatty acids in health and disease. Aliment Pharmacol Ther, 1998. 12(6): p. 499-507.

121. Roediger, W.E., Role of anaerobic bacteria in the metabolic welfare of the colonic mucosa in man. Gut, 1980. 21(9): p. 793-8.

122. Mortensen, P.B. and M.R. Clausen, Short-chain fatty acids in the human colon: relation to gastrointestinal health and disease. Scand J Gastroenterol Suppl, 1996. 216: p. 132-48.

123. Le Poul, E., et al., Functional characterization of human receptors for short chain fatty acids and their role in polymorphonuclear cell activation. J Biol Chem, 2003. 278(28): p. 25481-9.

124. Brown, A.J., et al., The Orphan G protein-coupled receptors GPR41 and GPR43 are activated by propionate and other short chain carboxylic acids. J Biol Chem, 2003. 278(13): p. 11312-9.

125. Kondo, T., et al., Acetic Acid Upregulates the Expression of Genes for Fatty Acid Oxidation Enzymes in Liver To Suppress Body Fat Accumulation. Journal of Agricultural and Food Chemistry, 2009. 57(13): p. 5982-5986.

126. Yamashita, H., et al., Effects of Acetate on Lipid Metabolism in Muscles and Adipose Tissues of Type 2 Diabetic Otsuka Long-Evans Tokushima Fatty (OLETF) Rats. Bioscience, Biotechnology, and Biochemistry, 2009. 73(3): p. 570-576.

127. Galisteo, M., J. Duarte, and A. Zarzuelo, Effects of dietary fibers on disturbances clustered in the metabolic syndrome. J Nutr Biochem, 2008. 19(2): p. 71-84.

128. Vinolo, M.A., et al., Regulation of inflammation by short chain fatty acids. Nutrients, 2011. 3(10): p. 858-76.

129. Van Loo, J., A. Franck, and M. Roberfroid, Functional food properties of non-digestible oligosaccharides. Br J Nutr, 1999. 82(4): p. 329.

130. Lehninger, A.L., Oxidative phosphorylation in normal and tumour cells. Acta Unio Int Contra Cancrum, 1958. 14(1): p. 52-3.

131. Morgan, H.D., et al., Epigenetic reprogramming in mammals. Hum Mol Genet, 2005. 14 Spec No 1: p. R47-58.

132. Sadoul, K., et al., Regulation of protein turnover by acetyltransferases and deacetylases. Biochimie, 2008. 90(2): p. 306-12.

133. Pandolfi, P.P., Histone deacetylases and transcriptional therapy with their inhibitors. Cancer Chemother Pharmacol, 2001. 48 Suppl 1: p. S17-9.

134. Thiagalingam, S., et al., Histone deacetylases: unique players in shaping the epigenetic histone code. Ann N Y Acad Sci, 2003. 983: p. 84-100.

135. Riggs, M.G., et al., n-Butyrate causes histone modification in HeLa and Friend erythroleukaemia cells. Nature, 1977. 268(5619): p. 462-4.

136. Sargeant, A.M., et al., OSU-HDAC42, a histone deacetylase inhibitor, blocks prostate tumor progression in the transgenic adenocarcinoma of the mouse prostate model. Cancer Res, 2008. 68(10): p. 3999-4009.

137. Donohoe, D.R., et al., The microbiome and butyrate regulate energy metabolism and autophagy in the mammalian colon. Cell Metab, 2011. 13(5): p. 517-26.

138. Li, C.J. and T.H. Elsasser, Butyrate-induced apoptosis and cell cycle arrest in bovine kidney epithelial cells: involvement of caspase and proteasome pathways. J Anim Sci, 2005. 83(1): p. 89-97.

139. Smith-Warner, S.A., et al., Types of dietary fat and breast cancer: a pooled analysis of cohort studies. Int J Cancer, 2001. 92(5): p. 767-74.

140. Renehan, A.G., D.L. Roberts, and C. Dive, Obesity and cancer: pathophysiological and biological mechanisms. Arch Physiol Biochem, 2008. 114(1): p. 71-83.

141. Haslam, D.W. and W.P. James, Obesity. Lancet, 2005. 366(9492): p. 1197-209.

142. Larsson, S.C. and A. Wolk, Overweight and obesity and incidence of leukemia: a meta-analysis of cohort studies. Int J Cancer, 2008. 122(6): p. 1418-21.

143. Hursting, S.D. and N.A. Berger, Energy balance, host-related factors, and cancer progression. J Clin Oncol, 2010. 28(26): p. 4058-65.

144. Carter, J.C. and F.C. Church, Obesity and breast cancer: the roles of peroxisome proliferator-activated receptor-gamma and plasminogen activator inhibitor-1. PPAR Res, 2009. 2009: p. 345320.

145. Polednak, A.P., Comorbid diabetes mellitus and risk of death after diagnosis of colorectal cancer: a population-based study. Cancer Detect Prev, 2006. 30(5): p. 466-72.

146. Harriss, D.J., et al., Lifestyle factors and colorectal cancer risk (2): a systematic review and meta-analysis of associations with leisure-time physical activity. Colorectal Dis, 2009. 11(7): p. 689-701.

147. Hanahan, D. and R.A. Weinberg, The hallmarks of cancer. Cell, 2000. 100(1): p. 57-70.

148. Hanahan, D. and R.A. Weinberg, Hallmarks of cancer: the next generation. Cell, 2011. 144(5): p. 646-74.

149. Pan, J.G. and T.W. Mak, Metabolic targeting as an anticancer strategy: dawn of a new era? Sci STKE, 2007. 2007(381): p. pe14.

150. DeBerardinis, R.J., et al., Beyond aerobic glycolysis: transformed cells can engage in glutamine metabolism that exceeds the requirement for protein and nucleotide synthesis. Proc Natl Acad Sci U S A, 2007. 104(49): p. 19345-50.

151. Warburg, O., F. Wind, and E. Negelein, The Metabolism of Tumors in the Body. J Gen Physiol, 1927. 8(6): p. 519-30.

152. Vander Heiden, M.G., L.C. Cantley, and C.B. Thompson, Understanding the Warburg effect: the metabolic requirements of cell proliferation. Science, 2009. 324(5930): p. 1029-33.

153. Hsu, P.P. and D.M. Sabatini, Cancer cell metabolism: Warburg and beyond. Cell, 2008. 134(5): p. 703-7.

154. DeBerardinis, R.J., et al., The biology of cancer: metabolic reprogramming fuels cell growth and proliferation. Cell Metab, 2008. 7(1): p. 11-20.

155. Nijsten, M.W. and G.M. van Dam, Hypothesis: using the Warburg effect against cancer by reducing glucose and providing lactate. Med Hypotheses, 2009. 73(1): p. 48-51.

156. Randle, P.J., P.J. England, and R.M. Denton, Control of the tricarboxylate cycle and its interactions with glycolysis during acetate utilization in rat heart. Biochem J, 1970. 117(4): p. 677-95.

157. Randle, P.J., et al., Regulation of pyruvate oxidation and the conservation of glucose. Biochem Soc Symp, 1978(43): p. 47-67.

158. Wolfe, R.R., Metabolic interactions between glucose and fatty acids in humans. Am J Clin Nutr, 1998. 67(3 Suppl): p. 519S-526S.

159. Higgins, J.A., Resistant starch: metabolic effects and potential health benefits. J AOAC Int, 2004. 87(3): p. 761-8.

160. Donohoe, D.R., et al., The warburg effect dictates the mechanism of butyrate-mediated histone acetylation and cell proliferation. Mol Cell, 2012. 48(4): p. 612-26.

161. Seyfried, T.N. and L.M. Shelton, Cancer as a metabolic disease. Nutr Metab (Lond), 2010. 7: p. 7.

162. Roden, M., How free fatty acids inhibit glucose utilization in human skeletal muscle. News Physiol Sci, 2004. 19: p. 92-6.

163. de Ruijter, A.J., et al., Histone deacetylases (HDACs): characterization of the classical HDAC family. Biochem J, 2003. 370(Pt 3): p. 737-49.

164. Weichert, W., HDAC expression and clinical prognosis in human malignancies. Cancer Lett, 2009. 280(2): p. 168-76.

165. Strahl, B.D. and C.D. Allis, The language of covalent histone modifications. Nature, 2000. 403(6765): p. 41-5.

166. Biel, M., V. Wascholowski, and A. Giannis, Epigenetics--an epicenter of gene regulation: histones and histone-modifying enzymes. Angew Chem Int Ed Engl, 2005. 44(21): p. 3186-216.

167. Eastwood, M. and D. Kritchevsky, Dietary fiber: how did we get where we are? Annu Rev Nutr, 2005. 25: p. 1-8.

168. Wong, J.M., et al., Colonic health: fermentation and short chain fatty acids. J Clin Gastroenterol, 2006. 40(3): p. 235-43.

169. Friedman, G., Diet and the irritable bowel syndrome. Gastroenterol Clin North Am, 1991. 20(2): p. 313-24.

170. Yamashita, H., et al., Improvement of Obesity and Glucose Tolerance by Acetate in Type 2 Diabetic Otsuka Long-Evans Tokushima Fatty (OLETF) Rats. Bioscience, Biotechnology, and Biochemistry, 2007. 71(5): p. 1236-1243.

171. Hong, Y.H., Acetate and Propionate Short Chain Fatty Acids Stimulate Adipogenesis via GPCR43. Endocrinology, 2005. 146(12): p. 5092-5099.

172. Cummings, J.H., Short chain fatty acids in the human colon. Gut, 1981. 22(9): p. 763-79.

173. Steliou, K., et al., Butyrate histone deacetylase inhibitors. Biores Open Access, 2012. 1(4): p. 192-8.

174. Tang, J., et al., Pharmacokinetics and biodistribution of itraconazole in rats and mice following intravenous administration in a novel liposome formulation. Drug Deliv, 2010. 17(4): p. 223-30.

175. Kosloski, M.J., et al., Effect of lipid vesicle (liposome) encapsulation of methotrexate on its chemotherapeutic efficacy in solid rodent tumors. Cancer Res, 1978. 38(9): p. 2848-53.

176. Papahadjopoulos, D., et al., New methodology for liposome targeting to specific cells. Ann N Y Acad Sci, 1985. 446: p. 341-8.

177. Allison, S.D., Liposomal drug delivery. J Infus Nurs, 2007. 30(2): p. 89-95; quiz 120.

178. Bangham, A.D., M.M. Standish, and J.C. Watkins, Diffusion of univalent ions across the lamellae of swollen phospholipids. J Mol Biol, 1965. 13(1): p. 238-52.

179. Davis, S.S., Coming of age of lipid-based drug delivery systems. Adv Drug Deliv Rev, 2004. 56(9): p. 1241-2.

180. Lian, T. and R.J. Ho, Trends and developments in liposome drug delivery systems. J Pharm Sci, 2001. 90(6): p. 667-80.

181. Stefaniak, A.B., et al., International guidelines for the *in vivo* assessment of skin properties in non-clinical settings: part 1. pH. Skin Res Technol, 2013. 19(2): p. 59-68.

182. Booysen, L.L., et al., *In vivo*/in vitro pharmacokinetic and pharmacodynamic study of spray-dried poly-(dl-lactic-co-glycolic) acid nanoparticles encapsulating rifampicin and isoniazid. Int J Pharm, 2013. 444(1-2): p. 10-7.

183. Schlieper, P. and R. Steiner, The effect of different surface chemical groups on drug binding to liposomes. Chem Phys Lipids, 1983. 34(1): p. 81-92.

184. Pollock, S., et al., Uptake and trafficking of liposomes to the endoplasmic reticulum. FASEB J, 2010. 24(6): p. 1866-78.

185. Dadashzadeh, S., A.M. Vali, and M. Rezaie, The effect of PEG coating on in vitro cytotoxicity and *in vivo* disposition of topotecan loaded liposomes in rats. Int J Pharm, 2008. 353(1-2): p. 251-9.

186. Levchenko, T.S., et al., Liposome clearance in mice: the effect of a separate and combined presence of surface charge and polymer coating. Int J Pharm, 2002. 240(1-2): p. 95-102.

187. Krause, H.J., R.L. Juliano, and S. Regen, In vivo behavior of polymerized lipid vesicles. J Pharm Sci, 1987. 76(1): p. 1-5.

188. Krause, W., et al., Preclinical characterization of iopromide-carrying liposomes. Invest Radiol, 1991. 26 Suppl 1: p. S172-4; discussion S175-6.

189. Moghimi, S.M. and J. Szebeni, Stealth liposomes and long circulating nanoparticles: critical issues in pharmacokinetics, opsonization and protein-binding properties. Prog Lipid Res, 2003. 42(6): p. 463-78.

190. Blume, G., et al., Specific targeting with poly(ethylene glycol)-modified liposomes: coupling of homing devices to the ends of the polymeric chains combines effective target binding with long circulation times. Biochim Biophys Acta, 1993. 1149(1): p. 180-4.

191. Klibanov, A.L., et al., Amphipathic polyethyleneglycols effectively prolong the circulation time of liposomes. FEBS Lett, 1990. 268(1): p. 235-7.

192. Gregoriadis, G., et al., Drug-carrier potential of liposomes in cancer chemotherapy. Lancet, 1974. 1(7870): p. 1313-6.

193. Symon, Z., et al., Selective delivery of doxorubicin to patients with breast carcinoma metastases by stealth liposomes. Cancer, 1999. 86(1): p. 72-8.

194. Northfelt, D.W., et al., Doxorubicin encapsulated in liposomes containing surface-bound polyethylene glycol: pharmacokinetics, tumor localization, and safety in patients with AIDS-related Kaposi's sarcoma. J Clin Pharmacol, 1996. 36(1): p. 55-63.

195. Torchilin, V.P., Targeted pharmaceutical nanocarriers for cancer therapy and imaging. AAPS J, 2007. 9(2): p. E128-47.

196. Matsumura, Y. and H. Maeda, A new concept for macromolecular therapeutics in cancer chemotherapy: mechanism of tumoritropic accumulation of proteins and the antitumor agent smancs. Cancer Res, 1986. 46(12 Pt 1): p. 6387-92.

197. Drummond, D.C., et al., Optimizing liposomes for delivery of chemotherapeutic agents to solid tumors. Pharmacol Rev, 1999. 51(4): p. 691-743.

198. Kuai, R., et al., Efficient delivery of payload into tumor cells in a controlled manner by TAT and thiolytic cleavable PEG co-modified liposomes. Mol Pharm, 2010. 7(5): p. 1816-26.

199. Willmann, J.K., et al., Molecular imaging in drug development. Nat Rev Drug Discov, 2008. 7(7): p. 591-607.

200. Cassidy, P.J. and G.K. Radda, Molecular imaging perspectives. J R Soc Interface, 2005. 2(3): p. 133-44.

201. Weissleder, R. and M.J. Pittet, Imaging in the era of molecular oncology. Nature, 2008. 452(7187): p. 580-9.

202. Wintermark, M. and J. Fiebach, Iodinated and gadolinium contrast media in computed tomography (CT) and magnetic resonance (MR) stroke imaging. Curr Med Chem, 2006. 13(22): p. 2717-23.

203. Raymond, K.N. and V.C. Pierre, Next generation, high relaxivity gadolinium MRI agents. Bioconjug Chem, 2005. 16(1): p. 3-8.

204. Bertini, I., et al., Persistent contrast enhancement by sterically stabilized paramagnetic liposomes in murine melanoma. Magn Reson Med, 2004. 52(3): p. 669-72.

205. Storrs, R.W., et al., Paramagnetic polymerized liposomes as new recirculating MR contrast agents. J Magn Reson Imaging, 1995. 5(6): p. 719-24.

206. Koole, R., et al., Paramagnetic lipid-coated silica nanoparticles with a fluorescent quantum dot core: a new contrast agent platform for multimodality imaging. Bioconjug Chem, 2008. 19(12): p. 2471-9.

207. Weissleder, R., Scaling down imaging: molecular mapping of cancer in mice. Nat Rev Cancer, 2002. 2(1): p. 11-8.

208. Phelps, M.E., et al., Application of annihilation coincidence detection to transaxial reconstruction tomography. J Nucl Med, 1975. 16(3): p. 210-24.

209. Inokuma, T., et al., Evaluation of pancreatic tumors with positron emission tomography and F-18 fluorodeoxyglucose: comparison with CT and US. Radiology, 1995. 195(2): p. 345-52.

210. Ford, E.C., et al., 18F-FDG PET/CT for image-guided and intensity-modulated radiotherapy. J Nucl Med, 2009. 50(10): p. 1655-65.

211. Massoud, T.F. and S.S. Gambhir, Molecular imaging in living subjects: seeing fundamental biological processes in a new light. Genes Dev, 2003. 17(5): p. 545-80.

212. Botchway, S.W., et al., A novel method for observing proteins in vivo using a small fluorescent label and multiphoton imaging. Biochem J, 2005. 390(Pt 3): p. 787-90.

213. Kamaly, N., et al., Bimodal paramagnetic and fluorescent liposomes for cellular and tumor magnetic resonance imaging. Bioconjug Chem, 2008. 19(1): p. 118-29.

214. Boddapati, S.V., et al., Mitochondriotropic liposomes. J Liposome Res, 2005. 15(1-2): p. 49-58.

215. Suckow, C., et al., Multimodality rodent imaging chambers for use under barrier conditions with gas anesthesia. Mol Imaging Biol, 2009. 11(2): p. 100-6.

216. Kenny, G.D., et al., Novel multifunctional nanoparticle mediates siRNA tumour delivery, visualisation and therapeutic tumour reduction in vivo. J Control Release, 2011. 149(2): p. 111-6.

217. Keller, M., et al., Thermodynamic aspects and biological profile of CDAN/DOPE and DC-Chol/DOPE lipoplexes. Biochemistry, 2003. 42(20): p. 6067-77.

218. Ali, M.H., et al., Solubilisation of drugs within liposomal bilayers: alternatives to cholesterol as a membrane stabilising agent. J Pharm Pharmacol, 2010. 62(11): p. 1646-55.

219. Ashok, B., et al., In vitro characterization of PEGylated phospholipid micelles for improved drug solubilization: effects of PEG chain length and PC incorporation. J Pharm Sci, 2004. 93(10): p. 2476-87.

220. Krishnadas, A., I. Rubinstein, and H. Onyuksel, Sterically stabilized phospholipid mixed micelles: in vitro evaluation as a novel carrier for water-insoluble drugs. Pharm Res, 2003. 20(2): p. 297-302.

221. Bach, D., et al., The oxysterol 3beta-hydroxy-5-oxo-5,6-secocholestan-6-al changes the phase behavior and structure of phosphatidylethanolamine-phosphatidylcholine mixtures. Chem Phys Lipids, 2011. 164(7): p. 672-9.

222. Hodenius, M., et al., Fluorescent magnetoliposomes as a platform technology for functional and molecular MR and optical imaging. Contrast Media Mol Imaging, 2012. 7(1): p. 59-67.

223. Heyes, D.M., et al., First derivative of the hard-sphere radial distribution function at contact. J Phys Condens Matter, 2006. 18(32): p. 7553-8.

224. Boyer, P.D., G.A. Ballou, and J.M. Luck, The combination of fatty acids and related compounds with serum albumin; the nature and extent of the combination. J Biol Chem, 1947. 167(2): p. 407-24.

225. Chatham, J.C. and J.R. Forder, Lactic acid and protein interactions: implications for the NMR visibility of lactate in biological systems. Biochim Biophys Acta, 1999. 1426(1): p. 177-84.

226. Wisse, E., et al., The liver sieve: considerations concerning the structure and function of endothelial fenestrae, the sinusoidal wall and the space of Disse. Hepatology, 1985. 5(4): p. 683-92.

227. Caravan, P., et al., Gadolinium(III) Chelates as MRI Contrast Agents: Structure, Dynamics, and Applications. Chem Rev, 1999. 99(9): p. 2293-352.

228. van Bochove, G.S., et al., Contrast enhancement by differently sized paramagnetic MRI contrast agents in mice with two phenotypes of atherosclerotic plaque. Contrast Media Mol Imaging, 2011. 6(1): p. 35-45.

229. Marik, J. and J.L. Sutcliffe, Fully automated preparation of n.c.a. 4-[18F]fluorobenzoic acid and N-succinimidyl 4-[18F]fluorobenzoate using a Siemens/CTI chemistry process control unit (CPCU). Appl Radiat Isot, 2007. 65(2): p. 199-203.

230. Keenan, M.J., et al., Effects of resistant starch, a non-digestible fermentable fiber, on reducing body fat. Obesity (Silver Spring), 2006. 14(9): p. 1523-34.

231. Al-Lahham, S.a.H., et al., Biological effects of propionic acid in humans; metabolism, potential applications and underlying mechanisms. Biochimica et Biophysica Acta (BBA) - Molecular and Cell Biology of Lipids, 2010. 1801(11): p. 1175-1183.

232. Englyst, H.N., et al., Dietary fiber and resistant starch. Am J Clin Nutr, 1987. 46(6): p. 873-4.

233. Roberfroid, M., Prebiotics: the concept revisited. J Nutr, 2007. 137(3 Suppl 2): p. 830S-7S.

234. Wettenhall, J.M. and G.K. Smyth, limmaGUI: a graphical user interface for linear modeling of microarray data. Bioinformatics, 2004. 20(18): p. 3705-6.

235. Lairon, D., Macronutrient intake and modulation on chylomicron production and clearance. Atheroscler Suppl, 2008. 9(2): p. 45-8.

236. Kennedy, A.R., et al., A high-fat, ketogenic diet induces a unique metabolic state in mice. Am J Physiol Endocrinol Metab, 2007. 292(6): p. E1724-39.

237. Akanji, A.O., M.A. Bruce, and K.N. Frayn, Effect of acetate infusion on energy expenditure and substrate oxidation rates in non-diabetic and diabetic subjects. Eur J Clin Nutr, 1989. 43(2): p. 107-15.

238. Akanji, A.O., et al., The relationship of plasma acetate with glucose and other blood intermediary metabolites in non-diabetic and diabetic subjects. Clin Chim Acta, 1989. 185(1): p. 25-34.

239. Smith, G.I., A.E. Jeukendrup, and D. Ball, Sodium acetate induces a metabolic alkalosis but not the increase in fatty acid oxidation observed following bicarbonate ingestion in humans. J Nutr, 2007. 137(7): p. 1750-6.

240. Kondo, T., et al., Acetic acid upregulates the expression of genes for fatty acid oxidation enzymes in liver to suppress body fat accumulation. J Agric Food Chem, 2009. 57(13): p. 5982-6.

241. Svendsen, A., Lipase protein engineering. Biochim Biophys Acta, 2000. 1543(2): p. 223-238.

242. Astbury, S.M. and B.M. Corfe, Uptake and metabolism of the short-chain fatty acid butyrate, a critical review of the literature. Curr Drug Metab, 2012. 13(6): p. 815-21.

243. Clausen, M.R. and P.B. Mortensen, Kinetic studies on colonocyte metabolism of short chain fatty acids and glucose in ulcerative colitis. Gut, 1995. 37(5): p. 684-9.

244. Thomas, E.L., et al., Hepatic triglyceride content and its relation to body adiposity: a magnetic resonance imaging and proton magnetic resonance spectroscopy study. Gut, 2005. 54(1): p. 122-7.

245. Powell, E.E., et al., The natural history of nonalcoholic steatohepatitis: a follow-up study of forty-two patients for up to 21 years. Hepatology, 1990. 11(1): p. 74-80.

246. Sun, Z. and M.A. Lazar, Dissociating fatty liver and diabetes. Trends Endocrinol Metab, 2013. 24(1): p. 4-12.

247. Fernandes, J., J. Vogt, and T.M. Wolever, Intravenous acetate elicits a greater free fatty acid rebound in normal than hyperinsulinaemic humans. Eur J Clin Nutr, 2012. 66(9): p. 1029-34.

248. Khandekar, M.J., P. Cohen, and B.M. Spiegelman, Molecular mechanisms of cancer development in obesity. Nat Rev Cancer, 2011. 11(12): p. 886-95.

249. Park, H., et al., The fatty acid composition of plasma cholesteryl esters and estimated desaturase activities in patients with nonalcoholic fatty liver disease and the effect of long-term ezetimibe therapy on these levels. Clin Chim Acta, 2010. 411(21-22): p. 1735-40.

250. Williams, K.W., M.M. Scott, and J.K. Elmquist, From observation to experimentation: leptin action in the mediobasal hypothalamus. Am J Clin Nutr, 2009. 89(3): p. 985S-990S.

251. Mizuno, T., et al., Effects of nutritional status and aging on leptin gene expression in mice: importance of glucose. Horm Metab Res, 1996. 28(12): p. 679-84.

252. Sonnenberg, L.M., et al., Diet and plasma lipids in women. II. Macronutrients and plasma triglycerides, high-density lipoprotein, and the ratio of total to high-density lipoprotein

cholesterol in women: the Framingham nutrition studies. J Clin Epidemiol, 1996. 49(6): p. 665-72.

253. Chan, T.F., et al., Adiponectin and glucose levels in women with negative or false positive glucose challenge test. Eur J Obstet Gynecol Reprod Biol, 2006. 129(1): p. 31-5.

254. Hotamisligil, G.S., N.S. Shargill, and B.M. Spiegelman, Adipose expression of tumor necrosis factor-alpha: direct role in obesity-linked insulin resistance. Science, 1993. 259(5091): p. 87-91.

255. Grayson, M.H. and M.J. Holtzman, Chemokine complexity: the case for CCL5. Am J Respir Cell Mol Biol, 2006. 35(2): p. 143-6.

256. Holt, J.E., et al., CXCR4/SDF1 interaction inhibits the primordial to primary follicle transition in the neonatal mouse ovary. Dev Biol, 2006. 293(2): p. 449-60.

257. Stefanovic, L., D.A. Brenner, and B. Stefanovic, Direct hepatotoxic effect of KC chemokine in the liver without infiltration of neutrophils. Exp Biol Med (Maywood), 2005. 230(8): p. 573-86.

258. Sethi, R., et al., Differential expression of caveolin-1 and caveolin-3: potential marker for cardiac toxicity subsequent to chronic ozone inhalation. Mol Cell Biochem, 2012. 369(1-2): p. 9-15.

259. Warzocha, K., et al., Tumor necrosis factor ligand-receptor system can predict treatment outcome in lymphoma patients. J Clin Oncol, 1997. 15(2): p. 499-508.

260. Hershey, G.K., et al., The association of atopy with a gain-of-function mutation in the alpha subunit of the interleukin-4 receptor. N Engl J Med, 1997. 337(24): p. 1720-5.

261. Liao, W., et al., Blocking microsomal triglyceride transfer protein interferes with apoB secretion without causing retention or stress in the ER. J Lipid Res, 2003. 44(5): p. 978-85.

262. Esposito, K., et al., Association of low interleukin-10 levels with the metabolic syndrome in obese women. J Clin Endocrinol Metab, 2003. 88(3): p. 1055-8.

263. Ishikawa, S., et al., Inverse association between serum lipoprotein(a) and cerebral hemorrhage in the Japanese population. Thromb Res, 2013. 131(2): p. e54-8.

264. Dudoit, S. and T.P. Speed, A score test for the linkage analysis of qualitative and quantitative traits based on identity by descent data from sib-pairs. Biostatistics, 2000. 1(1): p. 1-26.

265. Chavin, K.D., et al., Obesity induces expression of uncoupling protein-2 in hepatocytes and promotes liver ATP depletion. J Biol Chem, 1999. 274(9): p. 5692-700.

266. Taylor, E.B., et al., Endurance training increases LKB1 and MO25 protein but not AMP-activated protein kinase kinase activity in skeletal muscle. Am J Physiol Endocrinol Metab, 2004. 287(6): p. E1082-9.

267. Tsuchida, A., et al., Peroxisome proliferator-activated receptor (PPAR)alpha activation increases adiponectin receptors and reduces obesity-related inflammation in adipose tissue: comparison of activation of PPARalpha, PPARgamma, and their combination. Diabetes, 2005. 54(12): p. 3358-70.

268. van Raalte, D.H., et al., Peroxisome proliferator-activated receptor (PPAR)-alpha: a pharmacological target with a promising future. Pharm Res, 2004. 21(9): p. 1531-8.

269. Faergeman, N.J. and J. Knudsen, Role of long-chain fatty acyl-CoA esters in the regulation of metabolism and in cell signalling. Biochem J, 1997. 323 (Pt 1): p. 1-12.

270. Fushimi, T., et al., Dietary acetic acid reduces serum cholesterol and triacylglycerols in rats fed a cholesterol-rich diet. Br J Nutr, 2006. 95(5): p. 916-24.

271. Monovich, L., et al., Suppression of HDAC nuclear export and cardiomyocyte hypertrophy by novel irreversible inhibitors of CRM1. Biochim Biophys Acta, 2009. 1789(5): p. 422-31.

272. Davie, J.R., Inhibition of histone deacetylase activity by butyrate. J Nutr, 2003. 133(7 Suppl): p. 2485S-2493S.

273. Mihaylova, M.M., et al., Class IIa histone deacetylases are hormone-activated regulators of FOXO and mammalian glucose homeostasis. Cell, 2011. 145(4): p. 607-21.

274. Wang, C., et al., Thailandepsins: bacterial products with potent histone deacetylase inhibitory activities and broad-spectrum antiproliferative activities. J Nat Prod, 2011. 74(10): p. 2031-8.

275. Bryzgalova, G., et al., Mechanisms of antidiabetogenic and body weight-lowering effects of estrogen in high-fat diet-fed mice. Am J Physiol Endocrinol Metab, 2008. 295(4): p. E904-12.

276. Soliman, M.L. and T.A. Rosenberger, Acetate supplementation increases brain histone acetylation and inhibits histone deacetylase activity and expression. Mol Cell Biochem, 2011. 352(1-2): p. 173-80.

277. Parker, K., et al., Class I histone deacetylase Thd1p promotes global chromatin condensation in Tetrahymena thermophila. Eukaryot Cell, 2007. 6(10): p. 1913-24.

278. Corfe, B.M., Hypothesis: butyrate is not an HDAC inhibitor, but a product inhibitor of deacetylation. Mol Biosyst, 2012. 8(6): p. 1609-12.

279. Randle, P.J., et al., The glucose fatty-acid cycle. Its role in insulin sensitivity and the metabolic disturbances of diabetes mellitus. Lancet, 1963. 1(7285): p. 785-9.

280. Hardie, D.G., Role of AMP-activated protein kinase in the metabolic syndrome and in heart disease. FEBS Lett, 2008. 582(1): p. 81-9.

281. Hardie, D.G. and D. Carling, The AMP-activated protein kinase--fuel gauge of the mammalian cell? Eur J Biochem, 1997. 246(2): p. 259-73.

282. Hardie, D.G., et al., Regulation of lipid metabolism by the AMP-activated protein kinase. Biochem Soc Trans, 1997. 25(4): p. 1229-31.

283. Kawaguchi, T., et al., Mechanism for fatty acid "sparing" effect on glucose-induced transcription: regulation of carbohydrate-responsive element-binding protein by AMP-activated protein kinase. J Biol Chem, 2002. 277(6): p. 3829-35.

284. Sakakibara, S., et al., Acetic acid activates hepatic AMPK and reduces hyperglycemia in diabetic KK-A(y) mice. Biochem Biophys Res Commun, 2006. 344(2): p. 597-604.

285. Watt, M.J., et al., Fatty acids stimulate AMP-activated protein kinase and enhance fatty acid oxidation in L6 myotubes. J Physiol, 2006. 574(Pt 1): p. 139-47.

286. Suzuki, A., et al., Leptin stimulates fatty acid oxidation and peroxisome proliferator-activated receptor alpha gene expression in mouse C2C12 myoblasts by changing the

subcellular localization of the alpha2 form of AMP-activated protein kinase. Mol Cell Biol, 2007. 27(12): p. 4317-27.

287. Lin, V.C., et al., Activation of AMPK by pterostilbene suppresses lipogenesis and cell-cycle progression in p53 positive and negative human prostate cancer cells. J Agric Food Chem, 2012. 60(25): p. 6399-407.

288. Zhou, G., et al., Role of AMP-activated protein kinase in mechanism of metformin action. J Clin Invest, 2001. 108(8): p. 1167-74.

289. Hue, L. and H. Taegtmeyer, The Randle cycle revisited: a new head for an old hat. Am J Physiol Endocrinol Metab, 2009. 297(3): p. E578-91.

290. Schreurs, M., F. Kuipers, and F.R. van der Leij, Regulatory enzymes of mitochondrial beta-oxidation as targets for treatment of the metabolic syndrome. Obes Rev, 2010. 11(5): p. 380-8.

291. Cani, P.D., et al., Oligofructose promotes satiety in healthy human: a pilot study. European Journal of Clinical Nutrition, 2006. 60(5): p. 567-72.

292. Hamer, H.M., et al., Review article: the role of butyrate on colonic function. Aliment Pharmacol Ther, 2008. 27(2): p. 104-19.

293. Scheffler, I.E., Mitochondria make a come back. Adv Drug Deliv Rev, 2001. 49(1-2): p. 3-26.

294. Randle, P.J., Regulatory interactions between lipids and carbohydrates: the glucose fatty acid cycle after 35 years. Diabetes Metab Rev, 1998. 14(4): p. 263-83.

295. Borowicki, A., et al., Fermented wheat aleurone inhibits growth and induces apoptosis in human HT29 colon adenocarcinoma cells. Br J Nutr, 2010. 103(3): p. 360-9.

296. Krasnici, S., et al., Effect of the surface charge of liposomes on their uptake by angiogenic tumor vessels. Int J Cancer, 2003. 105(4): p. 561-7.

297. Abu Lila, A.S., T. Ishida, and H. Kiwada, Recent advances in tumor vasculature targeting using liposomal drug delivery systems. Expert Opin Drug Deliv, 2009. 6(12): p. 1297-309.

298. Campbell, R.B., et al., Fighting cancer: from the bench to bedside using second generation cationic liposomal therapeutics. J Pharm Sci, 2009. 98(2): p. 411-29.

299. Normura, T., Further studies on X-ray and chemically induced germ-line alterations causing tumors and malformations in mice. Prog Clin Biol Res, 1986. 209B: p. 13-20.

300. Rodrigues, N.R., et al., p53 mutations in colorectal cancer. Proc Natl Acad Sci U S A, 1990. 87(19): p. 7555-9.

301. Bhattacharyya, N.P., et al., Mutator phenotypes in human colorectal carcinoma cell lines. Proc Natl Acad Sci U S A, 1994. 91(14): p. 6319-23.

302. Zhang, G., et al., Unraveling the mystery of cancer metabolism in the genesis of tumor-initiating cells and development of cancer. Biochim Biophys Acta, 2013. 1836(1): p. 49-59.

303. Long, J.S., et al., Extracellular Adenosine Sensing-A Metabolic Cell Death Priming Mechanism Downstream of p53. Mol Cell, 2013. 50(3): p. 394-406.

304. Yeung, M.C. and A.S. Lau, Tumor suppressor p53 as a component of the tumor necrosis factor-induced, protein kinase PKR-mediated apoptotic pathway in human promonocytic U937 cells. J Biol Chem, 1998. 273(39): p. 25198-202.

305. Gelman, M.S., et al., Identification of cell surface and secreted proteins essential for tumor cell survival using a genetic suppressor element screen. Oncogene, 2004. 23(49): p. 8158-70.

306. Jones, R.G., et al., AMP-activated protein kinase induces a p53-dependent metabolic checkpoint. Mol Cell, 2005. 18(3): p. 283-93.

307. Inoue, Y., et al., Light emission requires exposure to the atmosphere in ex vivo bioluminescence imaging. Mol Imaging, 2006. 5(2): p. 53-6.

308. Marks, P.A., et al., Histone deacetylase inhibitors as new cancer drugs. Curr Opin Oncol, 2001. 13(6): p. 477-83.

309. Marks, P.A., et al., Inhibitors of histone deacetylase are potentially effective anticancer agents. Clin Cancer Res, 2001. 7(4): p. 759-60.

310. Kramer, O.H., et al., The histone deacetylase inhibitor valproic acid selectively induces proteasomal degradation of HDAC2. EMBO J, 2003. 22(13): p. 3411-20.

311. Piscitelli, S.C., et al., Disposition of phenylbutyrate and its metabolites, phenylacetate and phenylacetylglutamine. J Clin Pharmacol, 1995. 35(4): p. 368-73.

312. Soliman, M.L., et al., Acetate supplementation modulates brain histone acetylation and decreases interleukin-1beta expression in a rat model of neuroinflammation. Journal of neuroinflammation, 2012. 9: p. 51.

313. Berwick, D.C., et al., The identification of ATP-citrate lyase as a protein kinase B (Akt) substrate in primary adipocytes. J Biol Chem, 2002. 277(37): p. 33895-900.

314. Wellen, K.E., et al., ATP-citrate lyase links cellular metabolism to histone acetylation. Science, 2009. 324(5930): p. 1076-80.

315. Qu, Y., et al., SIRT1 promotes proliferation and inhibits apoptosis of human malignant glioma cell lines. Neurosci Lett, 2012. 525(2): p. 168-72.

316. Bonnet, S., et al., A mitochondria-K+ channel axis is suppressed in cancer and its normalization promotes apoptosis and inhibits cancer growth. Cancer Cell, 2007. 11(1): p. 37-51.

317. Shahrzad, S., et al., Sodium dichloroacetate (DCA) reduces apoptosis in colorectal tumor hypoxia. Cancer Lett, 2010. 297(1): p. 75-83.

318. Babu, E., et al., Role of SLC5A8, a plasma membrane transporter and a tumor suppressor, in the antitumor activity of dichloroacetate. Oncogene, 2011. 30(38): p. 4026-37.

319. Munoz-Pinedo, C., N. El Mjiyad, and J.E. Ricci, Cancer metabolism: current perspectives and future directions. Cell Death Dis, 2012. 3: p. e248.

320. Dang, C.V., Links between metabolism and cancer. Genes Dev, 2012. 26(9): p. 877-90.

321. Dang, C.V., Cancer cell metabolism: there is no ROS for the weary. Cancer Discov, 2012. 2(4): p. 304-7.

322. Zhou, M., et al., Warburg effect in chemosensitivity: targeting lactate dehydrogenase-A re-sensitizes taxol-resistant cancer cells to taxol. Mol Cancer, 2010. 9: p. 33.

323. Tennant, D.A., R.V. Duran, and E. Gottlieb, Targeting metabolic transformation for cancer therapy. Nat Rev Cancer, 2010. 10(4): p. 267-77.

324. Zhao, Y., E.B. Butler, and M. Tan, Targeting cellular metabolism to improve cancer therapeutics. Cell Death Dis, 2013. 4: p. e532.

325. Kim, W.H., et al., AICAR potentiates ROS production induced by chronic high glucose: roles of AMPK in pancreatic beta-cell apoptosis. Cell Signal, 2007. 19(4): p. 791-805.

326. Myers, R.B., et al., Fatty acid synthase: an early molecular marker of progression of prostatic adenocarcinoma to androgen independence. J Urol, 2001. 165(3): p. 1027-32.

327. Kuhajda, F.P., Fatty acid synthase and cancer: new application of an old pathway. Cancer Res, 2006. 66(12): p. 5977-80.

328. Jeon, S.M., N.S. Chandel, and N. Hay, AMPK regulates NADPH homeostasis to promote tumour cell survival during energy stress. Nature, 2012. 485(7400): p. 661-5.

329. Abu-Elheiga, L., et al., The subcellular localization of acetyl-CoA carboxylase 2. Proc Natl Acad Sci U S A, 2000. 97(4): p. 1444-9.

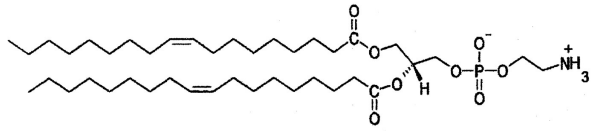
330. Heitjan, D.F., Biology, models, and the analysis of tumor xenograft experiments. Clin Cancer Res, 2011. 17(5): p. 949-51.

Appendices

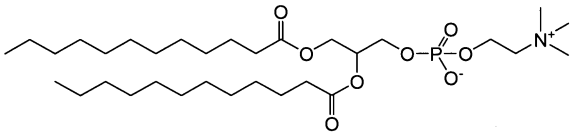
Appendix I- Lipid structures

Lipids used in liposome formulations used in Chapter 2 in attempts to encapsulate acetate: **(A)** DOPE, **(B)** DLPC C12, **(C)** DLPC C20, **(D)** DDAB, **(E)** DC cholesterol.

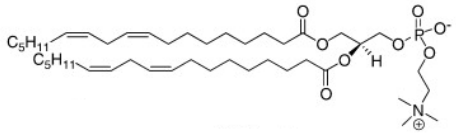
(A) DOPE



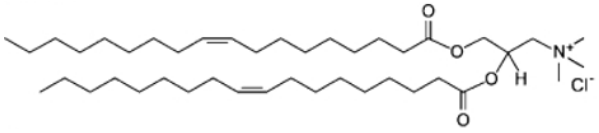
(B) DLPC C12



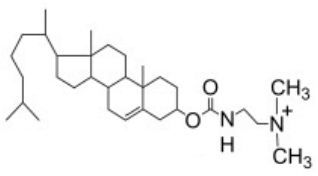
(C) DLPC C20



(D) DDAB



(E) DC cholesterol



Appendix II- Work arisen from this thesis

Publications

Metabolic re-engineering of cellular deregulation by a novel nanoparticle-encapsulated small molecule system

Leigh Brody; Meliz Sahuri-Arisoylu, James R.C. Parkinson; Nabil Hajji; Harry G. Parkes; Andrew D. Miller, E. Louise Thomas; Gary Frost and Jimmy D. Bell (2013) *Submitted*

Patents

Patent number 1215289.8

28 August, 2012

Awards

Multi-parametric vascular/functional imaging in preclinical PET/CT: Maximizing the information using contrast enhanced CT

Leigh Brody, Mohammed Hankir, Jimmy Bell and Magdy Khalil

Best Presented “Image of the Year”. World Molecular Imaging Congress, 2011.

SUMMARY

Dietary supplementation with fibre ameliorates features of the metabolic syndrome and inhibits malignant growth in certain cancer types, effects attributed to the production of short-chain fatty acids (SCFA), such as acetate. However, the ubiquitous role of SCFAs in metabolism, combined with a short tissue half-life and the non-targeted nature of oral and peripheral administrations limit their therapeutic potential. PEGylated liposomal vectors overcome these issues by protecting against degradation, increasing circulation time and passively targeting both the liver and tumour tissue. Here, we employ a SCFA encapsulated vector in animal models of both obesity and malignancy. Chronic administration of liposome encapsulated acetate (LITA) nanoparticles led to a significant reduction in adiposity, intrahepatocellular lipid, inflammatory tone and improvements in liver function, as well as an inhibition of tumour growth in a murine colorectal cancer xenograft model. These results indicate that LITA nanoparticles can be used to improve multiple metabolic pathways, *in vivo*.

INTRODUCTION

Impaired cellular energy metabolism is a defining characteristic of cancer and the metabolic syndrome. Dysfunctional pathways common to both disorders underpin their co-morbidity and represent a potential target for therapeutic intervention at a molecular level. Obesity, arising from an imbalance between surplus energy intake and decreased energy expenditure, leads to excess triglyceride synthesis and hepatic lipid accumulation (Eriksson et al., 1986). The consequences of “fatty liver” are increased mitochondrial fat oxidation without compensatory electron transport chain activity, leading to “stressed” mitochondria and the production of reactive oxygen species (Begriche et al., 2013). These events are thought to play a pivotal role in the subsequent development of inflammation and lipotoxicity, creating an aberrant cellular environment which contributes to non-alcoholic steatohepatitis (NASH), hepatic fibrosis and cirrhosis (Neuschwander-Tetri, 2010; Park et al., 2010). In turn, these disorders are strongly associated with the progression of specific cancers, including colorectal cancer and hepatocellular carcinoma (HCC) (Caldwell et al., 2004; Muhidin et al., 2012).

Supplementation with dietary fibre has been shown to ameliorate features of the metabolic syndrome and attenuate malignant growth in certain cancers (Donohoe et al., 2012; Higgins, 2004). Component carbohydrates are fermented by the microflora of the large intestine, producing short-chain fatty acids (SCFA), such as acetate, proprionate and butyrate (Higgins, 2004). Acetate plays a central role in cellular metabolism, functioning as a key intermediate in the tricarboxylic acid (TCA) cycle and synthesis of fatty acids and cholesterol in the liver. Furthermore, oxidation of acetate is the initial step in the TCA cycle, a fundamental energy producing pathway in all aerobic organisms. Oxidative phosphorylation generates the majority of energy required for cellular function in normal differentiated cells.

In contrast, cancer cells rely primarily on aerobic glycolysis; a metabolic shift termed the Warburgh effect that comprises attenuation of energy production via mitochondrial beta-oxidation (Vander Heiden et al., 2009). In malignant cells, the inhibition of glucose uptake and metabolism by products of SCFA breakdown is thought to preferentially inhibit aerobic glycolysis and supress the uncontrolled cellular proliferation (Roden, 2004; Seyfried and Shelton, 2010).

Reductions in fat mass, inflammation and improvements in insulin sensitivity have also been attributed to acetate administration in animal studies (Kondo et al., 2009; Vinolo et al., 2011; Yamashita et al., 2007; Yamashita et al., 2009). However, current evidence regarding the underlying mechanisms is unclear, with exogenous acetate delivery demonstrating inconsistent effects on weight gain, mitochondrial function and markers of lipogenic and lipolytic activity. This ambiguity may arise from the ubiquitous role acetate plays in cellular metabolism, combined with the non-targeted nature of oral and peripheral administration. In addition, the adversely low pH of acetate and its rapid clearance from the circulation limit its therapeutic potential when administered systemically (Cummings, 1981). The therapeutic limitations of SCFA also extend to cancer models, where reductions in tumour growth, mediated by butyrate inhibition of histone deacetylase (HDAC) enzymes that control transcriptional regulation, are thwarted by a short half-life and first-pass hepatic clearance (Steliou et al., 2012).

Liposomal encapsulation of therapeutic agents addresses a number of these issues by improving bio-availability, extending treatment effects and reducing dosing (Allison, 2007). Liposomes are also preferentially delivered to the liver, an organ central to the control of whole body metabolism and a primary target for treatments and therapies aiming to correct the metabolic deregulation associated with obesity and the metabolic syndrome (Dardevet et

al., 2006). In addition, the enhanced permeability and retention (EPR) effect; comprising increased liposomal uptake through leaky tumour microvasculature and prolonged retention due to reduced lymphatic drainage, is an efficient means of passively targeting malignant tissue (Maruyama, 2011). Here, we hypothesise that preferential delivery of liposome encapsulated acetate (LITA) nanoparticles to key sites of metabolic control will provide beneficial therapeutic effects in animal models of both obesity and cancer.

RESULTS AND DISCUSSION

Nanoparticle preparation and bio-distribution

Various imaging modalities were employed to confirm the passive, non-targeted delivery of our liposomal vector to both the liver and malignant tissue. Liposomal conjugations were distinguished by their encapsulated products or moieties introduced into the lipid bilayer (Supplementary Figure 1). Short term biodistribution was assessed in C57BL/6 mice following intraperitoneal (i.p.) injection with 18F-FDG encapsulated liposomes (LIP-FDG) or 18F-FDG. Representative PET, CT and PET/CT fusion images from the LIP-FDG group acquired 30min post-injection are shown in Figure 1A. Increased liposomal uptake was observed in the heart and muscle for the initial 30min post-injection as measured by area under the curve (AUC) (Figure 1B). Tissue-specific accumulation of liposomes conjugated with rhodamine (LIP-Rhd) was examined using histological techniques; representative images from the liver, heart and muscle at 2h post-injection are shown in Figure 1C-G. The highest concentrations of LIP-Rhd were observed in the liver and spleen, with lower quantities in the kidneys, brain and heart (Supplementary Figure 2).

Xenograft uptake of nanoparticles formulated for enhanced delivery to malignant tissue (LIP-XG) is shown in Figure 1H. Long-term nanoparticle accumulation was assessed by tracking biodistribution of liposomes formulated with gadolinium embedded into the lipid membrane (LIP-Gd, Supplementary Figure 1) using magnetic resonance imaging (MRI). Following a baseline scan, mice received an i.p. injection of either LIP-Gd or control and were scanned at 24h and 48h post-injection. T1 signal intensity recorded in the liver, kidney, and subcutaneous fat are shown in Figure 1I-K, respectively. Nanoparticles accumulated preferentially in the liver, indicated by the significant reduction in T1 signal, at 24h and 48h post-injection (Liver T1 24h: LIP-Gd: 495.9 ± 37.4msec, Control: 804.1 ± 81.8msec; $p<0.05$; Liver T1 48h: LITA-Gd: 503 ± 66msec, Control: 738 ± 80msec; $p<0.05$).

Liposomal encapsulated acetate (LITA) formulation and quantification

Following the confirmation of preferential uptake in target tissues, liposomes were prepared, encapsulated with either acetate (LITA), or low ionic strength buffer (HEPES) for use as a control. 1H-NMR spectroscopy was performed to quantify acetate concentrations and assess nanoparticle integrity. LITA formulations and a liposome-free control solution were both scanned with and without the addition of albumin, which binds to acetate in free solution reducing its NMR signal (Chatham and Forder, 1999). Albumin suppressed the NMR signal for acetate in free solution, whereas no reduction was observed in LITA nanoparticle solution (Supplementary Figure 3A-D); indicating acetate is successfully encapsulated within the liposome. To enable quantification of liposomal acetate, LITA formulations were scanned with a known concentration of lactate, for use as an internal standard. Liposomal acetate concentration was calculated to be 52.9µg (4.4mM) per 200µl (Supplementary Figure 3E-F) and was used in all subsequent studies. The concentration of acetate per LITA injection was

2.6mg/kg, an order of magnitude lower than previously used for intragastric or oral delivery in murine models (Kondo et al., 2009; Yamashita et al., 2007). There was no difference in liposome size (LITA: 102.3 ± 7.5nm; Control: 95.9 ± 9.0nm, p=0.6, Supplementary Figure 3G-I), indicating uptake would not differ between groups.

The *in vitro* effects of acetate on mitochondrial respiration

In vitro mitochondrial respiration was assessed to determine if acetate was used as an energy source, at a concentration comparable to the dosage used in all subsequent chronic injection protocols (4.4mM per 200µl injection). Acetate (5mM) was found to increase ATP production ($p<0.01$) with no significant different in spare respiration between the acetate or control group (Supplementary Figure 4).

The reparative effects of chronic LITA nanoparticle administration in C57BL/6 mice placed on a high fat diet

The metabolic potential of LITA nanoparticles was assessed in multiple *in vivo* models, examining a wide range of metabolic outcomes. In the first model, an obesogenic background was established by placing mice on a high fat diet (HFD) for 5 weeks. Mice subsequently received i.p. injection of LITA or control nanoparticles every 3 days for an additional 5 weeks, while maintained on a HFD. No differences in body weight (Figure 2A) or cumulative food intake (Figure 2B) were observed between groups. Whole body 1H MRS and localised 1H liver MRS were performed after the initial 5 weeks of HFD, and again following 5 weeks of chronic injection. The change in whole body adiposity (LITA: 9.0 ±

16.7%; Control: 40 ± 21.8%, p=0.02) (Figure 2C) and IHCL (LITA: -0.11 ± 0.06, Control: 2.4 ± 0.9, p<0.0001) (Figure 1D) were significantly reduced in LITA injected animals. White adipose tissue (WAT) was also reduced (LITA: 3.4 ± 1.2g, Control: 4.3 ± 1.2g, p<0.01) (Supplementary Figure 5A). No changes were observed in circulating levels of glucose, insulin or lipids (Figure 2E). However, LITA injected animals did demonstrate a reduction in serum levels of the chemokine KC/GRO (p<0.05), signifying reduced inflammatory tone (Stefanovic et al., 2005), and increased levels of IL-10 (p<0.05) (Figure 2F), a marker for the inhibition of pro-inflammatory cytokine production (Esposito et al., 2003). Quantitative RT-PCR of liver mRNA also revealed a significant reduction in the expression of UCP-2 in LITA injected animals (Figure 2G).

RT-PCR analysis demonstrated a LITA-induced reduction in HDAC1 expression (p<0.001) (Figure 2G), while western blot analysis of liver samples showed a significant differences in HDAC2 (p<0.01) and HDAC7 (p<0.001) in LITA injected animals (Figure 2H). Normalisation of histone lysine proteins to total histone protein expression revealed a reduction in residue acH4K12 in LITA compared to control samples (Figure 2I). Microarray analysis also confirmed significant changes in the expression of metabolic related genes of interest, including the HDAC class 1 (Supplementary Figure 5B).

The preventative effects of chronic LITA nanoparticle administration in C57BL/6 mice placed on a high fat diet

In the second dietary model, we assessed the potential of LITA nanoparticles to prevent the development of outcomes associated with an obesogenic diet. C57BL/6 mice placed on a HFD received i.p. injections of LITA or control nanoparticles every 3 days for 6 weeks. No

differences were observed in body weight (Figure 3A) or weekly food intake (Supplementary Figure 6A). However, in accord with the previous model, chronic LITA injection was found to significantly reduce the change in both whole body adiposity (LITA: 24.1 ± 9.7%; Control: 30.8 ± 9.7%, p=0.03) (Figure 3B) and IHCL (LITA: -0.01 ± 0.7, Control: 0.03 ± 0.05, p=0.05) (Figure 3C). LITA injection resulted in reduced fed serum levels of insulin (LITA: 0.6 ± 0.3ng/ml, Control: 1.1 ± 0.7ng/ml, $p<0.05$), while fasting glucose levels were elevated (LITA: 8.6 ± 1.8mmol/L, Control: 7.4 ± 1.5mmol/L, p=0.02) (Figure 3D). A non-significant trend towards reduced glucose clearance was seen in LITA-injected mice following a glucose tolerance test (GTT) (Supplementary Figure 6B). No differences in insulin sensitivity were recorded when assessed using the homeostatic model assessment (HOMA) index (LITA: 6.1 ± 2.5, Control: 6.7 ± 2.3, p=NS).

Additional serum analysis revealed a non-significant trend toward reduced levels of inflammatory markers in LITA-injected animals (TNF-α: LITA: 5.4 ± 3.4pg/ml, Control: 10.6 ± 8.5pg/ml, p=0.06; IL-6: LITA: 17.4 ± 17.6pg/ml, Control: 39.7 ± 35.5pg/ml, p=0.06), with no differences in leptin, ghrelin or adiponectin (Supplementary Figure 6C). There were no differences in serum lipid concentrations (Figure 3E), despite LITA-injected mice presenting reduced subcutaneous adipose tissue (SAT) mRNA expression of adipose triglyceride lipase (ATGL) ($p<0.01$) (Figure 3F), suggestive of a reduced mobilisation of peripheral lipids (Zechner et al., 2012). No differences in the weight of individual fat depots or mean adipocyte number and size were recorded between groups (data not shown). However, there was a notable decrease in serum free fatty acids (FFA) in LITA-injected animals (LITA: 0.36 ± 0.08nmol/L, Control: 0.75 ± 0.2nmol/L, $p<0.05$), while serum concentrations of the ketone, 3-hydroxybutyrate, were increased (LITA: 0.29 ± 0.1nmol/L, Control: 0.18 ± 0.03nmol/L, $p<0.05$) (Figure 3E).

Hepatic function was assessed via standard liver function tests and quantitative RT-PCR of mRNA. A decrease in serum levels of the liver function markers AST and ALP was observed in LITA-injected animals (AST: LITA: 106 ± 26U/L, Control: 201 ± 87U/L, p=0.02 and ALP: LITA: 57.5 ± 14U/L, Control: 76.9 ± 20U/L, p=0.02) (Supplementary Figure 6D). Chronic LITA injection also led to a significant reduction in mRNA expression of genes involved in fatty acid synthesis (FAS); including sterol regulatory element-binding protein-1 (SREBP1), acetyl coenzyme-A carboxylase (ACC) and fatty acid synthase gene (FASN) (Figure 3G). LITA administration also led to a significant reduction in mRNA expression of genes responsible for both β-oxidation; carnitine palmitoyltransferase-1 (CPT1), acyl coenzyme-A oxidase-1 (ACOX1), and VLDL synthesis; microsomal triglyceride transfer protein (Mttp) (Figure 3G). In accord with the previous HFD model, LITA-injected mice demonstrated reduced levels of UCP-2 (Figure 3G). Furthermore, LITA treated mice demonstrated reduced microvacuolation in the liver compared control treated mice (Figure 3H). Transmission electron microscopy analysis of hepatic mitochondrial morphology revealed no difference in mitochondrial number and a trend towards increased cristae / perimeter length in LITA-injected mice (p=0.07, Supplementary Figure 7D). No differences in oxidative phosphorylation complex I, III or V activity were observed between LITA and control animals (Supplementary Figure 7E). Chronic LITA injection led to a reduction in hepatic expression in forkhead box protein O1 (FOXO1) mRNA (Figure 3G), indicative of reduced gluconeogenesis (Gross et al., 2008). Furthermore, a reduction in hepatic uptake of glucose was also observed following LITA administration, as revealed by a reduction in glucose transporter 2 (GLUT2) mRNA (Figure 3G), and the increased fasting levels of glucose (Figure 3D), without a concomitant difference in food intake.

The preventative effects of chronic LITA nanoparticle administration in C57BL/6 mice placed on a normal fat diet

The next model assessed the effects of LITA delivery on a normal dietary background. Mice placed on a normal fat diet (NFD) received i.p. injections of LITA or control nanoparticles every 3 days for 6 weeks. There were no differences in body weight change (Figure 4A) or weekly food intake (Supplementary Figure 8A). Unlike previous HFD models, no difference was observed in whole body adiposity (LITA: 3.9 ± 4.4%, Control: 6.6 ± 9.1%, p=NS) (Figure 4B). However, a significant reduction in IHCL was again seen in LITA injected mice (LITA: -0.01 ± 0.08, Control: 0.05 ± 0.05, $p<0.05$) (Figure 4C). No differences were recorded regarding fed or fasted levels of insulin or glucose (Figure 4D), or following a GTT performed after 5 weeks of chronic injection (Supplementary Figure 8B). However, a significant reduction in the HOMA-IR index was recorded in LITA injected animals, suggesting improved insulin sensitivity (LITA: 1.9 ± 1.4; Control: 3.6 ± 1.5, p=0.03).

Serum inflammatory markers resistin and TNF-α were significantly reduced in mice that received LITA injection (Resistin: LITA: 13.6 ± 1.8ng/ml, Control: 17.2 ± 4.8ng/ml, $p<0.05$; TNF-α: LITA: 14.8 ± 8.5pg/ml, Control: 46.9 ± 33.1pg/ml, $p<0.01$). Serum levels of triglycerides (LITA: 0.79 ± 0.09mmol/L, Control: 1.03 ± 0.22mmol/L, p=0.05) (Figure 4E) and leptin (LITA: 1921 ± 935pg/ml, Control: 2889 ± 1209pg/ml, $p<0.001$) (Supplementary Figure 8C) were also significantly decreased in LITA injected animals, with no differences were observed in cholesterol, HDL or LDL (Figure 4E). Total white fat (TWF) and mesenteric adipose tissue were significantly reduced following LITA administration (TWF: LITA: 1.36 ± 0.24g, Control: 1.5 ± 0.17g, $p<0.05$; mesenteric: LITA: 0.16 ± 0.04g, Control: 0.19 ± 0.01g, $p<0.05$) (Supplementary Figure 8D). Isolated adipocytes from epididymal and subcutaneous depots revealed no differences in mean number, volume or surface area between groups (data not shown). However, AT isolated from LITA-injected animals demonstrated reduced

expression of hormone sensitive lipase (HSL) mRNA (Fold change in compared to control: 0.05 ± 0.08, $p<0.001$) (Figure 4F), reflecting a reduced mobilisation of peripheral lipids (Zechner et al., 2012).

Similar to the results of the preventative HFD model, quantitative RT-PCR of liver mRNA samples revealed a LITA-induced reduction in expression of genes involved in VLDL metabolism (Apo-B, Mttp), β- oxidation (ACOX-1, CPT-1), mitochondrial oxidation (PPARγ, PGC-1), glucose metabolism (GLUT-2, IRS-1, IRS-2) and inflammation (TNFα) (Figure 4G). Histological examination revealed normal liver architecture for all mice on a NFD, with LITA injected mice revealing less microvacuolation compared controls (Figure 4H), indicative of reduced inflammation. Similar to the previous HFD model, no differences in mitochondrial oxidative phosphorylation complex activity were seen between groups (Supplementary Figure 7F).

The respiratory effects of LITA nanoparticles in mice as measured by metabolic cages

Following a week of daily day administration of LITA or control injections, mice were monitored over a period of 48 hours in CLAMS metabolic cages. No differences were seen in food intake or cumulative food intake between groups (data not shown). While the expected diurnal variations in ambulatory activity, VCO2, VO2 and RER were observed, no significant differences between LITA and control injected animals were recorded in any of these parameters (Supplementary Figure 9).

The metabolic effects of LITA nanoparticle administration on xenograft tumour metastasis

The administration of LITA-XG nanoparticles led to a significant reduction in tumour size (LITA: 107 ± 113mm2, Control: 270 ± 87mm2, p=0.04) and tumour weight (0.05 ± 0.03mg, Control: 0.33 ± 0.04mg, p=0.003) compared to controls (Figure 5A-C). Progression of tumour volume was significantly reduced in LITA-XG injected animals (Tumour volume (week 4): LITA: 123 ± 119mm3, Control: 254 ± 93 mm3, $p<0.05$) (Figure 5D). Quantitative RT-PCR of xenograft mRNA revealed a significant decrease in expression of Class I HDACs; HDAC 1 ($p<0.05$), HDAC 2 ($p<0.05$), HDAC 3 ($p<0.001$) and HDAC 4 ($p<0.01$) in LITA-XG injected animals (Figure 5E). In addition, the expression of "silent mating type information regulation homologues" or SirT proteins, responsible for epigenetic silencing mRNA, was also significantly reduced in LITA-XG injected animals (SirT1, $p<0.05$) (Figure 5E).

Discussion

The intertwining developmental trajectories of cancer and obesity have a shared origin in impaired cellular metabolism, with mitochondrial dysfunction at their core. In order to correct the aberrant pathways associated with these conditions we have manufactured and evaluated an acetate carrying liposomal-based vector that is preferentially delivered to key sites of metabolic control. Our results indicate that nanoparticle encapsulated acetate acts as a potent multifunctional active pharmaceutical ingredient (API), capable of preventing and reversing the development of pathogenic signatures indicative of both obesity and cancer. Assessment of the bio-distribution of FDG, rhodamine and gadolinium conjugated liposomes using histological and imaging techniques confirmed that LITA nanoparticles are naturally liver tropic. In accordance with our previous work (Kenny et al., 2011), the increased molarity percentage of DSPE-PEG2000 in the liposome membrane led to a preferential accumulation of liposomes in tumour tissue.

In all dietary models examined chronic LITA administration significantly reduced IHCL, and reduced whole body adiposity and white adipose tissue in both reparative and preventative HFD paradigms. These changes occurred independently of the potentially confounding effects of a reduced food intake or body weight. Importantly, more than merely slowing accumulation, LITA delivery actively reduced IHCL. Hepatic lipid accumulation represents a key intermediary in a succession of increasingly debilitating liver conditions and is strongly associated with the development of insulin resistance and diabetes (Powell et al., 1990; Sun and Karin, 2012). The LITA-induced reduction in IHCL suggests our nanoparticle is not only capable of preventing NAFLD, but may also modulate subsequent progression to HCC.

Consistent with previous studies showing a fall in plasma lipids following chronic acetate administration (Kondo et al., 2009; Yamashita et al., 2007), LITA injection was found to reduce circulating levels of FFA and triglycerides, in HFD and NFD models respectively. Data indicating LITA administration decreases the expression of proteins involved in peripheral mobilisation of lipids, hepatic lipogenesis and lipid uptake, provide a prospective mechanism for the robust reduction in IHCL. In addition to the reductions in body fat and IHCL, further investigation of liver function revealed a number of additional beneficial effects following LITA delivery. The reduction in UCP-2 expression, observed in both HFD and NFD models, reflects reduced proton leakage across the mitochondrial membrane, less disruption in electrochemical potential and increased organelle efficiency (Chavin et al., 1999). Furthermore, the LITA-induced reduction in serum levels of AST and ALP, and the trend toward an increase in the number of cristae per perimeter length are also indicative of improved function (Wu et al., 2011).

In accord with previous studies demonstrating a reduction in inflammatory markers following acetate administration (Reisenauer et al., 2011; Vinolo et al., 2011), LITA delivery led to the

reduced expression of TNF-α in liver in both NFD and HFD models, with a trend towards lower serum concentrations of TNF-α, IL-6 and resistin. Furthermore, were LITA administration to continue, the reductions in fat mass and IHCL observed in all dietary paradigms would be expected to contribute to an additional long-term improvement in inflammatory tone (Eckel et al., 2005). It should be noted that the range of effects following LITA administration were not consistent across all dietary models, with reductions in fatty acid synthesis, circulating FFA, insulin and serum markers of inflammation and liver function, limited to HFD paradigms. Under normal dietary conditions an increase in hepatic acetate is associated with the up-regulation of fatty acid oxidation that occurs during prolonged fasting (Seufert et al., 1974). It is conceivable that compensatory homeostatic mechanisms interpreting the elevated level of hepatic acetate as a starvation signal led to the muted metabolic response to LITA administration on a NFD background; a hypothesis supported by trend towards increased food intake and bodyweight seen in the LITA-injected animals on a NFD.

Acetate supplementation leads to an increase in the production of acetyl Co-A in the liver, (Reisenauer et al., 2011), which following mitochondrial uptake, can enter either the TCA cycle, increasing ATP production as we observe in *in vitro* cultured cell analysis, or enter ketogenic pathways, as seen in the preventative HFD model. As ketogenesis occurs exclusively in liver mitochondrion, the LITA-induced increase in serum concentrations of the ketone body, hydroxybutyrate, is an important finding, indirectly confirming *in vivo* delivery of acetate to hepatic mitochondria. Given the apparent absence of expression of the mitochondrial form of acetyl-CoA synthetase (AceCS2) in the liver (Fujino et al., 2001), we predict that acetate from LITA nanoparticles is converted to acetyl-CoA by the cytosolic form of the enzyme (AceCS1), which subsequently enters the mitochondria. Previous studies have reported that systemic acetate delivery leads to an increase in hepatic fatty acid β-oxidation (Kondo et al., 2009; Yamashita et al., 2009). However, our data indicates the reverse, with chronic LITA injection reducing expression of genes controlling β-oxidative

pathways in both NFD and HFD models. The manner and rate of acetate metabolism may account for these differences, with the comparatively stable and predominantly hepatic delivery afforded by liposomal nanoparticles, contrasting with the more immediate, global uptake following bolus injection or oral gavage (Henriksen-Lacey et al., 2011).

Together, our results support a mechanism by which the LITA-induced mitochondrial accumulation of acetyl-CoA, the end-product of SCFA catabolism, inhibits β-oxidation and subsequently reduce lipid uptake, lipogenesis and hepatic uptake (Supplementary Figure 10). Furthermore, the changes we observe are consistent with the Randle hypothesis; whereby the availability of acetate as a fuel source generates metabolic signals that impair the use of glucose through inhibition of glycolytic and gluconeogenic pathways (Hue and Taegtmeyer, 2009). A shift away from carbohydrate metabolism might be expected to result in altered respiratory outcomes in LITA-injected animals yet we observed no differences following metabolic cage analysis. However, these results are in accord with several papers that demonstrate energy expenditure is maintained following acetate infusion, as acetate replaces fat as an oxidative fuel (Akanji et al., 1989; Smith et al., 2007).

The anti-tumorigenic effects attributed to SCFAs have been linked to changes in expression of HDAC enzymes, important epigenetic markers that play a key role in cellular gene expression (Soliman et al., 2012; Steliou et al., 2012). The ineffectual metabolism of SCFA in cancer cells is thought to lead to the accumulation of acetyl-CoA in the nucleus, where it functions as an HDAC inhibitor altering the expression of genes involved in cellular proliferation, apoptosis, and differentiation (Waldecker et al., 2008). Previous studies have attempted to target and disrupt the altered cellular metabolism in colonic cancer cells via supplementation with the SCFA, butyrate (Donohoe et al., 2012; Hamer et al., 2008). Our results support this hypothesis; chronic administration of LITA nanoparticles led to a

significant reduction in tumour growth and decreased mRNA expression in several classes of HDACs. We predict LITA supplementation induces a switch in fuel selection, from aerobic glycolysis to mitochondrial beta-oxidation, representing a metabolic reprogramming of cancer cells towards a normal, non-proliferative state. The decreased expression of the histone deacetylase, SirT1, is of note given its established role as an inhibitor of apoptosis and promoter for tumorigenesis (Qu et al., 2012). However, more work is required to clearly define the downstream effectors of epigenetic modification. Indeed, recent data indicates SCFA are also able to upregulate specific classes of histone acetylase (HAT) proteins, representing an additional cascade of regulatory elements (Donohoe et al., 2012). The inconsistencies we see in LITA effects on HDAC expression between xenograft and reparative HFD models serves to highlight that the metabolic state of the cell further influences how exogenous signals are interpreted.

Overall, LITA administration resulted in a comprehensive improvement in metabolic profile in animal models of both obesity and cancer; including reductions in tumour growth and amelioration of a wide range of metabolic syndrome associated outcomes, including reductions in IHCL, body fat, serum insulin, FFA and inflammatory tone. More work will be required to fully elucidate the numerous, interconnected metabolic pathways underpinning these effects. However, these results present LITA nanoparticles as a novel approach for the positive modulation of both obesity and malignant transformation *in vivo*.

Material and methods

Materials and experimental animals

All *in vivo* experiments were carried out in compliance with the Animals (Scientific Procedure) Act 1986. Mice were supplied by Harlan, UK. Mice were housed 4 per cage, in a temperature controlled room at approximately 25°C with alternating 12h periods of light and

dark (light: 8:00-20:00) in filter-topped cages with ad libitum access to water. Normal fat diet (NFD) was the RM3 diet supplied by Special Diet Services (Essex, UK). 60% of the caloric content of the HFD was fat (EF D12402; Special Diet Services).

Preparation of liposome nanoparticles

Nanoparticle design was based upon our previous studies, where PEGylated liposomes were formulated for labelling and visualization of cells (Oliver et al., 2006), or specifically designed for preferential uptake in xenograft tumours (Kenny et al., 2011). Liposomes were prepared by the thin film hydration method (Bhalerao and Raje Harshal, 2003). Design principles and molar components are shown in Supplementary Figure 1.

Bio-distribution of liposome nanoparticles

Nanoparticles were formulated and encapsulated with 160mBq fluorodeoxyglucose [18F]FDG. Nanoparticles (200µl) containing encapsulated [18F]FDG (10MBq) were injected intraperitoneally (i.p.) into C57/BL6 black mice (n=4/group). Images were acquired and analysed using IRW (Siemens Medical solutions). The intensity of [18F]FDG uptake was quantified for organ specific regions-of-interest (ROI) for 30min following injection. Area under the curve (AUC) data for each ROI was calculated.

Formulation of LITA nanoparticles

Liposomes were prepared with either acetate (1M, pH 2.3) to form liposome encapsulated acetate (LITA) nanoparticles or HEPES for use as a control. Particle size was determined using a Malvern Zetasizer (Malvern Instruments, UK).

Quantification of acetate encapsulated within LITA nanoparticles

The presence and concentration of acetate within liposomes was determined using 1H NMR spectroscopy. 200µl of LITA formulation was scanned with addition of albumin, which binds to acetate in free solution reducing the NMR signal for the compound (Chatham and Forder, 1999). A liposome free control solution containing an equivalent concentration of acetate (4mM) was also scanned with and without the addition of albumin (2g). LITA solution was scanned following the addition of lactate (5.2mg sodium lactate) to act as a quantitative control. Spectra were obtained using a Bruker DRX 11.74T NMR spectrometer. Spectra were analysed using MestRe-C NMR spectroscopy software (Santiago de Compostela, Spain).

Ex vivo histology of nanoparticle distribution

C57BL/6 mice were injected i.p. with 200µL of LITA-Rhd (n=12). Animals were euthanized at 2, 16, 24 and 48h post administration (n=3/time point). Tissue samples were collected and frozen at -80°C and sliced (7µm) using a cryostat (Leica, Milton Keynes, UK) then stained with DAPI. Images were obtained using an Olympus IX71 microscope (Olympus, U.S.A).

Long-term nanoparticle bio-distribution as measured by contrast-enhanced MRI

Mice were anesthetized with 2-3% isofluorane 1/min oxygen and placed in a birdcage coil. A fast-spin echo sequence was performed. A fast-spin echo sequence (TR 8500 msec, TEeff 20msec, ETL 8, k zero at 2, FOV 50 x 50 mm, matrix 256 x 256, one average, 40 slices of 2 mm thickness) was performed at various TI values. After the baseline scan, animals received an i.p. injection of either LITA or LITA-Gd solution (n=4/group) and were scanned again at 2, 16, 24 and 48h post-injection. Signal intensity was measured in each ROI using ImageJ software.

The *in vitro* effects of acetate on mitochondrial metabolism

HT-29 cells were obtained from the American Tissue Culture Collection (Rockville, USA). Cells were maintained in standard culture conditions at 37°C in a humidified atmosphere containing 5% CO2. The metabolic profile of HT-29 cells was determined using a Seahorse XF24 Extracellular Flux Analyser (Seahorse Biosciences, Billerica, MA). Cells were treated with a concentration of acetate (5mM) comparable to the amount delivered per injection in our LITA nanoparticle.

The reparative effects of chronic LITA nanoparticle administration in C57BL/6 mice placed on a high fat diet

After 5 weeks on a high fat diet (HFD) C56BL/6 mice (n=16) received an i.p. injection (200µl) of either LITA (n=8) or control (n=8) every 3 days, for an additional 5 weeks while maintained on a HFD. Food intake and body weight were measured weekly. Whole body 1H MRS and localised liver 1H MRS were performed after the initial 5 weeks of HFD and at the end of study. Following scanning organs and serum were collected and stored at -80°C.

The preventative effects of chronic LITA nanoparticle administration in C57BL/6 mice placed on a HFD or NFD

C57BL/6 mice were placed on either a HFD (n=48) or NFD (n=48) for 6 weeks. Within each dietary group mice received an i.p. injection of either LITA nanoparticles (n=24) or control (HEPES) (n=24) three times per week. Whole body 1H MRS and liver 1H MRS were performed prior to dietary intervention and after 4 weeks of the study. At the start of week 5, a fasted GTT was performed, (n=10-12/group). After week 6 animals were euthanized; blood

samples and organs, including the liver, epididymal, mesenteric and subcutaneous fat depots were collected and stored at -80°C. The homeostatic model assessment method was used to quantify insulin resistance (HOMA-IR) (Matthews et al., 1985).

Serum analysis

Serum samples were analysed for a panel of clinical biomarkers; ghrelin, total GLP-1 and adiponectin were measured using 2-site electrochemical luminescence immunoassays from MesoScale Discovery (Gaithersburg, USA). FFA: using the Non-Esterified Free Fatty Acid kit (Roche). 3-OH butyrate was measured using a Liquicolour Beta Hydroxybutyrate kit (Stanbio, USA). Creatinine, ALT, AST, alkaline phosphate, triglyceride, high density lipoprotein (HDL) and cholesterol were measured on the Dimension RXL autoanalyser (Siemens Healthcare). Low density lipoprotein (LDL) was calculated using the Friedwald formula. C-Peptide, Ghrelin, GIP, interleukin-6 (IL-6), glucagon, insulin, leptin, MCP-1, Tumour necrosis factor- α (TNF-α) and resistin were measured by Mouse Metabolic Magnetic Bead Panel (Millipore, UK). Additional markers of inflammation (IL-1, IL-2, IL-4, IL-5, IL-10, KC/GRO, IFN-γ) were measured with Mouse ELISA kit (Abcam, USA). Fasting levels of insulin were measured by using Ultrasentive Mouse Insulin Elisa (Mercodia AB, Sweden).

Whole body lipid and intrahepatocellular lipid

Animals were fasted overnight for 16-18h prior to scanning on a 4.7T Unity Inova MR scanner (Varian Inc, USA). Whole body 1H MRS was carried out using the SPULS sequence (TR 10s, Pulse angle 45°, 4 averages and spectral width (SW) 20,000Hz). Localised 1H liver MRS was performed using a PRESS sequence with a 2x2x2mm voxel placed using liver MRI (TR 10s, TE 9ms, averages 64 and SW 20,000Hz) (So et al., 2007).

Adipocyte Isolation and Counting

Adipocyte number and size were measured in epididymal and subcutaneous fat depots of LITA and control animals (n=8-10/group) from Experiment 3B and Experiment 3C as in (Frost et al., 1996). The adipocytes sized using a Multisizer™ 4 Coulter Counter (Beckman Coulter, USA).

Hepatic histology, immunohistochemistry, and immunofluorescence

Liver tissue was fixed in 10% formalin or embedded in Tissue-Tek OCT compound for frozen block preparation. Paraffin-embedded liver tissue was stained with haemotoxylin and eosin (H&E), TUNEL (Roche), and bromodeoxyuridine (Marik et al., 2007). TUNEL and BrdU-positive cells were quantified using Image tool. Frozen tissue sections were stained with oil-red O (ORO) for lipid detection (Oliver et al., 2006).

Electron microscopy of the liver mitochondrial

Liver slices were prepared using a cryostat (70-90nm) and stained. Sections were examined on a FEI Tecnai 12 transmission microscope operated at 120 kV. Images were acquired with an AMT 16000M digital camera. For each 36 random and different images with magnification 1400x were acquired where the number of mitochondria was counted per image. Images were also obtained with magnification 4800x (12/liver) with the perimeter of cross-sectional view of mitochondria and number of cristae in the mitochondria recorded.

Hepatic expression of oxidative phosphorylation complexes I, III and V

Mitochondrial oxidative phosphorylation was investigated by using Rat/Mouse Oxidative Phosphorylation Magnetic Bead Panel (Millipore, USA), according to manufacturer's instructions using 20ug of total liver protein.

Hepatic and adipose tissue mRNA expression assessed via quantitative RT-PCR and microarray

Total mRNA was isolated from mouse liver using RNeasy (Qiagen, USA) following the manufacturer's instructions. Mouse Gene 1.0ST microarrays were performed on mRNA isolated from LITA (n=5) and control (n=5) animals and analysed using linear model for microarray (LIMMA) (Smyth et al., 2005). Total mRNA was isolated from subcutaneous and mesenteric fat depots of animals from HFD models using RNeasy Lipid Tissue Mini Kit (Qiagen, USA). RT reactions for all tissues were performed using a SuperScript II RT Kit (Invitrogen) and used in both RT-PCR and microarray analysis. Quantitative PCR reactions were performed using Assays-on-Demand FAM-MGB primer/probe sets Taqman Universal PCR Master Mix (Applied Biosystems, USA) (n=6-8 per group).

Hepatic histone deacetylase expression

Western blotting was performed on liver samples from LITA and control animals from the preventative HFD (n=8/group) to examine the expression of HDAC proteins in classes I, II and IV. Raw signals for each protein target of interest were quantified and background subtracted using the Li-COR Odyssey software and normalised to β-actin. Quantification of protein expression was performed using ImageJ software (NIH, Bethesda, MA).

The respiratory effects of LITA nanoparticles in mice as measured by metabolic cages

C57BL/6 mice were injected daily with either the control or LITA nanoparticles (n=8/group) for seven days and placed individually into the Comprehensive laboratory animal monitoring systems (CLAMS) cages (Columbus Instruments, USA) for 48 hours. Parameter data recorded and analysed as in (Semjonous et al., 2009).

The metabolic effects of LITA nanoparticle administration on xenograft tumour metastasis

Tumourigenicity was initiated by injecting $2.5x10^5$ colon cancer cell line of HT-29, subcutaneously into the left flank of 6-8 week-old nude mice (BALB/C nu/nu). For staining LITA-Rhd was injected (i.p.) and animals euthanized at 2 hours post administration (n=3/group). For chronic analysis, i.p. injections of LITA or Control nanoparticles were given every three days for 4 weeks (n=6/group). Tumour volume was monitored every 2-4d by calliper to determine the volume estimated assuming an ellipsoid shape using the following equation: $V= L \times W \times D \times \pi/6$. After 4 weeks animals were euthanized with tumour tissue isolated and stored at -80°C for subsequent extraction of mRNA as previously described above.

Statistical Analysis

All statistical analyses were performed using GraphPad Prism (San Diego, CA), unless otherwise noted. Data are presented as means ± standard deviation (SD). Statistical significance was calculated with Student's t test, two-way ANOVA with Bonferroni post-hoc test for multiple comparisons and generalised estimating equation (GEE) analysis where appropriate. Metabolic cage data was analysed by the Mann-Whitney U test and presented as mean ± sem. Significance was accepted at the level of * = $p<0.05$, ** = $p< 0.01$, *** = $p<0.001$.

References

Akanji, A.O., Bruce, M.A., and Frayn, K.N. (1989). Effect of acetate infusion on energy expenditure and substrate oxidation rates in non-diabetic and diabetic subjects. Eur J Clin Nutr 43, 107-115.

Allison, S.D. (2007). Liposomal drug delivery. Journal of infusion nursing : the official publication of the Infusion Nurses Society 30, 89-95; quiz 120.

Begriche, K., Massart, J., Robin, M.A., Bonnet, F., and Fromenty, B. (2013). Mitochondrial adaptations and dysfunctions in nonalcoholic fatty liver disease. Hepatology.

Bhalerao, S.S., and Raje Harshal, A. (2003). Preparation, optimization, characterization, and stability studies of salicylic acid liposomes. Drug development and industrial pharmacy 29, 451-467.

Caldwell, S.H., Crespo, D.M., Kang, H.S., and Al-Osaimi, A.M. (2004). Obesity and hepatocellular carcinoma. Gastroenterology 127, S97-103.

Chatham, J.C., and Forder, J.R. (1999). Lactic acid and protein interactions: implications for the NMR visibility of lactate in biological systems. Biochim Biophys Acta 1426, 177-184.

Chavin, K.D., Yang, S., Lin, H.Z., Chatham, J., Chacko, V.P., Hoek, J.B., Walajtys-Rode, E., Rashid, A., Chen, C.H., Huang, C.C., Wu, T.C., Lane, M.D., and Diehl, A.M. (1999). Obesity induces expression of uncoupling protein-2 in hepatocytes and promotes liver ATP depletion. J Biol Chem 274, 5692-5700.

Cummings, J.H. (1981). Short chain fatty acids in the human colon. Gut 22, 763-779.

Dardevet, D., Moore, M.C., Remond, D., Everett-Grueter, C.A., and Cherrington, A.D. (2006). Regulation of hepatic metabolism by enteral delivery of nutrients. Nutr Res Rev 19, 161-173.

Donohoe, D.R., Collins, L.B., Wali, A., Bigler, R., Sun, W., and Bultman, S.J. (2012). The warburg effect dictates the mechanism of butyrate-mediated histone acetylation and cell proliferation. Mol Cell 48, 612-626.

Eckel, R.H., Grundy, S.M., and Zimmet, P.Z. (2005). The metabolic syndrome. Lancet 365, 1415-1428.

Eriksson, S., Eriksson, K.F., and Bondesson, L. (1986). Nonalcoholic steatohepatitis in obesity: a reversible condition. Acta Med Scand 220, 83-88.

Esposito, K., Pontillo, A., Giugliano, F., Giugliano, G., Marfella, R., Nicoletti, G., and Giugliano, D. (2003). Association of low interleukin-10 levels with the metabolic syndrome in obese women. J Clin Endocrinol Metab 88, 1055-1058.

Frost, G., Keogh, B., Smith, D., Akinsanya, K., and Leeds, A. (1996). The effect of low-glycemic carbohydrate on insulin and glucose response in vivo and in vitro in patients with coronary heart disease. Metabolism 45, 669-672.

Fujino, T., Kondo, J., Ishikawa, M., Morikawa, K., and Yamamoto, T.T. (2001). Acetyl-CoA synthetase 2, a mitochondrial matrix enzyme involved in the oxidation of acetate. J Biol Chem 276, 11420-11426.

Gross, D.N., van den Heuvel, A.P., and Birnbaum, M.J. (2008). The role of FoxO in the regulation of metabolism. Oncogene 27, 2320-2336.

Hamer, H.M., Jonkers, D., Venema, K., Vanhoutvin, S., Troost, F.J., and Brummer, R.J. (2008). Review article: the role of butyrate on colonic function. Alimentary pharmacology & therapeutics 27, 104-119.

Henriksen-Lacey, M., Korsholm, K.S., Andersen, P., Perrie, Y., and Christensen, D. (2011). Liposomal vaccine delivery systems. Expert opinion on drug delivery 8, 505-519.

Higgins, J.A. (2004). Resistant starch: metabolic effects and potential health benefits. J AOAC Int 87, 761-768.

Hue, L., and Taegtmeyer, H. (2009). The Randle cycle revisited: a new head for an old hat. American journal of physiology. Endocrinology and metabolism 297, E578-591.

Kenny, G.D., Kamaly, N., Kalber, T.L., Brody, L.P., Sahuri, M., Shamsaei, E., Miller, A.D., and Bell, J.D. (2011). Novel multifunctional nanoparticle mediates siRNA tumour delivery, visualisation and therapeutic tumour reduction in vivo. Journal of controlled release : official journal of the Controlled Release Society 149, 111-116.

Kondo, T., Kishi, M., Fushimi, T., and Kaga, T. (2009). Acetic Acid Upregulates the Expression of Genes for Fatty Acid Oxidation Enzymes in Liver To Suppress Body Fat Accumulation. Journal of Agricultural and Food Chemistry 57, 5982-5986.

Marik, J., Tartis, M.S., Zhang, H., Fung, J.Y., Kheirolomoom, A., Sutcliffe, J.L., and Ferrara, K.W. (2007). Long-circulating liposomes radiolabeled with [18F]fluorodipalmitin ([18F]FDP). Nucl Med Biol 34, 165-171.

Maruyama, K. (2011). Intracellular targeting delivery of liposomal drugs to solid tumors based on EPR effects. Adv Drug Deliv Rev 63, 161-169.

Matthews, D.R., Hosker, J.P., Rudenski, A.S., Naylor, B.A., Treacher, D.F., and Turner, R.C. (1985). Homeostasis model assessment: insulin resistance and beta-cell function from fasting plasma glucose and insulin concentrations in man. Diabetologia 28, 412-419.

Muhidin, S.O., Magan, A.A., Osman, K.A., Syed, S., and Ahmed, M.H. (2012). The relationship between nonalcoholic fatty liver disease and colorectal cancer: the future challenges and outcomes of the metabolic syndrome. Journal of obesity 2012, 637538.

Neuschwander-Tetri, B.A. (2010). Hepatic lipotoxicity and the pathogenesis of nonalcoholic steatohepatitis: the central role of nontriglyceride fatty acid metabolites. Hepatology 52, 774-788.

Oliver, M., Ahmad, A., Kamaly, N., Perouzel, E., Caussin, A., Keller, M., Herlihy, A., Bell, J., Miller, A.D., and Jorgensen, M.R. (2006). MAGfect: a novel liposome formulation for MRI labelling and visualization of cells. Organic & biomolecular chemistry 4, 3489-3497.

Park, E.J., Lee, J.H., Yu, G.Y., He, G., Ali, S.R., Holzer, R.G., Osterreicher, C.H., Takahashi, H., and Karin, M. (2010). Dietary and genetic obesity promote liver inflammation and tumorigenesis by enhancing IL-6 and TNF expression. Cell 140, 197-208.

Powell, E.E., Cooksley, W.G., Hanson, R., Searle, J., Halliday, J.W., and Powell, L.W. (1990). The natural history of nonalcoholic steatohepatitis: a follow-up study of forty-two patients for up to 21 years. Hepatology 11, 74-80.

Qu, Y., Zhang, J., Wu, S., Li, B., Liu, S., and Cheng, J. (2012). SIRT1 promotes proliferation and inhibits apoptosis of human malignant glioma cell lines. Neurosci Lett 525, 168-172.

Reisenauer, C.J., Bhatt, D.P., Mitteness, D.J., Slanczka, E.R., Gienger, H.M., Watt, J.A., and Rosenberger, T.A. (2011). Acetate supplementation attenuates lipopolysaccharide-induced neuroinflammation. Journal of neurochemistry 117, 264-274.

Roden, M. (2004). How free fatty acids inhibit glucose utilization in human skeletal muscle. News in physiological sciences : an international journal of physiology produced jointly by the International Union of Physiological Sciences and the American Physiological Society 19, 92-96.

Semjonous, N.M., Smith, K.L., Parkinson, J.R., Gunner, D.J., Liu, Y.L., Murphy, K.G., Ghatei, M.A., Bloom, S.R., and Small, C.J. (2009). Coordinated changes in energy intake

and expenditure following hypothalamic administration of neuropeptides involved in energy balance. Int J Obes (Lond) 33, 775-785.

Seufert, C.D., Graf, M., Janson, G., Kuhn, A., and Soling, H.D. (1974). Formation of free acetate by isolated perfused livers from normal, starved and diabetic rats. Biochem Biophys Res Commun 57, 901-909.

Seyfried, T.N., and Shelton, L.M. (2010). Cancer as a metabolic disease. Nutrition & metabolism 7, 7.

Smith, G.I., Jeukendrup, A.E., and Ball, D. (2007). Sodium acetate induces a metabolic alkalosis but not the increase in fatty acid oxidation observed following bicarbonate ingestion in humans. J Nutr 137, 1750-1756.

Smyth, G.K., Michaud, J., and Scott, H.S. (2005). Use of within-array replicate spots for assessing differential expression in microarray experiments. Bioinformatics 21, 2067-2075.

So, P.W., Yu, W.S., Kuo, Y.T., Wasserfall, C., Goldstone, A.P., Bell, J.D., and Frost, G. (2007). Impact of resistant starch on body fat patterning and central appetite regulation. PLoS One 2, e1309.

Soliman, M.L., Smith, M.D., Houdek, H.M., and Rosenberger, T.A. (2012). Acetate supplementation modulates brain histone acetylation and decreases interleukin-1beta expression in a rat model of neuroinflammation. J Neuroinflammation 9, 51.

Stefanovic, L., Brenner, D.A., and Stefanovic, B. (2005). Direct hepatotoxic effect of KC chemokine in the liver without infiltration of neutrophils. Experimental biology and medicine (Maywood, N.J.) 230, 573-586.

Steliou, K., Boosalis, M.S., Perrine, S.P., Sangerman, J., and Faller, D.V. (2012). Butyrate histone deacetylase inhibitors. BioResearch open access 1, 192-198.

Sun, B., and Karin, M. (2012). Obesity, inflammation, and liver cancer. J Hepatol 56, 704-713.

Vander Heiden, M.G., Cantley, L.C., and Thompson, C.B. (2009). Understanding the Warburg effect: the metabolic requirements of cell proliferation. Science 324, 1029-1033.

Vinolo, M.A., Rodrigues, H.G., Nachbar, R.T., and Curi, R. (2011). Regulation of inflammation by short chain fatty acids. Nutrients 3, 858-876.

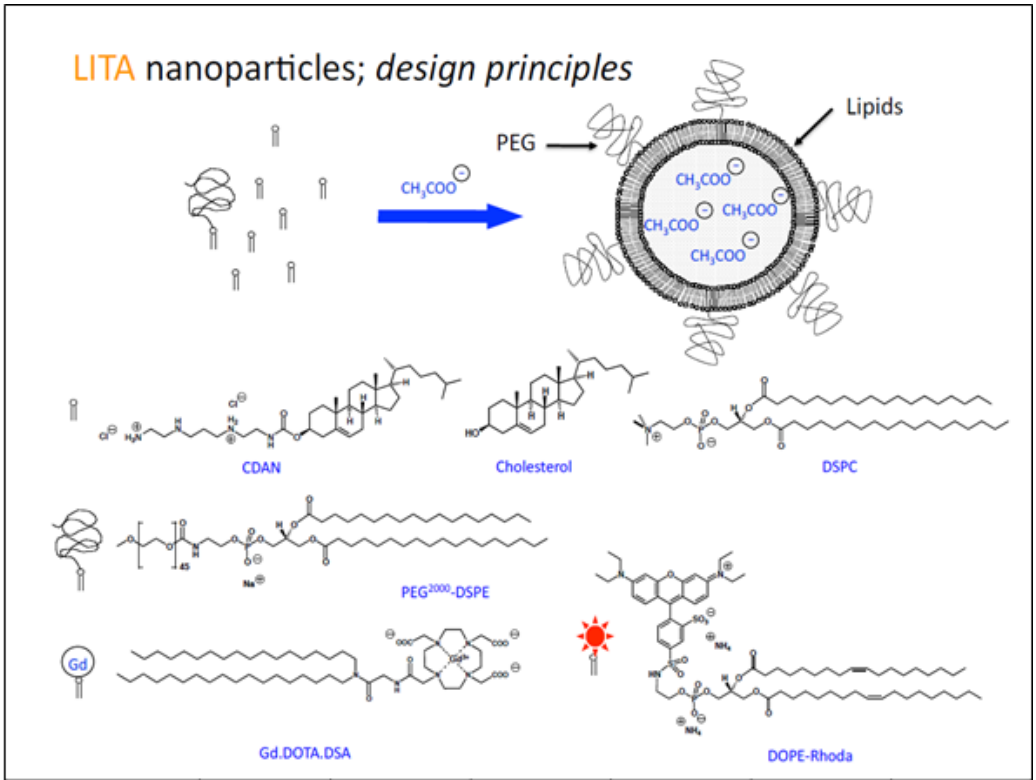
Waldecker, M., Kautenburger, T., Daumann, H., Busch, C., and Schrenk, D. (2008). Inhibition of histone-deacetylase activity by short-chain fatty acids and some polyphenol metabolites formed in the colon. The Journal of nutritional biochemistry 19, 587-593.

Wu, T.C., Chen, L.K., Tsai, S.H., Liaw, Y.H., and Hwang, B. (2011). Hepatic steatosis: an experimental model for quantification. Arch Gerontol Geriatr 52, 164-166.

Yamashita, H., Fujisawa, K., Ito, E., Idei, S., Kawaguchi, N., Kimoto, M., Hiemori, M., and Tsuji, H. (2007). Improvement of Obesity and Glucose Tolerance by Acetate in Type 2 Diabetic Otsuka Long-Evans Tokushima Fatty (OLETF) Rats. Bioscience, Biotechnology, and Biochemistry 71, 1236-1243.

Yamashita, H., Maruta, H., Jozuka, M., Kimura, R., Iwabuchi, H., Yamato, M., Saito, T., Fujisawa, K., Takahashi, Y., Kimoto, M., Hiemori, M., and Tsuji, H. (2009). Effects of Acetate on Lipid Metabolism in Muscles and Adipose Tissues of Type 2 Diabetic Otsuka Long-Evans Tokushima Fatty (OLETF) Rats. Bioscience, Biotechnology, and Biochemistry 73, 570-576.

Zechner, R., Zimmermann, R., Eichmann, T.O., Kohlwein, S.D., Haemmerle, G., Lass, A., and Madeo, F. (2012). FAT SIGNALS--lipases and lipolysis in lipid metabolism and signaling. Cell Metab 15, 279-291.



Molar Component (%)	DSPC	CDAN	Cholesterol	DSPE PEG^{2000}	DOPE Rhodamine	Gadolinium DOTA DSA
(1) LIP	32	32	35	1	-	-
(2) LIP-XG	32	32	31	5	-	-
(3) LIP-Rhd	32	32	34	1	1	-
(4) LIP-XG-Rhd	32	32	30	5	1	-
(5) LIP-Gd	32	32	34	1	-	1

Supplementary Figure 1 – LITA nanoparticle design principles and percentage molar component of formulations. (1) LIP: Standard liposome conjugation used for the encapsulation of ^{18}F-FDG, acetate and HEPES; **(2) LIP-XG:** Liposomes conjugated with a higher DSPE PEG^{2000} percentage to increase tumour uptake in animal models of malignancy; **(3) LIP-Rhd:** Liposomes contained 1% of rhodamine (Rhd), a fluorescent lipid used for histological analysis; **(4) LIP-XG-Rhd**: LIP-XG contained an additional 1% of rhodamine for histological analysis. **(5) LIP-Gd:** Liposomes conjugated with gadolinium (Gd) for use in MRI bio-distribution analysis; LIP: Liposome; LITA: Liposome encapsulated acetate; DSPC: 1,2-distearoyl-sn-glycero-3-phosphocholine; CDAN: N1-cholesteryloxycarbonyl-3,7-diazanonane-1,9-diamine; DSPE PEG^{2000}: 1,2-distearoyl-sn-glycero-3-phosphoethanolamine-N-methoxy (polyethylene glycol)-2000; DOTA: gadoterate meglumine; DOPE - Rhodamine:1,2-dioleoyl-sn-glycero-3-phosphoethanolamine-N-(lissamine rhodamine B sulfonyl); DSA: digital subtraction angiography.

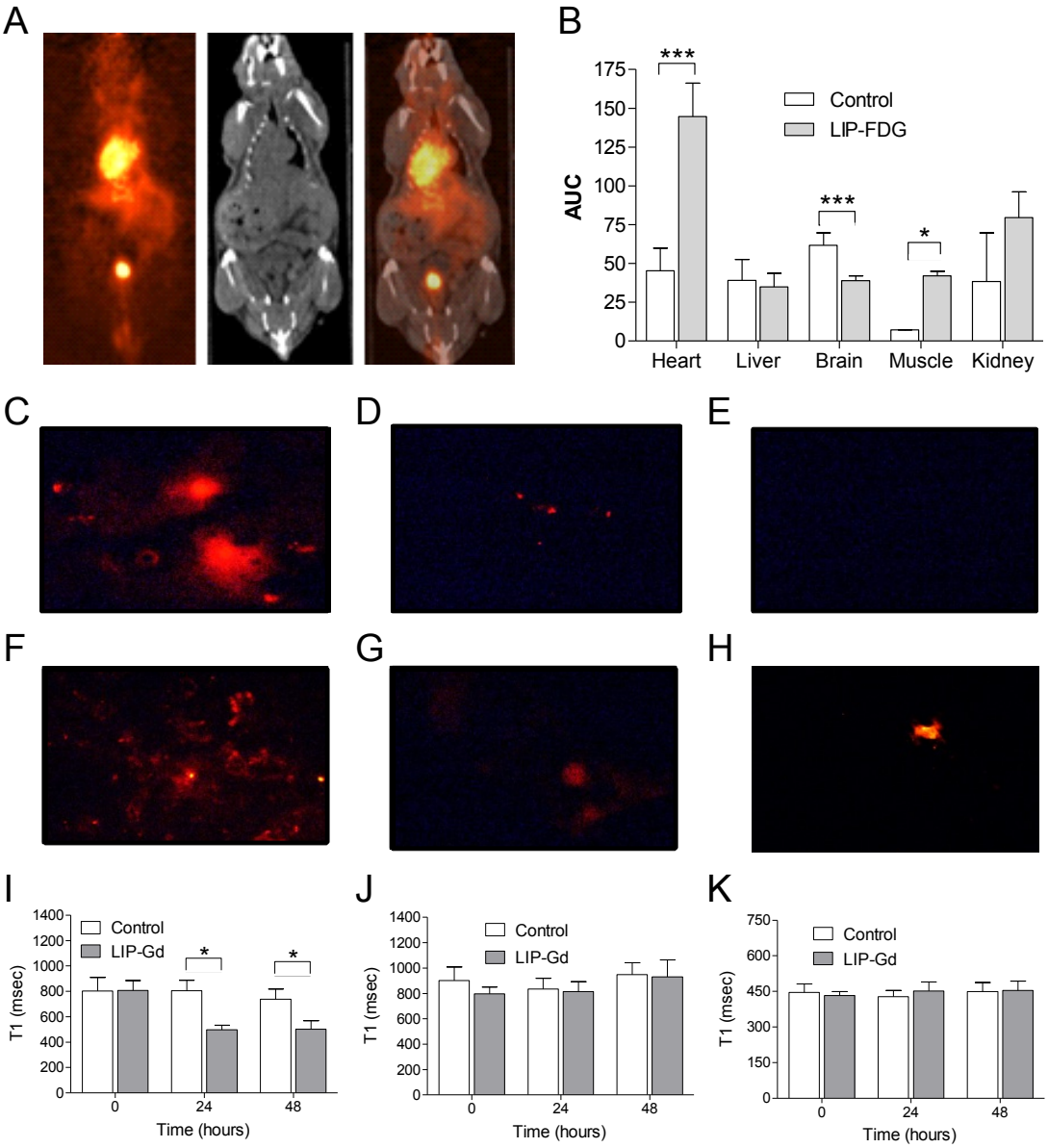
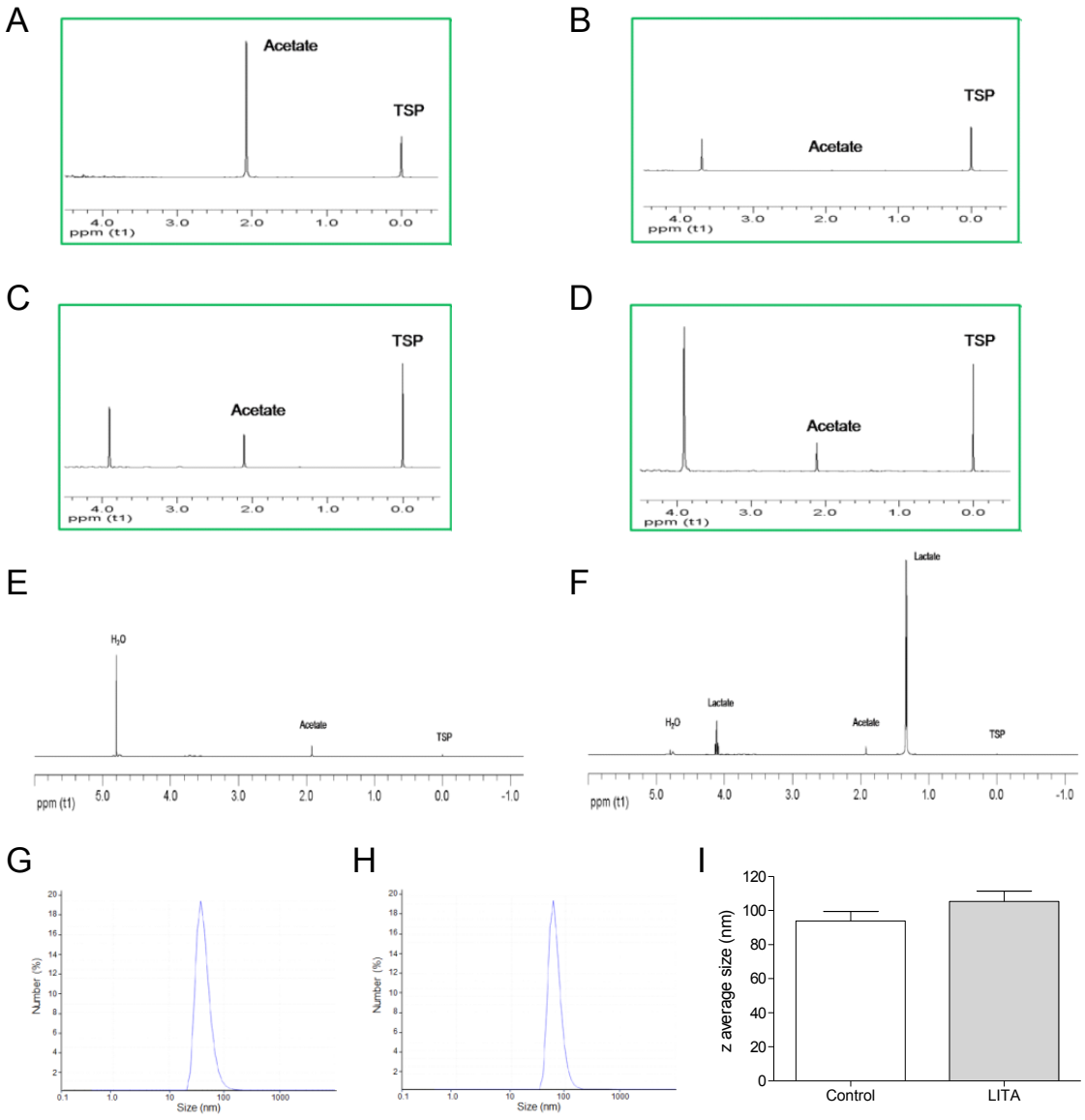


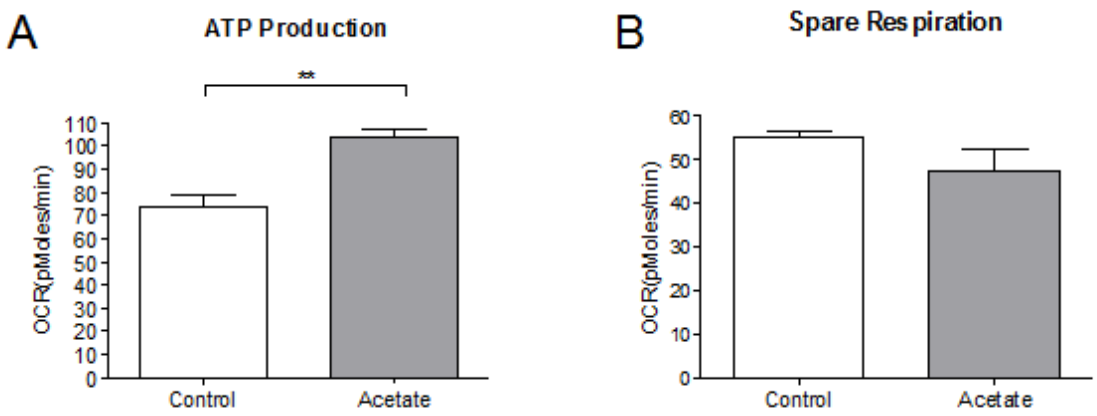
Figure 1 Bio-distribution of liposomal conjugations. (A) Representative PET, CT and PET/CT fusion images at 2h post injection in C57BL/6 mice injected with LIP-FDG nanoparticles (10 MBq of encapsulated ^{18}F-FDG) **(B)** Area under the curve (AUC) data recorded from regions of interest (ROI) at 30min post-injection of ^{18}F-FDG (Control) or LIP-FDG (n=4/group). **(C-G)** are representative histological images from C57BL/6 mice, collected 2h post i.p. injection of LIP-Rhd; **(C)** Liver, **(D)** Heart, **(E)** Muscle, **(F)** Spleen and **(G)** Lung. **(H)** Representative histological image of xenograft tumour collected 2h post i.p. injection of LIP-XG-Rhd. **(I-K)** are T1 values recorded at 0, 24 and 48 hours in ROI post i.p. injection of LITA-Gd or LITA (Control) nanoparticles (n=4/group); **(I)** Liver, **(J)** Kidney and **(K)** Subcutaneous fat. Results are displayed as mean ± SD. Data analysed by student's t-test; * = $p<0.05$, *** =$p<0.001$.

	Liver	Spleen	Kidney	Lungs	Heart	Brain	Muscle	Pancreas
2h	✓	✓	✓	✓	✓	✓	-	✓
16h	✓	✓	✓	-	✓	✓	-	✓
24h	✓	✓	✓	-	-	✓	-	✓
48h	✓	✓	-	-	-	✓	-	-

Supplementary Figure 2 - Bio-distribution of rhodamine conjugated LIP nanoparticles. Mice were injected i.p. with 200µl of LIP-Rhd nanoparticle solution. Organs were collected and stained for rhodamine at 2, 16, 24 and 48h post injection (n=3/time point); indicates the presence (✓) or absence (-) of rhodamine at these time points.



Supplementary Figure 3 – Acetate encapsulation and quantification. ^{1}H NMR spectra from 4.5ppm to -0.5ppm of **(A)** 4mM acetate solution, **(B)** 4mM acetate solution with albumin, **(C)** LITA solution with albumin (2g); **(D)** LITA solution with albumin (4g). Trimethylsilyl propionate (TSP) provides a reference at 0ppm. The peak for acetate is normally observed at 2.03ppm. The NMR spectra of LITA nanoparticles without lactate **(E)** and with lactate (5.2mg sodium lactate) **(F)** are shown. The size of liposome preparations was measured using a Zetasizer Nano (Malvern, UK), **(G)** and **(H)** show the size distribution of control (containing HEPES) and LITA (liposome encapsulated acetate) respectively, **(I)** average size of control and LITA liposomes.



Supplementary Figure 4 - Mitochondrial calorimetry HT-29 cells were treated with acetate (5mM) or without (Control) and assessed for ATP production by the Seahorse assay *in vitro*. **(A)** ATP production; **(B)** Spare respiration; n=4/group; **=p<0.01; data analysed using student t-test (GraphPad Prism); OCR: Oxygen consumption rate.

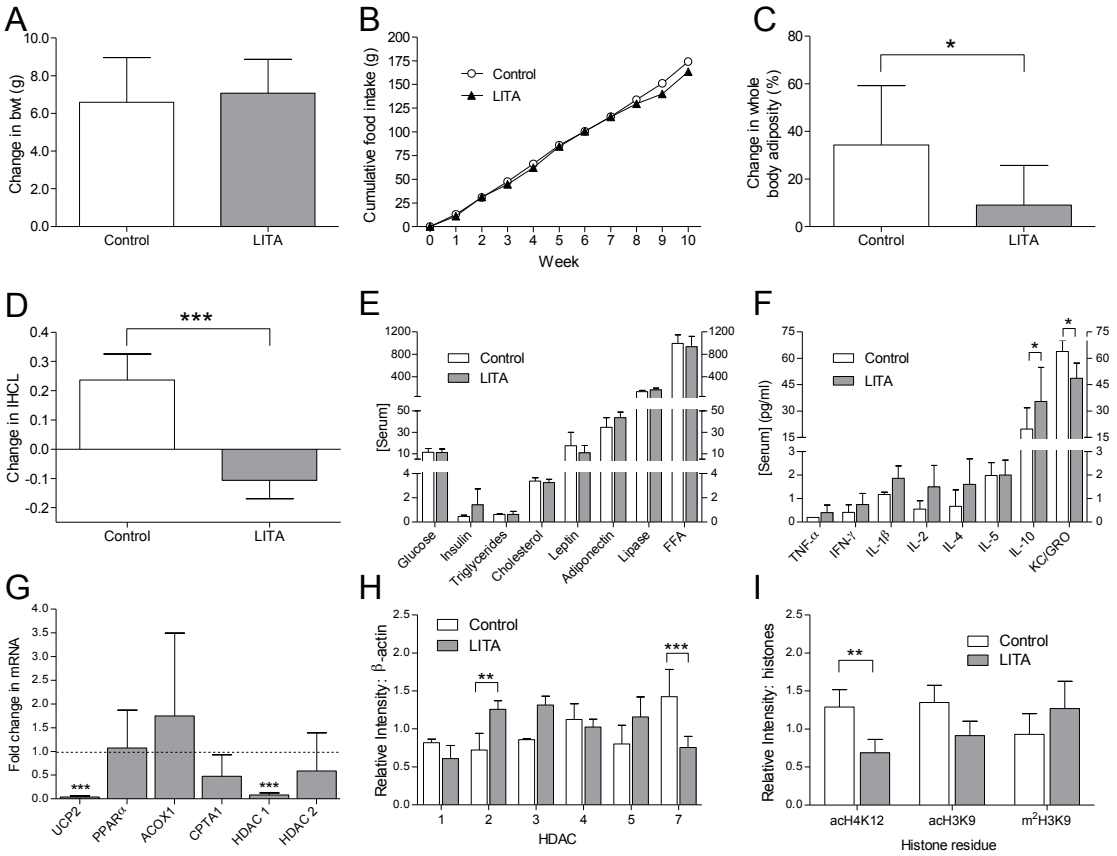
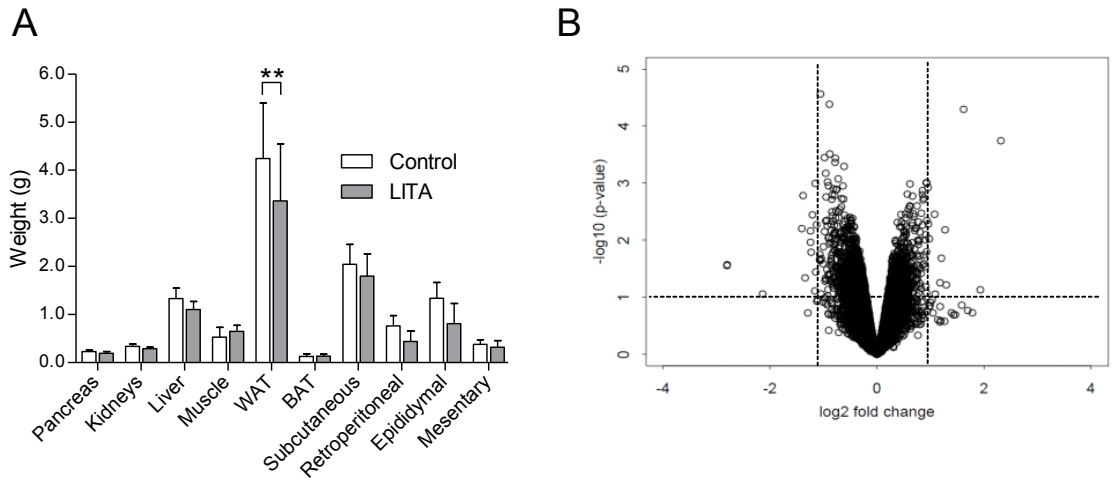


Figure 2 - The reparative effects of LITA nanoparticles in mice placed on a HFD diet. After 5 weeks placed on a high fat diet (HFD) mice were injected every three days with either liposome encapsulated acetate (LITA) nanoparticles or control (HEPES) for an additional 5 weeks. **(A)** Change in body weight (g); **(B)** Cumulative food intake (g/week); **(C)** Whole body adiposity (%); **(D)** IHCL; **(E)** Plasma lipids and additional circulating peptides (glucose (mmol/L), insulin, triglycerides (mmol/L), triglycerides (mmol/L), Leptin (ng/ml), Adiponectin (ng/ml), Lipase (U/L), Free fatty acids (FFA) (µmol/L); **(F)** Serum levels of inflammatory markers; **(G)** The fold change in hepatic mRNA levels in LITA compared to control groups; **(H)** Expression of HDAC proteins (normalised to β-actin); **(I)** Expression of histone residues (normalised to total histone). Data analysed by Student's t-test or two-way ANOVA with Bonferroni post hoc test; n=8/group; * = $p<0.05$, ** = $p<0.01$, *** = $p<0.001$.



Supplementary Figure 5 - The reparative effects of LITA nanoparticles in mice placed on a HFD diet. Mice were placed on a high fat diet (HFD) for 5 weeks. Chronic injections then began every three days with either liposome encapsulated acetate (LITA) nanoparticles or control (HEPES) for an additional 5 weeks (n=8/group). **(A)** Organ weight, **(B)** Microarray data; n=8/group; *=p<0.05, **=p<0.01, ***=p<0.001. Data analysed by 2-way ANOVA with Bonferroni post-hoc test (GraphPad Prism).

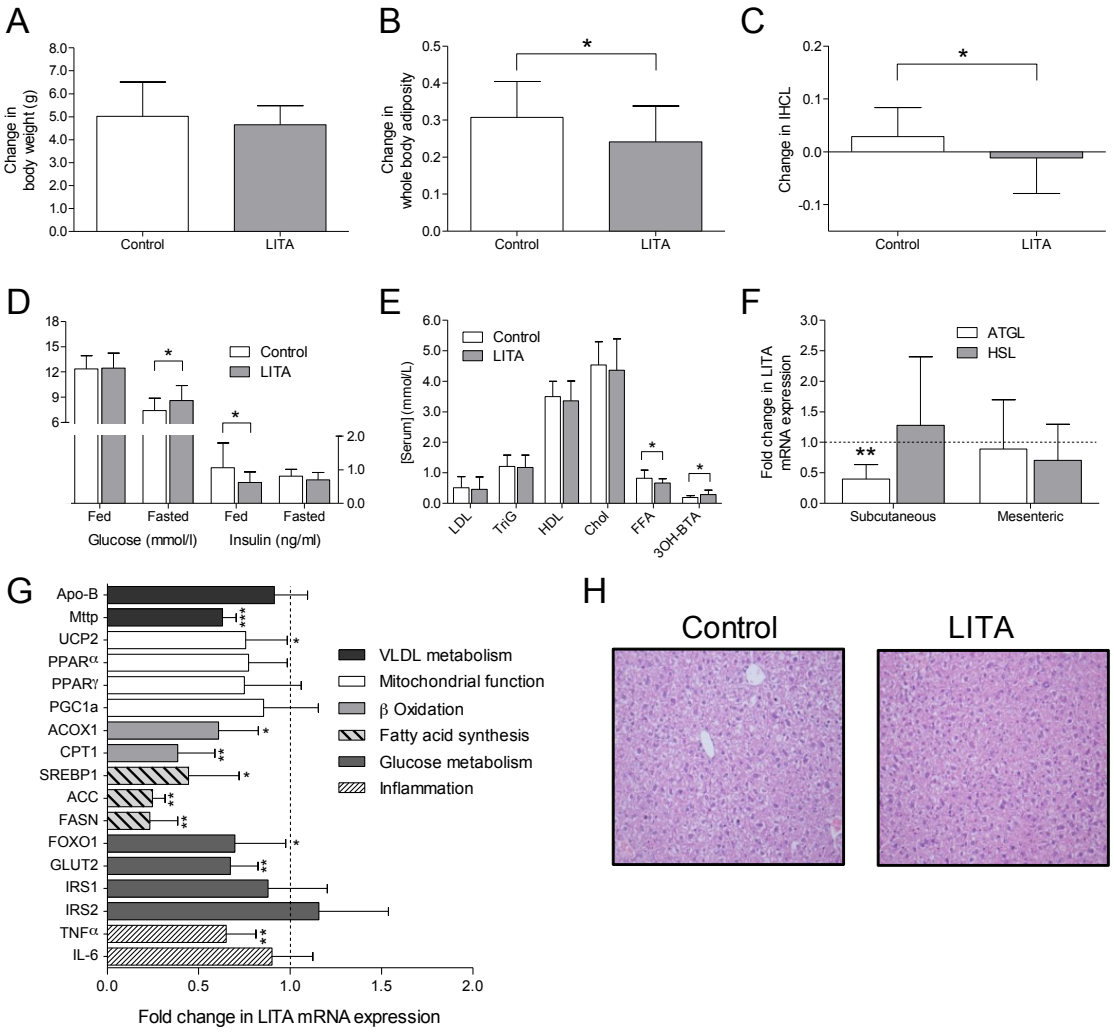
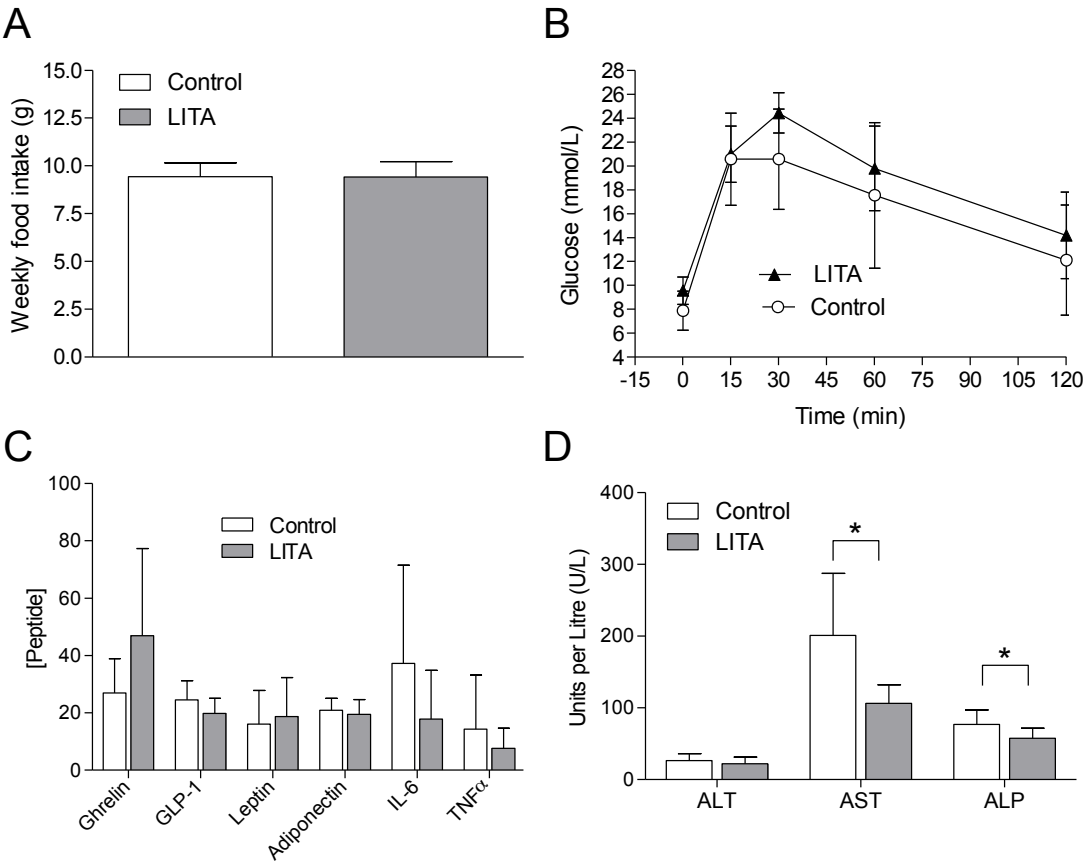
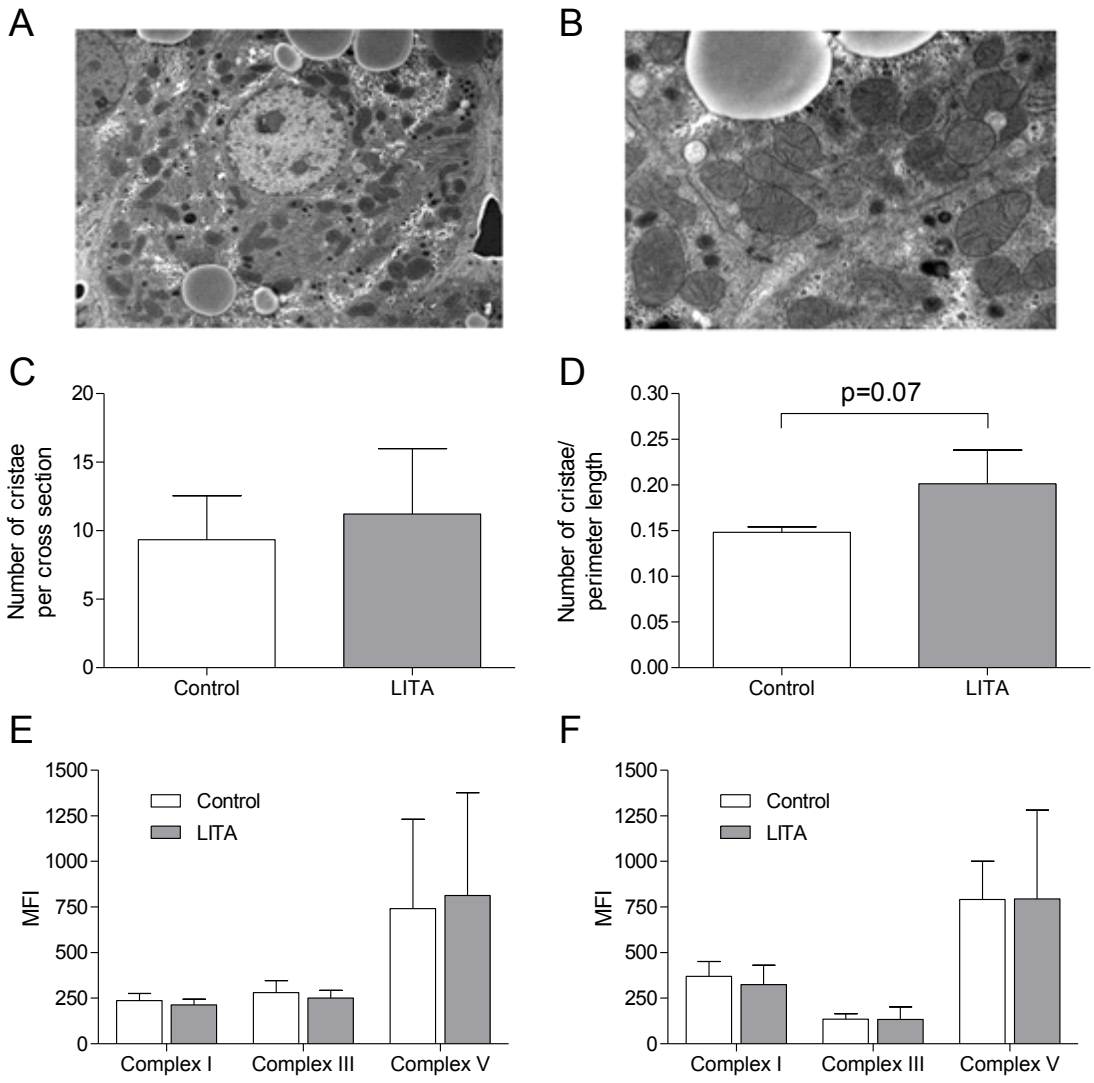


Figure 3 - The preventative effects of LITA nanoparticles in mice placed on a HFD diet. Mice were placed on a high fat diet (HFD) and injected every three days with either liposome encapsulated acetate (LITA) nanoparticles or control (HEPES) for 6 weeks. Overall change in; **(A)** Body weight (g), **(B)** Whole body adiposity, **(C)** IHCL. Fed and fasted levels of plasma **(D)** Plasma lipids (mmol/L) (n=12/group), **(E)** Fed and fasted levels of serum glucose and insulin (n=18/group), **(F)** Fold change in adipose tissue mRNA expression in LITA compared to control animals (n=6-8/group) **(G)** Fold change in hepatic mRNA expression in LITA compared to control animals (n=6-8/group), genes grouped by function. **(H)** H&E staining of liver cross-section. Data analysed by 2 way ANOVA with Bonferroni test for multiple comparisons (GraphPad Prism); n=24/group; * = $p<0.05$, ** = $p<0.01$, *** = $p<0.001$.



Supplementary Figure 6 - The preventative effects of LITA nanoparticles in mice placed on a HFD diet. Mice were placed on a high fat diet (HFD) and injected every three days with either liposome encapsulated acetate (LITA) nanoparticles or control (HEPES) for 6 weeks. **(A)** Average weekly food intake (g), **(B)** A glucose tolerance test (GTT) was performed following an overnight fast at the start of week 5 (n=10/group). **(C)** Additional circulating peptides (Adiponectin (ng/ml), ghrelin (ng/ml) and GIP (ng/ml) (n=6/group), Leptin (pg/ml), and interleukin-6 (pg/ml) (n=18/group), **(D)** Serum concentrations of 3 markers of liver function: Alanine transaminase (ALT), Aspartate transaminase (AST) and Alkaline phosphatase (ALP) (all U/L) (n=12/group); n=24/group; **=p<0.01; Data analysed by 2 way ANOVA with Bonferroni post-hoc test (GraphPad Prism).



Supplementary Figure 7 - The effects of chronic LITA nanoparticle administration on mitochondrial morphology and oxidative phosphorylation. Mitochondrial morphology of mice placed on a HFD and injected with either LITA or control nanoparticles for 6 weeks, **(A)** A representative transmission electron microscopy image (TEM) obtained at 1200x magnification used to calculate the number mitochondria, **(B)** A representative TEM image at 4800x magnification used to calculate the number cristae per mitochondrion, **(C)** Number of mitochondria per image, **(D)** Number of cristae per perimeter length of mitochondrion (n=4/group); The mean fluorescence intensity (MFI) of oxidative phosphorylation complexes 1, III and V in control and LITA injected mice from **(E)** Preventative HFD and **(F)** Preventative NFD studies; n=12/group; data analysed by 2-way ANOVA.

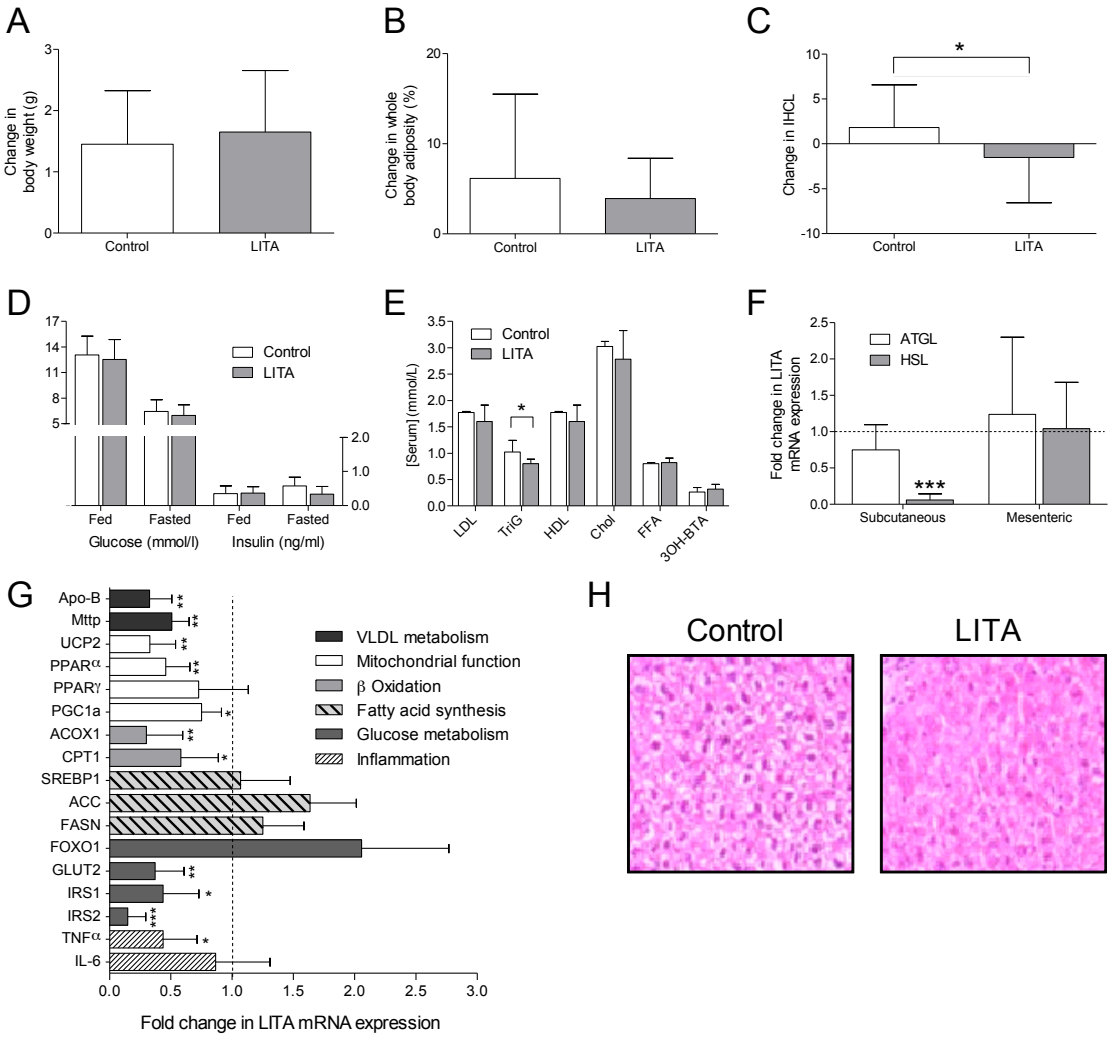
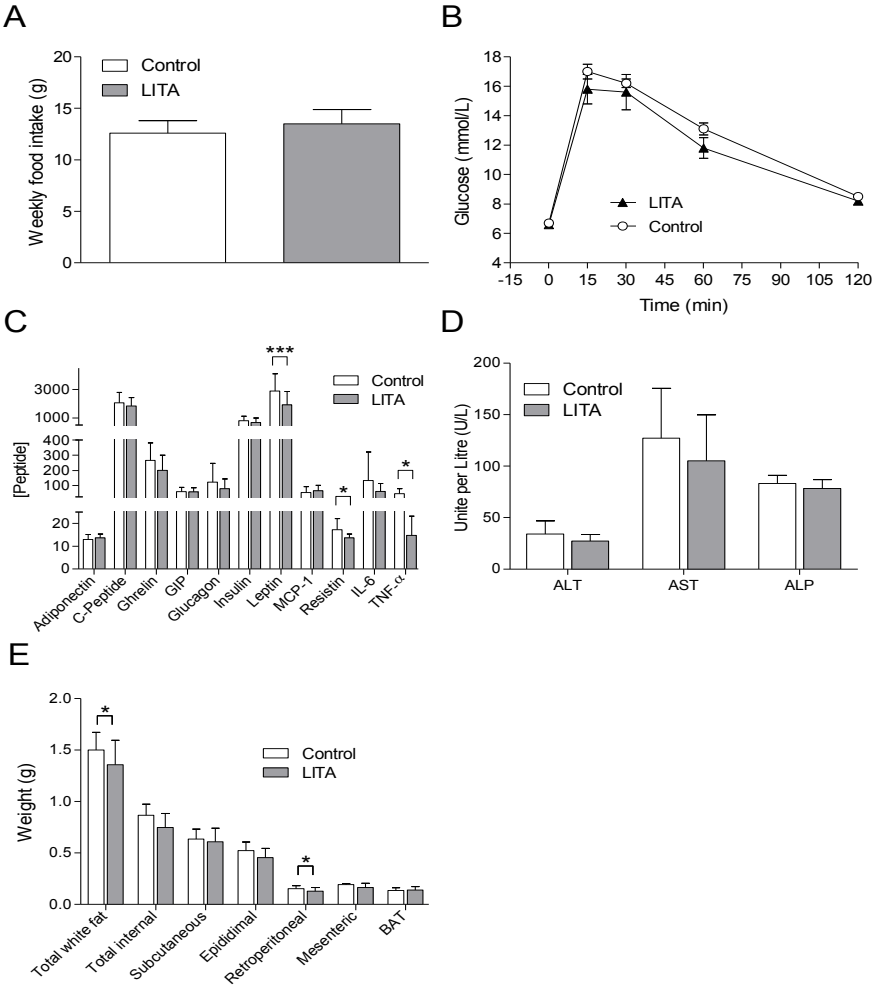
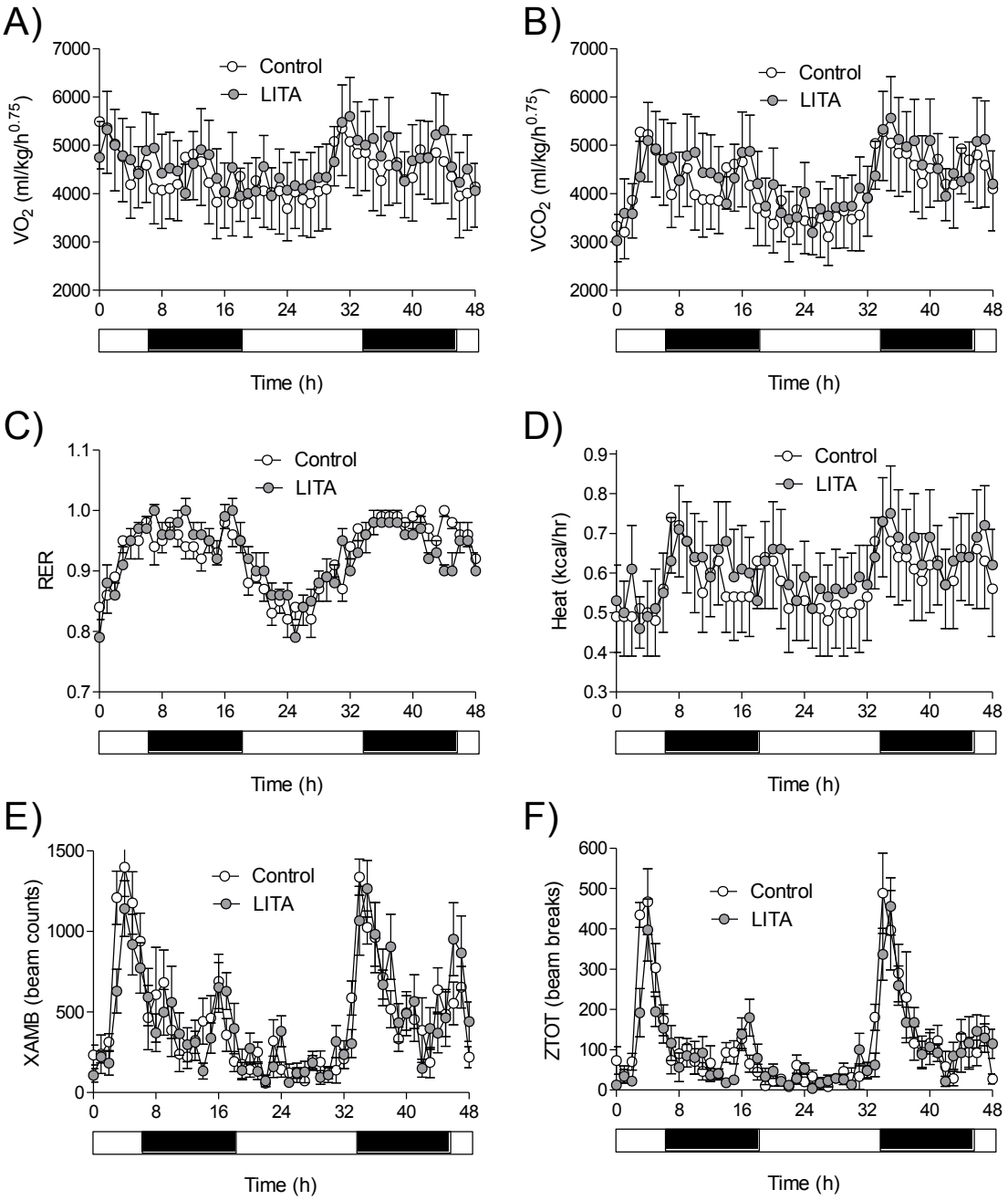


Figure 4 - The preventative effects of LITA nanoparticles in mice placed on a NFD diet. Mice were placed on a normal fat diet (NFD) and injected every three days with either liposome encapsulated acetate (LITA) nanoparticles or control (HEPES) for 6 weeks. Overall change in**(A)** Body weight (g), **(B)** Whole body adiposity, **(C)** IHCL. Fed and fasted levels of plasma **(D)** Plasma lipids (mmol/L) (n=6/group), **(E)** Fed and fasted levels of serum glucose and insulin (n=8/group), **(F)** Fold change in adipose tissue mRNA expression in LITA compared to control animals (n=6/group) **(G)** Fold change in hepatic mRNA expression in LITA compared to control animals (n=6/group), genes grouped by function. **(H)** H&E staining of liver cross-section. Data analysed by 2 way ANOVA with Bonferroni test for multiple comparisons (GraphPad Prism); n=24/group; * = $p<0.05$, ** = $p<0.01$, *** = $p<0.001$.



Supplementary Figure 8 - The preventative effects of LITA nanoparticles in mice placed on a NFD diet. Mice were placed on a normal fat diet (NFD) and injected every three days with either LITA nanoparticles or control (HEPES) for 6 weeks. **(A)** Average weekly food intake (g) (n=24/group), **(B)** A glucose tolerance test (GTT) was performed following an overnight fast at the start of week 5 (n=10/group). **(C)** Additional circulating peptides (Adiponectin (ng/ml) (n=6/group), C-peptide (pg/ml), ghrelin (pg/ml), GIP (pg/ml), glucagon (pg/ml), insulin (pg/ml), Leptin (pg/ml), MCP-1 (pg/ml), Resistin (ng/ml), interleukin-6 (pg/ml) and TNF-α (pg/ml) (n=12/group), **(D)** Serum concentrations of 3 markers of liver function: Alanine transaminase (ALT), Aspartate transaminase (AST) and Alkaline phosphatase (ALP) (all U/L) (n=6/group). **(E)** Weights of adipose tissue depots (n=12/group). **=p<0.01; Data analysed by 2 way ANOVA with Bonferroni post-hoc test (GraphPad Prism).



Supplementary Figure 9 - The subsequent effects of LITA nanoparticles on respiratory and ambulatory parameters as measured by CLAMS metabolic cages. C57BL/6 mice were injected daily with either control liposomes or LITA nanoparticles for seven days and then individually housed in CLAMS metabolic cages for 48 hours. **(A)** VO_2, **(B)** VO_2, **(C)** RER, **(D)** Heat, **(E)** XAMB, **(F)** ZTOT. The 12-hour light/dark cycle is indicated by the open (light) and black (dark) bars below each graph. Results are mean ± sem; data analysed by the Mann-Whitney U test; n=8/group; *=p<0.05.

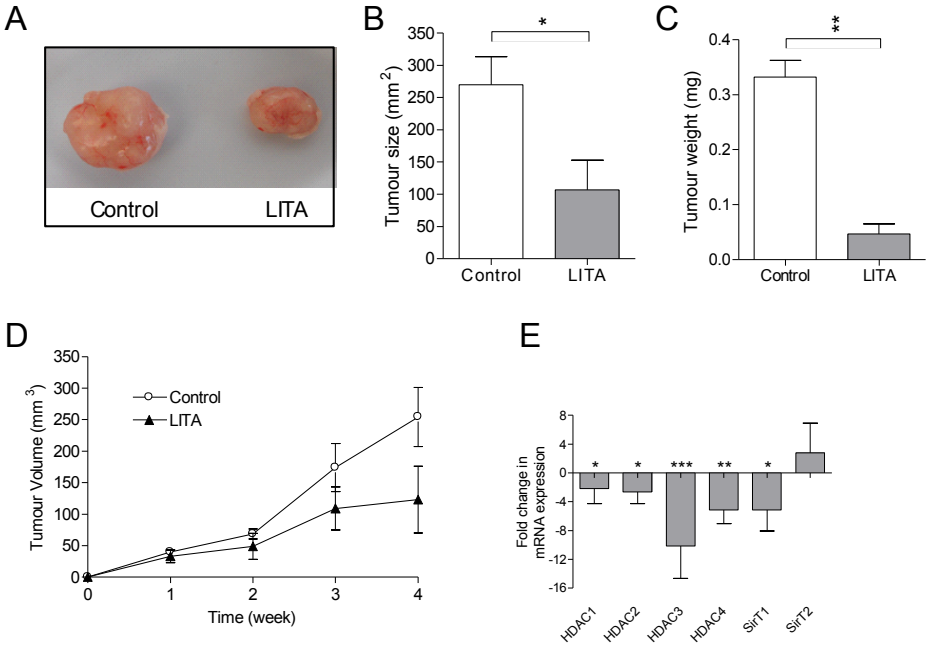
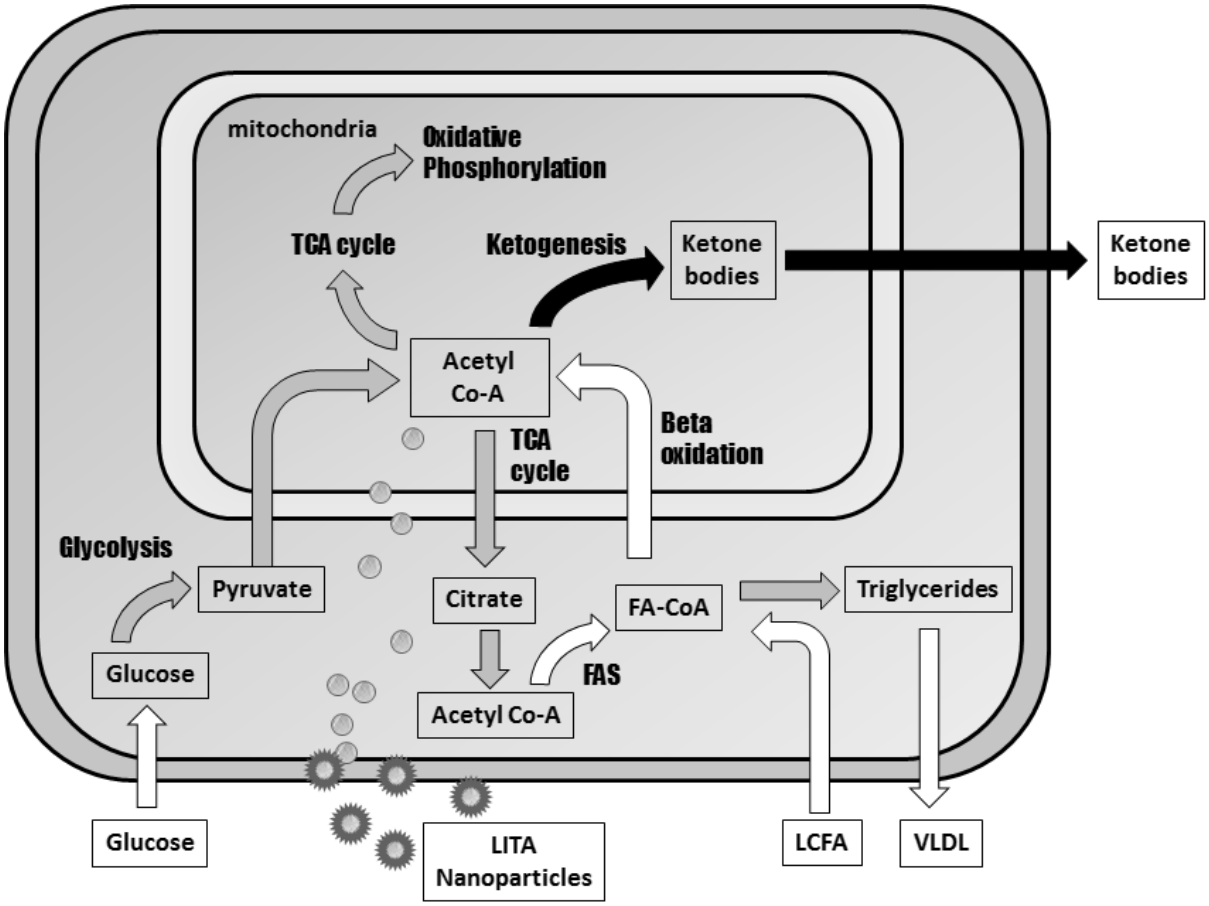


Figure 5 - The effects of LITA nanoparticles in murine HT-29 colorectal tumours. Mice were inoculated with HT-29 colorectal cancer cells and were injected every three days with either LITA nanoparticles or control (HEPES) nanoparticles for 4 weeks, once tumour was confirmed palpable. **(A)** Representative tumour grafts from LITA and Control injected animals, **(B)** Tumour size (mm^2), **(C)** Tumour weight (mg), **(D)** Tumour volume (mm^3) during the 4 week protocol, **(E)** Quantitative mRNA changes in xenograft tumour after chronic LITA administration normalized to control HEPES liposomes. Data analysed by Student's t-test or two-way ANOVA with Bonferroni post hoc test (GraphPad Prism); n=6/group; * = $p<0.05$, ** = $p<0.01$, *** = $p<0.001$.



Supplementary Figure 10 – Proposed mechanism of LITA action following hepatic delivery. The effects of LITA nanoparticles on key cellular pathways in the cytoplasm and mitochondria are shown. LITA nanoparticle administration leads to cellular uptake of acetate (grey circles) followed by mitochondrial accumulation of acetyl-CoA. Colour coded arrows represent the effects of LITA delivery; white arrows indicate down-regulation, black arrows indicate up-regulation. FAS: fatty acid synthesis; LCFA: Long chain fatty acids; VLDL: very low density lipoprotein

INTELLECTUAL PROPERTY OFFICE

Concept House
Cardiff Road
South Wales
NP10 8QQ
United Kingdom

Telephone +44 (0) 1633 814000
Minicom +44 (0) 8459 222250

DX 722540/41 Cleppa Park 3

Website www.ipo.gov.uk

Electronic Filing Receipt

Withers & Rogers LLP
4 More London Riverside
London
United Kingdom
SE1 2AU

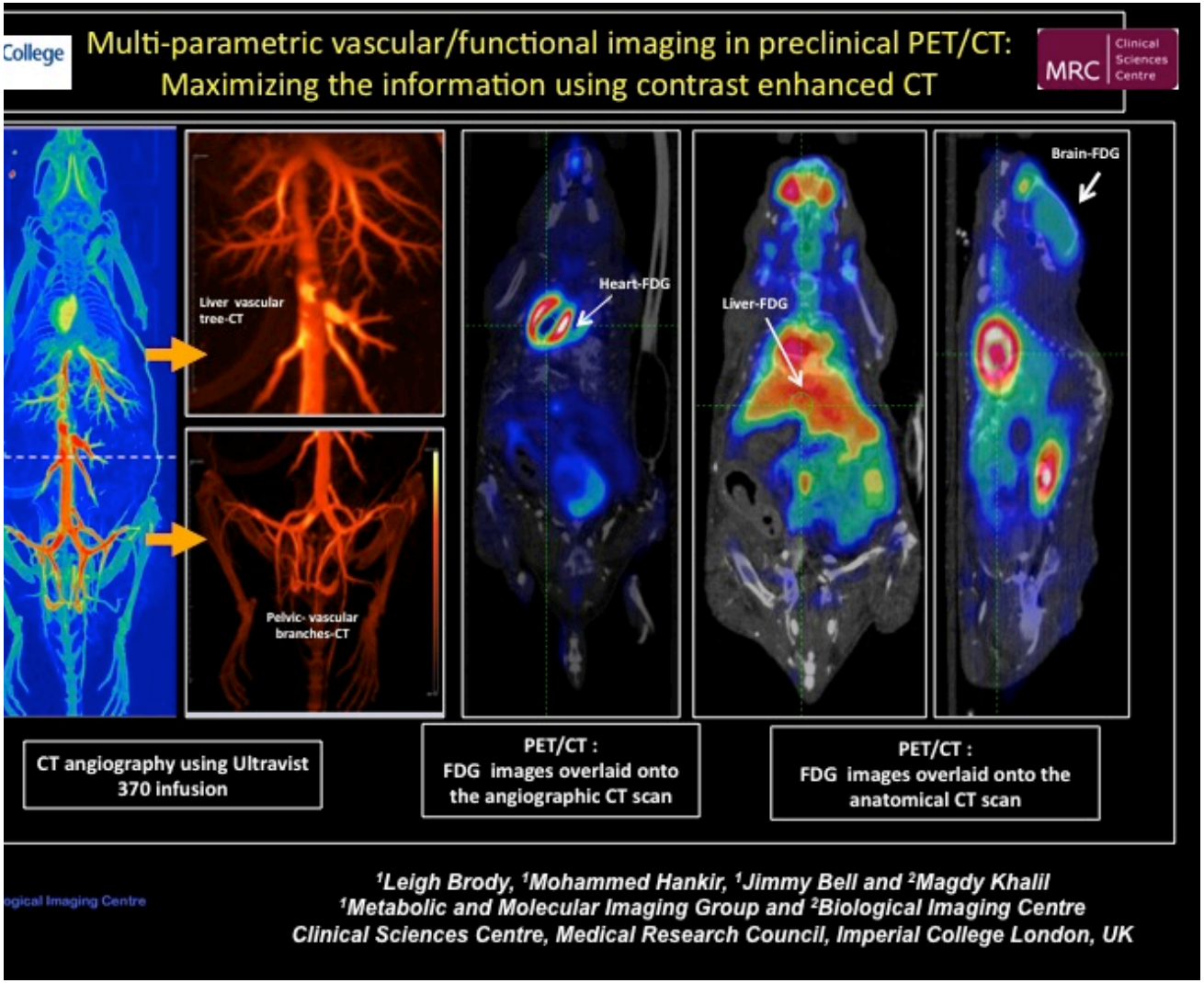
Your Ref: P527798GB/NAJ

28 August 2012

PATENT APPLICATION NUMBER 1215289.8

We have received your request for grant of a patent and recorded its details as follows:

Filing date(*)	28 August 2012	
Earliest priority date (if any)		
Applicant(s) / contact point	Medical Research Council, Imperial Innovations Ltd	
Application fee paid	No, pay by 28 August 2013	
Description (number of pages or reference)	22	
Certified copy of referenced application	Not applicable	
If description not filed	Not applicable	
Claims (number of pages)	3	
Drawings (number of pages)	6	
Abstract (number of pages)	1	
Statement of inventorship (Form 7)	No, file by 28 December 2013	
Request for search (Form 9A)	No, file by 28 August 2013	
Request for examination (Form 10)	None	
Priority Documents	None	
Other Attachments Received	Fee Sheet	FeeSheet.pdf
	Validation Log	ValidLog.pdf


College
Multi-parametric vascular/functional imaging in preclinical PET/CT:
Maximizing the information using contrast enhanced CT
MRC Clinical Sciences Centre
Liver vascular tree-CT
Pelvic- vascular branches-CT
Heart-FDG
Liver-FDG
Brain-FDG
CT angiography using Ultravist 370 infusion
PET/CT : FDG images overlaid onto the angiographic CT scan
PET/CT : FDG images overlaid onto the anatomical CT scan
[1]Leigh Brody, [1]Mohammed Hankir, [1]Jimmy Bell and [2]Magdy Khalil
[1]Metabolic and Molecular Imaging Group and [2]Biological Imaging Centre
Clinical Sciences Centre, Medical Research Council, Imperial College London, UK